Dissertation zur Erlangung des Doktorgrades

der Fakultät für Chemie und Pharmazie

der Ludwig-Maximilians-Universität München

# The Ion Exchange Approach

# –

# Expanding Elemental Variety in Nitridosilicate Chemistry

Philipp Bielec

aus

Dingolfing, Deutschland

2019

# Erklärung

Diese Dissertation wurde im Sinne von § 7 der Promotionsordnung vom 28. November 2011 von Herrn Prof. Dr. Wolfgang Schnick betreut.

# Eidesstattliche Versicherung

Diese Dissertation wurde eigenständig und ohne unerlaubte Hilfe erarbeitet.

München, 23.07.2019

.....

Philipp Bielec

| | |
|---|---|
| Dissertation eingereicht am | 02. April 2019 |
| 1. Gutachter: | Prof. Dr. W. Schnick |
| 2. Gutachter: | Prof. Dr. O. Oeckler |
| Mündliche Prüfung am | 17. Mai 2019 |

Dedicated to my beloved family.

# Acknowledgements

Mein besonderer Dank gilt Herrn Prof. Dr. Wolfgang Schnick für die Möglichkeit diese Dissertation in seinem Arbeitskreis unter hervorragenden Arbeitsbedingungen anfertigen zu können. Durch die Chance zur freien und eigenständigen Gestaltung meines Forschungsgebiets sowie zur aktiven Teilnahme an Fachtagungen konnte ich mich neben der fachlichen Seite, vor allem auch in persönlicher Hinsicht enorm weiterentwickeln. Ich möchte mich zudem für unzählige inspirierende Gespräche sowie seine den Mitarbeitern entgegengebrachte Wertschätzung bedanken.

Ganz besonderer Dank gilt Herrn Prof. Dr. Oliver Oeckler für die Übernahme des Koreferats meiner Dissertation sowie die wirklich sehr schöne Zusammenarbeit in unseren gemeinsamen Projekten.

Herrn Prof. Dr. Hubert Huppertz, Herrn Prof. Dr. Heinz Langhals, Herrn Prof. Dr. Konstantin Karaghiosoff und Herrn Prof. Dr. Hans-Christian Böttcher danke ich herzlich für ihre Bereitschaft als Teil der Prüfungskommission meiner Doktorarbeit zur Verfügung zu stehen.

Vielen Dank an meine Laborkollegen Dr. Dominik Baumann, Dr. Alexey Marchuk, Dr. Frank Tambornino, Dr. Matthias Wörsching, Dr. Eva-Maria Bertschler, Dr. Simon Kloß, Sebastian Wendl, Sebastian Vogel, Tobias Gifthaler und Stefanie Schneider sowie meinen Schreibstubenkollegen Dr. Christian Maak für die tolle Zeit und die vielen spaßigen „D2.110 & friends“ Nachsitzungen. Danke natürlich auch allen anderen Mitgliedern des Arbeitskreises für die schöne und lustige gemeinsame Zeit.

Ein großer Dank gilt Theresa Block, Lucien Eisenburger, Lars Deubner, Daniel Günther, Ann-Kathrin Henß, Dr. Ryky Nelson, Dr. Ralf Stoffel, Dr. Jonathan P. Wright, PD Dr. Oliver Janka, Prof. Dr. Rainer Pöttgen, Prof. Dr. Florian Kraus, Prof. Dr. Oliver Oeckler und Prof. Dr. Richard Dronskowski für die großartige Zusammenarbeit in diversen Projekten.

Vielen Dank auch an meine fleißigen Praktikanten Zehra Kilinc, Florian Engelsberger, Max Ellias und Marlene Fadel, die alle hervorragende Beiträge zu meiner Arbeit geleistet haben.

Herzlichen Dank auch an Wolfgang Wünschheim, Thomas Miller, Dr. Dieter Rau und Olga Lorenz für die Unterstützung bei allen technischen und organisatorischen Angelegenheiten. Bei Christian Minke und Jarka Obel bedanke ich mich für unzählige REM und ICP-OES Messungen.

In besonderer Weise möchte ich mich bei PD Dr. Constantin Hoch für seine stets offene Tür für diverse Fragestellungen und seine Fürsprache bedanken.

Vielen Dank auch an unseren Glasbläser Rudolf Klinger und seine Mitarbeiter, die wirklich für jede Fragestellung eine passende Antwort parat hatten. Ihre Arbeit war von unschätzbarem Wert für die verwendete Schutzgastechnik.

Bei allen anderen Mitgliedern des Lehrstuhls für Anorganische Festkörperchemie bedanke ich mich für die tolle Arbeitsatmosphäre und die unvergessliche Zeit im 2. Stock.

Mein größter Dank gilt meiner Familie, insbesondere meinen Eltern und meiner Frau Joanna. Ohne eure jahrelange Unterstützung und Liebe hätte ich diesen Weg nicht gehen können.

"*No one who achieves success does so without the help of others. The wise and confident acknowledge this help with gratitude.*"

Alfred North Whitehead (1862–1947)

"Every aspect of the world today – even politics and international relations – is affected by chemistry."

Linus Pauling (1901–1994)

# Abbreviations

| | |
|---|---|
| *AE* | alkaline earth metal |
| ca. | circa |
| CHARDI | charge distribution |
| *CN* | coordination number |
| DFT | density functional theory |
| DOS | density of states |
| DPS | density of phonon states |
| DSC | differential scanning calorimetry |
| DTA | differential thermal analysis |
| *E* | energy |
| EDX | energy dispersive X-ray spectroscopy |
| *EN* | electronegativity |
| FC | field cooled |
| GGA | generalized gradient approximation |
| *GOF* | goodness of Fit |
| HAADF | high-angle annular dark-field imaging |
| *Hal* | halogen element |
| HR | high resolution |
| HT | high temperature |
| ICP-MS | inductively coupled plasma mass spectrometry |
| ICP-OES | inductively coupled plasma optical emission spectroscopy |
| $\kappa$ | condensation degree (Si/N) |
| LDA | local-density approximation |
| LED | light emitting diode |
| no. | number |
| opt. | optimized |
| pc-LED | phosphor converted LED |
| iCOHP | integrated crystal orbital Hamilton population |
| *M* | magnetization / metal (sum formula) |
| PAW | projector-augumented wave |
| pCOHP | projected crystal orbital Hamilton population |
| PBE | Perdew, Burke and Ernzerhof |
| PPMS | physical property measurement system |
| PXRD | powder X-ray diffraction |
| *RE* | rare earth metal |
| SAED | selected area diffraction |
| SDI | "$Si(NH)_2$" |
| SOC | spin orbit coupling |
| STEM | scanning transmission electron microscopy |
| *T* | temperature |
| $T_N$ | Néel temperature |
| TDPXRD | temperature dependent X-ray powder diffraction |
| TEM | transmission electron microscopy |
| TGA | thermogravimetric analysis |
| UV | ultraviolett |
| VASP | Vienna *ab initio* simulation package |
| Vis | visible |
| VLS | vapour-liquid-solid |
| $\chi$ | magnetic suszeptibility |
| XPS | X-ray photoelectron spectroscopy |
| XRD | X-ray diffraction |
| ZFC | zero-field cooled |

# Table of Contents

# 1 Introduction

"*Der Fernerstehende, der nur die Fortschritte der empirischen Metalltechnik vor Augen hat, wird vielleicht nach dem Nutzen solcher Arbeit fragen. Wir treiben aber auch in der Wissenschaft eine Politik auf weite Sicht, und wir erstreben durch Grundlagenforschung eine umfassende Theorie, weil sie uns dem höchsten Ziel aller Wissenschaft näherbringt. Es besteht darin, Neues vorauszusagen. […] Damit aber wird alle Grundlagenforschung letzten Endes zur Zweckforschung auf weite Sicht.*"[1]

With this pleading for fundamental research, Eduard Zintl closed his revolutionary work "Intermetallische Verbindungen" emphasizing the importance of research based on curiosity without forseeable profit for applications. Simultaneously, Zintl proposed the following relationship between basic and applied research: In the long term, knowledge generated by fundamental research represents the foundation for applied research. Indeed, many phenomena discovered by basic research, e.g. X-rays,[2] radioactivity or the giant magnetoresistance effect, are now, after commercialization, an inherent part of daily life and of enormous technological importance.[3] Some phenomena have even been discovered by pure chance. In 1907, Henry J. Round first described the electroluminescence effect with the words: "*During an investigation of the unsymmetrical passage of current through a contact of carborundum and other substances a curious phenomenon was noted.*"[4] Now, over a century later,[5] LED based light sources are state of the art and slowly but surely replacing incandescent lamps and mercury containing fluorescent lamps.[6] In 2030, approximately 640 TWh, which is equivalent to the current total energy consumption of Canada, are going to be saved globally by efficient lighting.[6] This energy saving accounts to a prevention of 3.3 gigatonnes of $CO_2$ being released, a significant step in the right direction in terms of global climate change.

One main step in the development for commercialization of LEDs has been the invention of phosphor-converted (pc)-LEDs.[7] Here, a primary LED-chip (blue or ultraviolet) is coated with phosphors, which absorb and convert the LED light to emit light of a longer wavelength (Stokes shift).[8] Many different compound classes such as oxides,[9] sulfides, or nitrides have been investigated as hosts for activator ions such as $Eu^{2+}$ or $Ce^{3+}$ to obtain phosphors with desirable properties.[10] Descending from purely academic interest,[11] nitridosilicates turned out to be one of the most relevant compound classes for application in pc-LEDs.[10b,12]

Various intrinsic advantages, like the good thermal and chemical stability,[13] the rigidity of highly condensed covalent anionic Si–N networks as well as the enormous structural variability make nitridosilicates a compound class intensively investigated by applied and fundamental researchers.[14] While applied research is so far primarily interested in nitridosilicates with luminescent properties, fundamental research in nitridosilicate chemistry is facing two targets:

1. **Preparation of nitridosilicates with novel structures**
2. **Access to an increased elemental variety**

With numerous nitridosilicates that have been discovered until 2016,[11,13,15] a great deal of knowledge about different Si–N networks and thus the enormous structural variability of nitridosilicates has been generated. Nevertheless, only 18 different metallic elements have been stabilized in nitridosilicates, thereof only 13 elements in compounds not related to simple *AB* (wurtzite) and $AB_2$ (fluorite) structure types (Figure 1.1).[11,13,15]

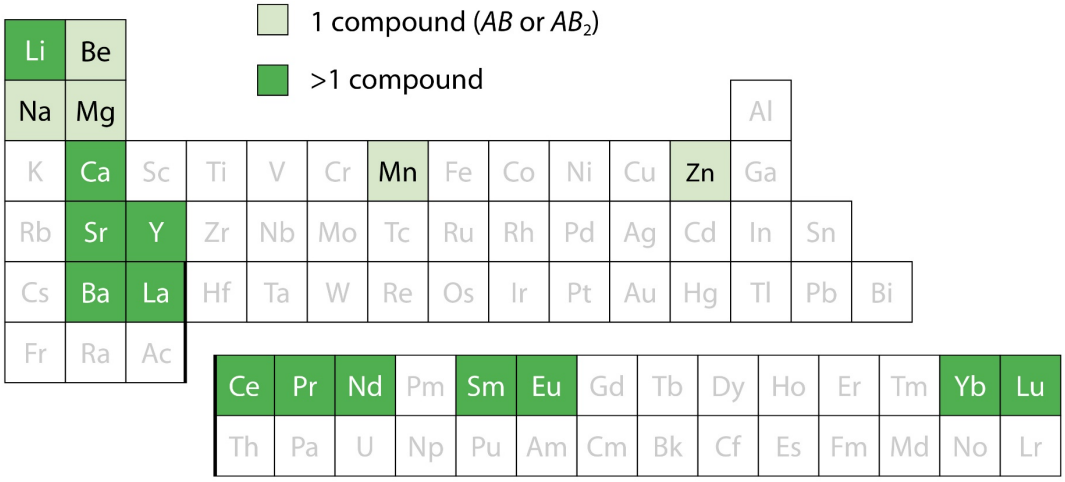


**Figure 1.1:** Section of the periodic table with elements marked in green that were observed as counter cations in nitridosilicates before this work.[11,13,15]

This thesis tackles the second challenge of increasing the elemental variety in nitridosilicates with the aim of providing a systematic access to yet unprecedented counter cations. Therefore, the latter have been chosen from each region of the periodic table of elements, that had so far been inaccessible for nitridosilicate chemistry, namely the transition metals, the *p*-block and the actinides.

## 1.1 Nitridosilicates – The Basics

Nitridosilicates are composed of anionic Si–N building units and counter cations $M^{n+}$. Although, formally labeled as $Si^{4+}$ and $N^{3-}$, Si–N bonds are predominantly covalent due to a comparatively low difference in electronegativities ($\Delta EN \approx 1.3$).[16] Therefore, the nonmetal-character of Si and its $sp^3$-hybridization are strengthened resulting in the fundamental building unit of nitridosilicates, namely the $SiN_4$ tetrahedron (Figure 1.2).[17]

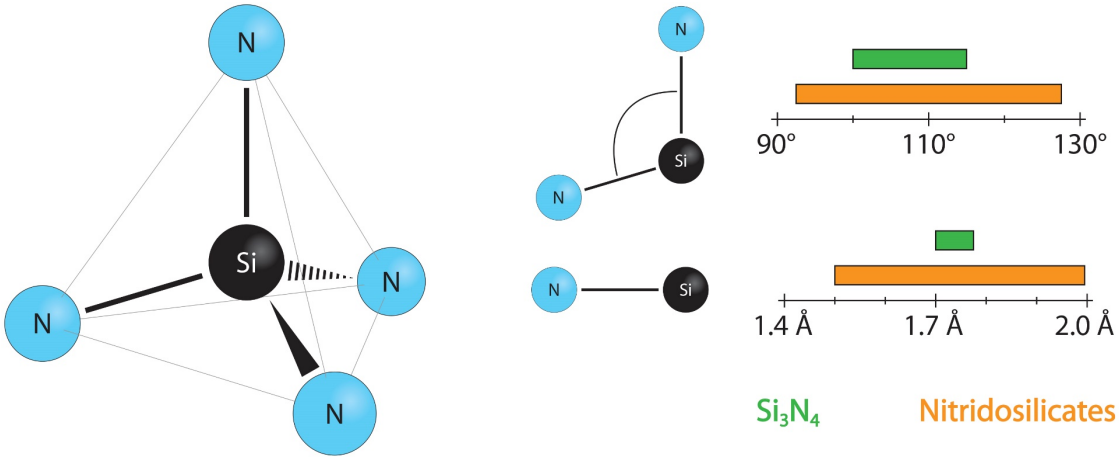


**Figure 1.2:** $SiN_4$ tetrahedron, the fundamental building unit of $Si_3N_4$ and nitridosilicates, with observed ranges for Si–N bond lengths and N–Si–N-angles.[11,13,15,18]

When comparing the reported Si–N bond lengths and N–Si–N angles in nitridosilicates with those in the parent compound $Si_3N_4$,[11,13,15,18] significant deviations are found (Figure 1.2). This can be mainly explained by the connectivity of N atoms. In the case of bridging N atoms the distances *d*(Si–N) typically grow with an increasing connectivity of the N atoms.[19] In both ambient pressure polymorphs α- and β-$Si_3N_4$ these atoms are exclusively in threefold coordination by Si, usually denominated $N^{[3]}$.[20] However, in nitridosilicates connectivities of terminal $N^{[1]}$, twofold-bridging $N^{[2]}$, and $N^{[3]}$ atoms have been observed, as well. Furthermore, even $N^{[4]}$ atoms, which connect four $SiN_4$ tetrahedra are possible in nitridosilicate chemistry.[11,13a,15p] Such fourfold bridging N atoms exhibit ammonium character and were first identified in $BaYbSi_4N_7$, a nitridosilicate disocvered by HUPPERTZ *et al.* in 1996.[13a]

In general, $SiN_4$ tetrahedra are most frequently connected by common vertices. Edge-sharing tetrahedra (first observed in $Ba_5Si_2N_6$),[13b,15m,15t,15ah] however, frequently occur in nitridosilicate chemistry, which is in stark contrast to oxosilicates, where $SiO_4$ tetrahedra exclusively share common corners aside from one unconfirmed exception, namely fibrous $SiO_2$.[17,21] The existence of edge-

sharing $SiN_4$ tetrahedra compared to $SiO_4$ tetrahedra may be explained in two ways, in line with PAULING'S RULES.[22] First, a formal $N^{3-}$ has a larger ionic radius than a formal $O^{2-}$.[23] Thus the distance of the two adjacent formal $Si^{4+}$ is increased. Secondly, the high amount of covalency in Si–N bonds reduces the effective charge of the adjacent $Si^{4+}$ in a way that electrostatic repulsion is less critical.

Despite the intrinsic higher stability of Si–O bonds compared to Si–N bonds,[24] nitridosilicates are known for their remarkable chemical and thermal stability,[14a] easily withstanding air and moisture, especially when $\kappa > {}^1/_2$. The reason for that is the increased range for the degree of condensation (${}^1/_4 \leq \kappa_{Si-N} \leq {}^3/_4$), compared to oxosilicates (${}^1/_4 \leq \kappa_{Si-O} \leq {}^1/_2$), which compensate the weaker Si–N interaction. Thus, nitridosilicates are often inert even in hot concentrated acids, alkaline solutions or at temperatures up to 1600 °C (in $N_2$).[14a]

Based on the building principles of $SiN_4$ tetrahedra and the wider range for $\kappa$, nitridosilicates exhibit a huge theoretical structural variability which even exceeds the one of the naturally occurring oxosilicates.[14b] Consequently, many structure types different to those in oxosilicates have already been observed in nitridosilicate chemistry at ambient pressure (Figure 1.3).[13,15a,15d,15f,15h-k,15m,15o,15r,15t,15v, 15x,15y,15aa,15ab,15ae,15ag-aj,15am,25]

## 1.2 Nitridosilicates – Structure Types

In principle, two general groups of nitridosilicates may be distinguished. First, there are compounds which arise from simple *AB* and $AB_2$ structures (α-ZnS and $CaF_2$)[26] where all formal cations $M^{n+}$ and $Si^{4+}$ are tetrahedrally coordinated by N atoms. These nitridosilicates have been denominated "double nitrides". All known instances ($Li_5SiN_3$, $MSiN_2$ with $M$ = Be, Mg, Mn, Zn and $MSi_2N_3$ with $M$ = Li, Na)[15a-g] had been discovered before 1995, when other *M*–Si–N compounds have been discovered, revealing the great structural variability of nitridosilicates.

In this second group, which includes the greater part of all known nitridosilicates, solely $SiN_4$ tetrahedra are observed with counter cations in diverse coordination environments. Among these nitridosilicates a wide range for $\kappa$ has been observed, reaching from the lowest possible value of ${}^1/_4$ of uncondensed $SiN_4$ tetrahedra ($CaSiN_4$)[15aj] up to ${}^{2.8}/_4$ ($BaSi_7N_{10}$),[13b] which is close to the maximum value as observed in $Si_3N_4$. In analogy to classical (oxo)silicates the compounds can be classified as

*inosilicates* ($RE_5Si_3N_9$,[15y] $Eu_2SiN_3$,[15aa] $LiCa_3Si_2N_5$)[15ah], *phyllosilicates* ($BaSiN_2$,[15t] $Ca_7Si_4N_{10}$)[15v] and *tectosilicates* (remaining ones) including zeolite like structures ($Ba_2Nd_7Si_{11}N_{23}$).[15o]

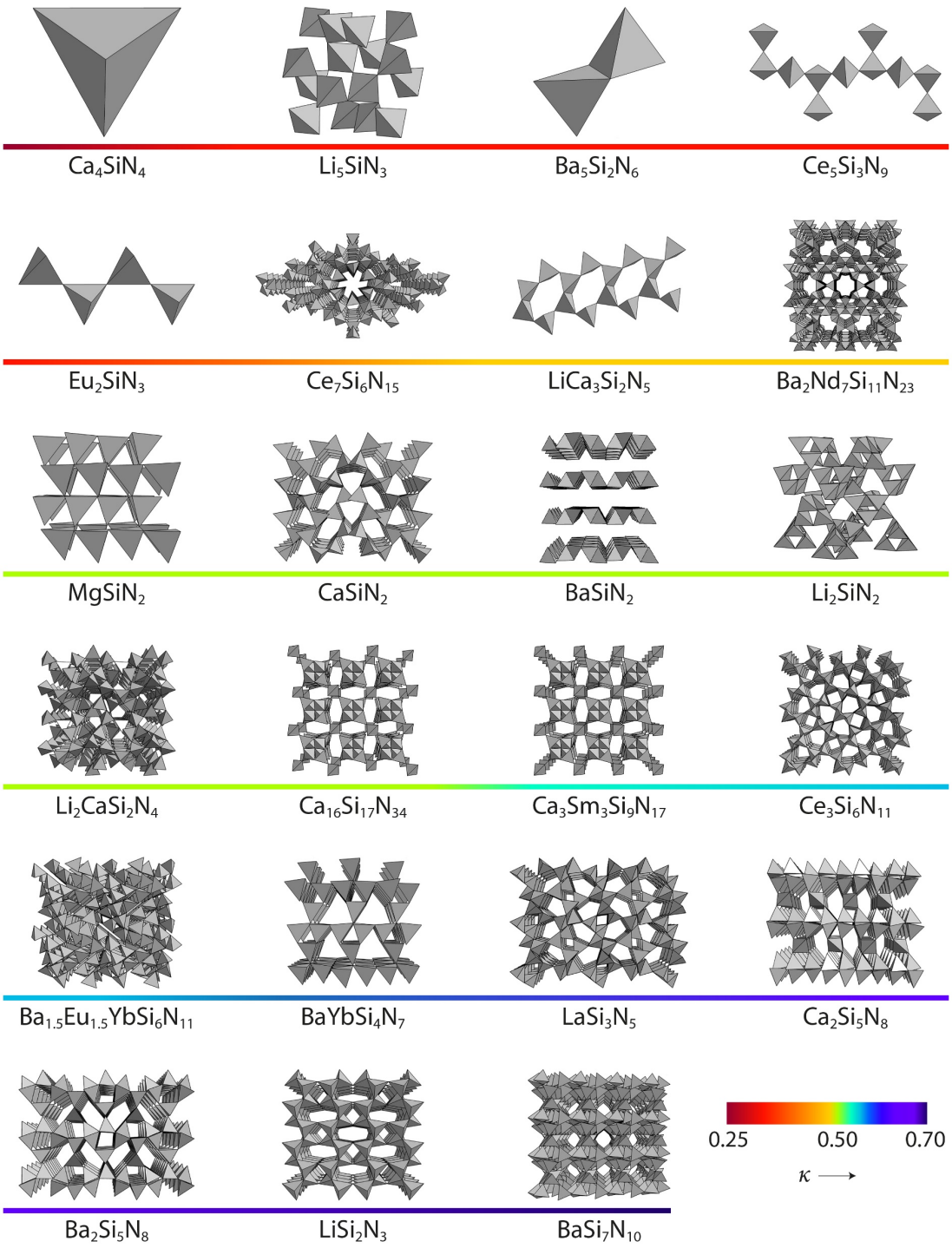


**Figure 1.3:** Different types of Si–N networks in nitridosilicates (ambient pressure), each displayed by its first representative, ordered by increasing degree of condensation $\kappa$. [13,15a,15d,15f,15h-k,15m,15o,15r,15t, 15v,15x,15y,15aa,15ab,15ae,15ag-aj,15am,25]

## 1.3 $M_2Si_5N_8$ – A Famous Group of Nitridosilicates

One group of nitridosilicates, that has so far probably drawn the most attention is $M_2Si_5N_8$ ($M$ = Ca, Sr, Ba, Eu).[11,15i,15j] These compounds were discovered in 1995 by SCHLIEPER *et al.* and in 1997 by HUPPERTZ *et al.*, belong to the first nitridosilicates not crystallizing in simple $AB$ or $AB_2$ structure types and they have been termed 2-5-8 (or 258) materials.

Beside of a high pressure polymorph, namely HP-$Ca_2Si_5N_8$,[27] $M_2Si_5N_8$ ($M$ = Ca, Sr, Ba, Eu) occurs in two ambient pressure polymorphs, a monoclinic structure which is formed by $Ca_2Si_5N_8$ and an orthorhombic one formed with the metals $M$ = Sr, Ba, Eu. As depicted in Figure 1.4, both structures are formally based on *dreier*-ring layers of condensed $SiN_4$ tetrahedra (gray), which are inter-connected to a three-dimensional network via further tetrahedra (dark gray).

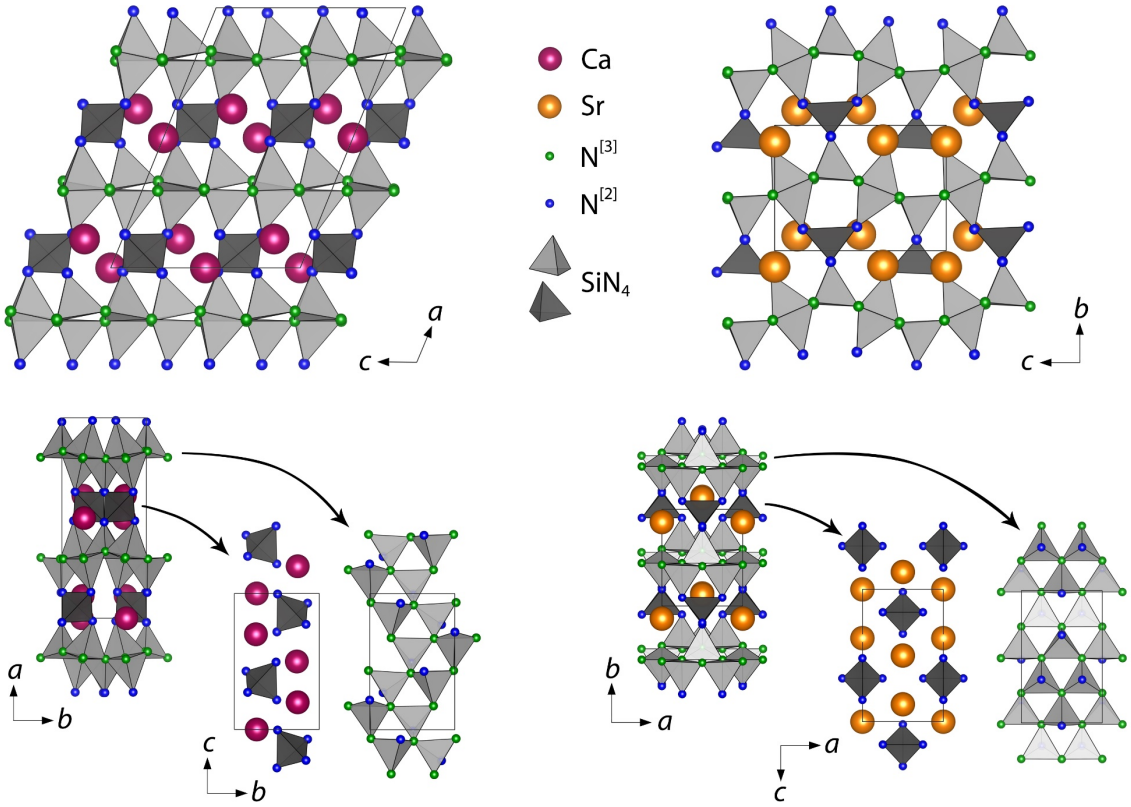


**Figure 1.4:** Crystal structures of monoclinic $Ca_2Si_5N_8$ (left) and orthorhombic $M_2Si_5N_8$ ($M$ = Sr, Ba, Eu) represented by $Sr_2Si_5N_8$ (right).

The layer-interconnecting tetrahedra (dark gray) are built up by $N^{[2]}$ atoms (blue) which are connected to two Si atoms, thus from a covalent point of view formally carrying one negative charge. This assumption is also supported by the cations' location in close proximity to these $N^{[2]}$ atoms in both cases, $Ca_2Si_5N_8$ as well as orthorhombic $M_2Si_5N_8$ ($M$ = Sr, Ba, Eu). By different up-down

sequences of the tetrahedra-vertices within the *dreier*-ring layers, the Si–N networks are able to adapt to small ions like $Ca^{2+}$ or large ones like $Sr^{2+}$, $Ba^{2+}$ and $Eu^{2+}$.

In 1997, HUPPERTZ discovered the luminescence effects of $Eu_2Si_5N_8$, when illuminated with UV light.[19] Subsequent investigations on $M_2Si_5N_8$ then revealed the extraordinary potential of $Eu^{2+}$ doped compounds as phosphors for pc-LED devices.[28] $M_2Si_5N_8$:$Eu^{2+}$ feature desirable properties like high chemical and thermal stability due to their rigid Si–N networks, tunable spectral positions of the emission bands by substitution of counter cations and a small Stokes shift that stabilizes the overall high luminescence efficiency at higher temperatures.[12a] Furthermore, due to the increased amount of covalency between N and the activator cation $Eu^{2+}$ compared to oxides that shifts the emission wavelength into the red spectral regions, $M_2Si_5N_8$:$Eu^{2+}$ compounds became a success story in solid-state lighting.[10b]

## 1.4 Nitridosilicates – Approaches to Synthesis

Many different approaches to the synthesis of nitridosilicates have been established since 1953 exhibiting two main common features.[15a] First, nitridosilicate syntheses typically require high reaction temperatures (T >700 °C). Secondly, it is crucial to exclude oxygen due to possible substitution N for O within the nitrides and due to the larger reactivity of $O_2$ compared to $N_2$. Four main synthesis routes leading to the discovery of novel nitridosilicate structure types are known, namely the *reaction of binary nitrides according to Lux and Flood*, the *nitridation of (inter)metallic compounds*, the *reactions in a metallic flux with azides as nitrogen source* and the *reaction of metals and silicon diimied*, which are discussed more detailed in the further text.

### Reaction of binary nitrides according to Lux and Flood

The Lux-Flood concept, initially designed for oxide chemistry, distinguishes between acids (oxygen acceptors) and bases (oxygen donors).[29] It can be applied to nitride chemistry analogously.

$$w\,M_xN_y + z\,Si_3N_4 \longrightarrow M_{wx}Si_{3z}N_{4z+wy} \qquad 1.1$$

Thus, a reaction as given in Equation 1.1 can be described as a formal transfer of $N^{3-}$ from $M_xN_y$ toward $Si_3N_4$ building up the anionic covalent Si–N network, whose charge is then balanced by the counterions $M^{n+}$. For example, the first investigations on nitridosilicates have been performed by

reaction of the binary nitrides $Li_3N$ and $Si_3N_4$, where a formal nitride ion $N^{3-}$ is transferred from $Li_3N$ onto $Si_3N_4$.[15a] Such a transfer of nitride typically decreases the degree of condensation $\kappa$.

### Nitridation of metallic compounds

Another early applied synthesis strategy is the reaction of metals or intermetallic phases with nitrogen (Equation 1.2). According to this strategy, the nitridosilicate $MgSiN_2$ has been prepared from nitridation of the intermetallic phase $Mg_2Si$.[15c]

$$M_xSi_y + z\,N_2 \rightarrow M_xSi_yN_{2z} \qquad 1.2$$

The strategy given in Equation 1.2 especially is suitable for $M^{3+}$ containing nitridosilicates as a possible strategy to avoid formation of thermodynamically stable binary nitrides $M$N due to the prior arrangement of $M$ and Si in intermetallics. Therefore, many rare earth ($RE^{3+}$) containing nitridosilicates like $RESi_3N_5$ ($RE$ = La, Ce, Pr, Nd, Sm) or $RE_3Si_6N_{11}$ ($RE$ = Ce, Pr, Nd) are readily accessible by this approach.[15h]

### Metallic flux with azide as nitrogen source

A strategy that typically yields well-formed crystals of nitridometallates in general and nitridosilicates in particular is using a metallic flux (Li or Na).[30] Here, Si and an electropositive metal are dissolved in the flux as well as *in situ* formed $N_2$ (corresponding Li or Na azides) in sealed ampoules (Equation 1.3).[15m]

$$x\,M + y\,Si + z\,(Na/Li)N_3 + w\,Na/Li \rightarrow M_xSi_yN_{3z} + (w+z)\,Na/Li \qquad 1.3$$

It is expected that oversaturation of soluble nitridic species, which are formed in the metallic flux, leads to crystallization at comparatively low temperatures of 700–1000 °C.

### Reactions of metals with SDI

So far, the most successful strategy in terms of expanding nitridosilicates' structural variety is the one exemplarily shown in Equation 1.4, developed by SCHNICK and coworkers.[15i-k]

$$x\,M + y\,\text{“}Si(NH)_2\text{”} \rightarrow M_xSi_yN_{2(y-z)} + z\,N_2 + y\,H_2 \qquad 1.4$$

From reaction between various metals and silicon diimide with the empirical formula $Si(NH)_2$,[31] a precursor for $Si_3N_4$ preparation,[32] the nitridosilicates $M_2Si_5N_8$ ($M$ = Ca, Sr, Ba, Eu),[11,15i,15j] $Ce_3Si_6N_{11}$,[15k] $MYbSi_4N_7$ ($M$ = Sr, Ba),[11,13a,15p] $BaSi_7N_{10}$,[13b] $Ba_2Nd_7Si_{11}N_{23}$,[13k] $Ba_{1.5}Eu_{1.5}YbSi_6N_{11}$,[15am]

$LiSi_2N_3$,[15f,15r] $RE_5Si_3N_9$ ($RE$ = La, Ce, Pr),[15y,15z] $RE_7Si_6N_{15}$ ($RE$ = La, Ce, Pr),[15x] $Eu_2SiN_3$ and $Ca_3RE_3Si_9N_{17}$ ($RE$ = Sm, Yb)[15aa,15ai] have been prepared and structurally characterized.

### Other routes

Many other nitridosilicates like $NaSi_2N_3$,[15g] $Li_4M_3Si_2N_6$ ($M$ = Ca, Sr),[15ac,15af] $LiCa_3Si_2N_5$,[15ac,15ah] $Li_5RE_5Si_4N_{12}$ ($RE$ = La, Ce),[15ad] $Li_2MSi_2N_4$ ($M$ = Ca, Sr),[15ae] or $AERESi_4N_7$:$Eu^{2+}$ ($AE$ = Sr, Ba; $RE$ = Y, La, Lu)[15an] have been discovered by combination of the above mentioned synthesis strategies or by use of additional starting materials (e.g. halides).

Further variation of the existing strategies like it has been done for preparation of $Li_2SiN_2$ by a modified precursor approach using $Si(CN_2)_2$ instead of SDI are also promising.[15ab]

Even ammonolysis of an oxide ($MnSiO_3$) by ammonia has been successfully applied for nitridosilicate preparation ($MnSiN_2$).[15e]

## 1.5 Elemental Variety – A Substantial Restriction in Nitridosilicate Chemistry

The great advantage of nitridosilicate chemistry, namely its enormous structural variability, is in stark contrast to its elemental variety.[11,13,15] Several reasons are responsible for this restriction. Among them, three main issues have been identified (Figure 1.5), and are discussed in more detail in further course.

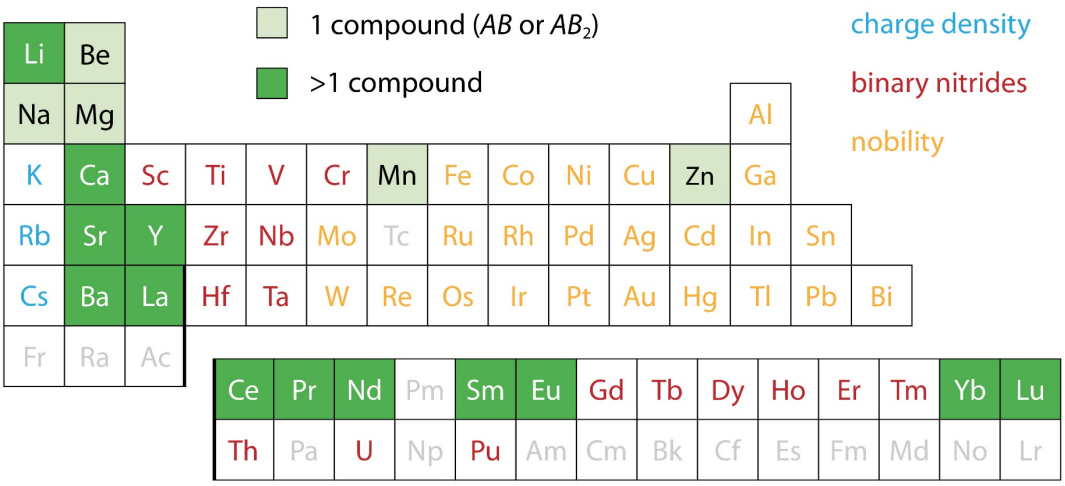


**Figure 1.5:** Section of the periodic table with elements marked in green which were observed as counter cations in nitridosilicates before this work. Issues jointly responsible for the non-existence of corresponding nitridosilicates are marked in blue, red, and orange.[11,13,15]

### Charge density

Focusing on the highly electropositive alkali metals (Figure 1.5), it can be seen, that only the small ones, namely Li and Na are quite suitable for preparation of nitridosilicates. In case of the alkali metals K, Rb and Cs it is likely that the combination of a low charge (+1) with a large ionic radius (>1.3 Å)[23] is not sufficient to stabilize anionic charges on nitrogen at the selected reaction conditions.[33] This charge density issue has also been proposed as a reason for the non-existence of the hypothetical binary nitrides "$Sr_3N_2$" and "$Ba_3N_2$".[32]

### Binary nitrides

The high stability of binary nitrides (NaCl- and wurtzite-type) *M*N of early transition metals, lanthanides and actinides represents a deep thermodynamic sinkhole, which often prevents nitridosilicate formation applying the classic synthesis strategies given in chapter 1.3.[34]

### Nobility

Due to the comparatively (e.g. to oxygen) low oxidative strength of nitrogen, syntheses of nitridosilicates require strong electron donors to reduce N or to prevent oxidation of anionic N species. This especially applies to late *d*- or *p*-block metals. First, the nobilty of these elements can be high enough to generally prevent reactions with nitrogen at ambient pressure as is the case with most platinoids or elements such as Pb, where reactions with $N_2$ are only observed by supporting electric discharges.[35] Second, slightly less noble metals rather form interstitial binary nitrides (e.g. Fe, Mo, W),[33d] which decompose into metallic phases and $N_2$ below the temperatures necessary for nitridosilicate syntheses.[36] Also less noble metals might rather form nitridometallates where these metals are not the counter ions but part of the anionic networks (e.g. Al, Ga).[37]

## 1.6 The Potential of Nitridosilicate Chemistry

Arranging the metals of the periodic table of elements according to their *EN* values,[33d,38] as it is done in Figure 1.6, it becomes clear that nitridosilicate chemistry exhibits a great potential for exploration that so far is completely unexploited due to synthetic inacessibility.

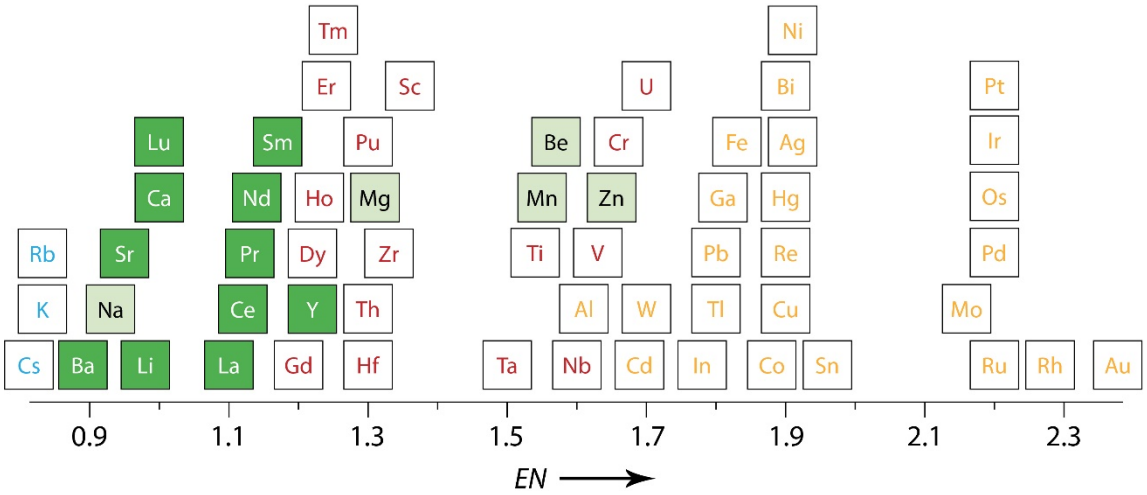


**Figure 1.6:** Metals sorted by increasing *EN* according to Pauling.[37] Elements marked in green have been incorporated into nitridosilicates before this thesis.

As depicted in Figure 1.6, elements that have been incorporated into highly covalent Si–N networks (not *AB* or $AB_2$ types) are limited to the narrow range of *EN* between 0.9 and 1.2.[37] That means, less than 19% of the possible *EN* range of metals have been accessible before this thesis. This offers a great expansion potential on nitridosilicates in case of solving the challenges posed by stable binary nitrides (red in Figure 1.6) and comparatively noble metals (yellow in Figure 1.6).

## 1.7 The Objective – Expanding Elemental Variety

The main objective of this thesis has been the access to nitridosilicates with unprecedented compositions in order to expand the elemental variety of this compound class. Since prior attempts have so far not been successful applying the known synthesis approaches toward nitridosilicates,[39] a crucial criterion for achieving this objective has been the development of a novel strategy.

Despite of different precursors used to prepare nitridosilicates, all synthesis routes known before this work are based on a *bottom-up* approach. Here, the nitridosilicate networks are built up after breaking down the starting materials' structures. Thus, the properties of the selected metals play a crucial role prior und during Si–N network formation. In case of the less electronegative metals, which had been stabilized in nitridosilicates before, electrons are easily transferred to N and anionic

N species are not oxidized by the corresponding cations, therefore enabling the formation of nitridosilicates. In contrast, when metals are used which form stable binary nitrides or those that are too noble, other thermodynamic sinkholes like *M*N or intermetallic compounds and $N_2$ become favoured, preventing nitridosilicate formation.

In order to disempower these two issues (*stable binary nitrides* and *nobility* of the selected metals), one possible strategy for a novel approach was to, at least partially, avoid the reaction step, in which Si–N bonds are formed. Based on the assumption that $SiN_4$ tetrahedra should be preformed, nitridosilicates have been used as starting materials.

Inspired by different solid-state compounds like β-alumina, oxoferrates or oxoaluminates where ion exchange reactions in salt melts have been successfully performed before,[40] the breakthrough has been achieved by a reaction (980 °C) that was designed for prevention of *M*N (*M* = Sc) formation, between $ScCl_3$, a highly reactive Sc compound, and α-$Ca_2Si_5N_8$, a nitridosilicate that was thought unlikely to offer its N atoms to form ScN, due to its highly condensed Si–N network ($\kappa = {}^5/_8$).

Two key messages were inferred from a PXRD of the product mixture. First, no ScN, but $CaCl_2$ was observed and secondly, the diffraction pattern of α-$Ca_2Si_5N_8$ was still present after the reaction but with decreased lattice parameters. EDX measurements then confirmed, that ion exchange has occurred between some $Ca^{2+}$ ions and 0.66 equivalents of $Sc^{3+}$ (equation 1.1)

$$\alpha\text{-}Ca_2Si_5N_8 + x\ ScCl_3 \rightarrow Ca_{2-1.5x}Sc_xSi_5N_8 + 1.5x\ CaCl_2 \qquad 1.5$$

This possibility to exchange cations in highly condensed nitridosilicates by salt melts in a *top-down* approach was subsequently employed to investigate selected elements that had so far not been stabilized in nitridosilicates. This thesis offers first insights into a so far by over 50% increased elemental variety in nitridosilicate chemistry applied to the model system $M_2Si_5N_8$.[41]

## 1.8 References

[1] E. Zintl, "Intermetallische Verbindungen", *Angew. Chem.* **1939**, *52*, 1–6.

[2] a) W. C. Röntgen, "ON A NEW KIND OF RAYS", *Science* **1896**, *3*, 227–231; b) W. C. Röntgen, "A NEW FORM OF RADIATION", *Science* **1896**, *3*, 726–729.

[3] a) A. H. Becquerel, "Sur les radiations émises par phosphorescence", *C. R. Hebd. Seances Acad. Sci.* **1896**, *122*, 420–421; b) A. H. Becquerel, "Sur les radiations invisibles émises par les corps phosphorescents", *C. R. Hebd. Seances Acad. Sci.* **1896**, *122*, 501–503; c) A. H.

Becquerel, "Sur diverses propriétés des rayons uraniques", *C. R. Hebd. Seances Acad. Sci.* **1896**, *123*, 855–858; d) M. N. Baibich, J. M. Broto, A. Fert, F. Nguyen Van Dau, F. Petroff, P. Etienne, G. Creuzet, A. Friederich, J. Chazelas, "Giant Magnetoresistance of (001)Fe/(001)Cr Magnetic Superlattices", *Phys. Rev. Lett.* **1988**, *61*, 2472–2475; e) G. Binasch, P. Grünberg, F. Saurenbach, W. Zinn, "Enhanced magnetoresistance in layered magnetic structures with antiferromagnetic interlayer exchange", *Phys. Rev. B* **1989**, *39*, 4828–4830.

[4] H. J. Round, "A Note on Carborundum", *Electr. World* **1907**, *9*, 309.

[5] a) O. V. Lossev, "CII. Luminous Carborundum Detector and Detection Effect and Oscillations with Crystals", *London, Edinburgh, Dublin Philos. Mag. J. Sci.* **1928**, *6*, 1024–1044; b) N. Holonyak, S. F. Bevacqua, "COHERENT (VISIBLE) LIGHT EMISSION FROM $Ga(As_{1-x}P_x)$ JUNCTIONS", *Appl. Phys. Lett.* **1962**, *1*, 82–83; c) H. Amano, M. Kito, K. Hiramatsu, I. Akasaki, "P-Type Conduction in Mg-Doped GaN Treated with Low-Energy Electron Beam Irradiation (LEEBI)", *Jpn. J. Appl. Phys.* **1989**, *28*, L2112–L2114; d) S. Nakamura, T. Mukai, M. Senoh, S.-i. Nagahama, N. Iwasa, "$In_xGa_{(1-x)}N/In_yGa_{(1-y)}N$ superlattices grown on GaN films", *J. Appl. Phys. (Melville, NY, U. S.)* **1993**, *74*, 3911–3915.

[6] United Nations Environment Programme, *Accelerating the global adoption of energy-efficient lighting – U4E policy guide serie* **2017**, http://hdl.handle.net/20.500.11822/20406, last time visited on 19th February, 2019.

[7] a) Nichia, *White LED lamp: Light emission with high luminous efficiency halving production costs* **1996**, Nikkei Sangyo Shimbun; b) K. Bando, K. Sakano, Y. Noguchi, Y. Shimizu, "Development and Application of High-brightness White LEDs", *Proc. 264th Keikohtai Dohgakkai, Tokyo* **1996**, *11*, 5–14; c) P. Schlotter, R. Schmidt, J. Schneider, "Luminescence conversion of blue light emitting diodes", *Appl. Phys. A: Mater. Sci. Process.* **1997**, *64*, 417–418; d) K. Bando, K. Sakano, Y. Noguchi, Y. Shimizu, "Development of High-bright and Pure-white LED Lamps", *J. Light Visual Environ.* **1998**, *22*, 2–5; e) G. Bogner, A. Debray, G. Heidel, K. Hoehn, U. Mueller, P. Schlotter, "White LED", *Proc. SPIE* **1999**, *3621*, 143–150.

[8] G. G. Stokes, "On the Change of Refrangibility of Light", *Philos. Trans. R. Soc. London* **1852**, *142*, 463–562.

[9] G. Blasse, A. Bril, "A NEW PHOSPHOR FOR FLYING-SPOT CATHODE-RAY TUBES FOR COLOR TELEVISION: YELLOW-EMITTING $Y_3Al_5O_{12}$–$Ce^{3+}$", *Appl. Phys. Lett.* **1967**, *11*, 53–55.

[10] a) W. Lehmann, F. M. Ryan, "Cathodoluminescence of CaS:$Ce^{3+}$ and CaS:$Eu^{2+}$ Phosphors", *J. Electrochem. Soc.* **1971**, *118*, 477–482; b) W. Schnick, "Shine a light with nitrides", *Phys. Status Solidi RRL* **2009**, *3*, A113–A114.

[11] H. Huppertz, W. Schnick, "$Eu_2Si_5N_8$ and $EuYbSi_4N_7$. The First Nitridosilicates with a Divalent Rare Earth Metal", *Acta Crystallogr., Sect. C: Cryst. Struct. Commun.* **1997**, *53*, 1751–1753.

[12] a) R. Mueller-Mach, G. Mueller, M. R. Krames, H. A. Höppe, F. Stadler, W. Schnick, T. Juestel, P. Schmidt, "Highly efficient all-nitride phosphor-converted white light emitting diode", *Phys. Status Solidi A* **2005**, *202*, 1727–1732; b) G. O. Mueller, R. Mueller-Mach, "WHITE LIGHT FROM LIGHT EMITTING DIODES", *Proc. – Electrochem. Soc.* **2000**, *99*, 91–105; c) R.-J. Xie, N. Hirosaki, "Silicon-based oxynitride and nitride phosphors for white LEDs—A review", *Sci. Technol. Adv. Mater.* **2007**, *8*, 588–600.

[13] a) H. Huppertz, "$BaYbSi_4N_7$ – Unexpected Structural Possibilities in Nitridosilicates", W. Schnick, *Angew. Chem., Int. Ed. Engl.* **1996**, *35*, 1983–1984; "$BaYbSi_4N_7$ – überraschende strukturelle Möglichkeiten in Nitridosilicaten", *Angew. Chem.* **1996**, *108*, 2115–2116; b) H. Huppertz, "Edge-sharing $SiN_4$ Tetrahedra in the Highly Condensed Nitridosilicate $BaSi_7N_{10}$", W. Schnick, *Chem. – Eur. J.* **1997**, *3*, 249–252.

[14] a) W. Schnick, H. Huppertz, "Nitridosilicates – A Significant Extension of Silicate Chemistry", *Chem. – Eur. J.* **1997**, *3*, 679–683; b) M. Zeuner, S. Pagano, W. Schnick, "Nitridosilicates and Oxonitridosilicates: From Ceramic Materials to Structural and Functional Diversity", *Angew. Chem., Int. Ed.* **2011**, *50*, 7754–7775; "Nitridosilicate und Oxonitridosilicate: von keramischen Materialien zu struktureller und funktioneller Diversität", *Angew. Chem.* **2011**, *123*, 7898–7920.

[15] a) R. Juza, H. H. Weber, E. Meyer-Simon, "Über ternäre Nitride und Oxonitride von Elementen der 4. Gruppe", *Z. Anorg. Allg. Chem.* **1953**, *273*, 48–64; b) P. Eckerlin, "Zur Kenntnis des Systems $Be_3N_2$–$Si_3N_4$. IV Die Kristallstruktur von $BeSiN_2$", *Z. Anorg. Allg. Chem.* **1967**, *353*, 225–235; c) J. David, J. Lang, "Sur un nitrure double de magnesium et de

silicium", *C. R. Hebd. Seances Acad. Sci.* **1965**, *261*, 1005–1007; d) J. David, Y. Laurent, J. Lang, "Structure de $MgSiN_2$ et $MgGeN_2$", *Bull. Soc. Fr. Mineral. Cristallogr.* **1970**, *93*, 153–159; e) R. Marchand, M. Maunaye, J. Lang, "Sur la préparation d'un nitrure double de silicium et manganèse", *C. R. Seances Acad. Sci., Ser. C* **1971**, *272*, 1654–1656; f) J. David, Y. Laurent, J.-P.Charlot, "Étude cristallographique d'un nitrure $I–IV_2–V_3$. La structure tétraédrique type wurtzite de $LiSi_2N_3$", J. Lang, *Bull. Soc. Fr. Mineral. Cristallogr.* **1973**, *96*, 21–24; g) H. Jacobs, H. Mengis, "Preparation and crystal structure of a sodium silicon nitride, $NaSi_2N_3$", *Eur. J. Solid State Inorg. Chem.* **1993**, *30*, 45–53; h) M. Woike, W. Jeitschko, "Preparation and Crystal Structure of the Nitridosilicates $Ln_3Si_6N_{11}$ (Ln = La, Ce, Pr, Nd, Sm) and $LnSi_3N_5$ (Ln = Ce, Pr, Nd)", *Inorg. Chem.* **1995**, *34*, 5105–5108; i) T. Schlieper, W. Schnick, "Nitrido-Silicate. I Hochtemperatur-Synthese und Kristallstruktur von $Ca_2Si_5N_8$", *Z. Anorg. Allg. Chem.* **1995**, *621*, 1037–1041; j) T. Schlieper, W. Milius, W. Schnick, "Nitrido-silicate. II Hochtemperatur-Synthesen und Kristallstrukturen von $Sr_2Si_5N_8$ und $Ba_2Si_5N_8$", *Z. Anorg. Allg. Chem.* **1995**, *621*, 1380–1384; k) T. Schlieper, W. Schnick, "Nitrido-silicate. II Hochtemperatur-Synthese, Kristallstruktur und magnetische Eigenschaften von $Ce_3[Si_6N_{11}]$", *Z. Anorg. Allg. Chem.* **1995**, *621*, 1535–1538; l) T. Schlieper, W. Schnick, "Crystal structure of tripraseodymium hexasiliconundecanitride, $Pr_3Si_6N_{11}$", *Z. Kristallogr.* **1996**, *211*, 254; m) H. Yamane, F. J. DiSalvo, "Preparation and crystal structure of a new barium silicon nitride, $Ba_5Si_2N_6$", *J. Alloys Compd.* **1996**, *240*, 33–36; n) H. Yamane, S. Kikkawa, M. Koizumi, "PREPARATION OF LITHIUM SILICON NITRIDES AND THEIR LITHIUM ION CONDUCTIVITY", *Solid State Ionics* **1987**, *25*, 183–191; o) H. Huppertz, W. Schnick, "$Ba_2Nd_7Si_{11}N_{23}$ – A Nitridosilicate with a Zeolite-Analogous Si–N Structure", *Angew. Chem., Int. Ed. Engl.* **1997**, *36*, 2651–2652; "$Ba_2Nd_7Si_{11}N_{23}$ – ein Nitridosilicat mit zeolithartiger Si–N-Gerüststruktur", *Angew. Chem.* **1997**, *109*, 2765–2767; p) H. Huppertz, W. Schnick, "Synthese, Kristallstruktur und Eigenschaften der Nitridosilicate $SrYbSi_4N_7$ und $BaYbSi_4N_7$", *Z. Anorg. Allg. Chem.* **1997**, *623*, 212–217; q) T. Endo, H. Takizawa, M. Shimada, "NEW II-IV-$V_2$ FAMILY OF PERIODIC COMPOUNDS SYNTHESIZED UNDER HIGH PRESSURE", *Ceram. Eng. Sci. Proc.* **1992**, *13*, 844–851; r) M. Orth, W. Schnick, "Zur Kenntnis von $LiSi_2N_3$: Synthese und Verfeinerung der Kristallstruktur", *Z. Anorg. Allg. Chem.* **1999**, *625*, 1426–1428; s) C. M. Fang, Y. Q. Li, H. T. Hintzen, G. de With, "Crystal and

electronic structure of the novel nitrides $MYSi_4N_7$ (M = Sr, Ba) with peculiar $NSi_4$ coordination", *J. Mater. Chem.* **2003**, *13*, 1480–1483; t) Z. A. Gál, P. M. Mallinson, H. J. Orchard, S. J. Clarke, "Synthesis and Structure of Alkaline Earth Silicon Nitrides: $BaSiN_2$, $SrSiN_2$, and $CaSiN_2$", *Inorg. Chem.* **2004**, *43*, 3998–4006; u) G. Pilet, H. A. Höppe, W. Schnick, S. Esmaeilzadeh, "Crystal structure and mechanical properties of $SrSi_7N_{10}$", *Solid State Sci.* **2005**, *7*, 391–396; v) F. Ottinger, I. Kroslakova, K. Hametner, E. Reusser, R. Nesper, D. Günther, "Analytical evidence of amorphous microdomains within nitridosilicate and nitridoaluminosilicate single crystals", *Anal. Bioanal. Chem.* **2005**, *383*, 489–499; w) F. Ottinger, R. Nesper, "Synthesis and Crystal Structure of the Nitridosilicates $Ca_5[Si_2N_6]$ and $Ca_7[NbSi_2N_9]$", *Z. Anorg. Allg. Chem.* **2005**, *631*, 1597–1602; x) C. Schmolke, O. Oeckler, D. Bichler, D. Johrendt, W. Schnick, "Complex Interrupted Tetrahedral Frameworks in the Nitridosilicates $M_7Si_6N_{15}$ (M = La, Ce, Pr)", *Chem. – Eur. J.* **2009**, *15*, 9215–9222; y) C. Schmolke, D. Bichler, D. Johrendt, W. Schnick, "Synthesis and crystal structure of the first chain-type nitridosilicates $RE_5Si_3N_9$ (RE = La, Ce)", *Solid State Sci.* **2009**, *11*, 389–394; z) S. Lupart, W. Schnick, "$Pr_5Si_3N_9$", *Acta Crystallogr., Sect. E: Struct. Rep. Online* **2009**, *65*, i43; aa) M. Zeuner, S. Pagano, P. Matthes, D. Bichler, D. Johrendt, T. Harmening, R. Pöttgen, W. Schnick, "Mixed Valence Europium Nitridosilicate $Eu_2SiN_3$", *J. Am. Chem. Soc.* **2009**, *131*, 11242–11248; ab) S. Pagano, M. Zeuner, S. Hug, W. Schnick, "Single-Crystal Structure Determination and Solid-State NMR Investigations of Lithium Nitridosilicate $Li_2SiN_2$ Synthesized by a Precursor Approach Employing Amorphous "$Si(CN_2)_2$"", *Eur. J. Inorg. Chem.* **2009**, 1579–1584; ac) S. Pagano, S. Lupart, M. Zeuner, W. Schnick, "Tuning the Dimensionality of Nitridosilicates in Lithium Melts", *Angew. Chem., Int. Ed.* **2009**, *48*, 6335–6338; "Tuning the Dimensionality of Nitridosilicates in Lithium Melts", *Angew. Chem.* **2009**, *121*, 6453–6456; ad) S. Lupart, M. Zeuner, S. Pagano, W. Schnick, "Chain-Type Lithium Rare-Earth Nitridosilicates – $Li_5Ln_5Si_4N_{12}$ with Ln = La, Ce", *Eur. J. Inorg. Chem.* **2010**, 2636–2641; ae) M. Zeuner, S. Pagano, S. Hug, P. Pust, S. Schmiechen, C. Scheu, W. Schnick, "$Li_2CaSi_2N_4$ and $Li_2SrSi_2N_4$ – a Synthetic Approach to Three-Dimensional Lithium Nitridosilicates", *Eur. J. Inorg. Chem.* **2010**, 4945–4951; af) S. Pagano, S. Lupart, S. Schmiechen, W. Schnick, "$Li_4Ca_3Si_2N_6$ and $Li_4Sr_3Si_2N_6$ – Quaternary Lithium Nitridosilicates with Isolated $[Si_2N_6]^{10-}$ Ions", *Z. Anorg. Allg. Chem.* **2010**, *636*, 1907–1909; ag) S. M. Hick, M.

I. Miller, R. B. Kaner, R. G. Blair, "Synthesis and Crystal Structure of Cubic $Ca_{16}Si_{17}N_{34}$", *Inorg. Chem.* **2012**, *51*, 12626–12629; ah) S. Lupart, W. Schnick, "$LiCa_3Si_2N_5$ – A Lithium Nitridosilicate with a $[Si_2N_5]^{7-}$ Double-Chain", *Z. Anorg. Allg. Chem.* **2012**, *638*, 2015–2019; ai) H. Huppertz, O. Oeckler, A. Lieb, R. Glaum, D. Johrendt, M. Tegel, R. Kaindl, W. Schnick, "$Ca_3Sm_3[Si_9N_{17}]$ and $Ca_3Yb_3[Si_9N_{17}]$ Nitridosilicates with Interpenetrating Nets that Consist of Star-Shaped $[N^{[4]}(SiN_3)_4]$ Units and $[Si_5N_{16}]$ Supertetrahedra", *Chem. – Eur. J.* **2012**, *18*, 10857–10864; aj) H. Yamane, H. Morito, "Synthesis and Crystal Structures of $Ca_4SiN_4$ and New Polymorph of $Ca_5Si_2N_6$", *Inorg. Chem.* **2013**, *52*, 5559–5563; ak) H. Yamane, H. Morito, "$Ba_4Mg[Si_2N_6]$, $Ba_3Ca_2[Si_2N_6]$ and $Ba_{1.6}Sr_{3.4}[Si_2N_6]$ – Quaternary barium alkaline-earth silicon nitrides containing isolated nitridosilicate anions of $[Si_2N_6]^{10-}$", *J. Alloys Compd.* **2013**, *555*, 320–324; al) F. Ottinger, R. Nesper, "SYNTHESIS AND STRUCTURE OF $CaSiN_2$", *Acta Crystallogr., Sect. A: Found. Adv.* **2002**, *58*, c337; am) H. Huppertz, W. Schnick, "Synthese und Kristallstruktur von $BaEu(Ba_{0,5}Eu_{0,5})YbSi_6N_{11}$", *Z. Anorg. Allg. Chem.* **1998**, *624*, 371–374; an) W. B. Park, K. H. Son, S. P. Singh, K.-S. Sohn, "Solid-State Combinatorial Screening of $ARSi_4N_7$:$Eu^{2+}$ (A = Sr, Ba, Ca; R = Y, La, Lu) Phosphors", *ACS Comb. Sci.* **2012**, *14*, 537–544.

[16] A. L. Allred, E. G. Rochow, "A SCALE OF ELECTRONEGATIVITY BASED ON ELECTROSTATIC FORCE", *J. Inorg. Nucl. Chem.* **1958**, *5*, 264–268.

[17] F. Liebau, "Silicates and Perovskites: Two Themes with Variations", *Angew. Chem., Int. Ed.* **1999**, *38*, 1733–1737; "Silicate und Perowskite: zwei Themen mit Variationen", *Angew. Chem.* **1999**, *111*, 1845–1850.

[18] D. Hardie, K. H. Jack, "Crystal Structures of Silicon Nitride", *Nature* **1957**, *180*, 332–333.

[19] H. Huppertz, "Strukturelle Erweiterung der Nitridosilicate", *Dissertation*, Universität Bayreuth, **1997**.

[20] a) F. Machatschki, "Konstitutionsformeln fiir den festen Zustand", *Monatsh. Chem.* **1947**, *77*, 333–342; b) J. Lima-de-Faria, E. Hellner, F. Liebau, E. Makovicky, E. Parthé, "Nomenclature of Inorganic Structure Types. Report of the International Union of Crystallography Commission on Crystallographic Nomenclature Subcommittee on the Nomenclature of Inorganic Structure Types", *Acta Crystallogr., Sect. A: Found. Crystallogr.* **1990**, *46*, 1–11.

[21] A. Weiss, A. Weiss, "Über Siliciumchalkogenide. VI. Zur Kenntnis der faserigen Silicium-dioxyd-Modifikation", *Z. Anorg. Allg. Chem.* **1954**, *276*, 95–112.

[22] L. Pauling, "The Principles Determining the Structure of Complex Ionic Crystals", *J. Am. Chem. Soc.* **1929**, *51*, 1010–1026.

[23] R. D. Shannon, "Revised Effective Ionic Radii and Systematic Studies of Interatomic Distances in Halides and Chalcogenides", *Acta Crystallogr., Sect. A: Found. Crystallogr.* **1976**, *32*, 751–767.

[24] A. F. Holleman, N. Wiberg, *Lehrbuch der Anorganischen Chemie, Vol. 102*, DeGruyter, Berlin, Boston, **2008**.

[25] Z. Inoue, M. Mitomo, N. Ii, "A crystallographic study of a new compound of lanthanum silicon nitride, $LaSi_3N_5$", *J. Mater. Sci.* **1980**, *15*, 2915–2920.

[26] a) W. L. Bragg, "The Crystalline Structure of Zinc Oxide", *London, Edinburgh, Dublin Philos. Mag. J. Sci.* **1920**, *39*, 647–651; b) G. Aminoff, "XI. Untersuchungen über die Kristallstrukturen von Wurtzit und Rotnickelkies", *Z. Kristallogr. – Cryst. Mater.* **1923**, *58*, 203–219; c) F. Ulrich, W. Zachariasen, "XIV. Über die Kristallstruktur des α- und β-CdS, sowie des Wurtzits", *Z. Kristallogr. – Cryst. Mater.* **1925**, *62*, 260–273; d) W. L. Bragg, "The Analysis of Crystals by the X-ray Spectrometer", *Proc. R. Soc. London, Ser. A* **1914**, *89*, 468–489.

[27] S. R. Römer, C. Braun, O. Oeckler, P. J. Schmidt, P. Kroll, W. Schnick, "HP-$Ca_2Si_5N_8$ – A New High-Pressure Nitridosilicate: Synthesis, Structure, Luminescence, and DFT Calculations", *Chem. – Eur. J.* **2008**, *14*, 7892–7902.

[28] H. A. Höppe, H. Lutz, P. Morys, W. Schnick A. Seilmeier, "Luminescence in $Eu^{2+}$-doped $Ba_2Si_5N_8$: fluorescence, thermoluminescence, and upconversion", *J. Phys. Chem. Solids* **2000**, *61*, 2001–2006.

[29] a) H. Lux, "„SÄUREN" UND „BASEN" IM SCHMELZFLUSS: DIE BESTIMMUNG DER SAUERSTOFFIONEN-KONZENTRATION", *Z. Elektrochem. Angew. Phys. Chem.* **1939**, *45*, 303–309; b) H. Flood, T. Förland, "The Acidic and Basic Properties of Oxides", *Acta Chem. Scand. (1947–1973)* **1947**, *1*, 592–604.

[30] a) H. Yamane, F. J. DiSalvo, "Synthesis and Crystal Structure of $Sr_2ZnN_2$ and $Ba_2ZnN_2$", *J. Solid State Chem.* **1995**, *119*, 375–379; b) H. Yamane, F. J. DiSalvo, "Sodium flux synthesis of nitrides", *Prog. Solid State Chem.* **2018**, *51*, 27–40.

[31] a) M. Persoz, "OBSERVATIONS SUR LES COMBINAISONS DU GAZ AMMONIAC AVEC LES CHLORURES MÉTALLIQUES", *Ann. Chim. Phys.* **1831**, *44*, 315; b) M. Blix, W. Wirbelauer, "Ueber das Siliciumsulfochlorid, $SiSCl_2$, Siliciumimid, $Si(NH)_2$, Siliciumstickstoffimid (Silicam), $Si_2N_3H$ und den Siliciumstickstoff, $Si_3N_4$", *Ber. Dtsch. Chem. Ges.* **1903**, *36*, 4220–4228.

[32] O. Glemser, P. Naumann, "Über den Thermischen Abbau von Siliciumdiimid $Si(NH)_2$", *Z. Anorg. Allg. Chem.* **1959**, *298*, 134–141.

[33] O. Reckeweg, F. J. DiSalvo, "Alkaline earth metal nitride compounds with the composition $M_2N_X$ (M = Ca, Sr, Ba; X = □, H, Cl or Br)", *Solid State Sci.* **2002**, *4*, 575–584.

[34] a) K. Becker, F. Ebert, "Die Kristallstruktur einiger binärer Carbide und Nitride", *Z. Phys.* **1925**, *31*, 268–272; b) W. Klemm, G. Winkelmann, "Zur Kenntnis der Nitride der Seltenen Erdmetalle", *Z. Anorg. Allg. Chem.* **1956**, *288*, 87–90; c) P. Höhn, R. Niewa, in *Handbook of Solid State Chemistry, Vol. Materials and Structure of Solids* (Eds.: R. Dronskowski, S. Kikkawa, A. Stein), Wiley-VCH, Weinheim, Deutschland, **2017**, pp. 251–359; d) W. M. Haynes, *Handbook of Chemistry and Physics, 96th Ed.*, CRC Press, **2015**.

[35] a) G. Berraz, "Acción del nitrógeno sobre los metales", *An. Soc. Cient. St. Fe* **1933**, *5*, 54–56; b) W. Janeff, "Herstellung von Metailnitriden in der Glimmentladung und einige ihrer Eigenschaften", *Z. Phys.* **1955**, *142*, 619–636.

[36] T. B. Massalski, H. Okamoto, P. R. Subramanian, L. Kacprzak, *Binary Alloy Phase Diagrams*, 2nd, ASM International, Novelty, **1990**.

[37] a) W. Blase, G. Cordier, M. Ludwig, R. Kniep, "$Sr_3[Al_2N_4]$: Ein Nitridoaluminat mit gewellten Tetraederketten $^1_\infty[AlN_{4/2}{}^{3-}]$", *Z. Naturforsch., B: J. Chem. Sci.* **1994**, *49*, 501–505; b) M. Ludwig, J. Jäger, R. Niewa, R. Kniep, "Crystal Structures of Two Polymorphs of $Ca_3[Al_2N_4]$", *Inorg. Chem.* **2000**, *39*, 5909–5911; c) P. Pust, V. Weiler, C. Hecht, A. Tücks, A. S. Wochnik, A.-K. Henß, D. Wiechert, C. Scheu, P. J. Schmidt, W. Schnick, "Narrow-band red-emitting $Sr[LiAl_3N_4]:Eu^{2+}$ as a next-generation LED-phosphor material", *Nat. Mater.* **2014**, *13*, 891–896; d) H. Yamane, F. J. DiSalvo, "$Ba_3Ga_2N_4$", *Acta Crystallogr., Sect. C: Cryst. Struct.*

*Commun.* **1996**, *52*, 760–761; e) S. J. Clarke, F. J. DiSalvo, "Synthesis and Structure of One-, Two-, and Three-Dimensional Alkaline Earth Metal Gallium Nitrides: $Sr_3Ga_2N_4$, $Ca_3Ga_2N_4$, and $Sr_3Ga_3N_5$", *Inorg. Chem.* **1997**, *36*, 1143–1148.

[38] L. Pauling, "THE NATURE OF THE CHEMICAL BOND. IV. THE ENERGY OF SINGLE BONDS AND THE RELATIVE ELECTRONEGATIVITY OF ATOMS", *J. Am. Chem. Soc.* **1932**, *54*, 3570–3582.

[39] H. Huppertz, N. Stock, W. Schnick, "The First Crystalline Hexagonal $Si_3N_4$ Microtubes", *Adv. Mater. (Weinheim, Ger.)* **1996**, *8*, 844–847.

[40] a) N. A. Toropov, M. M. Stukalova, "ЗМАЕЩЕНИЕ НАТРИЯ В КРИСТАЛЛАХ β-ГЛИНОЗЕМА КАЛЬЦИЕМ, СТРОНЦИЕМ И БАРИЕМ" engl. "Replacement of sodium crystals of β-alumina with calcium, strontium and barium", *Dokl. Akad. Nauk SSSR* **1940**, *27*, 974–977; b) R. D. Shannon, D. B. Rogers, C. T. Prewitt, "Chemistry of Noble Metal Oxides. I. Syntheses and Properties of $ABO_2$ Delafossite Compounds", *Inorg. Chem.* **1971**, *10*, 713–718; c) L. Dloczik, Y. Tomm, R. Könenkamp, M. C. Lux-Steiner, T. Dittrich, "$CuAlO_2$ prepared by ion exchange from $LiAlO_2$", *Thin Solid Films* **2004**, *451–452*, 116–119.

[41] a) P. Bielec, W. Schnick, "Increased Synthetic Control – Gaining Access to Predicted $Mg_2Si_5N_8$ and β-$Ca_2Si_5N_8$", *Angew. Chem., Int. Ed.* **2017**, *56*, 4810–4813; "Increased Synthetic Control – Gaining Access to Predicted $Mg_2Si_5N_8$ and β-$Ca_2Si_5N_8$", *Angew. Chem.* **2017**, *129*, 4888–4891; b) P. Bielec, O. Janka, T. Block, R. Pöttgen, W. Schnick, "$Fe_2Si_5N_8$: Access to Open-Shell Transition-Metal Nitridosilicates", *Angew. Chem., Int. Ed.* **2018**, *57*, 2409–2412; "$Fe_2Si_5N_8$: Access to Open-Shell Transition-Metal Nitridosilicates", *Angew. Chem.* **2018**, *130*, 2433–2436; c) P. Bielec, L. Eisenburger, H. L. Deubner, D. Günther, F. Kraus, O. Oeckler, W. Schnick, "Targeting Vacancies in Nitridosilicates: Aliovalent Substitution of $M^{2+}$ ($M$ = Ca, Sr) by $Sc^{3+}$ and $U^{3+}$", *Angew. Chem., Int. Ed.* **2019**, *58*, 840–843; "Targeting Vacancies in Nitridosilicates: Aliovalent Substitution of $M^{2+}$ ($M$ = Ca, Sr) by $Sc^{3+}$ and $U^{3+}$", *Angew. Chem.* **2019**, *131*, 850–853; d) P. Bielec, R. Nelson, R. P. Stoffel, L. Eisenburger, D. Günther, A.-K. Henß, J. P. Wright, O. Oeckler, R. Dronskowski, W. Schnick, "Cationic $Pb_2$ Dumbbells Stabilized in the Highly Covalent Lead Nitridosilicate $Pb_2Si_5N_8$", *Angew. Chem., Int. Ed.* **2019**, 58, 1432–1436; "Cationic $Pb_2$ Dumbbells Stabilized in the Highly Covalent Lead Nitridosilicate $Pb_2Si_5N_8$", *Angew. Chem.* **2019**, *131*, 1446–1450.

# 2 Increased Synthetic Control – Gaining Access to Predicted $Mg_2Si_5N_8$ and β-$Ca_2Si_5N_8$

*Angew. Chem., Int. Ed.* **2017**, *56*, 4810–4813; *Angew. Chem.* **2017**, *129*, 4888–4891.

Philipp Bielec and Wolfgang Schnick

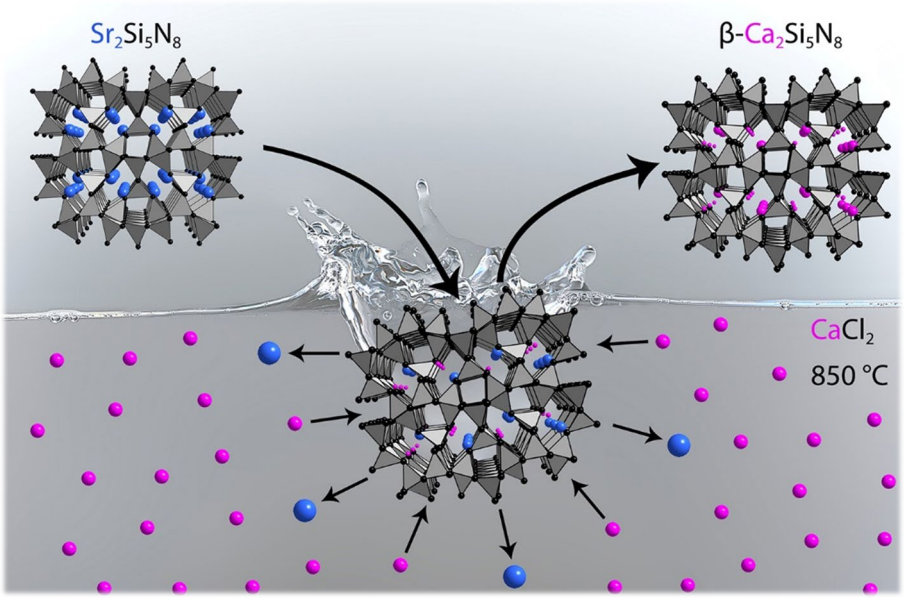


## Abstract

Nitridosilicates represent an intriguing class of materials and are typically made up of highly condensed tetrahedral network structures. Alkaline-earth nitridosilicates emerged as unique host materials for $Eu^{2+}$ doped luminophores which found broad application in pc-LEDs. In contrast to common strategies of preparing nitridosilicates by *bottom-up* syntheses, we have now succeeded to post-synthetically design nitridosilicates by ion exchange in metal halide melts. We describe the syntheses of hitherto unknown but predicted alkaline-earth nitridosilicates, $Mg_2Si_5N_8$ and β-$Ca_2Si_5N_8$. Both compounds were obtained by ion exchange starting from pre-synthesized nitridosilicates. *In situ* investigations of the ion-exchange process show that the Si–N network topology remains preserved. Therefore, the reaction offers a significant increase of synthetic control with respect to classical *bottom-up* syntheses.

## 2.1 Introduction with Results and Discussion

Nitridosilicates are being thoroughly exploited for development of novel host compounds for $Eu^{2+}$ doped luminophores to efficiently tune emission characteristics of pc-LEDs.[1–5] Light-emitting diodes have exceptional energetic efficiencies of more than 50% in contrast to incandescent lamps (ca. 5%).[6] For example $M_2Si_5N_8:Eu^{2+}$ ($M$ = Sr, Ba) shows intense luminescence and is applied in commercial LED-based lighting products.[7–9] To gradually modify and optimize luminescence properties in $M_2Si_5N_8:Eu^{2+}$ ($M$ = Sr, Ba), attempts were undertaken to synthesize solid solution series, such as $Sr_{2-x}Ca_xSi_5N_8:Eu^{2+}$.[10] Targeting compounds with $x$ >0.6, side phases were formed instead of the desired products as a result of the restricted solubility of $Ca^{2+}$ in $Sr_2Si_5N_8$ under the selected conditions. The difference in ionic radii of $Ca^{2+}$ and $Sr^{2+}$, which is crucial for the formation of the different structure types of $M_2Si_5N_8$,[7,11] also seems to be the reason why solid solutions $Sr_{2-x}Ca_xSi_5N_8:Eu^{2+}$ with $x$ >0.6 were not accessible in *bottom-up* syntheses. The *bottom-up* approach is based on building up anionic networks after breaking down the starting materials' structures in high-temperature reactions. Typical *bottom-up* syntheses leading to nitridosilicates are given in Equations 2.1–2.3 ($T$ >1000 °C).[11–14]

$$2\ Ca + 5\ \text{“}Si(NH)_2\text{”} \rightarrow Ca_2Si_5N_8 + 5\ H_2\uparrow + N_2\uparrow \qquad 2.1$$

$$2\ \text{“}LaSi_3\text{”} + 5\ N_2 \rightarrow 2\ LaSi_3N_5 \qquad 2.2$$

$$6\ SrO + 6\ C + 5\ Si_3N_4 + 2\ N_2 \rightarrow 3\ Sr_2Si_5N_8 + 6\ CO\uparrow \qquad 2.3$$

Besides high-temperature reactions, approaches with reduced temperature, such as the synthesis of $Ba_5Si_2N_6$ in Na-flux have been reported as well.[15] Generally, many different starting materials for example, metals, binary nitrides, alloys containing Si, amides, imides or even oxides in carbothermic reactions have been employed preparing nitridosilicates.

However, synthesis planning seems to be hardly possible in solid-state chemistry in general and in nitridosilicate synthesis in particular. Choosing a stoichiometry to target a desired sum formula, it is possible to try to influence the degree of condensation, but the influence on structural details still remains restricted. For example, $Ca_2Si_5N_8$ and $Sr_2Si_5N_8$ both contain layers of corner-sharing $SiN_4$ tetrahedra building up *dreier* rings (rings made up of three tetrahedra) with $SiN_4$ tetrahedra interconnecting the layers, but within the layers the up/down sequence of the tetrahedra vertices is different.[7,11]

DFT calculations of a hypothetical $Ca_2Si_5N_8$ polymorph "o-$Ca_2Si_5N_8$" in the structure type of $Sr_2Si_5N_8$ indicate that this compound would be dynamically instable.[16] In contrast to that, hypothetical $Mg_2Si_5N_8$ (with $Ca_2Si_5N_8$ structure type)[17] was predicted to be a metastable compound concerning the decomposition into $MgSiN_2$ and $Si_3N_4$.

Using explorative strategies we discovered the possibility to exchange cations of highly condensed nitridosilicates in metal halide melts maintaining the rigid nitridosilicate precursor networks. Applying this strategy to the model system $M_2Si_5N_8$ the predicted compound $Mg_2Si_5N_8$ and a polymorph of $Ca_2Si_5N_8$, which is closely related to the calculated "o-$Ca_2Si_5N_8$", were synthesized for the first time (Equations 2.4–2.5). For easier distinction the novel $Ca_2Si_5N_8$ polymorph is named β-$Ca_2Si_5N_8$ and $Ca_2Si_5N_8$ is renamed as α-$Ca_2Si_5N_8$.

$$\alpha\text{-}Ca_2Si_5N_8 + 2\ MgCl_2 \rightarrow Mg_2Si_5N_8 + 2\ CaCl_2 \qquad 2.4$$

$$Sr_2Si_5N_8 + 2\ CaCl_2 \rightarrow \beta\text{-}Ca_2Si_5N_8 + 2\ SrCl_2 \qquad 2.5$$

To ensure complete cation exchange (Figure 2.1) a three equivalent excess $MCl_2$ ($M$ = Mg, Ca) was used (details on the reactions given in chapter A.4). For synthesis of β-$Ca_2Si_5N_8$ a repetition of the ion exchange was performed to achieve complete conversion. The colorless solid $Mg_2Si_5N_8$ as well as off-white β-$Ca_2Si_5N_8$ (pictures given in chapter A.9) were analyzed by PXRD.

As predicted $Mg_2Si_5N_8$ was refined in the monoclinic space group *Cc* (no. 9) applying the structure model of α-$Ca_2Si_5N_8$.[11,17] The lattice parameters of $Mg_2Si_5N_8$ are significantly smaller than those of α-$Ca_2Si_5N_8$ and deviate only slightly from the predicted values (Table 2.1).

β-$Ca_2Si_5N_8$ was refined using a modified structure model of $Sr_2Si_5N_8$ in the monoclinic space group $P2_1$ (no. 4) which is a maximal *translationsgleiche* subgroup of $Pmn2_1$ (no. 31).[7] The distortion from the orthorhombic parental structure to monoclinic β-$Ca_2Si_5N_8$ could be one reason why "o-$Ca_2Si_5N_8$" should be dynamically instable according to DFT calculations.[16] Apart from the symmetry reduction, all refined crystallographic data of β-$Ca_2Si_5N_8$ deviate only slightly from the predicted values (Table 2.2, for clarity reasons unique axis *c* is chosen).

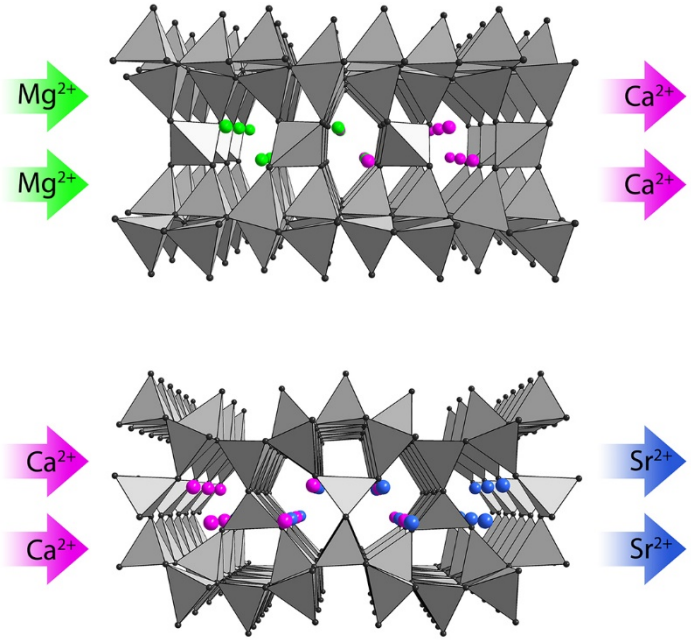


**Figure 2.1:** Top: Crystal structure of α-$Ca_2Si_5N_8$ (view along *b*) and bottom: of $Sr_2Si_5N_8$ (view along *a*) with exchange of ions leading to $Mg_2Si_5N_8$ and β-$Ca_2Si_5N_8$.

RIETVELD refinements (chapters A.5 and A.7) of PXRD data reveal products of high purity. The elemental compositions of both products were analyzed by EDX and ICP-OES confirming the sum formulas $Mg_2Si_5N_8$ and $Ca_2Si_5N_8$ (chapters A.10 and A.11).

**Table 2.1:** Crystallographic data of $Mg_2Si_5N_8$ (RIETVELD refinement),[18] calculated values for predicted $Mg_2Si_5N_8$ (LDA, GGA)[17] and α-$Ca_2Si_5N_8$.[11]

| | | $Mg_2Si_5N_8$ | LDA | GGA | α-$Ca_2Si_5N_8$ |
|---|---|---|---|---|---|
| **Crystal system** | | monoclinic | | | |
| **Space group** | | *Cc (no. 9)* | | | |
| ***Z*** | | 4 | | | |
| **Lattice parameters / Å, °** | *a* | 14.0672(2) | 14.0615 | 14.2161 | 14.347(8) |
| | *b* | 5.35002(7) | 5.3176 | 5.2878 | 5.606(3) |
| | *c* | 9.57993(10) | 9.4843 | 9.6122 | 9.686(7) |
| | *β* | 111.0127(7) | 111.00 | 110.97 | 112.03(8) |
| ***V* / Å³** | | 673.04(2) | 662.07 | 687.47 | 723.0 |
| ***ρ* / g · cm⁻³** | | 2.97144(6) | 3.02 | 2.91 | 3.057 |

**Table 2.2:** Crystallographic data of β-$Ca_2Si_5N_8$ (RIETVELD refinement),[18] calculated values for predicted "o-$Ca_2Si_5N_8$" (LDA, GGA)[16] and $Sr_2Si_5N_8$.[7]

| | | β-$Ca_2Si_5N_8$ | LDA | GGA | $Sr_2Si_5N_8$ |
|---|---|---|---|---|---|
| **Crystal system** | | monoclinic | orthorhombic | | |
| **Space group** | | $P2_1$ (no. 4) | $Pmn2_1$ (no. 31) | | |
| ***Z*** | | 2 | 2 | | |
| **Lattice parameters / Å, °** | *a* | 5.66713(12) | 5.622 | 5.704 | 5.712(3) |
| | *b* | 9.2818(2) | 6.650 | 6.753 | 6.817(3) |
| | *c* | 6.6889(2) | 9.262 | 9.379 | 9.336(1) |
| | *β* | 90.1164(10) | 90 | 90 | 90 |
| ***V* / Å³** | | 351.843(13) | 346.26 | 361.24 | 363.9(2) |
| ***ρ* / g · cm⁻³** | | 3.13978(12) | 3.19 | 3.06 | 3.904 |

Both compounds exhibit the same Si–N network topology as their parental structures, but are distorted due to incorporation of smaller cations. Consequently, Si–N distances in $Mg_2Si_5N_8$(1.60–1.83 Å) and β-$Ca_2Si_5N_8$ (1.54–1.95 Å) differ slightly from their parental nitridosilicates (1.64–1.80 Å). Figure 2.2 illustrates the distortion for the coordination of Mg2 ($Mg_2Si_5N_8$). The equivalent cation Ca2 in the starting material (α-$Ca_2Si_5N_8$) is coordinated fivefold by N atoms as a heavily distorted singly capped tetrahedron. By exchanging the cations from $Ca^{2+}$ to $Mg^{2+}$ their distances to N are contracted except for the capping N4 atom.

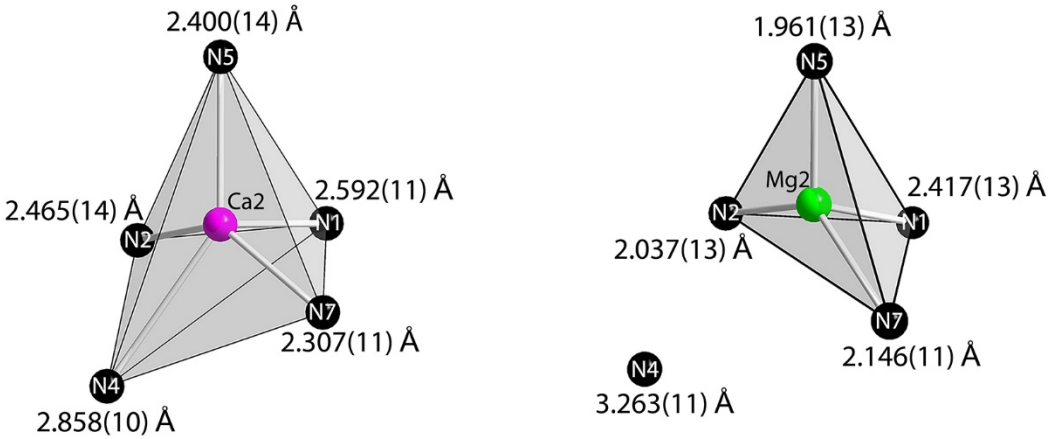


**Figure 2.2:** Coordination environment of Ca2 (left, *CN* = 5) in α-$Ca_2Si_5N_8$ and Mg2 (right, *CN* = 4) in $Mg_2Si_5N_8$.

This enlargement (>3 Å) ends in a distorted tetrahedral coordination for Mg2. In general, distances between $Mg^{2+}$/$Ca^{2+}$and N atoms in $Mg_2Si_5N_8$ (1.9–2.8 Å) and β-$Ca_2Si_5N_8$ (2.3–3.2 Å) are consistent with other nitride compounds containing $Mg^{2+}$ or $Ca^{2+}$ for example, $M[Mg_3SiN_4]$ (*M* = Ca, Sr, Eu) or

$Ca_5[Si_2N_6]$.[11,16,19,20] Further structural details on $Mg_2Si_5N_8$ and β-$Ca_2Si_5N_8$ are given in chapters A.6 and A.8.[21]

To illustrate the reaction progress, an *in situ* investigation of the ion exchange leading to $Mg_2Si_5N_8$ was performed by TDPXRD. Diffraction diagrams (Figure 2.3) of the reaction mixture described in Equation 2.4 were measured at different temperatures (chapter A.12). Figure 2.3 shows the presence of a crystalline nitridosilicate phase at each temperature step throughout the entire reaction. The reflections assigned to α-$Ca_2Si_5N_8$ shift to higher angles after melting of $MgCl_2$.

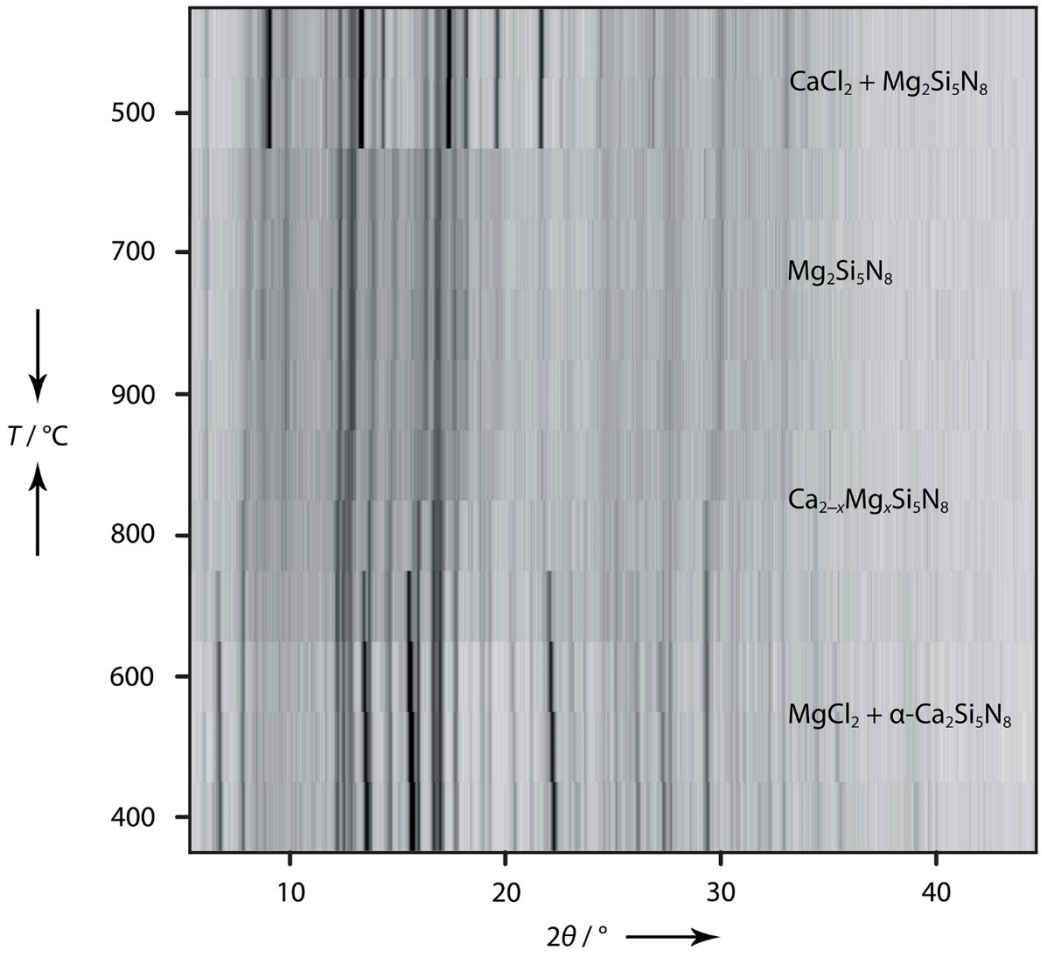


**Figure 2.3:** *In situ* TDPXRD. Dark areas symbolize high intensities ($T_{max}$ = 900 °C for 0.5 h, heating and cooling rate of 5 °C · $min^{-1}$, 100 °C step size).

This decrease of lattice parameters is caused by the continuous transformation of α-$Ca_2Si_5N_8$ into $Mg_2Si_5N_8$ through an intermediate solid solution ($Ca_{2-x}Mg_xSi_5N_8$, $0 \le x \le 2$). $Ca_{2-x}Mg_xSi_5N_8$ (Figure 2.3) indicates that the structural motifs of the starting material are present throughout the entire conversion. Therefore, this reaction is basically different to all other nitridosilicate syntheses. Although the reaction temperature is significantly lower than for the *bottom-up* synthesis of the

starting materials (1600 °C) cation mobility in the pre-synthesized nitridosilicates seems to be sufficiently high at the selected reaction temperatures. Therefore, the conversion can be interpreted as ion exchange similar to materials like β-alumina, where exchange of Na with Ca, Sr, or Ba has been reported employing $MCl_2$ ($M$ = Ca, Sr, Ba).[22] A cause of this ion exchange could be the difference in ionic radii between $Mg^{2+}$ and $Ca^{2+}$. First, Coulomb's law is dependent on the distance between cations and anions leading to stronger interactions for smaller cations. Secondly, assumed that cation mobility in the nitridosilicate is sufficiently high, entropy driven cation exchange between halide melt and nitridosilicate could occur leading to the intermediate solid solution $Ca_{2-x}Mg_xSi_5N_8$. The decrease in lattice parameters and distortion of the Si–N networks then reduces the probability of released $Ca^{2+}$ to reenter the nitridosilicate, enriching the nitridosilicate with $Mg^{2+}$.

Thermal stability of $Mg_2Si_5N_8$ and β-$Ca_2Si_5N_8$ was also investigated under $N_2$ atmosphere up to 1500 °C indicating that both nitridosilicates are less stable than their parental compounds (0). Under these conditions $Mg_2Si_5N_8$ decomposes into volatile Mg compounds and solid $Si_3N_4$ remains in the crucible. This is consistent with known behavior of Mg nitrides at such temperatures. At 1500 °C α-$Ca_2Si_5N_8$ was formed from β-$Ca_2Si_5N_8$ through a reconstructive transformation. "o-$Ca_2Si_5N_8$" which is closely related to β-$Ca_2Si_5N_8$ has been calculated to be a second high pressure phase besides HP-$Ca_2Si_5N_8$ but higher in enthalpy than HP-$Ca_2Si_5N_8$.[16] Therefore, the transformation of denser β-$Ca_2Si_5N_8$ ($\rho$ = 3.14 g · cm$^{-3}$) to less dense α-$Ca_2Si_5N_8$ ($\rho$ = 3.06 g · cm$^{-3}$) may be interpreted as transformation of a high pressure polymorph into the thermodynamically stable ambient pressure phase.

In conclusion we discovered an unprecedented possibility of post-synthetic cation exchange in nitridosilicates using metal halide melts at comparatively low temperatures. As proof of concept we prepared the hitherto inaccessible compounds $Mg_2Si_5N_8$ (α-$Ca_2Si_5N_8$ type) and β-$Ca_2Si_5N_8$ (distorted $Sr_2Si_5N_8$ structure) from α-$Ca_2Si_5N_8$ and $Sr_2Si_5N_8$. Both compounds are not stable at conditions commonly used for nitridosilicate syntheses. At such conditions $Mg_2Si_5N_8$ decomposes and β-$Ca_2Si_5N_8$ undergoes a reconstructive transformation into α-$Ca_2Si_5N_8$. An *in situ* investigation of the $Mg_2Si_5N_8$ synthesis by TDPXRD showed continuous transformation of α-$Ca_2Si_5N_8$ through an intermediate solid solution $Ca_{2-x}Mg_xSi_5N_8$ into $Mg_2Si_5N_8$ preserving the network topology. Maintaining the rigid Si–N substructure significantly increases synthetic control. Planning structures by combining known nitridosilicate networks with other metal cations is going to lead to novel compounds of elemental compositions, which have not been accessible with classical *bottom-up*

syntheses so far. This potential of establishing unprecedented nitrides could generate materials with intriguing properties.

## 2.2 References


[1] J. W. H. van Krevel, "On new rare-earth doped M-Si-Al-O-N materials: luminescence properties and oxidation resistance", *Ph.D. thesis*, TU Eindhoven, **2000**.

[2] H. A. Höppe, H. Lutz, P. Morys, W. Schnick, A. Seilmeier, "Luminescence in $Eu^{2+}$-doped $Ba_2Si_5N_8$: fluorescence, thermoluminescence, and upconversion", *J. Phys. Chem. Solids* **2000**, *61*, 2001–2006.

[3] R.-J. Xie, N. Hirosaki, "Silicon-based oxynitride and nitride phosphors for white LEDs – A review", *Sci. Technol. Adv. Mater.* **2007**, *8*, 588–600.

[4] H. A. Höppe, "Recent Developments in the Field of Inorganic Phosphors", *Angew. Chem., Int. Ed.* **2009**, *48*, 3572–3582; "Aktuelle Entwicklungen auf dem Gebiet der anorganischen Leuchtstoffe", *Angew. Chem. 121*, 3626–3636.

[5] S. Nakamura, T. Mukai, M. Senoh, "Candela-class high-brightness InGaN/AlGaN double-heterostructure blue-light-emitting diodes", *Appl. Phys. Lett.* **1994**, *64*, 1687–1689.

[6] C. Feldmann, "Technical Revolution Underway – Nitride-based Phosphors for LED Application", *Z. Anorg. Allg. Chem.* **2012**, *638*, 2169–2171.

[7] T. Schlieper, W. Milius, W. Schnick, "Nitrido-silicate. II Hochtemperatur-Synthesen und Kristallstrukturen von $Sr_2Si_5N_8$ und $Ba_2Si_5N_8$", *Z. Anorg. Allg. Chem.* **1995**, *621*, 1380–1384.

[8] R. Mueller-Mach, G. Mueller, M. R. Krames, H. A. Höppe, F. Stadler, W. Schnick, T. Juestel, P. Schmidt, "Highly efficient all-nitride phosphor-converted white light emitting diode", *Phys. Status Solidi A* **2005**, *202*, 1727–1732.

[9] W. Schnick, "Shine a light with nitrides", *Phys. Status Solidi RRL* **2009**, *3*, A113–A114.

[10] Y. Q. Li, H. T. Hintzen, "The effect of replacement of Sr by Ca on the structural and luminescence properties of the red-emitting $Sr_2Si_5N_8$:$Eu^{2+}$ LED conversion phosphor", *J. Solid State Chem.* **2008**, *181*, 515–524.

[11] T. Schlieper, W. Schnick, "Nitrido-Silicate. I Hochtemperatur-Synthese und Kristallstruktur von $Ca_2Si_5N_8$", *Z. Anorg. Allg. Chem.* **1995**, *621*, 1037–1041.

[12] M. Zeuner, S. Pagano, W. Schnick, "Nitridosilicates and Oxonitridosilicates: From Ceramic Materials to Structural and Functional Diversity", *Angew. Chem., Int. Ed.* **2011**, *50*, 7754–7775; "Nitridosilicate und Oxonitridosilicate: von keramischen Materialien zu struktureller und funktioneller Diversität", *Angew. Chem.* **2011**, *123*, 7898–7920.

[13] a) Z. Inoue, M. Mitomo, N. Ii, "A crystallographic study of a new compound of lanthanum silicon nitride, $LaSi_3N_5$", *J. Mater. Sci.* **1980**, *15*, 2915–2920; b) M. Woike, W. Jeitschko, "Preparation and Crystal Structure of the Nitridosilicates $Ln_3Si_6N_{11}$ (Ln = La, Ce, Pr, Nd, Sm) and $LnSi_3N_5$ (Ln = Ce, Pr, Nd)", *Inorg. Chem.* **1995**, *34*, 5105–5108.

[14] X. Piao, T. Horikawa, H. Hanzawa, K.-i. Machida, "Characterization and luminescence properties of $Sr_2Si_5N_8$:$Eu^{2+}$ phosphor for white light-emitting-diode illumination", *Appl. Phys. Lett.* **2006**, *88*, 161908.

[15] H. Yamane, F. J. DiSalvo, "Preparation and crystal structure of a new barium silicon nitride, $Ba_5Si_2N_6$", *J. Alloys Compd.* **1996**, *240*, 33–36.

[16] S. R. Römer, C. Braun, O. Oeckler, P. J. Schmidt, P. Kroll, W. Schnick, "HP-$Ca_2Si_5N_8$ – A New High-Pressure Nitridosilicate: Synthesis, Structure, Luminescence, and DFT Calculations", *Chem. – Eur. J.* **2008**, *14*, 7892–7902.

[17] S. R. Römer, "Density Functional Calculations of Pressure-Induced Phase Transformations of Group II Element Nitrides, Nitridosilicates and Nitridophosphates", *Dissertation*, Ludwig-Maximilians-Universität München, **2008**.

[18] A. A. Coelho, *TOPAS-Academic*, Version 4.1, Coelho Software, Brisbane (Australia), **2007**.

[19] a) J. David, J. Lang, "Sur un nitrure double de magnesium et de silicium", *C. R. Hebd. Seances Acad. Sci.* **1965**, *261*, 1005–1007; b) H. Yamane, H. Morito, "$Ba_4Mg[Si_2N_6]$, $Ba_3Ca_2[Si_2N_6]$ and $Ba_{1.6}Sr_{3.4}[Si_2N_6]$ – Quaternary barium alkaline-earth silicon nitrides containing isolated nitridosilicate anions of $[Si_2N_6]^{10-}$", *J. Alloys Compd.* **2013**, *555*, 320–324; c) S. Schmiechen, H. Schneider, P. Wagatha, C. Hecht, P. J. Schmidt, W. Schnick, "Toward New Phosphors for Application in Illumination-Grade White pc-LEDs: The Nitridomagnesosilicates $Ca[Mg_3SiN_4]$:$Ce^{3+}$, $Sr[Mg_3SiN_4]$:$Eu^{2+}$, and $Eu[Mg_3SiN_4]$", *Chem. Mater.* **2014**, *26*, 2712–2719; d) S. Schmiechen, F. Nietschke, W. Schnick, "Structural Relationship between the Mg-Containing Nitridosilicates $Ca_2Mg[Li_4Si_2N_6]$ and $Li_2Ca_2[Mg_2Si_2N_6]$", *Eur. J. Inorg. Chem.* **2015**, 1592–1597.

[20] a) Z. A. Gál, P. M. Mallinson, H. J. Orchard, S. J. Clarke, "Synthesis and Structure of Alkaline Earth Silicon Nitrides: $BaSiN_2$, $SrSiN_2$, and $CaSiN_2$", *Inorg. Chem.* **2004**, *43*, 3998–4006; b) F. Ottinger, R. Nesper, "Synthesis and Crystal Structure of the Nitridosilicates $Ca_5[Si_2N_6]$ and $Ca_7[NbSi_2N_9]$", *Z. Anorg. Allg. Chem.* **2005**, *631*, 1597–1602; c) H. Yamane, H. Morito, "Synthesis and Crystal Structures of $Ca_4SiN_4$ and New Polymorph of $Ca_5Si_2N_6$", *Inorg. Chem.* **2013**, *52*, 5559–5563.

[21] Further details on the crystal structures can be obatined from the Fachinformations-Zentrum Karlsruhe, 76344 Eggenstein-Leopoldshafen, Germany (Fax: (+49)7247-808-666; E-Mail: Crysdata@fiz-Karlsruhe.de) on quoting the depository numbers CSD-432573 ($Mg_2Si_5N_8$) and CSD-432574 (β-$Ca_2Si_5N_8$).

[22] N. A. Toropov, M. M. Stukalova, "ЗМАЕЩЕНИЕ НАТРИЯ В КРИСТАЛЛАХ β-ГЛИНОЗЕМА КАЛЬЦИЕМ, СТРОНЦИЕМ И БАРИЕМ" engl. "Replacement of sodium crystals of β-alumina with calcium, strontium and barium", *Dokl. Akad. Nauk SSSR* **1940**, *27*, 974–977.

[23] Picture for TOC provided by Thomas Eisenhut (http://www.xeta.at/)

# 3 $Fe_2Si_5N_8$: Access to Open-Shell Transition-Metal Nitridosilicates

*Angew. Chem., Int. Ed.* **2018**, *57*, 2409–2412; *Angew. Chem.* **2018**, *130*, 2433–2436.

**Corrigendum:** *Angew. Chem., Int. Ed.* **2019**, *58*, 10398; *Angew. Chem.* **2019**, *131*, 10506.

Philipp Bielec, Oliver Janka, Theresa Block, Rainer Pöttgen and Wolfgang Schnick

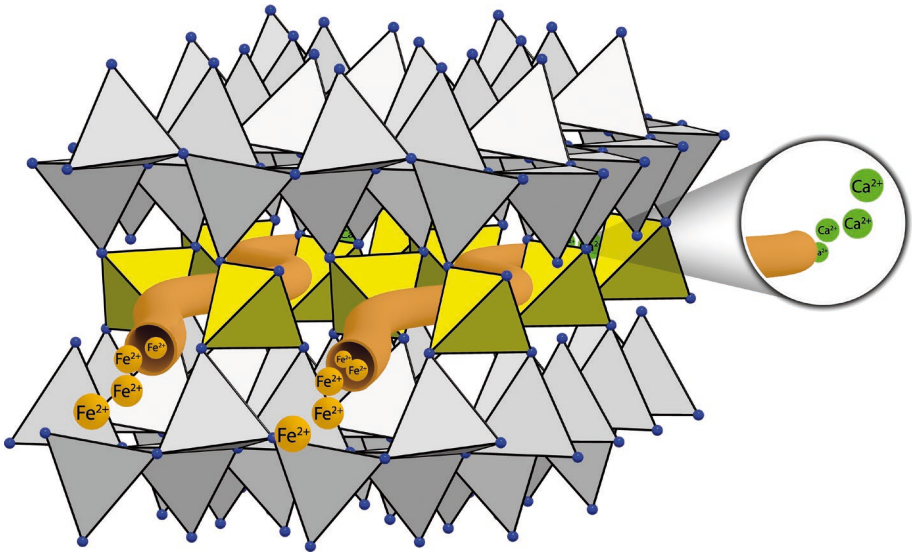


## Abstract

Highly condensed nitridosilicates doped with $Eu^{2+}$ or $Ce^{3+}$ play an important role in saving energy by converting the blue light of (In,Ga)N-LEDs. Although nitridosilicates are known for great structural variety based on covalent anionic Si–N networks, elemental variety is restricted. Presenting a significant extension of the latter, this work describes a general access to open-shell transition-metal nitridosilicates. As a proof-of-principle, the first iron nitridosilicate, namely $Fe_2Si_5N_8$, was prepared by exchanging $Ca^{2+}$ in α-$Ca_2Si_5N_8$ applying a $FeCl_2$ melt (salt metathesis). The title compound was analyzed by PXRD, EDX, ICP-OES, CHNS analysis, TGA/DSC, Mößbauer spectroscopy and magnetic susceptibility measurements. Furthermore, the structure of α-$Ca_2Si_5N_8$ was determined at 800 and 900 °C confirming the anionic network of α-$Ca_2Si_5N_8$ providing possible migration pathways for the ion exchange reaction.

## 3.1 Introduction with Results and Discussion

In a world of rising demand for high-tech materials, the availability of elemental resources becomes an increasingly critical issue.[1] At this point, development of nitridosilicates, a compound class mainly consisting of earth abundant elements Si and N,[2] can contribute to save natural resources. Besides the ecologic advantage, highly condensed nitridosilicates possess extraordinary chemical and thermal stability owing to rigid polymeric Si–N networks such as the parent compound $Si_3N_4$.[3] Therefore, these covalent network structures often are excellent host compounds for open-shell activator cations such as $Eu^{2+}$ and $Ce^{3+}$, leading to highly efficient luminophores for state-of-the-art LED applications.[4–6]

Cations with unpaired electrons may contribute favorable materials properties such as luminescence or magnetism.[7] Thus, opening a general access to transition-metal nitridosilicates has been a great challenge for decades. For example, an early attempt starting from Co metal and SDI yielded hexagonal $Si_3N_4$ microtubes filled with intermetallic Co/Si compounds. These microtubes grew out of metal droplets by a VLS mechanism instead of formation of Co-nitridosilicates.[8] This example illustrates one of the main obstacles of synthetic attempts towards transition-metal nitridosilicates. Under the typical conditions, reduction of the late transition metals and formation of thermodynamically more stable metallic compounds prohibits formation of the desired products.[9,10] In contrast, early transition metals form highly stable binary compounds *M*N (*M* = Sc, Ti, V, Cr) with rock-salt type of structure,[11] preventing the formation of multinary nitridosilicates as well.

Recently, we developed an ion exchange reaction route (salt metathesis) in metal halide melts for syntheses of hitherto inaccessible nitridosilicates (Eqations 3.1–3.2).[12–14]

$$\alpha\text{-}Ca_2Si_5N_8 + 2\ MgCl_2 \rightarrow Mg_2Si_5N_8 + 2\ CaCl_2 \qquad 3.1$$

$$Sr_2Si_5N_8 + 2\ CaCl_2 \rightarrow \beta\text{-}Ca_2Si_5N_8 + 2\ SrCl_2 \qquad 3.2$$

The reaction conditions of this ion exchange route are fundamentally different from other nitridosilicate syntheses in which the anionic polymeric tetrahedral network is formed in presence of the cations to be incorporated.

Besides introducing $Mg^{2+}$ into the nitridosilicate network of α-$Ca_2Si_5N_8$ and realizing a novel structural variant β-$Ca_2Si_5N_8$ resembling $Sr_2Si_5N_8$, we now succeeded to extend this approach to open-shell transition-metal nitridosilicates. As proof of concept, the first iron nitridosilicate $Fe_2Si_5N_8$ was prepared at 980 °C in sealed quartz ampoules according to Equation 3.3.

$$\alpha\text{-}Ca_2Si_5N_8 + 2\ FeCl_2 \rightarrow Fe_2Si_5N_8 + 2\ CaCl_2 \qquad 3.3$$

To ensure complete cation exchange (chapter B.6.1), a three equivalent excess of $FeCl_2$ was used. $Fe_2Si_5N_8$ was obtained as a crystallographic phase pure brown solid (chapter B.6.10), stable towards air, moisture, and concentrated acids. Detailed information on the RIETVELD refinement and the elemental composition, determined by EDX, ICP-OES, and CHNS analysis, are given in chapters B.6.2, B.6.5, B.6.6 and B.6.7.[15]

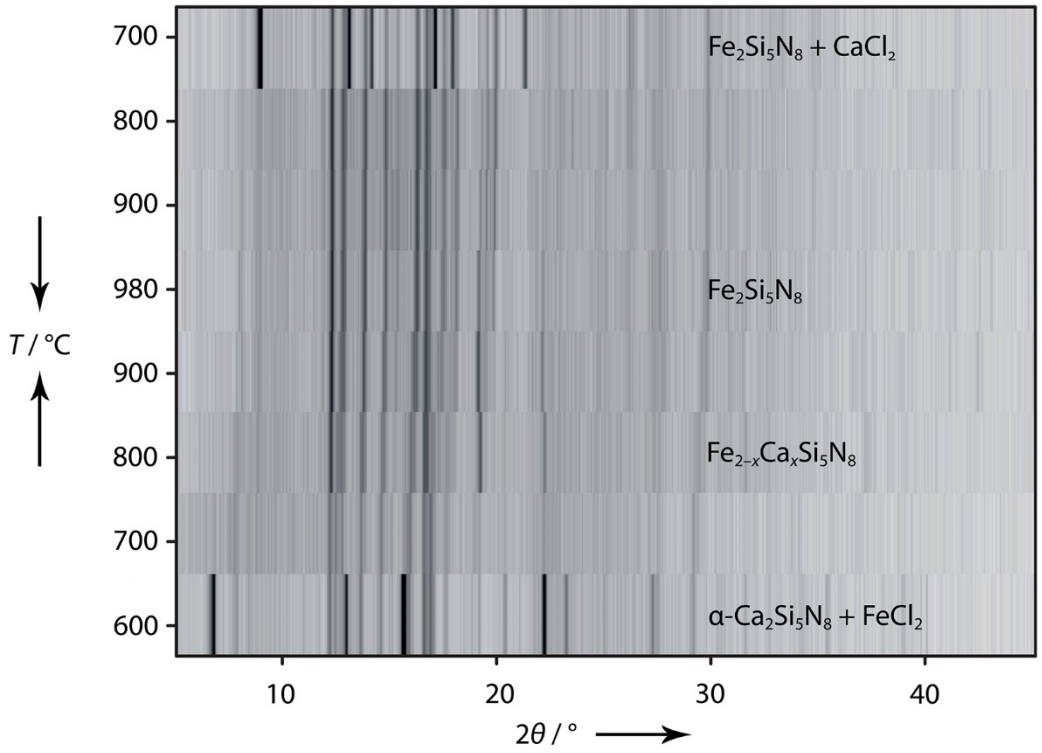


**Figure 3.1:** *In situ* TDPXRD. Dark colors symbolize high intensities ($T_{max}$ = 980 °C for 10 min, heating and cooling rate of 5 °C · $min^{-1}$, 100 °C/80 °C step size).

As for the synthesis of $Mg_2Si_5N_8$,[14] TDPXRD shows continuous ion exchange between α-$Ca_2Si_5N_8$ and two equivalents of $FeCl_2$, leading to $Fe_2Si_5N_8$ (Figure 3.1 and chapter B.6.13).

As mentioned in our previous work,[14] we suspect cation mobility at the reaction temperature in α-$Ca_2Si_5N_8$ to enable ion exchange while the covalent network structure is widened with increasing

temperature but structurally preserved. To elucidate the reaction mechanism of the ion exchange, HR-TDPXRD was performed to determine the structure of the starting material α-$Ca_2Si_5N_8$ at 800 (Figure 3.2 and chapter B.4.2) and 900 °C (chapter B.4.3), respectively. As expected, the unit cell of α-$Ca_2Si_5N_8$ expands (*a* + 0.1%, *b* + 0.3%, *c* + 0.4%) with temperature, preserving the layers of $SiN_4$-tetrahedra *dreier* rings (gray) connected by $SiN_4$-tetrahedra (purple, yellow). Based on geometrical calculations, we identified possible migration pathways for $Ca^{2+}$ using TOPOS (Figure 3.2 and chapter B.5).[16] The migration pathways (blue, orange) are running along the planar $SiN_4$ tetrahedra layers (gray), winding around the layer-connecting $SiN_4$-tetrahedra (purple, yellow).[17] Based on these geometrical calculations we suggest that ion conductivity of cations such as $Mg^{2+}$, $Ca^{2+}$, or $Fe^{2+}$ is the reason for the continuous ion exchange in α-$Ca_2Si_5N_8$ at the selected reaction temperatures. This mechanism of ion conductivity can also explain why the ion exchange reaction for $Fe_2Si_5N_8$ requires higher temperature (980 °C) for complete $Ca^{2+}$ exchange than for $Mg_2Si_5N_8$ synthesis (850 °C).[14] Owing to the higher *EN* of Fe compared to Mg, Fe–N bonds are expected to be more covalent than those between Mg and N.[18] Since covalent interactions are intrinsically directed in space compared to spherical ionic interactions, the energy barrier for movement of $Fe^{2+}$ in the anionic network is assumed to be increased.

Applying Mößbauer spectroscopy (Figure 3.3), we could confirm high-spin states at $Fe^{2+}$, as it is expected from crystal field theory owing to distorted tetrahedral environments in $Fe_2Si_5N_8$. Two major signals (1 and 2) in Figure 3.3 with a fixed area ratio of 1:1, in line with the crystallographic information, show an isomer shift of 0.837(2) and 0.816(2) mm · $s^{-1}$, respectively, which is in the usual range for high-spin $Fe^{2+}$ ions.[19] The quadrupole splitting of 1.587(6) and 1.952(6) mm · $s^{-1}$ is in good agreement with a non-cubic site symmetry of the Fe atoms. Both signals show line broadening in accordance with other $^{57}$Fe Mößbauer spectroscopic measurements, possibly caused by disorder owing to statistical distribution of Fe split positions in the sample (chapters B.6.3 and B.6.4). Furthermore, two minor signals with area ratios of 5.2(3) and 2.9(4)% belonging to side phases were necessary to completely reproduce the recorded spectrum (chapter B.6.11).

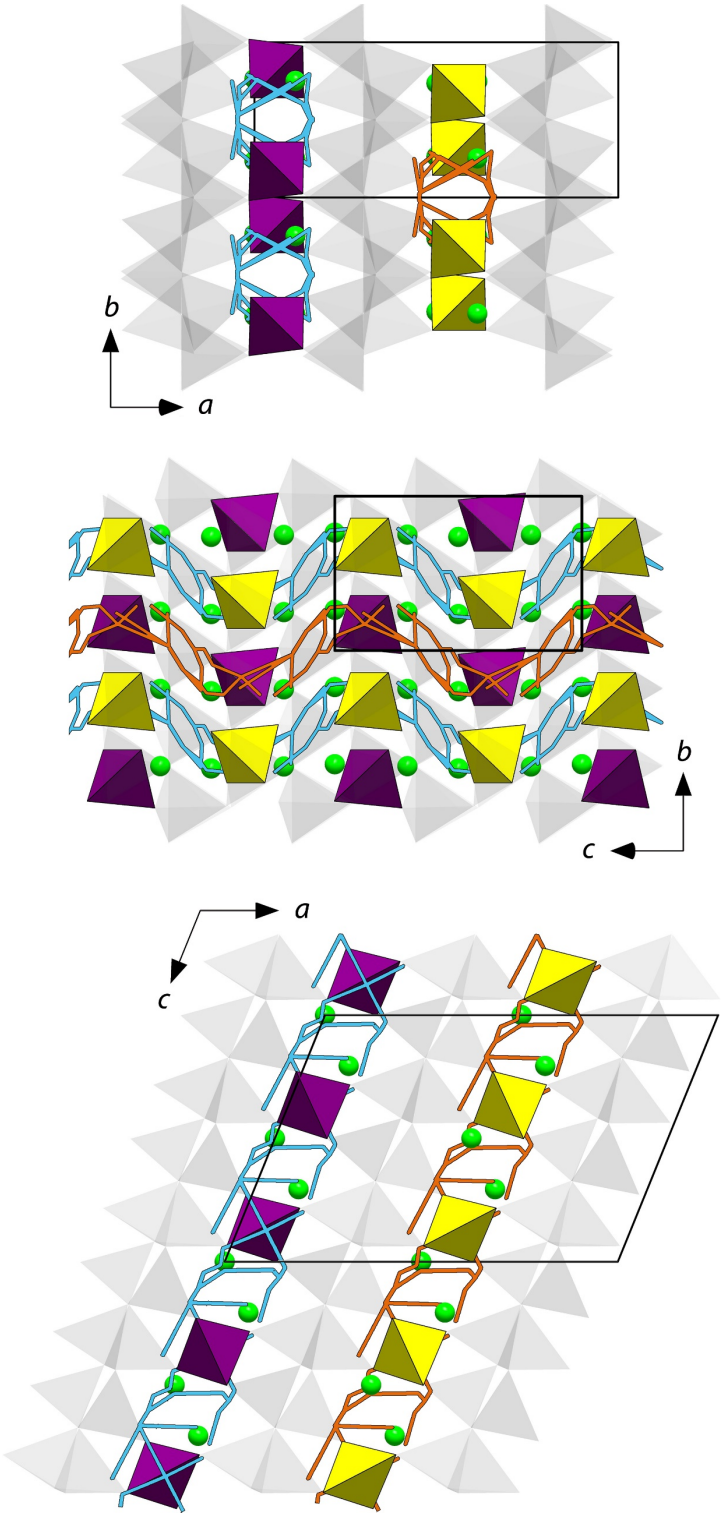


**Figure 3.2:** Structure of α-$Ca_2Si_5N_8$ at 800 °C along *c* (top), along *a* (middle), and along *b* (bottom) with planar $SiN_4$-tetrahedral layers (gray), connecting $SiN_4$-tetrahedra (purple, yellow) and calculated migration pathways (blue, orange) for $Ca^{2+}$ (green).

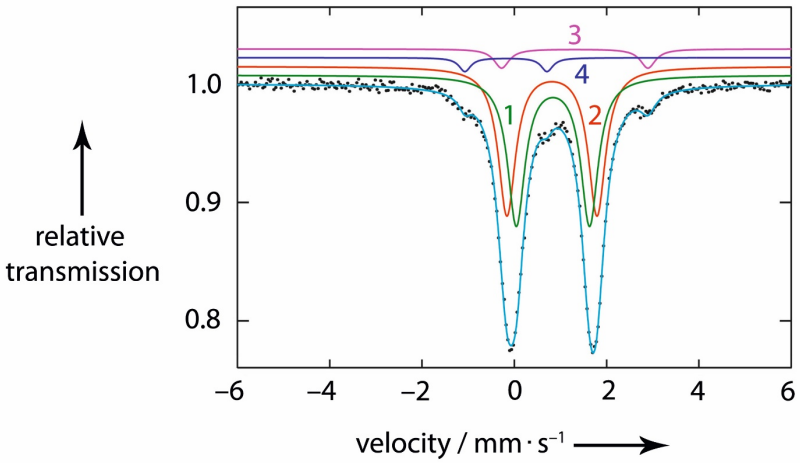


**Figure 3.3:** Experimental (data points) and simulated (continuous lines) $^{57}$Fe Mößbauer spectrum of $Fe_2Si_5N_8$ at 78 K. The obtained fitting parameters are listed in Table B.19.

According to magnetic susceptibility measurements ($\chi$) at an external field of 10 kOe (details given in chapter B.6.12), $Fe_2Si_5N_8$ shows paramagnetism and a presumably antiferromagnetic magnetic anomaly ($T_N$ = 36.1 K) at low temperatures. By applying ZFC/FC measurements at different external fields (Figure 3.4, top) combined with a magnetization isotherm at 10 K (Figure 3.4, middle), we could show that this anomaly can be ascribed to an impurity phase. Comparison with literature values of $Fe_2Si_2O_6$ ($T_N$ = 43 K)[20] and $CaFeSi_2O_6$ ($T_N$ = 38 K)[21] combined with Mößbauer spectroscopy results (chapter B.6.11) indicate $Fe_{2-x}Ca_xSi_2O_6$ to be the impurity phase. The effective magnetic moment of the investigated sample was calculated according to $\mu_{eff} = \sqrt{4} \cdot \chi \cdot T$ and plotted versus the temperature in Figure 3.4 (bottom). The effective moment reaches $\mu_{eff}$ = 3.2(1) $\mu_B$ at 27 °C. This is higher compared to the expected 2.83 $\mu_B$; however, owing to the magnetically active impurity phase with a contribution of about 8% (Figure 3.3), it can be confirmed that at least the majority phase exhibits Fe atoms in the divalent oxidation state.

$$3\ Fe_2Si_5N_8 \rightarrow 6\ Fe + 5\ Si_3N_4 + 2\ N_2\uparrow \qquad 3.4$$

Finally, thermal stability of $Fe_2Si_5N_8$ was investigated by TGA/DSC under nitrogen atmosphere showing an exothermal process combined with mass loss indicating decomposition at 1097 °C (chapter B.6.8). Decomposition products were determined by PXRD of a $Fe_2Si_5N_8$ sample heated to 1200 °C in a radio-frequency furnace pointing to the reaction shown in Equation 3.4 (chapter B.6.9). These results are in good agreement with the observed behavior of systems containing transition metals, Si and N.[8]

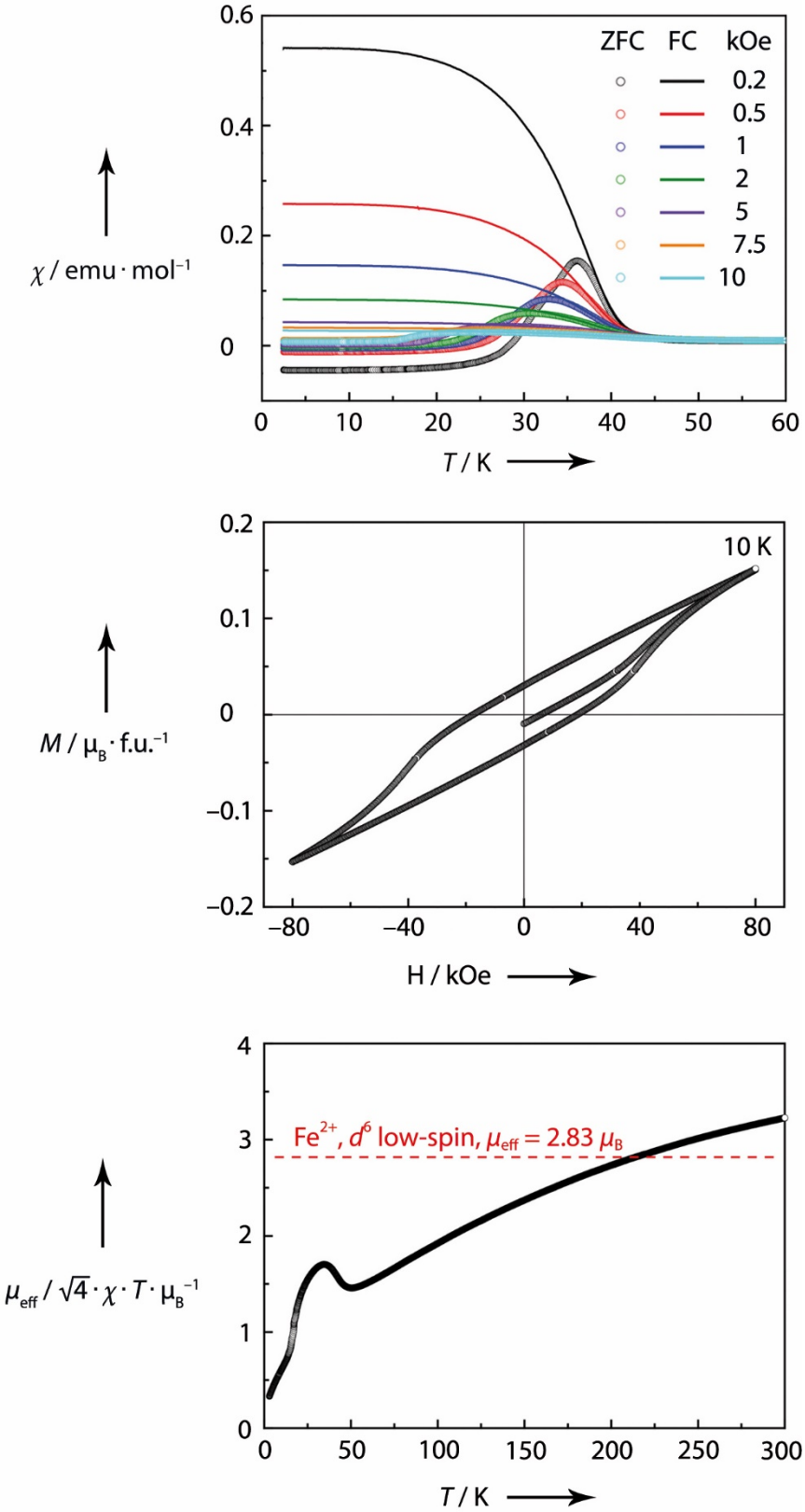


**Figure 3.4:** Magnetic properties of $Fe_2Si_5N_8$: Top: temperature dependence of zero-field-cooled/ field cooled (ZFC/FC) measurements conducted at different applied fields; middle: magnetization isotherm at 10 K; bottom: temperature dependence of the effective magnetic moment $\mu_{eff}$.

In conclusion, we established a general access (so far also successful results with $Mn^{2+}$ and $Co^{2+}$) to open-shell transition-metal nitridosilicates by the exchange of alkaline-earth with transition-metal cations. As a proof-of-concept, the first iron nitridosilicate, namely $Fe_2Si_5N_8$, was prepared, representing a significant extension of elemental variety in nitridosilicates. Occurrence of high-spin $Fe^{II}$ in paramagnetic $Fe_2Si_5N_8$ could be confirmed by Mößbauer spectroscopy and magnetic susceptibility measurements. Applying HR-TDPXRD, we elucidated the structure of α-$Ca_2Si_5N_8$ at 800 and 900 °C, enabling the localization of possible migration pathways for cations in the Si–N networks. Since $\kappa$ in nitridosilicates with formula type $M_2Si_5N_8$ is comparatively high, it can be expected that migration pathways can occur in many other nitridosilicates at elevated temperatures. Furthermore, incorporating small cations such as $Mg^{2+}$ into structures, initially built up with larger cations like $Ca^{2+}$ or $Sr^{2+}$, migration pathways of the final compounds could even occur at temperatures close to ambient conditions.

## 3.2 References


[1] European Commission, "Report on critical raw materials for the EU", **2014**.

[2] M. Zeuner, S. Pagano, W. Schnick, "Nitridosilicates and Oxonitridosilicates: From Ceramic Materials to Structural and Functional Diversity", *Angew. Chem., Int. Ed.* **2011**, *50*, 7754–7775; "Nitridosilicate und Oxonitridosilicate: von keramischen Materialien zu struktureller und funktioneller Diversität", *Angew. Chem.* **2011**, *123*, 7898–7920.

[3] a) H. Huppertz, W. Schnick, "$BaYbSi_4N_7$ – Unexpected Structural Possibilities in Nitridosilicates", *Angew. Chem., Int. Ed. Engl.* **1996**, *35*, 1983–1984; "$BaYbSi_4N_7$ – überraschende strukturelle Möglichkeiten in Nitridosilicaten", *Angew. Chem.* **1996**, *108*, 2115–2116; b) D. Hardie, K. H. Jack, "Crystal Structures of Silicon Nitride", *Nature* **1957**, *180*, 332–333.

[4] R. Mueller-Mach, G. Mueller, M. R. Krames, H. A. Höppe, F. Stadler, W. Schnick, T. Juestel, P. Schmidt, "Highly efficient all-nitride phosphor-converted white light emitting diode", *Phys. Status Solidi A* **2005**, *202*, 1727–1732.

[5] W. Schnick, "Shine a light with nitrides", *Phys Status Solidi RRL* **2009**, *3*, A113–A114.

[6] a) Z. Inoue, M. Mitomo, N. Ii, "A crystallographic study of a new compound of lanthanum silicon nitride, $LaSi_3N_5$", *J. Mater. Sci.* **1980**, *15*, 2915–2920; b) M. Woike, W. Jeitschko, "Preparation and Crystal Structure of the Nitridosilicates $Ln_3Si_6N_{11}$ (Ln = La, Ce, Pr, Nd, Sm)

and $LnSi_3N_5$ (Ln = Ce, Pr, Nd)", *Inorg. Chem.* **1995**, *34*, 5105–5108; c) L. Y. Cai, X. D. Wei, H. Li, Q. L. Liu, "Synthesis, structure and luminescence of $LaSi_3N_5:Ce^{3+}$ phosphor", *J. Lumin.* **2009**, *129*, 165–168; d) T. Seto, N. Kijima, N. Hirosaki, "A New Yellow Phosphor $La_3Si_6N_{11}:Ce^{3+}$ for White LEDs", *ECS Trans.* **2009**, *25*, 247–252.

[7] T. Schlieper, W. Schnick, "Nitrido-silicate. II Hochtemperatur-Synthese, Kristallstruktur und magnetische Eigenschaften von $Ce_3[Si_6N_{11}]$", *Z. Anorg. Allg. Chem.* **1995**, *621*, 1535–1538.

[8] a) H. Huppertz, N. Stock, W. Schnick, "The First Crystalline Hexagonal $Si_3N_4$ Microtubes", *Adv. Mater. (Weinheim, Ger.)* **1996**, *8*, 844–847; b) H. Huppertz, "Strukturelle Erweiterung der Nitridosilicate", *Dissertation*, Universität Bayreuth, **1997**.

[9] W. Schnick, H. Huppertz, "Nitridosilicates – A Significant Extension of Silicate Chemistry", *Chem. – Eur. J.* **1997**, *3*, 679–683.

[10] T. B. Massalski, H. Okamoto, P. R. Subramanian, L. Kacprzak, *Binary Alloy Phase Diagrams*, 2nd Edition, ASM International, Novelty, **1990**.

[11] K. Becker, F. Ebert, "Die Kristallstruktur einiger binärer Carbide und Nitride", *Z. Phys.* **1925**, *31*, 268–272.

[12] T. Schlieper, W. Schnick, "Nitrido-Silicate. I Hochtemperatur-Synthese und Kristallstruktur von $Ca_2Si_5N_8$", *Z. Anorg. Allg. Chem.* **1995**, *621*, 1037–1041.

[13] T. Schlieper, W. Milius, W. Schnick, "Nitrido-silicate. II Hochtemperatur-Synthesen und Kristallstrukturen von $Sr_2Si_5N_8$ und $Ba_2Si_5N_8$", *Z. Anorg. Allg. Chem.* **1995**, *621*, 1380–1384.

[14] P. Bielec, W. Schnick, "Increased Synthetic Control – Gaining Access to Predicted $Mg_2Si_5N_8$ and β-$Ca_2Si_5N_8$", *Angew. Chem., Int. Ed.* **2017**, *56*, 4810–4813; "Increased Synthetic Control – Gaining Access to Predicted $Mg_2Si_5N_8$ and β-$Ca_2Si_5N_8$", *Angew. Chem.* **2017**, *129*, 4888–4891.

[15] A. A. Coelho, *TOPAS-Academic*, Version 4.1, Coelho Software, Brisbane (Australia), **2007**.

[16] a) V. A. Blatov, A. P. Shevchenko, TOPOS Version 4.0, Samara State University, **1989–2010**; b) V. A. Blatov, A. P. Shevchenko, V. N. Serezhkin, "*TOPOS*3.1 – program package for multipurpose geometrical and topological analysis of crystal structures", *J. Appl. Crystallogr.* **1999**, *32*, 377; c) V. A. Blatov, "VORONOI–DIRICHLET POLYHEDRA IN CRYSTAL CHEMISTRY: THEORY AND APPLICATIONS", *Crystallogr. Rev.* **2004**, *10*, 249–318; d) V.

A. Blatov, G. D. Ilyushin, O. A. Blatova, N. A. Anurova, A. K. Ivanov-Schits, L. N. Dem'yanets, "Analysis of migration paths in fast-ion conductors with Voronoi-Dirichlet partition", *Acta Crystallogr., Sect. B: Struc. Sci.* **2006**, *62*, 1010–1018.

[17] Further details on crystal structures can be obtained from the Fachinformations-Zentrum Karlsruhe, 76344 Eggenstein-Leopoldshafen, Germany (Fax: (+49)7247-808-666; E-Mail: Crysdata@fiz-Karlsruhe.de) on quoting the depository numbers CSD-433575 (α-$Ca_2Si_5N_8$ at 800 °C), CSD-433576 (α-$Ca_2Si_5N_8$ at 900 °C) and CSD-433577 ($Fe_2Si_5N_8$).

[18] A. L. Allred, E. G. Rochow, "A SCALE OF ELECTRONEGATIVITY BASED ON ELECTROSTATIC FORCE", *J. Inorg. Nucl. Chem.* **1958**, *5*, 264–268.

[19] G. K. Shenoy, F. E. Wagner, *Mössbauer Isomer Shifts*, North-Holland Publishing Company, Amsterdam, **1978**.

[20] A. Sawaoka, S. Miyahara, S.-i. Akimoto, "Magnetic Properties of Several Metasilicates and Metagermanates with Pyroxene Structure", *J. Phys. Soc. Jpn.* **1968**, *25*, 1253–1257.

[21] J. M. D. Coey, S. Ghose, "MAGNETIC ORDER IN HEDENBERGITE: $CaFeSi_2O_6$", *Solid State Commun.* **1985**, *53*, 143–145.

## 3.3 Corrigendum

In Figure 3.4 of this communication, $Fe^{2+}$ was assigned as high-spin (Figure 3.4). In fact, the Mössbauer spectroscopic measurements do not allow to distinguish between high- and low-spin states in $Fe_2Si_5N_8$. However, according to the spin-only formula, the observed value of 3.2(1) $\mu_B$ indicate approximately two unpaired electrons and thus low-spin states of $Fe^{2+}$ ($d^6$) for the present heavily distorted tetrahedral environments. No part of the quintessence in the Communication is affected. The authors sincerely apologize for this misassignment.

# 4 Targeting Vacancies in Nitridosilicates: Aliovalent Substitution of $M^{2+}$ ($M$ = Ca, Sr) by $Sc^{3+}$ and $U^{3+}$

*Angew. Chem., Int. Ed.* **2019**, *58*, 840–843; *Angew. Chem.* **2019**, *131*, 850–853.

Philipp Bielec, Lucien Eisenburger, H. Lars Deubner, Daniel Günther, Florian Kraus, Oliver Oeckler and Wolfgang Schnick

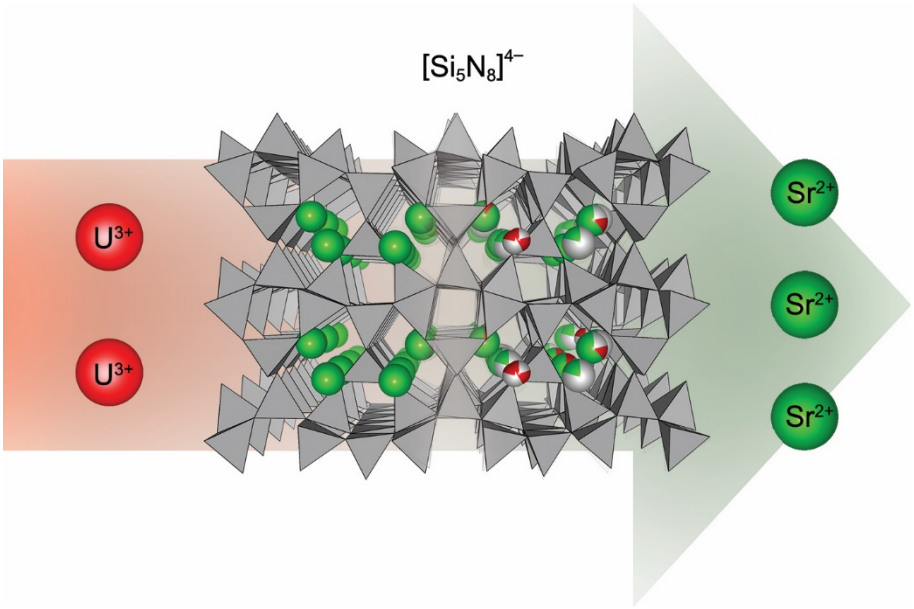


## Abstract

Based on the known linking options of their fundamental building unit, i.e. $SiN_4$ tetrahedra, nitridosilicates belong to the inorganic compound classes with the greatest structural variability. Although facilitating the discovery of novel Si–N networks, this variability represents a challenge when targeting non-stoichometric compounds. Meeting this challenge, we report on a strategy for targeted creation of vacancies in highly condensed nitridosilicates by exchanging divalent $M^{2+}$ by trivalent $M^{3+}$ via the ion exchange approach. As proof of concept, the first Sc and U nitridosilicates were prepared from α-$Ca_2Si_5N_8$ and $Sr_2Si_5N_8$. PXRD and synchrotron single-crystal XRD showed random vacancy distribution in $Sc_{0.2}Ca_{1.7}Si_5N_8$ and partial vacancy ordering in $U_{0.5x}Sr_{2-0.75x}Si_5N_8$ with $x \approx 1.05$. The high chemical stability of U nitridosilicates makes them interesting candidates for immobilization of actinides.

## 4.1 Introduction with Results and Discussion

The beneficial effect of vacancies in crystal structures on properties like ion conductivity for both cations (e.g. $Li^+$, $Na^+$)[1] and anions (e.g. $O^{2-}$)[2] is well known. Moreover, vacancies play an important role in nuclear fuel materials. The process of fission gas incorporation (e.g. Xe) into vacancies is expected to have a positive effect on the fission process by reducing swelling of the materials and therefore improving mechanical properties.[3] Nevertheless, high amounts of vacancies may have a destabilizing effect on solid-state materials and can only be incorporated into compounds that withstand such an effect.

Highly condensed nitridosilicates with $\kappa \geq {}^1/_2$ are well known for their intrinsic stability.[4] As known from the parental compound $Si_3N_4$,[5] the stability of these compounds arises from highly covalent networks built up from $SiN_4$ tetrahedra. As the Si–N bond energy is almost equal to that of C–C in diamond,[6] highly condensed Si–N network structures typically exhibit high mechanical, thermal and chemical stability. This enables applications as sheath materials, ball bearings or even as internal combustion engine materials such as in pistons or gas turbines.[5b, 7] Despite their stability, highly covalent Si–N networks can exhibit great flexibility as well. Preserving the connectivity, nitridosilicates like $M_2Si_5N_8$ ($M$ = Ca, Sr, Ba, Eu)[8] or $MSi_7N_{10}$ ($M$ = Sr, Ba)[9] may incorporate cations of different sizes only by distortion of the networks. Moreover, nitridosilicate networks are even flexible enough to compensate a change in cation charge. In $La_{3-x}Ca_{1.5x}Si_6N_{11}:Eu^{2+}$ ($x \approx 0.77$)[10] substitution of $La^{3+}$ by $Ca^{2+}$ leads to $Ca^{2+}$ located on former $La^{3+}$ sites as well as on additional interstitial sites to provide electroneutrality.

In contrast to an exchange of $M^{3+}$ by $M^{2+}$, which leads to additional cation sites, we now investigated the concept of targeting vacancies in nitridosilicates by substitution of $M^{2+}$ by $M^{3+}$. The incorporation of two $M^{3+}$ cations results in three $M^{2+}$ cations being removed, creating one cation vacancy. In order to ensure this process instead of forming stoichiometric compounds containing both $M^{2+}$ and $M^{3+}$ or multiple phases due to the enormous structural variability of Si–N networks,[11] cations of pre-synthesized nitridosilicates were exchanged by reaction with metal chlorides.[8d, 12]

As a proof of concept, we incorporated $Sc^{3+}$ and $U^{3+}$, both not yet observed in nitridosilicates, into Si–N networks. Applying $MCl_3$ ($M$ = Sc, U)[13] melts, $Sc^{3+}$ replaced $Ca^{2+}$ in α-$Ca_2Si_5N_8$ and $Sr^{2+}$ was exchanged by $U^{3+}$ in $Sr_2Si_5N_8$ according to Equation 4.1 ($AE$ = alkaline-earth metal).

$$0.2\ MCl_3 + AE_2Si_5N_8 \rightarrow 0.3\ AECl_2 + M_{0.2}AE_{1.7}Si_5N_8 \qquad 4.1$$

Detailed information on the reaction conditions and the elemental composition determined by EDX and ICP-OES are given in chapters C.3.1, C.3.3, C.3.4, C.5.1 and C.5.3.

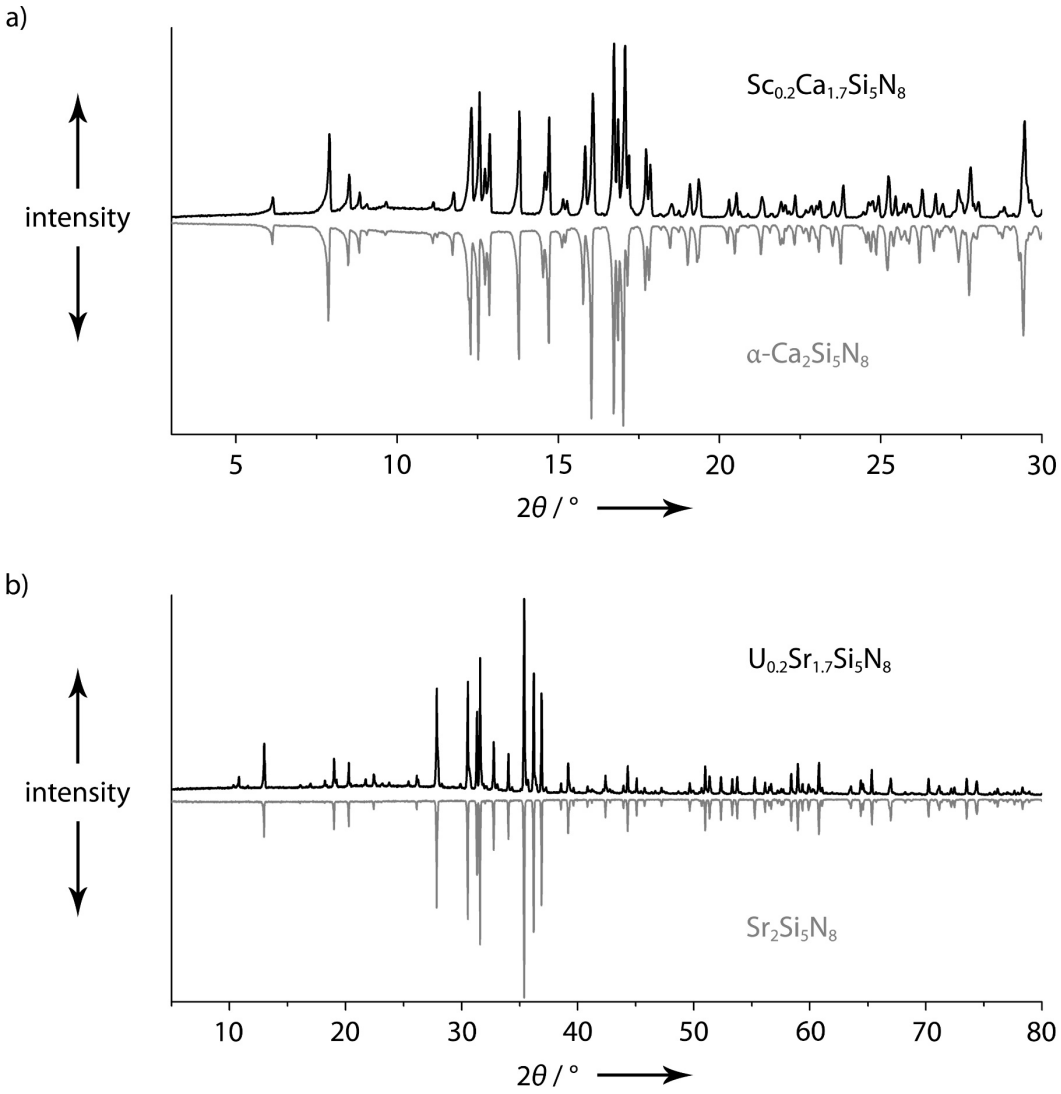


**Figure 4.1:** Powder X-ray diffractograms (Cu-Kα$_1$) of a) $Sc_{0.2}Ca_{1.7}Si_5N_8$ and b) $U_{0.2}Sr_{1.7}Si_5N_8$ compared to the parental compounds α-$Ca_2Si_5N_8$ and $Sr_2Si_5N_8$.

Powder XRD patterns of $M_{0.2}AE_{1.7}Si_5N_8$ show that the Si–N networks of the parental compounds are preserved during the vacancy incorporation (Figure 4.1). Carefully examining the powder patterns, two different types of vacancy distributions are observed. In the diffraction pattern of $Sc_{0.2}Ca_{1.7}Si_5N_8$ (Figure 4.1a, picture in chapter C.3.5), no considerable additional reflections compared to pristine α-$Ca_2Si_5N_8$ ($V$ = 723.0 Å$^3$) were observed. This indicates that the vacancies in this compound are statistically distributed over the cation positions. In fact, RIETVELD refinement for $Sc_{0.2}Ca_{1.7}Si_5N_8$ ($V$ = 718.24(2) Å$^3$) confirms less electron density on the former $Ca^{2+}$ sites (chapter C.3.2) due to incorporation of $Sc^{3+}$,[14] which is isoelectronic to $Ca^{2+}$.[15] Considering possible approaches toward

$M^{2+}$ ion conductors, targeting such a statistical distribution of vacancies could be a promising attempt.[1] In the diffraction pattern of a bulk sample with nominal composition $U_{0.2}Sr_{1.7}Si_5N_8$ (picture in chapter C.5.5), additional reflections are observed (mainly at low $2\theta$ values, Figure 4.1b). These reflections arise from $U_{0.525}Sr_{1.212}Si_5N_8$,[16] which exhibits an approximately tripled *a* lattice parameter ($a$ = 17.1295(3) Å) compared to that of $Sr_2Si_5N_8$ ($a$ = 5.710(2) Å). Due to the reaction conditions, $U_{0.525}Sr_{1.212}Si_5N_8$ is better described as a member of the solid solution series $U_{0.5x}Sr_{2-0.75x}Si_5N_8$, $x \approx 1.05$. According to RIETVELD refinement (Figure 4.2 and chapter C.5.4),[14] the bulk sample with a nominal composition of $U_{0.2}Sr_{1.7}Si_5N_8$ can approximately be described as a heterogeneous mixture of $Sr_2Si_5N_8$ and $U_{0.5x}Sr_{2-0.75x}Si_5N_8$ ($x \approx 1.05$).

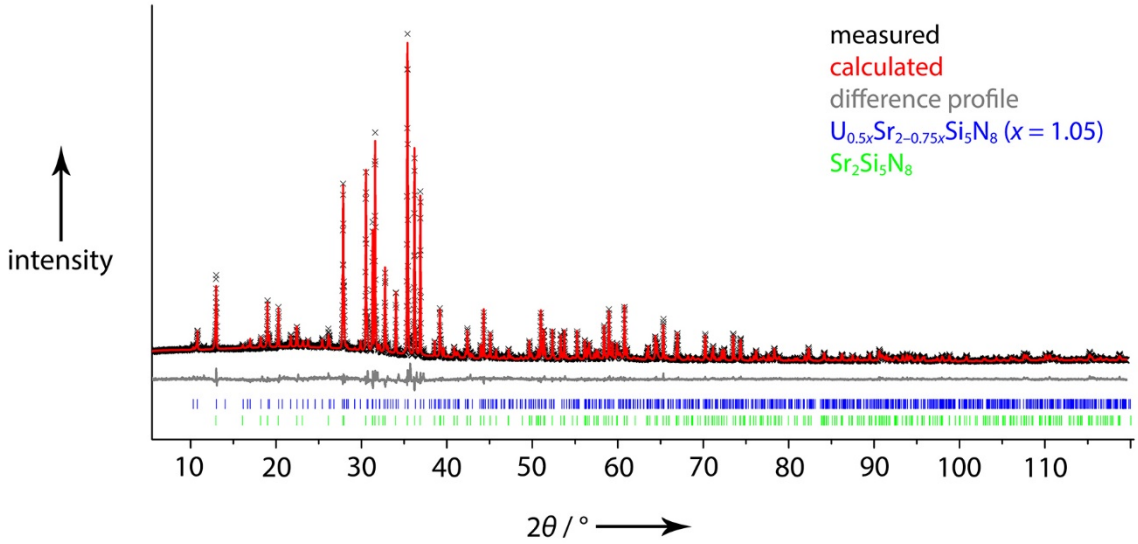


**Figure 4.2:** RIETVELD refinement (Cu-Kα₁) for a bulk sample with the nominal composition $U_{0.2}Sr_{1.7}Si_5N_8$ composed of $U_{0.5x}Sr_{2-0.75x}Si_5N_8$ ($x \approx 1.05$) and $Sr_2Si_5N_8$.

The crystal structure of $U_{0.5x}Sr_{2-0.75x}Si_5N_8$ ($x \approx 1.05$) is shown in Figure 4.3; it exhibits a partially ordered distribution of $U^{3+}$ and vacancies. Along the red arrow, Sr4 (21.2% occupied), two mixed Sr/U positions and another Sr4 site break the symmetry of pristine $Sr_2Si_5N_8$, where only Sr atoms are arranged along [100] (blue arrows), resulting in the tripled *a* lattice parameter. The ordered distribution of $U^{3+}$ and vacancies confirms the enormous flexibility of the $[Si_5N_8]^{4-}$ network. Derived from a position suitable for $M^{2+}$ cations the CHARDI value of ≈ 2 changed to ≈ 0.4 for the Sr4 site due to network distortion, providing a suitable site for vacancies (chapter C.4.3).[17] In case of a vacancy on the Sr4 site (Figure 4.3b), Sr2A/U2A and U1A are occupied, compensating the anionic charge surrounding the empty Sr4 site. If Sr4 is present, the more distant U1B and Sr2B sites are occupied.

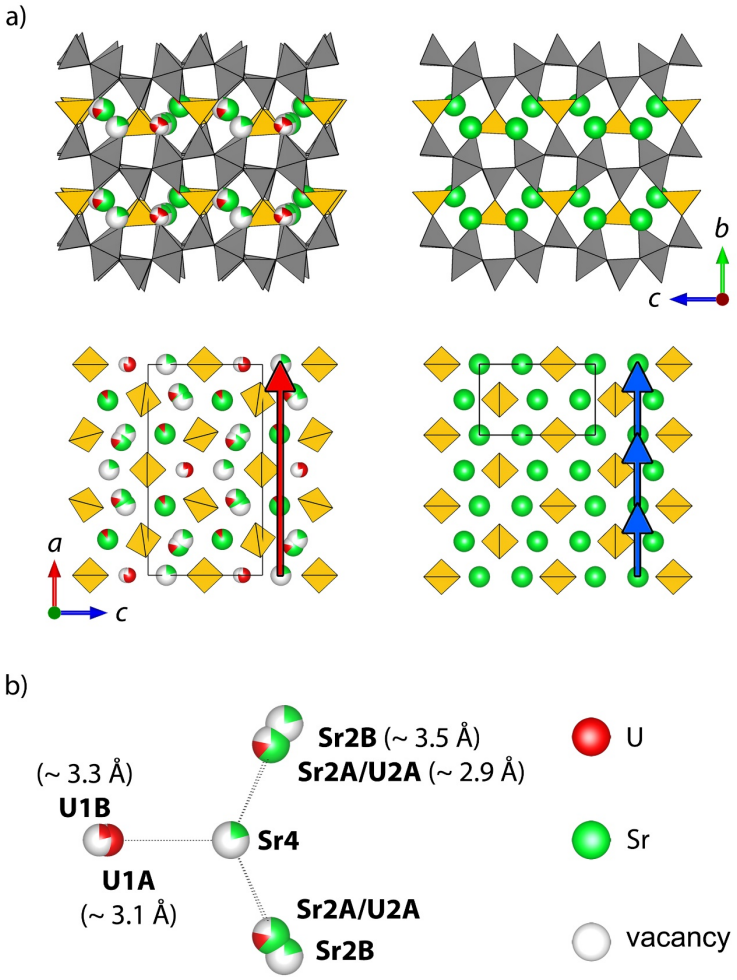


**Figure 4.3:** a) Crystal structures of $U_{0.5x}Sr_{2-0.75x}Si_5N_8$ ($x \approx 1.05$) (left) and $Sr_2Si_5N_8$ (right) along [100] (top) and along [010] (bottom); b) Cationic environment of Sr4 (21.2% occupation) in $U_{0.5x}Sr_{2-0.75x}Si_5N_8$ ($x \approx 1.05$) including distances *M*–Sr4 (*M* = Sr, U).

The ability of the flexible $[Si_5N_8]^{4-}$ network to incorporate different cations as well as vacancies combined with the intrinsic stability of highly condensed nitridosilicates makes the nominal bulk phase $U_{0.2}Sr_{1.7}Si_5N_8$ a compound interesting for immobilization of uranium. As the basic requirement for such an application, the chemical stability of a powder sample was investigated by treatment with $HNO_3$ (69%), KOH (10%) and several times with $H_2O$, each for 24 h at 90 °C (chapter C.5.2). The U contents dissolved in this process were determined by ICP-MS. While the corrosive conditions in $HNO_3$ and KOH only dissolved around 11.4% and 6.8% of the total U content, less than 0.2% was released by the treatments with $H_2O$. In summary, more than 81% of the total U quantity introduced as highly reactive $UCl_3$ could be immobilized toward treatments with $HNO_3$, KOH or $H_2O$.

Since nitridosilicates do not occur in nature, no data on long-term stability are available. However, $Si_3N_4$ has been found in chondrites containing samples with putatively presolar origin.[18] Obviously,

such $Si_3N_4$ particles had withstood the ionizing space radiation. Moreover, $Si_3N_4$ has been considered as diluent for burning of plutonium fuels due to its high durability.[19] Nitridosilicates derive from a formal substitution of Si in $Si_3N_4$. Therefore, its properties indicate that consideration of highly condensed covalent host lattices like $[Si_5N_8]^{4-}$ or those with even higher condensation degrees could be worthwhile in order to develop highly durable nuclear waste forms. The dominant part of bond energy in a highly condensed nitridosilicate arises from the covalent Si–N network, resulting in a decreased influence of actinide–N interactions on the total energy of the compound. Thus, the loss of actinide–N bond energy throughout a radioactive decay would have a minor destabilizing effect on the nitridosilicate itself. The ability of Si–N networks to compensate a local change in charge on the cation site by network distortion could possibly benefit immobilization of daughter nuclides with different charges after radioactive decays.

In conclusion, we opened up a route for targeting vacancies in nitridosilicate chemistry substituting $M^{2+}$ by $M^{3+}$ while preserving the Si–N connectivity. As proof of concept, the first scandium and uranium nitridosilicates were prepared. In $Sc_{0.2}Ca_{1.7}Si_5N_8$, vacancies were found to be statistically distributed over the cation positions. In the light of a desired $M^{2+}$ cation conductivity, such a distribution may be beneficial. In contrast, the incorporation of $U^{3+}$ into $Sr_2Si_5N_8$ yields $U_{0.5x}Sr_{2-0.75x}Si_5N_8$ ($x \approx 1.05$), which exhibits a partially ordered distribution of $U^{3+}$ and vacancies. In fact, the $[Si_5N_8]^{4-}$ network is distorted in a way that one of the $Sr^{2+}$ sites of $Sr_2Si_5N_8$ may contain only around 20% cations and almost 80% vacancies. Despite this significant amount of vacancies in the nitridosilicate, the stability of a bulk sample containing $U_{0.5x}Sr_{2-0.75x}Si_5N_8$ ($x \approx 1.05$) was still sufficient to immobilize more than 80% of $U^{3+}$ cations even against concentrated mineral acids like $HNO_3$ (69%) and corrosive bases like KOH (10%). Due to this pronounced chemical stability combined with the ability to adapt to vacancies which could possibly be able to incorporate gaseous products of the radioactive decay, highly condensed nitridosilicates are interesting candidates for actinide immobilization. As a next step, investigations on the radiation stability are needed to check the suitability of nitridosilicates for nuclear waste storage.

## 4.2 References


[1] a) J. Emery, J. Y. Buzare, O. Bohnke, J. L. Fourquet, "Lithium-7 NMR and ionic conductivity studies of lanthanum lithium titanate electrolytes", *Solid State Ionics* **1997**, *99*, 41–51; b) M. Iqbal, K. Suzuki, G. Kobayashi, G. Zhao, M. Hirayama, R. Kanno, "Lithium ion conduction in doped $LaLiO_2$ system", *Solid State Ionics* **2016**, *285*, 33–37; c) N. J. J. de Klerk, M. Wagemaker, "Diffusion Mechanism of the Sodium-Ion Solid Electrolyte $Na_3PS_4$ and Potential Improvements of Halogen Doping", *Chem. Mater.* **2016**, *28*, 3122–3130; d) M. Duchardt, U. Ruschewitz, S. Adams, S. Dehnen, B. Roling, "Vacancy-Controlled $Na^+$ Superion Conduction in $Na_{11}Sn_2PS_{12}$", *Angew. Chem., Int. Ed.* **2018**, *57*, 1351–1355; "Vacancy-Controlled $Na^+$ Superion Conduction in $Na_{11}Sn_2PS_{12}$", *Angew. Chem.* **2018**, *130*, 1365–1369.

[2] a) F. Shimojo, T. Okabe, F. Tachibana, M. Kobayashi, H. Okazaki, "Molecular Dynamics Studies of Yttria Stabilized Zirconia. I. Structure and Oxygen Diffusion", *J. Phys. Soc. Jpn.* **1992**, *61*, 2848–2857; b) F. Shimojo, H. Okazaki, "Molecular Dynamics Studies of Yttria Stabilized Zirconia. II. Microscopic Mechanism of Oxygen Diffusion", *J. Phys. Soc. Jpn.* **1992**, *61*, 4106–4118.

[3] a) A. E. Thompson, C. Wolverton, "First-principles study of noble gas impurities and defects in $UO_2$", *Phys. Rev. B* **2011**, *84*, 134111; b) S. T. Murphy, A. Chartier, L. Van Brutzel, J.-P. Crocombette, "Free energy of Xe incorporation at point defects and in nanovoids and bubbles in $UO_2$", *Phys. Rev. B* **2012**, *85*, 144102; c) N. Kuganathan, P. S. Ghosh, C. O. T. Galvin, A. K. Arya, B. K. Dutta, G. K. Dey, R. W. Grimes, "Fission gas in thoria", *J. Nucl. Mater.* **2017**, *485*, 47–55.

[4] M. Zeuner, S. Pagano, W. Schnick, "Nitridosilicates and Oxonitridosilicates: From Ceramic Materials to Structural and Functional Diversity", *Angew. Chem., Int. Ed.* **2011**, *50*, 7754–7775; "Nitridosilicate und Oxonitridosilicate: von keramischen Materialien zu struktureller und funktioneller Diversität", *Angew. Chem.* **2011**, *123*, 7898–7920.

[5] a) D. Hardie, K. H. Jack, "Crystal Structures of Silicon Nitride", *Nature* **1957**, *180*, 332–333; b) F. L. Riley, "Silicon Nitride and Related Materials", *J. Am. Ceram. Soc.* **2000**, *83*, 245–265.

[6] A. F. Holleman, N. Wiberg, *Lehrbuch der Anorganischen Chemie, Vol. 102*, DeGruyter, Berlin, Boston, **2008**.

[7] J. F. Collins, R. W. Gerby, "New Refractory Uses For Silicon Nitride Reported", *J. Met.* **1955**, *7*, 612–615.

[8] a) T. Schlieper, W. Schnick, "Nitrido-Silicate. I Hochtemperatur-Synthese und Kristallstruktur von $Ca_2Si_5N_8$", *Z. Anorg. Allg. Chem.* **1995**, *621*, 1037–1041; b) T. Schlieper, W. Milius, W. Schnick, "Nitrido-silicate. II Hochtemperatur-Synthesen und Kristallstrukturen von $Sr_2Si_5N_8$ und $Ba_2Si_5N_8$", *Z. Anorg. Allg. Chem.* **1995**, *621*, 1380–1384; c) H. Huppertz, W. Schnick, "$Eu_2Si_5N_8$ and $EuYbSi_4N_7$. The First Nitridosilicates with a Divalent Rare Earth Metal", *Acta Crystallogr., Sect. C: Cryst. Struct. Commun.* **1997**, *53*, 1751–1753; d) P. Bielec, W. Schnick, "Increased Synthetic Control – Gaining Access to Predicted $Mg_2Si_5N_8$ and β-$Ca_2Si_5N_8$", *Angew. Chem., Int. Ed.* **2017**, *56*, 4810–4813; "Increased Synthetic Control – Gaining Access to Predicted $Mg_2Si_5N_8$ and β-$Ca_2Si_5N_8$", *Angew. Chem.* **2017**, *129*, 4888–4891.

[9] a) H. Huppertz, W. Schnick, "Edge-sharing $SiN_4$ Tetrahedra in the Highly Condensed Nitridosilicate $BaSi_7N_{10}$", *Chem. – Eur. J.* **1997**, *3*, 249–252; b) G. Pilet, H. A. Höppe, W. Schnick, S. Esmaeilzadeh, "Crystal structure and mechanical properties of $SrSi_7N_{10}$", *Solid State Sci.* **2005**, *7*, 391–396.

[10] C. Maak, D. Durach, C. Martiny, P. J. Schmidt, W. Schnick, "Narrow-Band Yellow-Orange Emitting $La_{3-x}Ca_{1.5x}Si_6N_{11}:Eu^{2+}$ ($x \approx 0.77$): A Promising Phosphor for Next-Generation Amber pcLEDs", *Chem. Mater.* **2018**, *30*, 3552–3558.

[11] W. Schnick, H. Huppertz, "Nitridosilicates – A Significant Extension of Silicate Chemistry", *Chem. – Eur. J.* **1997**, *3*, 679–683.

[12] P. Bielec, O. Janka, T. Block, R. Pöttgen, W. Schnick, "$Fe_2Si_5N_8$: Access to Open-Shell Transition-Metal Nitridosilicates", *Angew. Chem., Int. Ed.* **2018**, *57*, 2409–2412; "$Fe_2Si_5N_8$: Access to Open-Shell Transition-Metal Nitridosilicates", *Angew. Chem.* **2018**, *130*, 2433–2436.

[13] a) L. F. Druding, J. D. Corbett, "Lower Oxidation States of the Lanthanides. Neodymium(II) Chloride and Iodide", *J. Am. Chem. Soc.* **1961**, *83*, 2462–2467; b) S. S. Rudel, F. Kraus, "Facile syntheses of pure uranium halides: $UCl_4$, $UBr_4$ and $UI_4$", *Dalton Trans.* **2017**, *46*, 5835–5842; c) S. S. Rudel, H. L. Deubner, B. Scheibe, M. Conrad, F. Kraus, "Facile Syntheses of pure Uranium(III) Halides: $UF_3$, $UCl_3$, $UBr_3$, and $UI_3$", *Z. Anorg. Allg. Chem.* **2018**, *644*, 323–329.

[14] H. M. Rietveld, "A Profile Refinement Method for Nuclear and Magnetic Structures", *J. Appl. Crystallogr.* **1969**, *2*, 65–71.

[15] Powder data for $Sc_{0.2}Ca_{1.7}Si_5N_8$: space group *Cc* (no. 9), $a = 14.2891(2)$, $b = 5.59340(8)$, $c = 9.69356(12)$ Å, $V = 718.24(2)$ Å$^3$, $Z = 4$, $\rho_{diff} = 3.049$ g · cm$^{-3}$, Stoe Stadi P diffractometer, modified Debye-Scherrer geometry, Ge(111)-monochromator, $\lambda = 0.7093$ Å, cylindrical absorption correction, RIETVELD refinement on 4623 data points, 1703 reflections, $R_p = 0.0355$, $R_{wp} = 0.0465$, $GOF = 1.421$, $R_{Bragg} = 0.0192$ for 117 parameters. Further details on the crystal structure investigation may be obtained from the CCDC/FIZ Karlsruhe deposition service (e-mail: deposit@ccdc.cam.ac.uk) on quoting the depository number 1860927.

[16] Crystal data for $U_{0.5x}Sr_{2-0.75x}Si_5N_8$: ($x \approx 1.05$): crystal size 2 × 1 × 0.2 µm, space group $Pmn2_1$ (no. 31), $a = 17.1295(3)$, $b = 6.7890(2)$, $c = 9.3079(2)$ Å, $V = 1082.44(4)$ Å$^3$, $Z = 6$, $\rho_{diff} = 4.452$ g · cm$^{-3}$, ESRF beamline ID11, $\lambda = 0.309$ Å, semiempirical scaling and absorption correction, 5984 reflections of which 3475 independent, $R_{int} = 0.082$, least-squares refinement on $F^2$, $R$ values (all data/$F^2 \geq 2\sigma(F^2)$): $R_1 = 0.099/0.087$, $wR_2 = 0.241/0.224$, $GOF = 1.013$ for 3475 reflections ($F^2 \geq 2\sigma(F^2)$ and 108 parameters. Further details on the crystal structure investigation may be obtained from the CCDC/FIZ Karlsruhe deposition service (e-mail: deposit@ccdc.cam.ac.uk) on quoting the depository number 1860926.

[17] a) R. Hoppe, S. Voigt, H. Glaum, J. Kissel, H. P. Müller, K. Bernet, "A NEW ROUTE TO CHARGE DISTRIBUTIONS IN IONIC SOLIDS", *J. Less-Common Met.* **1989**, *156*, 105–122; b) K. Momma, F. Izumi, "VESTA 3 for three-dimensional visualization of crystal, volumetric and morphology data", *J. Appl. Crystallogr.* **2011**, *44*, 1272–1276.

[18] a) M. R. Lee, S. S. Russell, J. W. Arden, C. T. Pillinger, "Nierite ($Si_3N_4$), a new mineral from ordinary and enstatite chondrites", *Meteoritics* **1995**, *30*, 387–398; b) S. S. Russell, M. R. Lee, J. W. Arden, C. T. Pillinger, "The isotopic composition and origins of silicon nitride from ordinary and enstatite chondrites", *Meteoritics* **1995**, *30*, 399–404.

[19] H. Kleykamp, "Selection of materials as diluents for burning of plutonium fuels in nuclear reactors", *J. Nucl. Mater.* **1999**, *275*, 1–11.

# 5 Cationic $Pb_2$ Dumbbells Stabilized in the Highly Covalent Lead Nitridosilicate $Pb_2Si_5N_8$

*Angew. Chem., Int. Ed.* **2019**, *58*, 1432–1436; *Angew. Chem.* **2019**, *131*, 1446–1450.

Philipp Bielec, Ryky Nelson, Ralf P. Stoffel, Lucien Eisenburger, Daniel Günther, Ann-Kathrin Henß, Jonathan P. Wright, Oliver Oeckler, Richard Dronskowski and Wolfgang Schnick

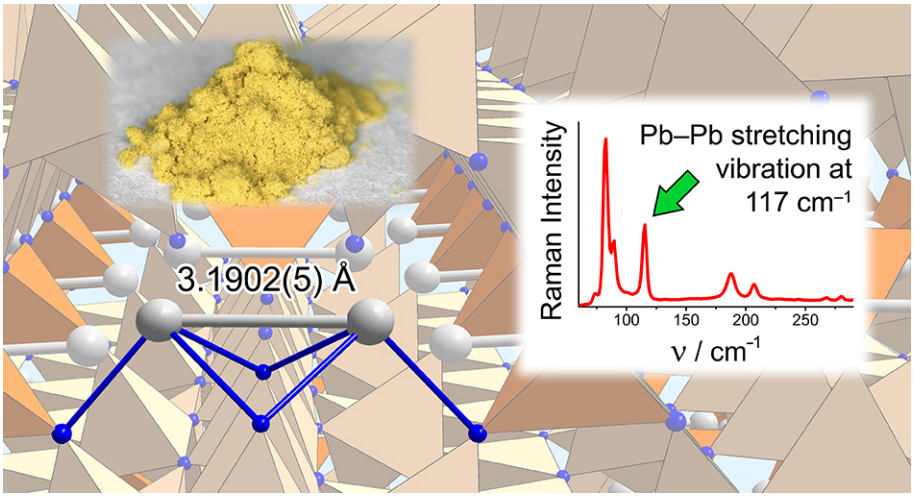


## Abstract

Due to the weak oxidative force of $N_2$, nitrides are only typically formed with the less electronegative metals. Meeting this challenge, we here present $Pb_2Si_5N_8$, the first nitridosilicate containing highly electron-affine cations of a metal from the right side of the Zintl border. By using advanced synchrotron XRD, the crystal structure was determined from a tiny single crystal of $1 \times 3 \times 3$ µm$^3$ in size, revealing a significantly different bonding situation compared to all other nitridosilicates known so far. Indeed, DFT calculations confirm distinct amounts of covalency not only between Pb and N but also between formal $Pb^{2+}$ cations. Thus, unprecedented cationic $Pb_2$ dumbbells with a stretching vibration at 117 cm$^{-1}$ were found in $Pb_2Si_5N_8$, the first representative of a crystallographically elucidated lead nitride, stabilized by high amounts of covalency.

## 5.1 Introduction with Results and Discussion

The element Pb is too noble to be oxidized by $N_2$. Therefore, reactions between $N_2$ and Pb yielding products with claimed compositions $Pb_2N_3$ and $Pb_3N_4$ have only been reported after reactions between Pb and $N_2$ supported by electric discharges (600–1500 V).[1] The challenge concerning these elements becomes clear when focusing on the single crystallographically characterized binary compound in the system Pb/N, namely the primary explosive lead azide $Pb(N_3)_2$.[2] Due to the *EN* of Pb,[3] which is comparatively high for a metal, and an electron affinity, which exceeds that of N significantly,[4] Pb is an element often found as anionic species in Zintl phases.[5] Therefore, interactions between cationic Pb and anionic N species have to withstand the tendency of electron transfer from N towards Pb, typically leading to decomposition into thermodynamically favored $N_2$ and Pb-containing byproducts. Apparently, such N species need to be covalently stabilized like in the azide anion of $Pb(N_3)_2$. This kind of covalent stabilization can also be realized by C–N bonds as known from ferrocyanides,[6] thiocyanates,[7] cyanamides,[8] dicyanamides,[9] tricyanomethanides and organo-lead(II) amides.[10] A similar effect is found for compounds where N is bound to the trimethylsilyl protecting group ($–SiMe_3$) to form trimethylsilylamides.[11] In order to not only stabilize Pb–N interactions but the entire compound itself, an increase of the covalent interconnectivity between these Pb–N containing complexes is desirable. Starting from silylamides, border cases of such hypothetical infinitely interconnected amides are nitridosilicates. Derived from (oxo)silicates by a formal exchange of O by N, nitridosilicates are typically built up from anionic $SiN_4$ tetrahedral networks and contain cations of the less electronegative metals.[12] In case of a high condensation degree ($\kappa \geq {}^1/_2$) these compounds usually exhibit remarkable thermal and chemical stability.[13]

The challenge at this point was to provide suitable reaction conditions for the incorporation of Pb cations into anionic Si–N networks, where the latter are typically formed in the presence of the least electronegative metals.[12–13,14] Recently, we established an approach towards the preparation of hitherto inaccessible nitridosilicates.[15] Instead of attempting to synthesize the nitridosilicate network directly in the presence of the desired cation, we devised a two-step process building up the tetrahedral network by first exploiting the easily oxidizable character of the alkaline-earth metals. Subsequently, the cations were exchanged in a molten salt by those of the desired metal. By applying this strategy, we no longer depend on $N_2$ as a metal oxidant but use the oxidative power of halides

instead to provide the metal in the desired oxidation state. In this way, the first lead nitridosilicate $Pb_2Si_5N_8$ was prepared according to the metathetic Equation 1 at 920 °C (chapter D.4).

$$Sr_2Si_5N_8 + PbCl_2 \rightarrow Pb_2Si_5N_8 + 2\ SrCl_2 \qquad 5.1$$

After washing in boiling concentrated nitric acid, the title compound was obtained as a brightly yellow solid (Figure 5.1, left) with an optical band gap, estimated to 2.6 eV from a UV-Vis reflectance spectrum (chapter D.10). The chemical composition of $Pb_2Si_5N_8$ was confirmed by EDX, ICP-OES and combustion analysis (chapters D.7, D.8 and D.9).

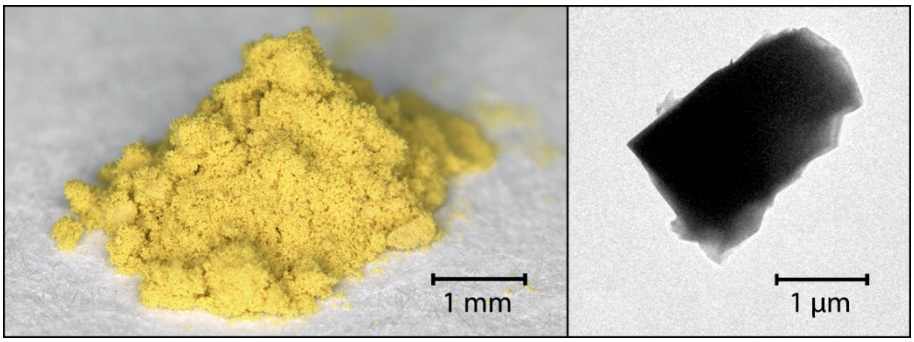


**Figure 5.1:** Left: Photograph of powderous $Pb_2Si_5N_8$; right: Brightfield TEM image of the single crystal used for single-crystal XRD.

The title compound crystallizes in a distorted variant of the $M_2Si_5N_8$ ($M$ = Sr, Ba) structure type,[16] made up from vertex-sharing $SiN_4$ tetrahedra.[17] These tetrahedra form corrugated layers consisting of highly condensed *dreier* rings (Figure 5.2a, yellow orange). The layers are interconnected by further $SiN_4$ tetrahedra (Figure 5.2a, orange) resulting in a 3D tectosilicate type of structure. Si–N distances between 1.703(9) and 1.770(11) Å are in the typical (and relatively narrow) range for nitridosilicates.[12a]

The phase purity of $Pb_2Si_5N_8$ was confirmed by RIETVELD refinement (Figure 5.2b) applying the crystal structure of the particle (Figure 5.1, right) received from single-crystal XRD (detailed crystallographic data in chapters D.5 and D.6). In order to minimize absorption effects of the Pb-containing sample using Cu-K$\alpha_1$ radiation ($\lambda$ = 1.5406 Å), 150 equivalents LiH were added to bulk $Pb_2Si_5N_8$ for powder XRD.

Although $Pb_2Si_5N_8$ crystallizes isopointal with $M_2Si_5N_8$ ($M$ = Sr, Ba),[16] clear deviations are found between the structures containing alkaline-earth cations and Pb. While Sr–N and Ba–N distances in $M_2Si_5N_8$ can be easily understood by an ionic model with $Ba^{2+}$ exhibiting a larger ionic radius than $Sr^{2+}$, the situation in $Pb_2Si_5N_8$ is significantly different. Despite similar ionic radii of $Sr^{2+}$ and $Pb^{2+}$ in

oxides,[18] Pb–N distances in $Pb_2Si_5N_8$ show a broad distribution between values that are significantly shorter than Sr–N in $Sr_2Si_5N_8$ and others which are even larger than Ba–N in $Ba_2Si_5N_8$ (Figure 5.3).

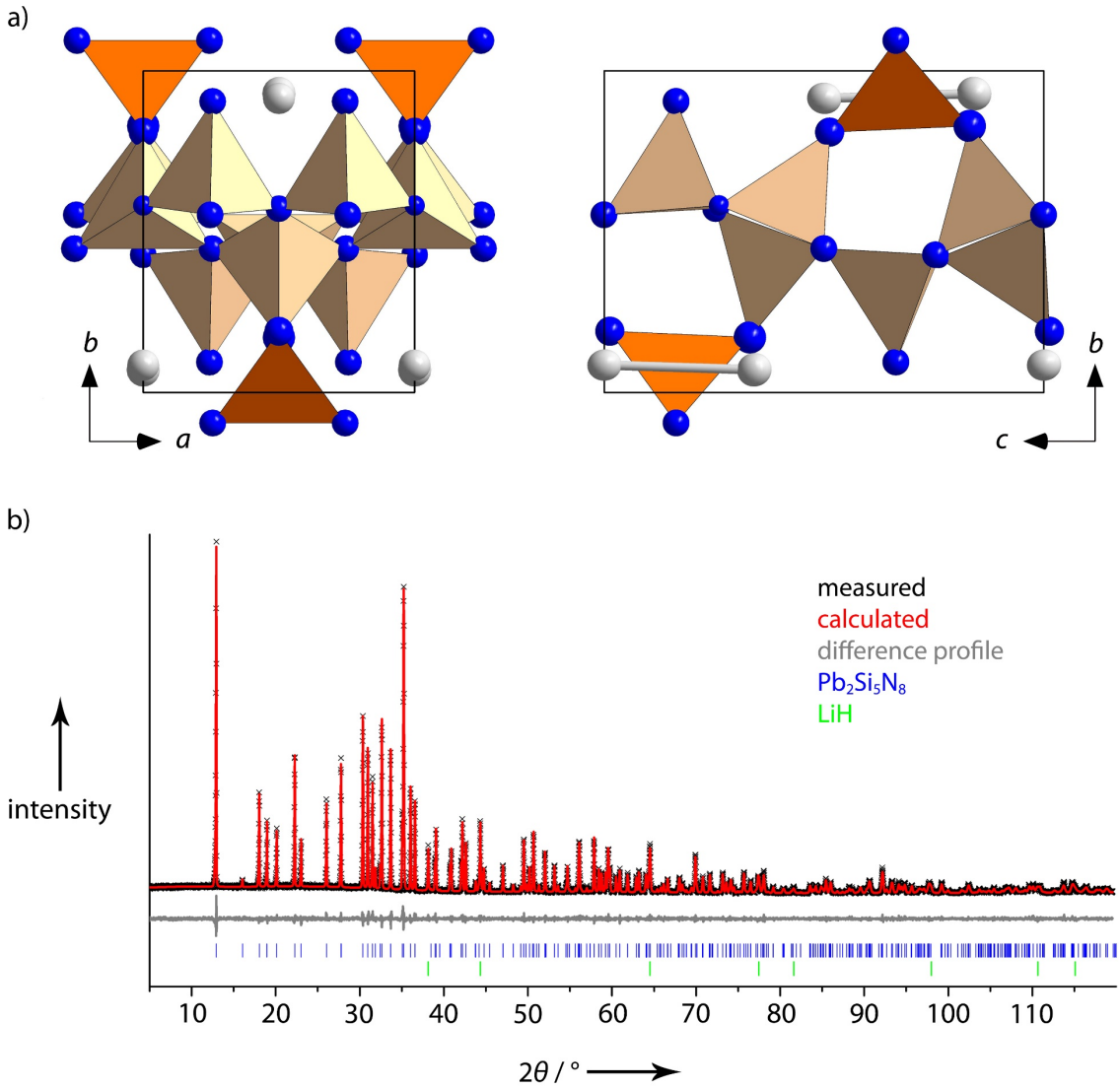


**Figure 5.2:** a) Crystal structure of $Pb_2Si_5N_8$ along [001] (left) and along [100] (right) with $SiN_4$ tetrahedra (yellow orange, orange), N atoms (blue) and $Pb_2$ dumbbells (gray); b) RIETVELD refinement of a $Pb_2Si_5N_8$ sample diluted with 150 equivalents LiH measured with Cu-K$\alpha_1$ radiation ($\lambda$ = 1.5406 Å).

Such distance distribution (Figure 5.3) and the smaller difference in *EN* between Pb and N[3] already indicate more covalent *M*–N interactions in $Pb_2Si_5N_8$ compared to common nitridosilicates. With respect to these findings the electronic DOS (Figure 5.4a) and projected crystal orbital Hamilton populations (pCOHPs)[19], given in Figure 5.4b, c and d were reconstructed from the ABINIT-derived PAW wavefunctions using LOBSTER.[20] Upon doing so, significant covalency in $Pb_2Si_5N_8$, both for

the lower part between −16±2 eV (Si and N mixing in) and the upper part at −6±5 eV (all atoms) was observed.

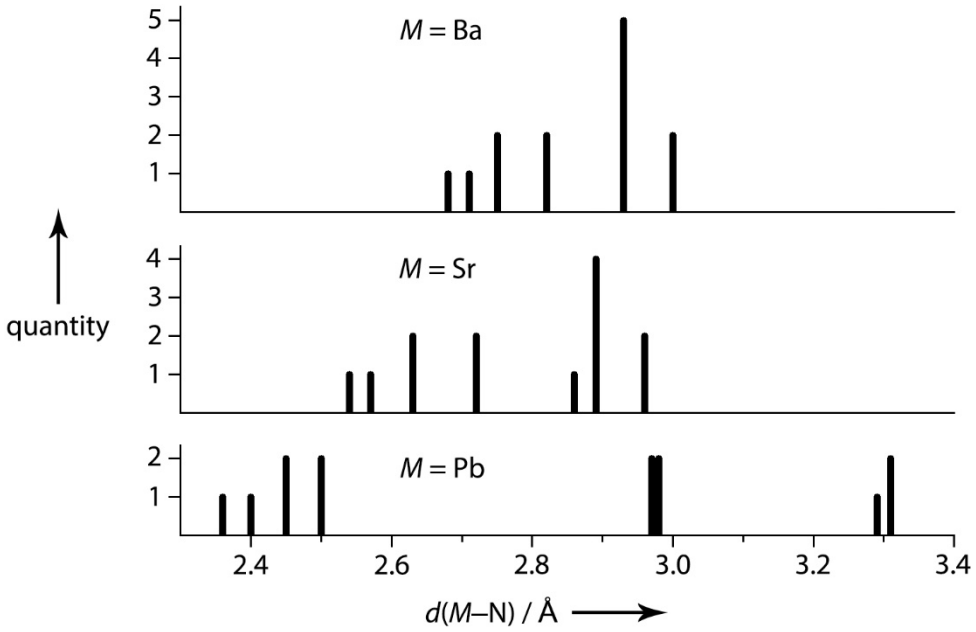


**Figure 5.3:** Distribution of the 13 shortest distances *M*–N in $M_2Si_5N_8$ (*M* = Sr, Ba, Pb).

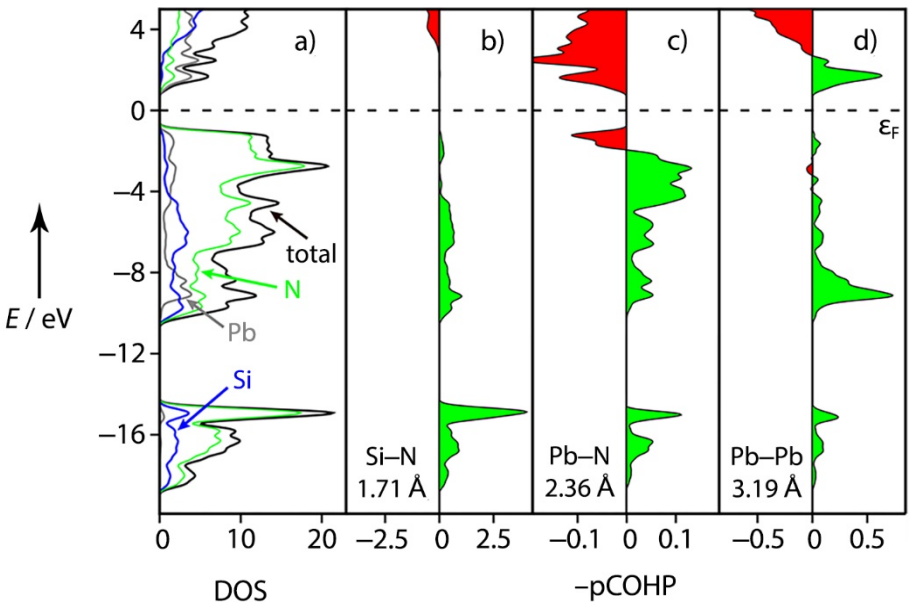


**Figure 5.4:** a) Total and partial DOS of $Pb_2Si_5N_8$ as well as projected COHP of b) Si–N, c) Pb–N, and d) Pb–Pb interactions as derived from DFT calculations including spin-orbit coupling (SOC). The energy axis is shown relative to the Fermi level ($\varepsilon_F$).

For quantification of the effective charge reduction by covalency in $Pb_2Si_5N_8$, Mulliken charges $Q_A$ as defined recently were calculated.[21] These charges arrive at +0.71, +1.73, and −1.18 for Pb, Si, and N, respectively, significantly lower than the idealized ionic charges +2, +4, and −3. Likewise,

experimental indications for charge reduction at the Pb atoms were also obtained by XPS (chapter D.11). As expected, the strongest covalent bond is Si–N with a length of 1.71 Å. This interaction has solely bonding contributions in the entire valence band and an impressive integrated COHP (ICOHP) value of −7.46 eV. The highly covalent Pb–N bond, starting at 2.36 Å, arrives at an ICOHP value of −2.63 eV, which is about ⅓ of the Si–N bond. However, much to our surprise the strength of the Pb–Pb bond of 3.19 Å (Figure 5.4d) reaches an ICOHP of −1.25 eV. Such a distance and bond strength between two Pb atoms would rather be expected for plumbanes, diplumbenes, plumbylenes or Zintl phases than between *cationic* Pb in a nitridosilicate.[5d,22]

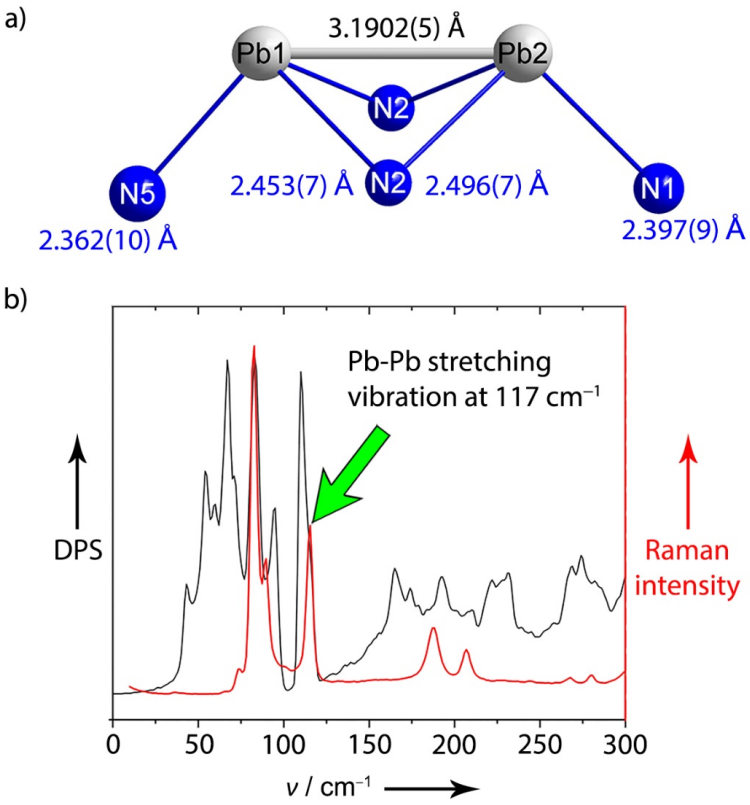


**Figure 5.5:** a) Pb environment in $Pb_2Si_5N_8$; b) Theoretically calculated DPS (black) and experimentally determined Raman spectrum (red).

Indeed, covalently attractive interactions between two formal $Pb^{2+}$ cations, as found in $Pb_2Si_5N_8$, which result from a $6s^2$ atomic configuration are unusual (or even unlikely) and require an explanation. Nonetheless, it is exactly this spring force leading to a signal in the experimental Raman spectrum at 117 $cm^{-1}$ (Figure 5.5b, chapter D.12) which can be easily assigned to the Pb–Pb stretching vibration based on DFT phonon calculations.[23] In contrast to such an unexpected $Pb^{2+}$–$Pb^{2+}$ interaction, $[Bi_2]^{4+}$ dumbbells are well known in literature,[24] but in the latter there is no problem in assigning a single bond between $Bi^{2+}$ cations with a valence configuration of $6s^26p^1$. For $[Bi_2]^{4+}$

dumbbells, stretching vibrations have been found in the range of 102–113 $cm^{-1}$. Due to the lighter mass of a formal $[Pb_2]^{4+}$ dumbbell compared to the Bi case, the stretching vibration of $[Pb_2]^{4+}$ at 117 $cm^{-1}$ also fits well to the experimental values in literature.[24a,24d]

In addition, we note that this intercationic Pb–Pb bonding effect does *not* go back to spin-orbit coupling because it is equally visible by almost the same amount in the non-SOC data. As shown in Figure 5.6 (left), such $6s^2$–$6s^2$ interaction between the $Pb^{2+}$ are reminiscent of the He–He ($1s^2$–$1s^2$) scenario because the bonding $1\sigma_g$ molecular orbital is cancelled by the antibonding $1\sigma_u^*$ such that there cannot be covalent bonding in $He_2$, at least as long as no electron is promoted into the empty 6*p*-centered $2\sigma_g$ molecular orbital like in the singly-bonded $He_2^*$ Rydberg molecule.

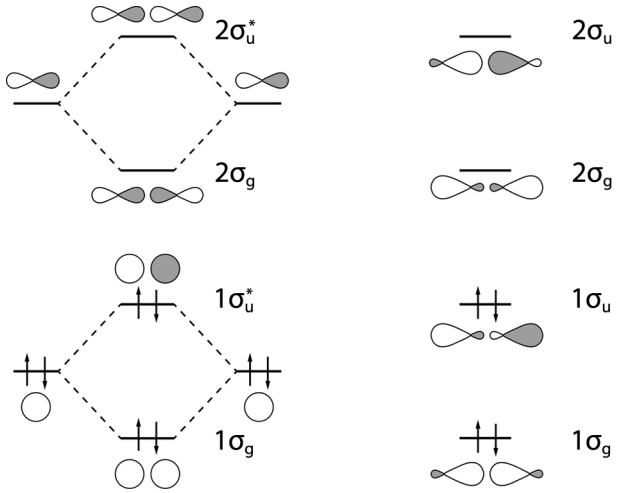


**Figure 5.6:** Hückel-type diagram of σ-type molecular-orbital interactions between two adjacent $Pb^{2+}$ as a function of zero (left) and strong (right) mixing between s and p orbitals.

If, however, the *s* and *p* orbitals become energetically comparable, further *sp* mixing sets in and yields another set of molecular orbitals (Figure 5.6, right) with a decisive difference. While the $1\sigma_g/1\sigma_u^*/2\sigma_g/2\sigma_u^*$ course stays the same, the bonding characters change from bonding / antibonding / bonding / antibonding (no *sp* mixing) to strongly bonding / weakly bonding / weakly antibonding / strongly antibonding (strong *sp* mixing), as also observed in the canonical MOs of the nitrogen molecule.[25] A comparable situation is indeed found for the intercationic Pb–Pb interaction, as depicted in Figure 5.7, owing to the covalency in $Pb_2Si_5N_8$.

Besides the previously shown total projected COHP between the two Pb cations given in Figure 5.7a we also present those interactions that arise solely from the *s* orbitals (Figure 5.7b). The bonding/antibonding $1\sigma_g/1\sigma_u^*$ pair of orbitals is present at −8±2 eV, and they cancel each other like in the $He_2$ ground state, as expected. If only *p* orbitals were involved (Figure 5.7d), bonding states

would show up around −5 eV, reminiscent of the $2\sigma_g$ of $He_2$ (Figure 5.6, left). Strong *sp* mixing, however, is at play, as visible from Figure 5.7c. The low-lying $1\sigma_g$ bonding level no longer gets cancelled by the higher-lying $1\sigma_u$* level (because the latter has turned weakly bonding, see Figure 5.6, right), and results in a bonding interaction between the $Pb^{2+}$. Some *p*–*p* bonding (see Figure 5.7d) further cancels the weakly antibonding leftover levels around −4±1 eV (see Figure 5.7c), and the result is the total interaction given in Figure 5.7a.

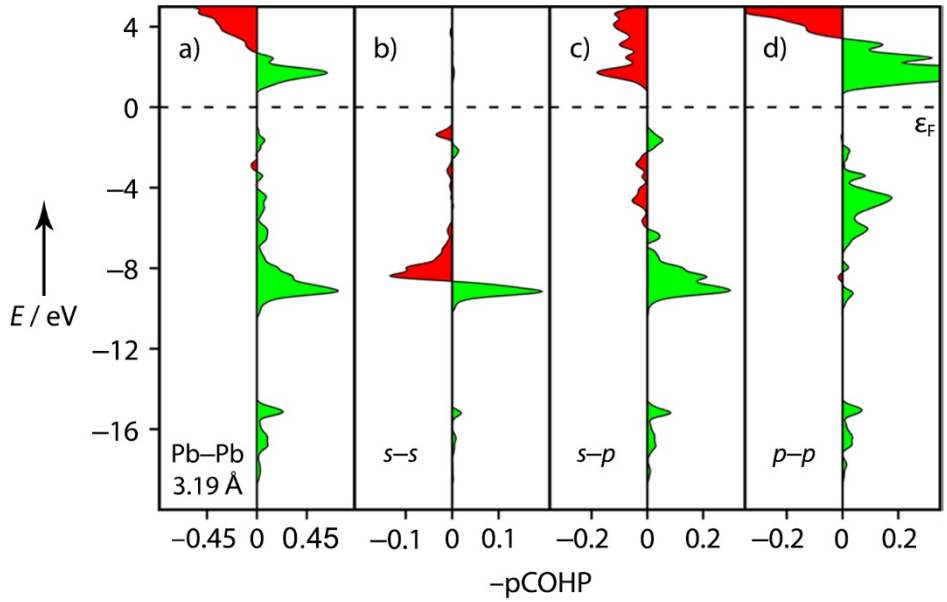


**Figure 5.7:** Projected COHP of the a) Pb–Pb bond put side by side with those contributions from pure b) *s*–*s*, c) *s*–*p*, and d) *p*–*p* interactions. The energy axis is shown relative to the Fermi level ($\varepsilon_F$).

Interestingly, indications for 6*sp* mixing in interconnected Pb atoms have also been observed in $Au_2PbP_2$, a compound with one dimensional Pb(0)-chains.[26] Therefore, the attractive interaction within the cationic $Pb_2$ dumbbells in $Pb_2Si_5N_8$ is strong enough to result in a similar Pb–Pb distance between cations (3.19 Å) compared to Pb(0)–Pb(0) in $Au_2PbP_2$ (3.20 Å).

In conclusion, the first lead nitridosilicate $Pb_2Si_5N_8$ was prepared by ion exchange circumventing thermodynamically more stable $N_2$ and elemental Pb. DFT calculations demonstrate that high covalency in $Pb_2Si_5N_8$ causes *sp* mixing at the Pb atoms resulting in attractive covalent interactions between formal $Pb^{2+}$ ions. These theoretical findings are proven by Raman spectroscopy, in harmony with phonon calculations. The title compound, able to easily withstand a treatment in boiling concentrated nitric acid and elevated temperatures (decomposition above 1000 °C in $N_2$; details in chapter D.14), is the first representative of a crystallographically characterized lead nitride.

Therefore, the synthetic approach toward $Pb_2Si_5N_8$ may serve as a general tool to unite the intrinsically reductive chemistry of nitrides with metals exhibiting high electron affinities.

## 5.2 References


[1] a) G. Berraz, "Acción del nitrógeno sobre los metales", *An. Soc. Cient. St. Fe* **1933**, *5*, 54–56; b) W. Janeff, "Herstellung von Metailnitriden in der Glimmentladung und einige ihrer Eigenschaften", *Z. Phys.* **1955**, *142*, 619–636.

[2] C. S. Choi, E. Prince, W. L. Garrett, "Refinement of α-Lead Azide by Neutron Diffraction", *Acta Crystallogr., Sect. B: Struct. Crystallogr. Cryst. Chem.* **1977**, *33*, 3536–3537.

[3] A. L. Allred, E. G. Rochow, "A SCALE OF ELECTRONEGATIVITY BASED ON ELECTROSTATIC FORCE", *J. Inorg. Nucl. Chem.* **1958**, *5*, 264–268.

[4] A. F. Holleman, N. Wiberg, *Lehrbuch der Anorganischen Chemie, Vol. 102*, DeGruyter, Berlin, Boston, **2008**.

[5] a) E. Zintl, H. Kaiser, "Über die Fähigkeit der Elemente zur Bildung negativer Ionen", *Z. Anorg. Allg. Chem.* **1933**, *211*, 113–131; b) E. Zintl, "Intermetallische Verbindungen", *Angew. Chem.* **1939**, *52*, 1–6; c) F. Laves, "Eduard Zintls Arbeiten über die Chemie und Struktur von Legierungen", *Naturwissenschaften (1913–2014)* **1941**, *29*, 244–255; d) C. Hoch, M. Wendorff, C. Röhr, "Synthesis and crystal structure of the tetrelides $A_{12}M_{17}$ (A = Na, K, Rb, Cs; M = Si, Ge, Sn) and $A_4Pb_9$ (A = K, Rb)", *J. Alloys Compd.* **2003**, *361*, 206–221.

[6] V. G. Zubkov, A. P. Tyutyunnik, I. F. Berger, L. G. Maksimova, T. A. Denisova, E. V. Polyakov, I. G. Kaplan, V. I. Voronin, "Anhydrous tin and lead hexacyanoferrates (II). Part I. Synthesis and crystal structure", *Solid State Sci.* **2001**, *3*, 361–367.

[7] J. A. A. Mokuolu, J. C. Speakman, "The Crystal Structure of Lead(II) Thiocyanate", *Acta Crystallogr., Sect. B: Struct. Crystallogr. Cryst. Chem.* **1975**, *31*, 172–176.

[8] X. Liu, A. Decker, D. Schmitz, R. Dronskowski, "Crystal Structure Refinement of Lead Cyanamide and the Stiffness of the Cyanamide Anion", *Z. Anorg. Allg. Chem.* **2000**, *626*, 103–105.

[9] B. Jürgens, H. A. Höppe, W. Schnick, "Synthesis, crystal structure, vibrational spectroscopy, and thermal behaviour of lead dicyanamide $Pb[N(CN)_2]_2$", *Solid State Sci.* **2002**, *4*, 821–825.

[10] a) V. M. Deflon, C. C. de Sousa Lopes, K. E. Bessler, L. L. Romualdo, E. Niquet, "Preparation, Characterization and Crystal Structure of Lead(II) Tricyanomethanide", *Z. Naturforsch., B: J. Chem. Sci.* **2006**, *61*, 33–36; b) A. C. Filippou, N. Weidemann, G. Schnakenburg, "Tungsten-Mediated Activation of a $Pb^{II}$–N Bond: A New Route to Tungsten-Lead Triple Bonds", *Angew. Chem., Int. Ed.* **2008**, *47*, 5799–5802; "Tungsten-Mediated Activation of a $Pb^{II}$–N Bond: A New Route to Tungsten-Lead Triple Bonds", *Angew. Chem.* **2008**, *120*, 5883–5886; c) W.-P. Leung, Q. W.-Y. Ip, S.-Y. Wong, T. C. W. Mak, "Syntheses and Structures of Group 14 1,3-Dimetallacyclobutanes", *Organometallics* **2003**, *22*, 4604–4609; d) W.-P. Leung, K.-W. Wong, Z.-X. Wang, T. C. W. Mak, "Synthesis and Structures of Novel Low-Valent Group 14 1,3-Dimetallacyclobutanes", *Organometallics* **2006**, *25*, 2037–2044.

[11] a) M. J. S. Gynane, D. H. Harris, M. F. Lappert, P. P. Power, P. Rivière, M. Rivière-Baudet, "Subvalent Group 4B Metal Alkyls and Amides. Part 5. The Synthesis and Physical Properties of Thermally Stable Amides of Germanium(II), Tin(II), and Lead(II)", *J. Chem. Soc., Dalton Trans.* **1977**, *0*, 2004–2009; b) A. Murso, M. Straka, M. Kaupp, R. Bertermann, D. Stalke, "A Heterotopically Chelated Low-Valent Lead Amide", *Organometallics* **2005**, *24*, 3576–3578.

[12] a) M. Zeuner, S. Pagano, W. Schnick, "Nitridosilicates and Oxonitridosilicates: From Ceramic Materials to Structural and Functional Diversity", *Angew. Chem., Int. Ed.* **2011**, *50*, 7754–7775; "Nitridosilicate und Oxonitridosilicate: von keramischen Materialien zu struktureller und funktioneller Diversität", *Angew. Chem.* **2011**, *123*, 7898–7920; b) W. Schnick, H. Huppertz, "Nitridosilicates – A Significant Extension of Silicate Chemistry", *Chem. – Eur. J.* **1997**, *3*, 679–683.

[13] a) T. Schlieper, W. Schnick, "Nitrido-silicate. II Hochtemperatur-Synthese, Kristallstruktur und magnetische Eigenschaften von $Ce_3[Si_6N_{11}]$", *Z. Anorg. Allg. Chem.* **1995**, *621*, 1535–1538; b) Z. Inoue, M. Mitomo, N. Ii, "A crystallographic study of a new compound of lanthanum silicon nitride, $LaSi_3N_5$", *J. Mater. Sci.* **1980**, *15*, 2915–2920; c) G. Pilet, H. A. Höppe, W. Schnick, S. Esmaeilzadeh, "Crystal structure and mechanical properties of $SrSi_7N_{10}$", *Solid State Sci.* **2005**, *7*, 391–396; d) F. Liebau, "Silicates and Perovskites: Two Themes with Variations", *Angew. Chem., Int. Ed.* **1999**, *38*, 1733–1737; "Silicate und Perowskite: zwei Themen mit Variationen", *Angew. Chem.* **1999**, *111*, 1845–1850.

[14] a) T. Schlieper, W. Schnick, "Nitrido-Silicate. I Hochtemperatur-Synthese und Kristallstruktur von $Ca_2Si_5N_8$", *Z. Anorg. Allg. Chem.* **1995**, *621*, 1037–1041; b) M. Woike, W. Jeitschko, "Preparation and Crystal Structure of the Nitridosilicates $Ln_3Si_6N_{11}$ (Ln = La, Ce, Pr, Nd, Sm) and $LnSi_3N_5$ (Ln = Ce, Pr, Nd)", *Inorg. Chem.* **1995**, *34*, 5105–5108.

[15] P. Bielec, W. Schnick, "Increased Synthetic Control – Gaining Access to Predicted $Mg_2Si_5N_8$ and β-$Ca_2Si_5N_8$", *Angew. Chem., Int. Ed.* **2017**, *56*, 4810–4813; "Increased Synthetic Control – Gaining Access to Predicted $Mg_2Si_5N_8$ and β-$Ca_2Si_5N_8$", *Angew. Chem.* **2017**, *129*, 4888–4891.

[16] T. Schlieper, W. Milius, W. Schnick, "Nitrido-silicate. II Hochtemperatur-Synthesen und Kristallstrukturen von $Sr_2Si_5N_8$ und $Ba_2Si_5N_8$", *Z. Anorg. Allg. Chem.* **1995**, *621*, 1380–1384.

[17] Space group $Pmn2_1$ (no. 31), $a$ = 5.774(1), $b$ = 6.837(1), $c$ = 9.350(1) Å, $V$ = 369.11(9) Å$^3$, $Z$ = 2, $\rho_{diff}$ = 6.001 g · cm$^{-3}$, $R_1$ (all data) = 0.023, $R_1$ [$F^2 > 2\sigma(F^2)$] = 0.023, $wR_2$ (all data) = 0.056, $wR_2$ [$F^2 > 2\sigma(F^2)$] = 0.055, $R_{int}$ = 0.051, $R_\sigma$ = 0.049, 60 parameters for 6540 reflections (1268 independent); Further details on the crystal structure can be obtained from the Fachinformationszentrum Karlsruhe, 76344 Eggenstein-Leopoldshafen, Germany (fax: +49-7247-808-666; e-mail: crysdata@fiz-karlsruhe.de) on quoting the depository number CSD-434801.

[18] R. D. Shannon, "Revised Effective Ionic Radii and Systematic Studies of Interatomic Distances in Halides and Chalcogenides", *Acta Crystallogr., Sect. A: Found. Crystallogr.* **1976**, 32, 751–767.

[19] a) R. Dronskowski, P. E. Blöchl, "Crystal Orbital Hamilton Populations (COHP): Energy-Resolved Visualization of Chemical Bonding in Solids Based on Density-Functional Calculations", *J. Phys. Chem.* **1993**, *97*, 8617–8624; b) V. L. Deringer, A. L. Tchougréeff, R. Dronskowski, "Crystal Orbital Hamilton Population (COHP) Analysis as Projected from Plane-Wave Basis Sets", *J. Phys. Chem. A* **2011**, *115*, 5461–5466.

[20] a) G. Kresse, J. Furthmüller, "Efficiency of ab-initio total energy calculations for metals and semiconductors using a plane-wave basis set", *Comput. Mater. Sci.* **1996**, *6*, 15–50; b) G. Kresse, D. Joubert, "From ultrasoft pseudopotentials to the projector augmented-wave method", *Phys. Rev. B* **1999**, *59*, 1758–1775; c) P. E. Blöchl, "Projector augmented-wave method", *Phys. Rev. B* **1994**, *50*, 17953–17979; d) J. P. Perdew, K. Burke, M. Ernzerhof,

"Generalized Gradient Approximation Made Simple", *Phys. Rev. Lett.* **1996**, *77*, 3865–3868; e) S. Grimme, J. Antony, S. Ehrlich, H. Krieg, "A consistent and accurate ab initio parametrization of density functional dispersion correction (DFT-D) for the 94 elements H–Pu", *J. Chem. Phys.* **2010**, *132*, 154104; f) S. Grimme, S. Ehrlich, L. Goerigk, "Effect of the Damping Function in Dispersion Corrected Density Functional Theory", *J. Comput. Chem.* **2011**, *32*, 1456–1465; g) H. J. Monkhorst, J. D. Pack, "Special points for Brillouin-zone integrations", *Phys. Rev. B* **1976**, *13*, 5188–5192; h) S. Maintz, V. L. Deringer, A. L. Tchougréeff, R. Dronskowski, "Analytic Projection From Plane-Wave and PAW Wavefunctions and Application to Chemical-Bonding Analysis in Solids", *J. Comput. Chem.* **2013**, *34*, 2557–2567; i) S. Maintz, V. L. Deringer, A. L. Tchougréeff, R. Dronskowski, "LOBSTER: A Tool to Extract Chemical Bonding from Plane-Wave Based DFT", *J. Comput. Chem.* **2016**, *37*, 1030–1035.

[21] W.-L. Li, C. Ertural, D. Bogdanovski, J. Li, R. Dronskowski, "Chemical Bonding of Crystalline $LnB_6$ (Ln = La–Lu) and Its Relationship with $Ln_2B_8$ Gas-Phase Complexes", *Inorg. Chem.* **2018**, *57*, 12999–13008.

[22] a) F. Stabenow, W. Saak, H. Marsmann, M. Weidenbruch, "Hexaarylcyclotriplumbane: A Molecule with a Homonuclear Ring System of Lead", *J. Am. Chem. Soc.* **2003**, *125*, 10172–10173; b) L. Pu, B. Twamley, P. P. Power, "Synthesis and Characterization of 2,6-$Trip_2H_3C_6PbPbC_6H_3$-2,6-$Trip_2$ (Trip = $C_6H_2$-2,4,6-*i*-$Pr_3$): A Stable Heavier Group 14 Element Analogue of an Alkyne", *J. Am. Chem. Soc.* **2000**, *122*, 3524–3525.

[23] a) A. Togo, I. Tanaka, "First principles phonon calculations in materials science", *Scr. Mater.* **2015**, *108*, 1–5; b) R. P. Stoffel, C. Wessel, M.-W. Lumey, R. Dronskowski, "Ab Initio Thermochemistry of Solid-State Materials", *Angew. Chem., Int. Ed.* **2010**, *49*, 5242–5266; "Ab-initio-Thermochemie fester Stoffe", *Angew. Chem.* **2010**, *122*, 5370–5395; c) R. P. Stoffel, R. Dronskowski, "Barium Peroxide: a Simple Test Case for First-Principles Investigations on the Temperature Dependence of Solid-State Vibrational Frequencies", *Z. Anorg. Allg. Chem.* **2012**, *638*, 1403–1406; d) R. P. Stoffel, K. Philipps, R. Conradt, R. Dronskowski, "A First-Principles Study on the Electronic, Vibrational, and Thermodynamic Properties of Jadeite and its Tentative Low-Density Polymorph", *Z. Anorg. Allg. Chem.* **2016**, *642*, 590–596.

[24] a) H. Kalpen, W. Hönle, M. Somer, U. Schwarz, K. Peters, H. G. von Schnering, R. Blachnik, "Bismut(II)-chalkogenometallate(III) $Bi_2M_4X_8$, Verbindungen mit $Bi_2^{4+}$-Hanteln (M = Al, Ga; X = S, Se)", *Z. Anorg. Allg. Chem.* **1998**, *624*, 1137–1147; b) B. Wahl, M. Ruck, "$Ag_3Bi_{14}Br_{21}$: ein Subbromid mit $Bi_2^{4+}$-Hanteln und $Bi_9^{5+}$-Polyedern – Synthese, Kristallstruktur und Chemische Bindung", *Z. Anorg. Allg. Chem.* **2008**, *634*, 2873–2879; c) A. Heerwig, M. Ruck, "The Low-Valent Bismuth Sulfide Bromide $Cu_3Bi_2S_3Br_2$", *Z. Anorg. Allg. Chem.* **2011**, *637*, 1814–1817; d) R. Groom, A. Jacobs, M. Cepeda, R. Drummey, S. E. Latturner, "$Bi_{13}S_{18}I_2$: (Re)discovery of a Subvalent Bismuth Compound Featuring $[Bi_2]^{4+}$ Dimers Grown in Sulfur/Iodine Flux Mixtures", *Chem. Mater.* **2017**, *29*, 3314–3323.

[25] R. Hoffmann, *Solids and Surfaces: A chemist's View of Bonding in Extended Structures*, VCH, Weinheim, **1988**.

[26] a) M. Eschen, W. Jeitschko, "$Au_2PbP_2$, $Au_2TlP_2$, and $Au_2HgP_2$: Ternary Gold Polyphosphides with Lead, Thallium, and Mercury in the Oxidation State Zero", *J. Solid State Chem.* **2002**, *165*, 238–246; b) X.-D. Wen, T. J. Cahill, R. Hoffmann, "Element Lines: Bonding in the Ternary Gold Polyphosphides, $Au_2MP_2$ with *M* = Pb, Tl, or Hg", *J. Am. Chem. Soc.* **2009**, *131*, 2199–2207.

# 6 Summary

The publications in this cumulative thesis illustrate the progress that was made while pursuing the aim of expanding elemental variety in nitridosilicates. "*Increased Synthetic Control – Gaining Access to Predicted $Mg_2Si_5N_8$ and β-$Ca_2Si_5N_8$*" describes the synthesis approach that has been developed and used in this thesis. Beside of elucidating the reaction mechanism of the ion exchange reaction, "*$Fe_2Si_5N_8$: Access to Open-Shell Transition-Metal-Nitridosilicates*" primarily deals with the challenges nitridosilicate chemists have to face when working with elements of the *d*-block in the periodic table. In "*Targeting Vacancies in Nitridosilicates: Aliovalent Substitution of $M^{2+}$ (M = Ca, Sr) by $Sc^{3+}$ and $U^{3+}$*" we show that the highly covalent nitridosilicate networks $[Si_5N_8]^{4-}$ reveal impressive flexibility beside of their intrinsic chemical, thermal and mechanical stability, making it possible to incorporate not only significant amounts of vacancies but also actinide cations into a nitridosilicate for the first time. Last but not least, in "*Cationic $Pb_2$ Dumbbells Stabilized in the Highly Covalent Lead Nitridosilicate $Pb_2Si_5N_8$*" the synthesis approach used in this thesis has proven to be sufficient to provide access to the first formal lead nitride, namely $Pb_2Si_5N_8$, which is also the first nitridosilicate with counter ions of a metal of the *p*-block in the periodic table of elements.

## 6.1 Increased Synthetic Control – Gaining Access to Predicted $Mg_2Si_5N_8$ and β-$Ca_2Si_5N_8$

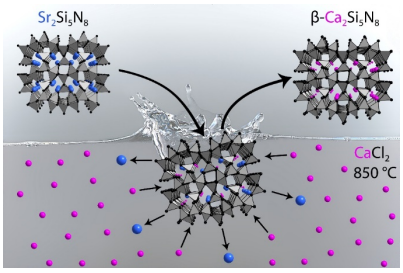


The first *top-down* synthesis approach toward preparation of nitridosilicates is presented. Cations in $M_2Si_5N_8$ ($M$ = Ca, Sr) have been exchanged applying salt melts $MCl_2$ ($M$ = Mg, Ca) yielding predicted $Mg_2Si_5N_8$ (space group *Cc* (no. 9), $a$ = 14.0672(2) Å, $b$ = 5.35002(7) Å, $c$ = 9.57993(10) Å and $\beta$ = 111.0127(7)°) and β-$Ca_2Si_5N_8$ (space group $P2_1$ (no. 4), $a$ = 5.66713(12) Å, $b$ = 9.2818(2) Å, $c$ = 6.6889(2) Å and $\beta$ = 90.1164(10)°). The reaction progress has been investigated by *in situ* X-ray methods revealing Si–N network preservation throughout the entire reaction. Furthermore, a concept for explanation of the driving forces is presented, based on a combination of effects by Coulomb's law and network distortion by incorporation of smaller cations.

## 6.2 $Fe_2Si_5N_8$: Access to Open-Shell Transition-Metal-Nitridosilicates

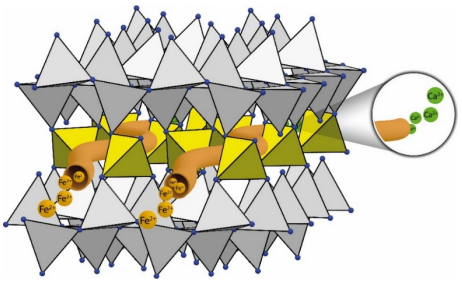

The first iron nitridosilicate, namely $Fe_2Si_5N_8$ (space group *Cc* (no. 9), $a = 14.04056(14)$ Å, $b = 5.32626(5)$ Å, $c = 9.59064(9)$ Å and $\beta = 110.7304(6)°$) has been prepared from a $FeCl_2$ melt and α-$Ca_2Si_5N_8$. The divalent oxidation state of $Fe^{2+}$ has been proven applying Mößbauer spectroscopy. Due to the unpaired *d*-electrons in $Fe^{2+}$, magnetic susceptibility measurements reveal paramagnetism of the compound with $\mu_{eff} = 3.2(1)\ \mu_B$. Since 2.83 $\mu_B$ indicate a number of two unpaired electrons in a distorted tetrahedral environment (spin-only formula), $Fe^{2+}$ in $Fe_2Si_5N_8$ can be ascribed as low-spin. In addition, the mechanism of the ion exchange reaction has been extensively investigated by further *in situ* and HR-HT X-ray methods. Thus, migration pathways for $Ca^{2+}$ enabling the ion exchange reaction have been identified in α-$Ca_2Si_5N_8$.

## 6.3 Targeting Vacancies in Nitridosilicates: Aliovalent Substitution of $M^{2+}$ ($M$ = Ca, Sr) by $Sc^{3+}$ and $U^{3+}$

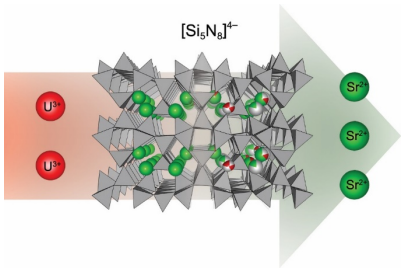


A strategy for targeted incorporation of vacancies into highly condensed nitridosilicate networks by exchange of trivalent by divalent cations is presented. As proof of concept the non-stoichiometric compounds $Sc_{0.2}Ca_{1.7}Si_5N_8$ (space group *Cc* (no. 9), $a = 14.2891(2)$ Å, $b = 5.59340(8)$ Å, $c = 9.69356(12)$ Å and $\beta = 112.0205(8)°$) and $U_{0.5x}Sr_{2-0.75x}Si_5N_8$ with $x \approx 1.05$ (space group $Pmn2_1$ (no. 31), $a = 17.1295(3)$ Å, $b = 6.7890(2)$ Å, $c = 9.3079(2)$ Å) have been prepared by ion exchange. The scandium compound exhibits a statistical distribution of the vacancies which could be beneficial for development of next generation ion conductors. In contrast, an ordered distribution of cations and vacancies have been found in the uranium nitridosilicate, making this compound a promising candidate for nuclear waste storage.

## 6.4 Cationic $Pb_2$ Dumbbells Stabilized in the Highly Covalent Lead Nitridosilicate $Pb_2Si_5N_8$

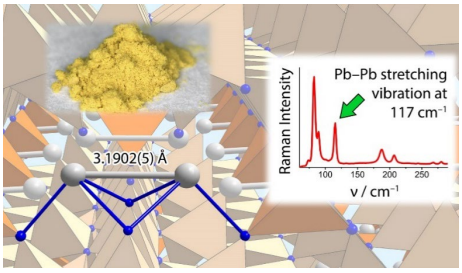


The first nitride of the element Pb, namely $Pb_2Si_5N_8$ (space group $Pmn2_1$ (no. 31), $a = 5.774(1)$ Å, $b = 6.837(1)$ Å, $c = 9.350(1)$ Å), has been discovered by the ion exchange approach. In contrast to all other nitridosilicates *M*–Si–N, this compound exhibits highly covalent interactions between *M* = Pb and N. This change in bond character influences the entire structure, resulting in a significant and unexpected distortion of the unit cell. This compound also exhibits unprecedented cationic $Pb_2$ dumbbells. According to DFT calculations, these dumbbells arise from *s*–*p* mixing combined with little *p*–*p* mixing of formal $Pb^{2+}$ cations. Additionally the experimental proof of a elastic force between the Pb cations have been shown by combination of Raman spectroscopy and phononic calculations revealing the Pb–Pb stretching vibration at 117 $cm^{-1}$.

# 7 Discussion and Outlook

## 7.1 Ion Exchange – A Novel Approach Toward Nitridosilicates

The synthesis approach developed in this thesis, namely the exchange of cations in highly condensed nitridosilicates $M_2Si_5N_8$ as the first *top-down* approach for this substance class, fundamentally differs from conventional preparation methods (*bottom-up*, chapter 1.3).[1] While those methods are based on the principle of building up anionic covalent Si–N networks in presence of suitable cations, here pre-synthesized nitridosilicates are used as starting materials according to equations 7.1 and 7.2.[2]

$$AE_2Si_5N_8 + 2\,MCl_2 \rightarrow M_2Si_5N_8 + 2\,AECl_2 \qquad 7.1$$

$$AE_2Si_5N_8 + x\,MCl_3 \rightarrow AE_{2-1.5x}M_xSi_5N_8 + 1.5x\,AECl_2 \qquad 7.2$$

The ion exchange approach turned out to be a valueable method for exploration of energy landscapes, especially concerning metastable compounds.[3] A prime example for this issue is the system containing Ca, Si and N in atomic ratio 2:5:8 (Figure 7.1). This ratio can be achieved, for example, through either of the three modifications α-, β- and HP-$Ca_2Si_5N_8$ or through combinations of $Ca_3N_2$, $Si_3N_4$ and $CaSiN_2$ in the respective stoichiometric ratio.[1g,2a,4]

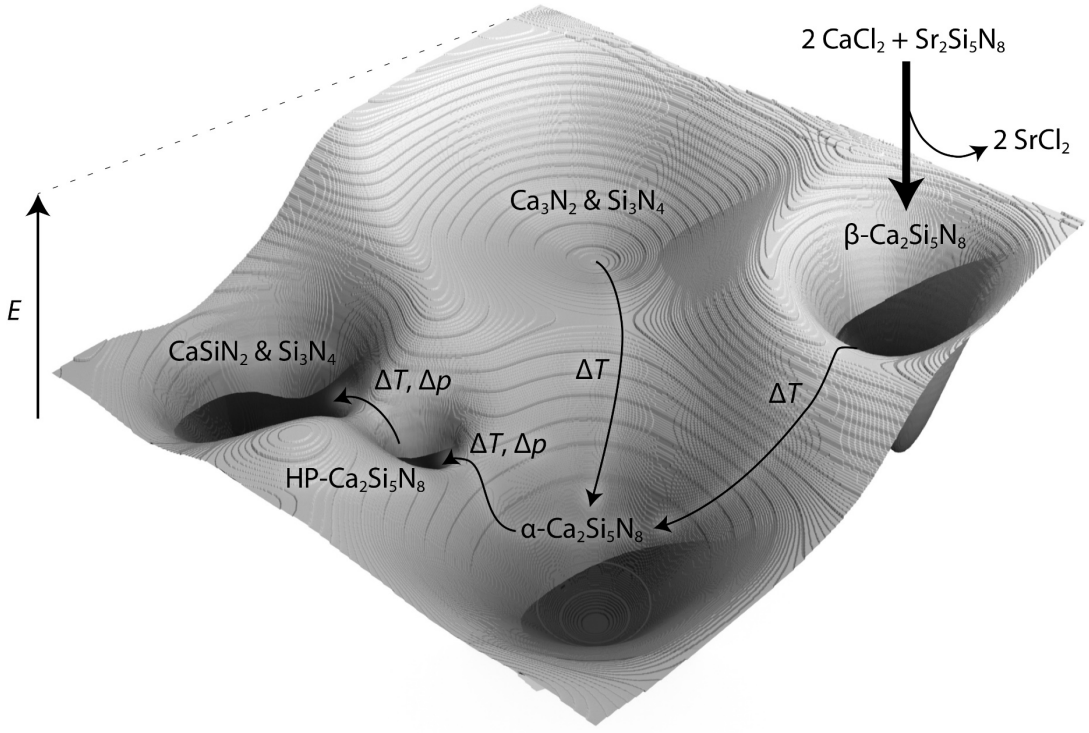


**Figure 7.1:** Schematic view on a section of the energy landscape of a system containing Ca, Si and N in the ratio 2:5:8 including $^2/_3\,Ca_3N_2 + {}^5/_3\,Si_3N_4$, $CaSiN_2 + Si_3N_4$ as well as all three modifications of $Ca_2Si_5N_8$ (α-, β- and HP-).

According to experimental experience, high temperature reactions of the binary nitrides $Ca_3N_2$ and $Si_3N_4$ in the given stoichometry yield α-$Ca_2Si_5N_8$, since this compound appears to represent an easily accessible energetic minimum in contrast to the β-modification.[1g,5] Two reasons mainly responsible for the inaccessibility of β-$Ca_2Si_5N_8$ applying *bottom-up* reactions have been identified so far. First, throughout the Si–N network formation in presence of $Ca^{2+}$, the energy barrier toward the $[Si_5N_8]^{4-}$ network of β-$Ca_2Si_5N_8$, which is preferentially built up in the presence of larger ions like $Sr^{2+}$ or $Ba^{2+}$, is expected to be significantly higher than toward the $[Si_5N_8]^{4-}$ network of α-$Ca_2Si_5N_8$. Secondly, the absolute energy of β-$Ca_2Si_5N_8$ is higher than the one of α-$Ca_2Si_5N_8$ (based on DFT calculations of a hypothetical "o-$Ca_2Si_5N_8$", which exhibits almost the same structure as β-$Ca_2Si_5N_8$).[5] This second point is also confirmed by the transformation of β-$Ca_2Si_5N_8$ into the α-modification at T ≥ 1500 °C.[2a] The reversion of this transformation has not been observed so far, not even when applying high pressure (β-$Ca_2Si_5N_8$ is 0.08 g · $cm^{-3}$ denser than α-$Ca_2Si_5N_8$).[2a] Under high pressure conditions α-$Ca_2Si_5N_8$ undergoes transformation into HP-$Ca_2Si_5N_8$ and as predicted by DFT calculations at even higher pressures the compound decomposes into $CaSiN_2$ and $Si_3N_4$.[5,6] Therefore, ion exchange between $Sr_2Si_5N_8$ and $CaCl_2$ so far is the only possible route for a targeted synthesis of β-$Ca_2Si_5N_8$, since it allows the utilization of $Sr^{2+}$ cation mobility in $Sr_2Si_5N_8$ at temperatures, which are not sufficient to break down the highly covalent Si–N network $[Si_5N_8]^{4-}$.[2a]

Due to the fact that nitridosilicates with unprecedented elemental compositions are most likely metastable compared to well known compounds like binary nitrides or intermetallic phases, the ion exchange approach, a valuable tool to discover local and hardly accessible minima on various energetic landscapes, is predestinated for the exploration of novel elemental compositions *M*–Si–N. As described in chapters 2 and 3, based on TDPXRD measurements the mechanism of the ion exchange reaction has been investigated in detail, revealing both, Si–N network preservation and a continuous exchange of mobile cations along the solid solution series $AE_{2-x}M_xSi_5N_8$ ($0 \leq x \leq 2$).[2a,2b] Thus, no redox reactions between N and the selected metal occur throughout the reactions.

Since N atoms in nitridosilicates are inert due to being tightly bound in the highly covalent Si–N network, the reaction behavior of different metals towards N does not play a crucial role in the ion exchange approach. Consequently, not only thermodynamic sinks like binary nitrides (e.g. ScN or UN)[7] can be well avoided by this approach, but it is also not impeded by the low oxidation force of N, since no redox reactions between the Si–N network and the cations occur, which could be problematic in the case of ions with a comparatively high redox potential, such as $Fe^{2+}$ and $Pb^{2+}$.[8]

## 7.2 Expanded Elemental Variety in Nitridosilicate Chemistry by Ion Exchange

Application of the ion exchange approach in the model system $M_2Si_5N_8$,[1f,1g,9] provided access to a new dimension in elemental variety. As described in chapter 1.5, the 13 different metals that had been incorporated into non-*AB* or $AB_2$-type nitridosilicates before this thesis (marked green in Figure 7.2), are all highly electropositive and either belong to the alkali, the alkaline earth or the rare earth elements.[1f–h,4, 9,10] Being not affected by these limitations, the ion exchange approach has so far been successfully applied to seven further metals that could be incorporated as counter ions in nitridosilicates (marked orange in Figure 7.2).

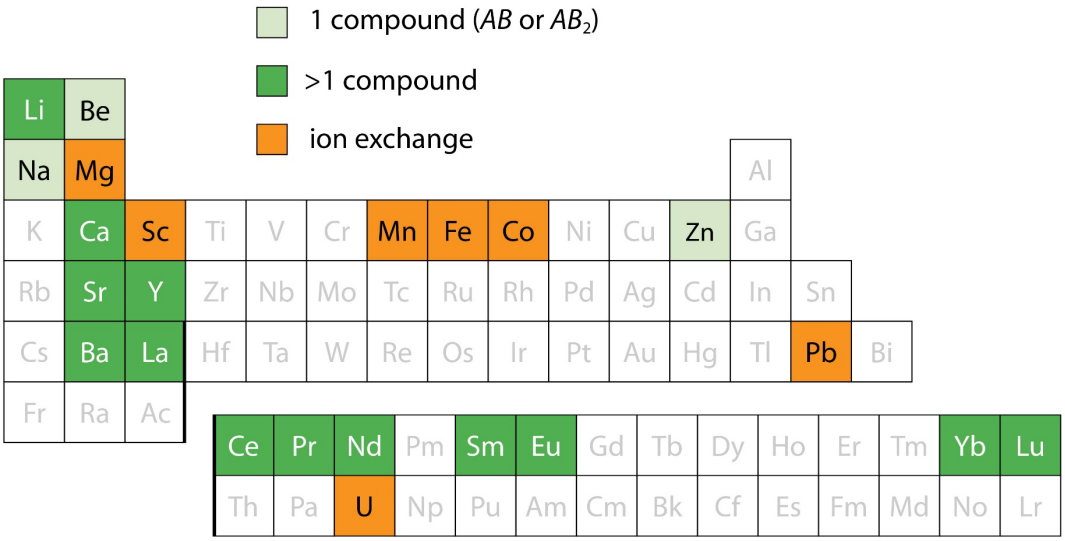


**Figure 7.2:** Section of the periodic table of elements. Metals marked in green have been incorporated into nitridosilicates before this work by *bottom-up* approaches, metals marked in orange by the ion exchange approach in this thesis.

After development of the ion exchange approach applying a $ScCl_3$ melt on α-$Ca_2Si_5N_8$, thus avoiding the thermodynamically highly stable phase ScN,[7a] the next logical step was to test this reaction type on more electronegative metals. Due to its similarity to $Ca^{2+}$, $Sr^{2+}$ and $Ba^{2+}$, which have often been incorporated into non-*AB* or $AB_2$-type nitridosilicates,[1f,1g,4,10e,10f,10h] $Mg^{2+}$ has been the second cation to be used in the ion exchange approach. Avoiding the formation of volatile Mg–N compounds at elevated temperatures and dealing with the increased electronegativity of Mg, that often leads to the integration of Mg into the anionic network,[11] the reaction of $MgCl_2$ and α-$Ca_2Si_5N_8$ yielded $Mg_2Si_5N_8$, a compound which had been predicted by DFT calculations but has not been accessible by *bottom-up* reactions.

A long sought-after issue and one of the main aims in nitridosilicate research has been a general access to open-shell transition metal containing compounds.[12] Before this thesis, the only known compounds with *d*-electrons in the counter cations' valence shells have been $M\mathrm{SiN_2}$ ($M$ = Mn, Zn).[10ae,10i] However, these compounds exhibit the *AB* type wurtzite structure. Furthermore, $Mn^{2+}$ (half full shell $3d^5$) and $Zn^{2+}$ (closed $3d^{10}$ shell) are known for their similar behavior to the alkaline earth cations. Therefore, these compounds can be prepared by classic *bottom-up* approaches. In contrast, with the novel *top-down* approach, applying salt melts of $MnCl_2$, $FeCl_2$ and $CoCl_2$, the first open-shell transition metal nitridosilicates $M_2Si_5N_8$ (colorful compounds as given in Figure 7.3, $M$ = Mn, Fe, Co) could be accessed, finally accomplishing a research objective, which has been set up more than two decades ago. Of these, $Fe_2Si_5N_8$, has been exemplarily investigated by Mößbauer spectroscopy and magentic susceptibility measurements, revealling the preservation of the divalent oxidation state of $Fe^{2+}$ as well as magnetic properties introduced by the unpaired electrons in $Fe^{2+}$.

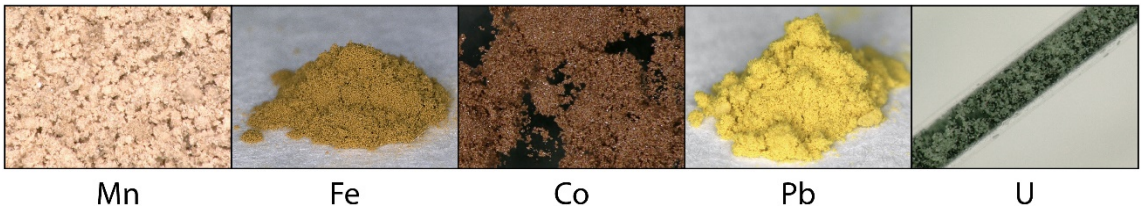


**Figure 7.3:** Optical micrographs of colorful $M_2Si_5N_8$ compounds containing Mn, Fe, Co, Pb and U.

Highly condensed nitridosilicates are well known for their intrinsic thermal, chemical and mechanical stability.[13] Although they do not occur in nature, these compounds seem to be predestined for beeing tested as host materials for immobilization of radioactive nuclides. However, due to the highly stable character of binary nitrides $M$N ($M$ = actinides) comparable to the early transition metals,[7b] no actinide nitridosilicates have been prepared before this work. Applying the ion exchange reaction, the 5*f* elements of the periodic table can now be incorporated into anionic Si–N networks as well. This has been demonstrated exemplarily for the element U. Moreover, since trivalent $UCl_3$ was used for U incorporation, the stability of the pre-synthesized $[Si_5N_8]^{4-}$ network against vacancy incorporation could be investigated in detail, as well. While the reaction of α-$Ca_2Si_5N_8$ with $ScCl_3$ yields a statistical distribution of vacancies, the ion exchange between $UCl_3$ and $Sr_2Si_5N_8$ revealed an impressive variability of highly covalent Si–N networks. In $U_{0.5x}Sr_{2-0.75x}Si_5N_8$ with $x \approx 1.05$ (black particles in Figure 7.3), the variability of the $[Si_5N_8]^{4-}$ network was found to be sufficient for compensation of trivalent $U^{3+}$ on the one hand and 80% vacancies on the other hand

located on former $Sr^{2+}$ sites. Despite this significant amount of vacancies the compound itself reveals an impressive stability against treatment in $H_2O$, $HNO_3$ and KOH.

Last, cations of an element from the right side of the Zintl border,[14] namely $Pb^{2+}$, have been incorporated into $M_2Si_5N_8$. With its electrode potential of −0.125 V ($Pb \longrightarrow Pb^{2+} + 2e^-$),[8] this element belongs to the most noble ones within the group of elements that exhibit a negative electrode potential. This fact, combined with the comparatively high electron affinity and electronegativity of Pb, has been the reason, why no Pb-nitride had been crystallographically elucidated before. However, due to these properties of Pb, $Pb_2Si_5N_8$ exhibits a highly covalent bonding situation, not only in case of Si–N but also for Pb–N. This highly covalent environment finally also enables the formation of the first covalently bound $Pb_2$ cations.

## 7.3 Prospects for Si–N Chemistry

### Nitridosilicates

Considering only the model system $M_2Si_5N_8$,[1f,1g,9] the elemental variety of nitridosilicates has been expanded by over 50% in this thesis. Choosing other $MCl_2$ or $MCl_3$ salts with melting points above ca. 700 °C and stable up to 1000 °C, it is likely to further expand the elemental variety while staying in the system $M_2Si_5N_8$. As depicted in chapter 3.1,[2b] the selected and comparatively high reaction temperatures for the ion exchange reactions in $M_2Si_5N_8$ have been necessary in order to open up channels in the pre-synthesized nitridosilicates by thermal expansion so that cation mobilty is enabled. Assuming that such channels open up in less condensed nitridosilicates ($\kappa \leq {}^5/_8$) at significantly lower temperatures, many different metal chlorides with melting points and decomposition temperatures below the temperature, at which cation mobility in $M_2Si_5N_8$ starts to occur, may be used for ion exchange reactions as well. Thus, the elemental variety, especially concerning more electronegative metals (still a great potential for expansion according to Figure 7.4), which often exhibit low melting points for $MCl_x$,[7b] could be further expanded. Since, for example transition metal chlorides like $HfCl_4$, $TaCl_5$ or $WCl_6$ exhibit high oxidation numbers, nitridosilicates with highly charged counter cations like $M^{4+}$, $M^{5+}$ or even $M^{6+}$ might also be accessible.

Furthermore, incoporation of counter cations $M^{n+}$, which are commonly found to be part of anionic networks of other metallate structures, could lead to novel classes of mixed nitridometallates where both, formal $Si^{4+}$ and $M^{n+}$ build up the anionic networks.

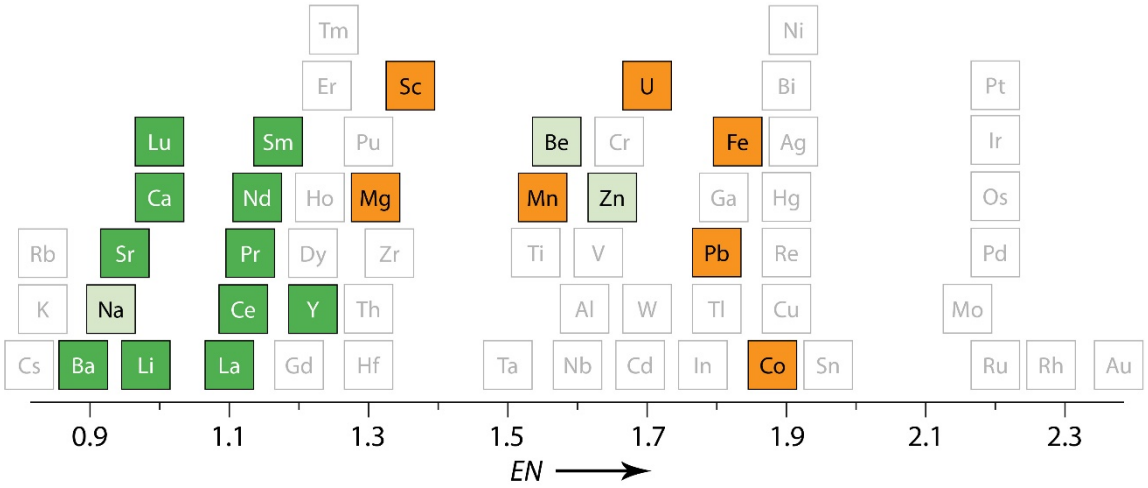


**Figure 7.4:** Metals sorted by increasing *EN* according to Pauling. Elements marked in green have been incorporated into nitridosilicates before this work, elements marked in orange throughout this thesis.

### Silicon nitride

Assuming that less condensed $SiN_4$ tetrahedra are able to withstand the conditions of ion exchange reactions at comparatively low temperatures, even an approach toward the preparation of novel networks with the sum formula "$Si_3N_4$" might be worth a try. For that, especially low condensed nitridosilicates could be used for reactions in liquid silicon halides.

$$Ba_5Si_2N_6 + 2.5\ SiCl_4 \rightarrow 1.5\ Si_3N_4 + 5\ BaCl_2 \qquad 7.3$$

According to the hypothetical equation 7.3, it might even be possible to partially design these compounds by using starting materials with desired Si–N building units like edge sharing $SiN_4$ tetrahedra.

### $M^{2+}$ ion conductors

The observed mobility of small ions like $Mg^{2+}$, $Fe^{2+}$ and $Ca^{2+}$, large ions ($Sr^{2+}$) or even trivalent ions such as $Sc^{3+}$ and $U^{3+}$ at elevated temperatures in $M_2Si_5N_8$ is remarkable, especially against the background of the high condensation degree ($\kappa = {}^5/_8$) of the latter. Based on these findings it seems possible to access solid-state ion conductors for divalent cations like $Mg^{2+}$. The objective would then be to reduce the temperature required for cation mobility. Two strategies seem auspicious to be pursued in order to do so. First, large ions like $Sr^{2+}$ could be exchanged against small ones such as $Mg^{2+}$ in pre-synthesized nitridosilicates. Then, the resulting compound would contain $Mg^{2+}$ cations located in an anionic Si–N network, which has been initially built up around $Sr^{2+}$ and thus actually

being to large for $Mg^{2+}$. Second, according to chapter 4.1, vacancies could subsequently be introduced into $M^{2+}$ containing nitridosilicates in order to positively influence $M^{2+}$ mobility even at comparatively low temperatures.

## 7.4 Prospects for Other Metallate Compound Classes

The ion exchange reaction is based on the principle that under the selected conditions in salt melts, ionic interactions between the counter cations and N in nitridosilicates are broken, while highly covalent Si–N bonds are preserved. Transferring this concept toward other metallate compound classes one has to consider the degree of covalency within the anionic networks. With decreasing degree of covalency, bonds within such networks would be expected to be more easily broken by highly ionic salt melts. By arranging network building atoms according to their difference in electronegativities,[15] as done in Figure 7.5, the degree of covalency for different compound classes like phosphates, borates, silicates, aluminates, berrylates and scandates may be estimated.

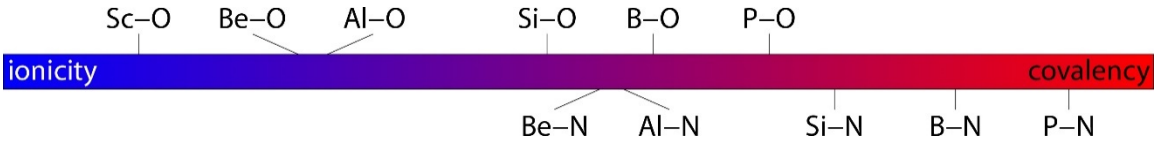


**Figure 7.5:** Various metallate network building atoms arranged by their difference in electronegativity.[15]

According to Figure 7.5, combined with the knowledge that ion exchange applying salt melts is possible in Si–N chemistry, nitridophosphates as well as nitridoborates seem to be promising candidates for further investigations due to their even higher degree of covalency within anionic networks compared to nitridosilicates. Indeed, ion exchange reactions analogously to the reactions described in this thesis applying modified reaction conditions have already been observed in nitridophosphates by WENDL. Such reactions may become a second pillar of expanding elemental variety in nitridophosphates beside of the very successful and closely related high-pressure metathesis route ($MHal_x + LiPN_2 \rightarrow MP_xN_{2x} + x\ LiHal$) eastablished by KLOß.[16]

Considering compound classes like nitridoaluminates or -berrylates,[17] which exhibit less covalent interactions within the anionic networks, experiments have to be performed in order to investigate their suitability for this synthesis approach.

In contrast to nitridometallates, where elemental variety is an issue due to the comparatively low oxidation force of nitrogen, oxometallate classes may also benefit from the ion exchange approach.

For example, the phosphor $Ca_xSr_{1-x}Sc_2O_4:Ce^{3+}$ has already been prepared from $SrSc_2O_4:Ce^{3+}$ applying a $CaCl_2$ melt analogously to the results of this thesis.[18] Since so far it is not clear weather the highly ionic $[Sc_2O_4]^{2-}$ network has been preserved throughout the entire reaction process, ion exchange reactions in more ionic metallate compound classes may even provide access to novel network types.

## 7.5 Concluding Remark

From the beginning, crystal structures of nitridosilicates have always been described to be composed of anionic Si–N building units on the one hand and counter cations located in between on the other hand. In this thesis, this kind of description has been taken literally and finally been confirmed by experiments that are able to distinguish between the two parts of these structures. Considering that the ion exchange approach was able to expand the elemental variety in nitridosilicate chemistry by more than 50% by working with only one model system, namely $M_2Si_5N_8$, it is hardly possible to predict the enormous impact of this synthesis strategy, not only on nitridosilicate but on nitride chemistry in general.

## 7.6 References

[1] a) H. Lux, "„SÄUREN" UND „BASEN" IM SCHMELZFLUSS: DIE BESTIMMUNG DER SAUERSTOFFIONEN-KONZENTRATION", *Z. Elektrochem. Angew. Phys. Chem.* **1939**, *45*, 303–309; b) H. Flood, T. Förland, "The Acidic and Basic Properties of Oxides", *Acta Chem. Scand. (1947–1973)* **1947**, *1*, 592–604; c) J. David, J. Lang, "Sur un nitrure double de magnesium et de silicium", *C. R. Hebd. Seances Acad. Sci.* **1965**, *261*, 1005–1007; d) H. Yamane, F. J. DiSalvo, "Synthesis and Crystal Structure of $Sr_2ZnN_2$ and $Ba_2ZnN_2$", *J. Solid State Chem.* **1995**, *119*, 375–379; e) H. Yamane, F. J. DiSalvo, "Sodium flux synthesis of nitrides", *Prog. Solid State Chem.* **2018**, *51*, 27–40; f) T. Schlieper, W. Milius, W. Schnick, "Nitrido-silicate. II Hochtemperatur-Synthesen und Kristallstrukturen von $Sr_2Si_5N_8$ und $Ba_2Si_5N_8$", *Z. Anorg. Allg. Chem.* **1995**, *621*, 1380–1384; g) T. Schlieper, W. Schnick, "Nitrido-Silicate. I Hochtemperatur-Synthese und Kristallstruktur von $Ca_2Si_5N_8$", *Z. Anorg. Allg. Chem.* **1995**, *621*, 1037–1041; h) T. Schlieper, W. Schnick, "Nitrido-silicate. II Hochtemperatur-Synthese, Kristallstruktur und magnetische Eigenschaften von $Ce_3[Si_6N_{11}]$", *Z. Anorg. Allg. Chem.* **1995**, *621*, 1535–1538.

[2] a) P. Bielec, W. Schnick, "Increased Synthetic Control – Gaining Access to Predicted $Mg_2Si_5N_8$ and β-$Ca_2Si_5N_8$", *Angew. Chem., Int. Ed.* **2017**, *56*, 4810–4813; "Increased Synthetic Control – Gaining Access to Predicted $Mg_2Si_5N_8$ and β-$Ca_2Si_5N_8$", *Angew. Chem.* **2017**, *129*, 4888–4891; b) P. Bielec, O. Janka, T. Block, R. Pöttgen, W. Schnick, "$Fe_2Si_5N_8$: Access to Open-Shell Transition-Metal Nitridosilicates", *Angew. Chem., Int. Ed.* **2018**, *57*, 2409–2412; "$Fe_2Si_5N_8$: Access to Open-Shell Transition-Metal Nitridosilicates", *Angew. Chem.* **2018**, *130*, 2433–2436; c) P. Bielec, L. Eisenburger, H. L. Deubner, D. Günther, F. Kraus, O. Oeckler, W. Schnick, "Targeting Vacancies in Nitridosilicates: Aliovalent Substitution of $M^{2+}$ ($M$ = Ca, Sr) by $Sc^{3+}$ and $U^{3+}$", *Angew. Chem., Int. Ed.* **2019**, *58*, 840–843; "Targeting Vacancies in Nitridosilicates: Aliovalent Substitution of $M^{2+}$ ($M$ = Ca, Sr) by $Sc^{3+}$ and $U^{3+}$", *Angew. Chem.* **2019**, *131*, 850–853; d) P. Bielec, R. Nelson, R. P. Stoffel, L. Eisenburger, D. Günther, A.-K. Henß, J. P. Wright, O. Oeckler, R. Dronskowski, W. Schnick, "Cationic $Pb_2$ Dumbbells Stabilized in the Highly Covalent Lead Nitridosilicate $Pb_2Si_5N_8$", *Angew. Chem., Int. Ed.* **2019**, 58, 1432–1436; "Cationic $Pb_2$ Dumbbells Stabilized in the Highly Covalent Lead Nitridosilicate $Pb_2Si_5N_8$", *Angew. Chem.* **2019**, *131*, 1446–1450.

[3] M. Jansen, "A Concept for Synthesis Planning in Solid-State Chemistry", *Angew. Chem., Int. Ed.* **2002**, *41*, 3746–3766; "Ein Konzept zur Syntheseplanung in der Festkörperchemie", *Angew. Chem.* **2002**, *114*, 3896–3917.

[4] Z. A. Gál, P. M. Mallinson, H. J. Orchard, S. J. Clarke, "Synthesis and Structure of Alkaline Earth Silicon Nitrides: $BaSiN_2$, $SrSiN_2$, and $CaSiN_2$", *Inorg. Chem.* **2004**, *43*, 3998–4006.

[5] S. R. Römer, "Density Functional Calculations of Pressure-Induced Phase Transformations of Group II Element Nitrides, Nitridosilicates and Nitridophosphates", *Dissertation*, Ludwig-Maximilians-Universität München, **2008**.

[6] S. R. Römer, C. Braun, O. Oeckler, P. J. Schmidt, P. Kroll, W. Schnick, "HP-$Ca_2Si_5N_8$ – A New High-Pressure Nitridosilicate: Synthesis, Structure, Luminescence, and DFT Calculations", *Chem. – Eur. J.* **2008**, *14*, 7892–7902.

[7] a) K. Becker, F. Ebert, "Die Kristallstruktur einiger binärer Carbide und Nitride", *Z. Phys.* **1925**, *31*, 268–272; b) D. R. Lide, *CRC Press – Handbook of Chemistry and Physics, Vol. 84$^{th}$*, National Institute of Standards & Technology, USA, **2004**.

[8] A. F. Holleman, N. Wiberg, *Lehrbuch der Anorganischen Chemie, Vol. 102*, DeGruyter, Berlin, Boston, **2008**.

[9] H. Huppertz, W. Schnick, "$Eu_2Si_5N_8$ and $EuYbSi_4N_7$. The First Nitridosilicates with a Divalent Rare Earth Metal", *Acta Crystallogr., Sect. C: Cryst. Struct. Commun.* **1997**, *53*, 1751–1753.

[10] a) M. Woike, W. Jeitschko, "Preparation and Crystal Structure of the Nitridosilicates $Ln_3Si_6N_{11}$ (Ln = La, Ce, Pr, Nd, Sm) and $LnSi_3N_5$ (Ln = Ce, Pr, Nd)", *Inorg. Chem.* **1995**, *34*, 5105–5108; b) T. Schlieper, W. Schnick, "Crystal structure of tripraseodymium hexasiliconundecanitride, $Pr_3Si_6N_{11}$", *Z. Kristallogr.* **1996**, *211*, 254; c) H. Yamane, F. J. DiSalvo, "Preparation and crystal structure of a new barium silicon nitride, $Ba_5Si_2N_6$", *J. Alloys Compd.* **1996**, *240*, 33–36; d) H. Yamane, S. Kikkawa, M. Koizumi, "PREPARATION OF LITHIUM SILICON NITRIDES AND THEIR LITHIUM ION CONDUCTIVITY", *Solid State Ionics* **1987**, *25*, 183–191; e) H. Huppertz, W. Schnick, "Edge-sharing $SiN_4$ Tetrahedra in the Highly Condensed Nitridosilicate $BaSi_7N_{10}$", *Chem. – Eur. J.* **1997**, *3*, 249–252; f) H. Huppertz, W. Schnick, "$BaYbSi_4N_7$ – Unexpected Structural Possibilities in Nitridosilicates", *Angew. Chem., Int. Ed. Engl.* **1996**, *35*, 1983–1984; "$BaYbSi_4N_7$ – überraschende strukturelle

Möglichkeiten in Nitridosilicaten", *Angew. Chem.* **1996**, *108*, 2115–2116; g) H. Huppertz, W. Schnick, "$Ba_2Nd_7Si_{11}N_{23}$ – A Nitridosilicate with a Zeolite-Analogous Si–N Structure", *Angew. Chem., Int. Ed. Engl.* **1997**, *36*, 2651–2652; "$Ba_2Nd_7Si_{11}N_{23}$ – ein Nitridosilicat mit zeolithartiger Si–N-Gerüststruktur", *Angew. Chem.* **1997**, *109*, 2765–2767; h) H. Huppertz, W. Schnick, "Synthese, Kristallstruktur und Eigenschaften der Nitridosilicate $SrYbSi_4N_7$ und $BaYbSi_4N_7$", *Z. Anorg. Allg. Chem.* **1997**, *623*, 212–217; i) T. Endo, H. Takizawa, M. Shimada, "NEW II-IV-$V_2$ FAMILY OF PERIODIC COMPOUNDS SYNTHESIZED UNDER HIGH PRESSURE", *Ceram. Eng. Sci. Proc.* **1992**, *13*, 844–851; j) C. M. Fang, Y. Q. Li, H. T. Hintzen, G. de With, "Crystal and electronic structure of the novel nitrides $MYSi_4N_7$ (M = Sr, Ba) with peculiar $NSi_4$ coordination", *J. Mater. Chem.* **2003**, *13*, 1480–1483; k) G. Pilet, H. A. Höppe, W. Schnick, S. Esmaeilzadeh, "Crystal structure and mechanical properties of $SrSi_7N_{10}$", *Solid State Sci.* **2005**, *7*, 391–396; l) F. Ottinger, I. Kroslakova, K. Hametner, E. Reusser, R. Nesper, D. Günther, "Analytical evidence of amorphous microdomains within nitridosilicate and nitridoaluminosilicate single crystals", *Anal. Bioanal. Chem.* **2005**, *383*, 489–499; m) F. Ottinger, R. Nesper, "Synthesis and Crystal Structure of the Nitridosilicates $Ca_5[Si_2N_6]$ and $Ca_7[NbSi_2N_9]$", *Z. Anorg. Allg. Chem.* **2005**, *631*, 1597–1602; n) C. Schmolke, O. Oeckler, D. Bichler, D. Johrendt, W. Schnick, "Complex Interrupted Tetrahedral Frameworks in the Nitridosilicates $M_7Si_6N_{15}$ (M = La, Ce, Pr)", *Chem. – Eur. J.* **2009**, *15*, 9215–9222; o) C. Schmolke, D. Bichler, D. Johrendt, W. Schnick, "Synthesis and crystal structure of the first chain-type nitridosilicates $RE_5Si_3N_9$ (RE = La, Ce)", *Solid State Sci.* **2009**, *11*, 389–394; p) S. Lupart, W. Schnick, "$Pr_5Si_3N_9$", *Acta Crystallogr., Sect. E: Struct. Rep. Online* **2009**, *65*, i43; q) M. Zeuner, S. Pagano, P. Matthes, D. Bichler, D. Johrendt, T. Harmening, R. Pöttgen, W. Schnick, "Mixed Valence Europium Nitridosilicate $Eu_2SiN_3$", *J. Am. Chem. Soc.* **2009**, *131*, 11242–11248; r) S. Pagano, M. Zeuner, S. Hug, W. Schnick, "Single-Crystal Structure Determination and Solid-State NMR Investigations of Lithium Nitridosilicate $Li_2SiN_2$ Synthesized by a Precursor Approach Employing Amorphous "$Si(CN_2)_2$"", *Eur. J. Inorg. Chem.* **2009**, 1579–1584; s) S. Pagano, S. Lupart, M. Zeuner, W. Schnick, "Tuning the Dimensionality of Nitridosilicates in Lithium Melts", *Angew. Chem., Int. Ed.* **2009**, *48*, 6335–6338; "Tuning the Dimensionality of Nitridosilicates in Lithium Melts", *Angew. Chem.* **2009**, *121*, 6453–6456; t) S. Lupart, M. Zeuner, S. Pagano, W. Schnick, "Chain-Type Lithium Rare-

Earth Nitridosilicates – $Li_5Ln_5Si_4N_{12}$ with Ln = La, Ce", *Eur. J. Inorg. Chem.* **2010**, 2636–2641; u) M. Zeuner, S. Pagano, S. Hug, P. Pust, S. Schmiechen, C. Scheu, W. Schnick, "$Li_2CaSi_2N_4$ and $Li_2SrSi_2N_4$ – a Synthetic Approach to Three-Dimensional Lithium Nitridosilicates", *Eur. J. Inorg. Chem.* **2010**, 4945–4951; v) S. Pagano, S. Lupart, S. Schmiechen, W. Schnick, "$Li_4Ca_3Si_2N_6$ and $Li_4Sr_3Si_2N_6$ – Quaternary Lithium Nitridosilicates with Isolated $[Si_2N_6]^{10-}$ Ions", *Z. Anorg. Allg. Chem.* **2010**, *636*, 1907–1909; w) S. M. Hick, M. I. Miller, R. B. Kaner, R. G. Blair, "Synthesis and Crystal Structure of Cubic $Ca_{16}Si_{17}N_{34}$", *Inorg. Chem.* **2012**, *51*, 12626–12629; x) S. Lupart, W. Schnick, "$LiCa_3Si_2N_5$ – A Lithium Nitridosilicate with a $[Si_2N_5]^{7-}$ Double-Chain", *Z. Anorg. Allg. Chem.* **2012**, *638*, 2015–2019; y) H. Huppertz, O. Oeckler, A. Lieb, R. Glaum, D. Johrendt, M. Tegel, R. Kaindl, W. Schnick, "$Ca_3Sm_3[Si_9N_{17}]$ and $Ca_3Yb_3[Si_9N_{17}]$ Nitridosilicates with Interpenetrating Nets that Consist of Star-Shaped $[N^{[4]}(SiN_3)_4]$ Units and $[Si_5N_{16}]$ Supertetrahedra", *Chem. – Eur. J.* **2012**, *18*, 10857–10864; z) H. Yamane, H. Morito, *Inorg. Chem.* **2013**, *52*, 5559–5563; aa) H. Yamane, H. Morito, "$Ba_4Mg[Si_2N_6]$, $Ba_3Ca_2[Si_2N_6]$ and $Ba_{1.6}Sr_{3.4}[Si_2N_6]$ – Quaternary barium alkaline-earth silicon nitrides containing isolated nitridosilicate anions of $[Si_2N_6]^{10-}$", *J. Alloys Compd.* **2013**, *555*, 320–324; ab) F. Ottinger, R. Nesper, "SYNTHESIS AND STRUCTURE OF $CaSiN_2$", *Acta Crystallogr., Sect. A: Found. Adv.* **2002**, *58*, c337; ac) H. Huppertz, W. Schnick, "Synthese und Kristallstruktur von $BaEu(Ba_{0,5}Eu_{0,5})YbSi_6N_{11}$", *Z. Anorg. Allg. Chem.* **1998**, *624*, 371–374; ad) W. B. Park, K. H. Son, S. P. Singh, K.-S. Sohn, "Solid-State Combinatorial Screening of $ARSi_4N_7:Eu^{2+}$ (A = Sr, Ba, Ca; R = Y, La, Lu) Phosphors", *ACS Comb. Sci.* **2012**, *14*, 537–544; ae) R. Marchand, M. Maunaye, J. Lang, "Sur la préparation d'un nitrure double de silicium et manganèse", *C. R. Seances Acad. Sci., Ser. C* **1971**, *272*, 1654–1656.

[11] a) T. M. Tolhurst, S. Schmiechen, P. Pust, P. J. Schmidt, W. Schnick, A. Moewes, "Electronic Structure, Bandgap, and Thermal Quenching of $Sr[Mg_3SiN_4]:Eu^{2+}$ in Comparison to $Sr[LiAl_3N_4]:Eu^{2+}$", *Adv. Opt. Mater.* **2016**, *4*, 584–591; b) S. Schmiechen, P. Strobel, C. Hecht, T. Reith, M. Siegert, P. J. Schmidt, P. Huppertz, D. Wiechert, W. Schnick, "Nitridomagnesosilicate $Ba[Mg_3SiN_4]:Eu^{2+}$ and Structure–Property Relations of Similar Narrow-Band Red Nitride Phosphors", *Chem. Mater.* **2015**, *27*, 1780–1785; c) S. Schmiechen, H. Schneider, P. Wagatha, C. Hecht, P. J. Schmidt, W. Schnick, "Toward New Phosphors for Application in Illumination-Grade White pc-LEDs: The Nitridomagnesosilicates

Ca[$Mg_3SiN_4$]:$Ce^{3+}$, Sr[$Mg_3SiN_4$]:$Eu^{2+}$, and Eu[$Mg_3SiN_4$]", *Chem. Mater.* **2014**, *26*, 2712–2719; d) P. Strobel, V. Weiler, C. Hecht, P. J. Schmidt, W. Schnick, "Luminescence of the Narrow-Band Red Emitting Nitridomagnesosilicate $Li_2(Ca_{1-x}Sr_x)_2[Mg_2Si_2N_6]:Eu^{2+}$ ($x$ = 0–0.06)", *Chem. Mater.* **2017**, *29*, 1377–1383.

[12] H. Huppertz, N. Stock, W. Schnick, "The First Crystalline Hexagonal $Si_3N_4$ Microtubes", *Adv. Mater. (Weinheim, Ger.)* **1996**, *8*, 844–847.

[13] W. Schnick, H. Huppertz, "Nitridosilicates – A Significant Extension of Silicate Chemistry", *Chem. – Eur. J.* **1997**, *3*, 679–683.

[14] a) E. Zintl, "Intermetallische Verbindungen", *Angew. Chem.* **1939**, *52*, 1–6; b) F. Laves, "Eduard Zintls Arbeiten über die Chemie und Struktur von Legierungen", *Naturwissenschaften (1913–2014)* **1941**, *29*, 244–255.

[15] A. L. Allred, E. G. Rochow, "A SCALE OF ELECTRONEGATIVITY BASED ON ELECTROSTATIC FORCE", *J. Inorg. Nucl. Chem.* **1958**, *5*, 264–268.

[16] a) S. D. Kloß, W. Schnick, "Rare-Earth-Metal Nitridophosphates through High-Pressure Metathesis", *Angew. Chem., Int. Ed.* **2015**, *54*, 11250–11253; "Seltenerdnitridophosphate durch Hochdruckmetathese", *Angew. Chem.* **2015**, *127*, 11402–11405; b) S. D. Kloß, S. Wandelt, A. Weis, W. Schnick, "Accessing Tetravalent Transition-Metal Nitridophosphates through High-Pressure Metathesis", *Angew. Chem., Int. Ed.* **2018**, *57*, 3192–3195; "Accessing Tetravalent Transition-Metal Nitridophosphates through High-Pressure Metathesis", *Angew. Chem.* **2018**, *130*, 3246–3249; c) S. D. Kloß, "The High-Pressure Metathesis Route for the Preparation of Rare-Earth and Transition Metal Nitridophosphates", *Dissertation*, Ludwig-Maximilians-Universität München, **2018**; d) S. D. Kloß, O. Janka, T. Block, R. Pöttgen, R. Glaum, W. Schnick, "Open-Shell 3d Transition Metal Nitridophosphates $M^{II}P_8N_{14}$ ($M^{II}$ = Fe, Co, Ni) by High-Pressure Metathesis", *Angew. Chem., Int. Ed.* **2019**, *58*, 4685; "Open-Shell 3d Transition Metal Nitridophosphates $M^{II}P_8N_{14}$ ($M^{II}$ = Fe, Co, Ni) by High-Pressure Metathesis", *Angew. Chem.* **2019**, *131*, 4733.

[17] a) W. Blase, G. Cordier, M. Ludwig, R. Kniep, "$Sr_3[Al_2N_4]$: Ein Nitridoaluminat mit gewellten Tetraederketten $^1_\infty[AlN_{4/2}^{3-}]$", *Z. Naturforsch., B: J. Chem. Sci.* **1994**, *49*, 501–505; b) M. Ludwig, J. Jäger, R. Niewa, R. Kniep, "Crystal Structures of Two Polymorphs of $Ca_3[Al_2N_4]$", *Inorg. Chem.* **2000**, *39*, 5909–5911; c) P. Strobel, V. Weiler, P. J. Schmidt, W. Schnick,

"$Sr[BeSi_2N_4]:Eu^{2+}/Ce^{3+}$ and $Eu[BeSi_2N_4]$: Nontypical Luminescence in Highly Condensed Nitridoberyllosilicates", *Chem. – Eur. J.* **2018**, *24*, 7243–7249.

[18] S. Wang, S. Ma, S. Liu, Z. Ye, "Facile Post-Synthesis of a $Ce^{3+}$-Doped $Ca_xSr_{1-x}Sc_2O_4$ Phosphor by Means of Cation Exchange", *ChemistrySelect* **2018**, *3*, 4387–4392.

# Appendix

# A Supporting Information – Chapter 2

## A.1 General

### Inert conditions

The weighted samples were prepared in a glove box (MBraun; $H_2O$, $O_2$ <1 ppm) filled with argon. The argon, that was used for the Schlenk line was purified over KOH, silica gel, molecular sieve (3 Å) and $P_4O_{10}$. Oxygen was removed by a BTS catalyst (170 °C). High vacuum pressures of the Schlenk line were measured to be $<7 \cdot 10^{-4}$ mbar at each work step provided by a rotary vane pump (RZ 8) by Vacuubrand.

### PXRD

The samples were measured on a Stoe Stadi P diffractometer ($\lambda$ = 1.5406 Å, Cu-K$\alpha_1$, Ge(111)-monochromator) in a parafocussing Debye-Scherrer geometry using a MYTHEN 1K Si-strip detector (Dectris, Baden, Switzerland). RIETVELD refinements were carried out with TOPAS-Academic Version 4.1.[1,2] Peak shapes were fitted using a fundamental parameter approach and the backround using a shifted Chebyshev function.[3,4]

### Visualization

RIETVELD refinements and PXRDs were visualized with Origin 6.1.[5] Crystal structures were visualized with Diamond 3k.[6]

### TDPXRD

The sample was measured on a Stoe Fixed Stage diffractometer ($\lambda$ = 0.7093 Å, Mo-K$\alpha_1$, Ge(111)-monochromator) with an IP detector (90°). This diffractometer is equipped with a graphite furnace for sample heating.

### SEM and EDX

SEM and EDX was performed on a Dualbeam Helios Nanolab G3 UC (FEI) microscope with X-Max 80 SDD detector.

### Optical microscopy

Optical microscopy was performed on a digital microscope "VHX-5000" (Keyence Microscope Europe) with the object lens VH-Z20T.

### Radio-frequency furnace

The radio-frequency furnace (TIG/100) by Trumpf Hüttinger is equipped with a pyrometer (METIS MI 3 by Sensortherm) and a water cooled reactor allowing work under inert atmosphere.

## A.2 Chemicals

**Table A.1:** List of chemicals.

| Substance | Information | Producer |
|---|---|---|
| $Ar_{(g)}$ | 99.999% | Air Liquide |
| KOH | >85% | Bernd Kraft |
| Silica gel | humidity indicator (orange gel) | VWR |
| Molecular sieve | 3 Å | Fluka |
| $P_4O_{10}$ | ≥ 99% | Carl Roth |
| BTS catalyst | operating temperature = 170 °C | Merck Millipore |
| α-$Ca_2Si_5N_8$ | commercial sample | Lumileds Development Center Aachen |
| $Sr_2Si_5N_8$ | commercial sample | Lumileds Development Center Aachen |
| $MgCl_2$ | 99.99% | Alfa Aesar |
| $CaCl_2$ | 99.99% | Alfa Aesar |

## A.3 Starting Materials α-$Ca_2Si_5N_8$ and $Sr_2Si_5N_8$

### A.3.1. α-$Ca_2Si_5N_8$

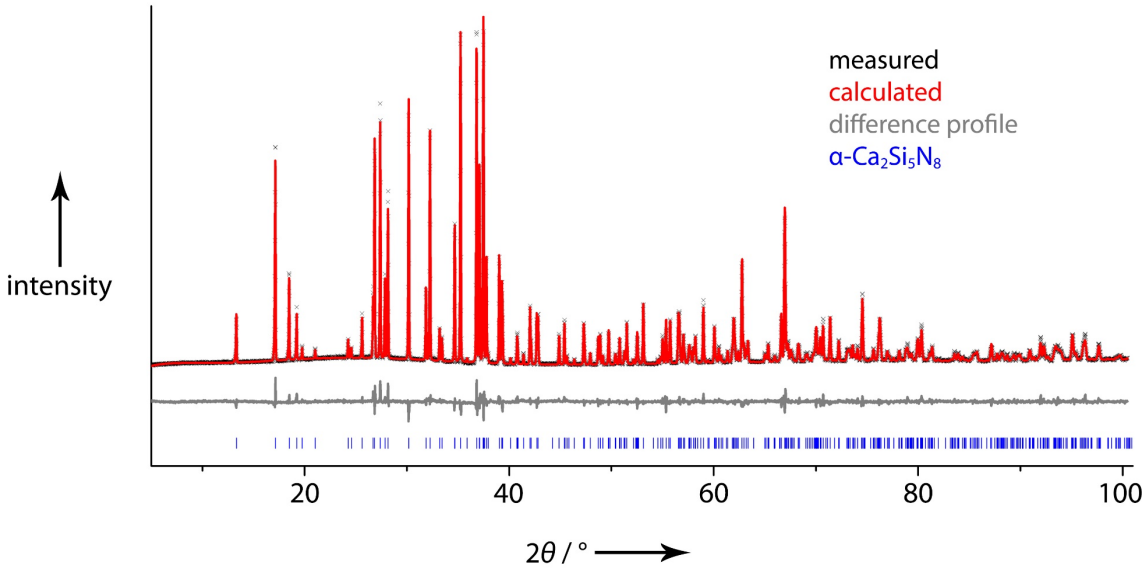


**Figure A.1:** RIETVELD refinement of α-$Ca_2Si_5N_8$.

RIETVELD refinement of α-$Ca_2Si_5N_8$ was performed using constraints for the isotropic thermal displacement parameters of silicon and nitrogen.[7]

### A.3.2. $Sr_2Si_5N_8$

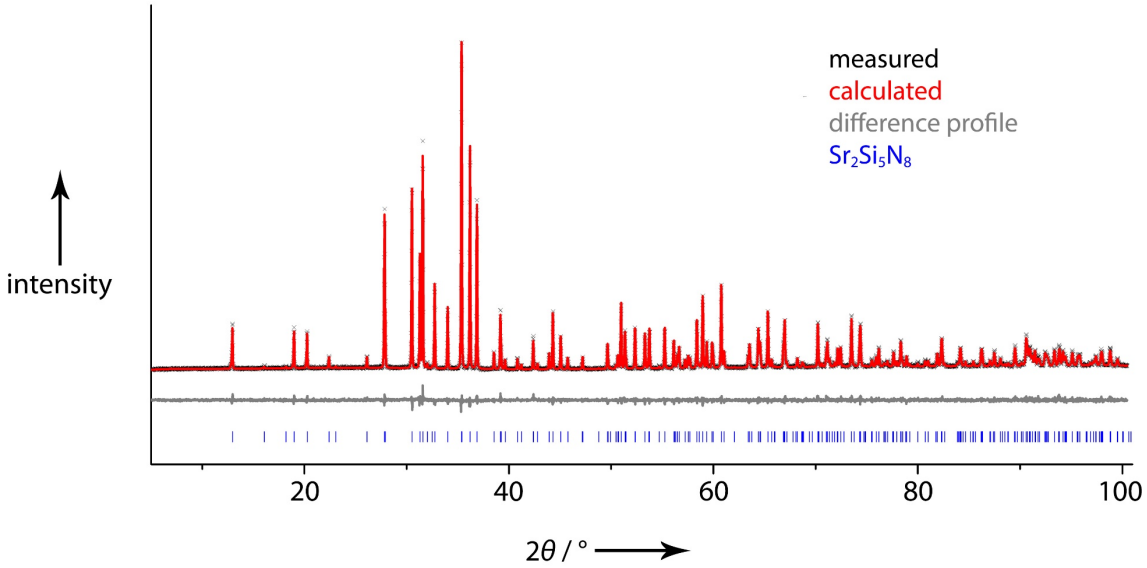


**Figure A.2:** RIETVELD refinement of $Sr_2Si_5N_8$.

RIETVELD refinement of $Sr_2Si_5N_8$ was performed with fixed isotropic thermal displacement parameters ($B_{iso}$ = 0.7) for silicon and nitrogen.[8]

**Table A.2:** Crystallographic information on the starting materials α-$Ca_2Si_5N_8$ and $Sr_2Si_5N_8$, standard deviations in parentheses.

| **Formula** | **α-$Ca_2Si_5N_8$** | **$Sr_2Si_5N_8$** |
|---|---|---|
| **Formula mass / g · mol$^{-1}$** | 301.09 | 332.64 |
| **Crystal system** | monoclinic | orthorhombic |
| **Space group** | *Cc* (no. 9) | *Pmn*2$_1$ (no. 31) |
| **Lattice parameters / Å, °** | *a* = 14.3259(2)<br>*b* = 5.61095(6)<br>*c* = 9.69254(12)<br>*β* = 112.1501(4) | *a* = 5.70871(13)<br>*b* = 6.8155(2)<br>*c* = 9.3342(2)<br>*β* = 90 |
| **Cell volume / Å$^3$** | 721.61(2) | 363.17(2) |
| ***Z*** | 4 | 2 |
| **X-ray density / g · cm$^{-3}$** | 3.06180(6) | 3.9114(2) |
| **Linear absorption coefficient / mm$^{-1}$** | 21.526 | 27.113 |
| **Radiation** | Cu-Kα$_1$ ($\lambda$ = 1.5406 Å) | |
| **Monochromator** | Ge(111) | |
| **Diffractometer** | Stoe StadiP | |
| **Detector** | MYTHEN 1K | |
| **2*θ*-range / °** | 5.010–100.470 | |
| **Temperature / °C** | 19 | |
| **Data points** | 6364 | |
| **Number of observed reflections** | 376 | 232 |
| **Number of parameters** | 78 | 56 |
| **Constraints** | 2 | 0 |
| **Program used** | TOPAS-Academic | |
| **Structure refinement** | RIETVELD-Method | |
| **Profile function** | fundamental parameters model | |
| **Backround function** | shifted Chebyshev | |
| ***R*$_{wp}$** | 5.536 | 8.839 |
| ***R*$_{exp}$** | 3.374 | 9.646 |
| ***R*$_p$** | 4.262 | 6.561 |
| ***R*$_{Bragg}$** | 2.643 | 2.125 |
| ***GOF*** | 1.641 | 0.916 |

**Table A.3:** Fractional atomic coordinates, isotropic thermal displacement parameters, and site occupancies for starting material α-$Ca_2Si_5N_8$, standard deviations in parentheses.

| Atom | Wyckoff symbol | *x* | *y* | *z* | $U_{iso}$ | Occupancy |
|---|---|---|---|---|---|---|
| Ca1 | 4*a* | 0.00000 | 0.7637 | 0.00000 | 0.0028(10) | 1 |
| Ca2 | 4*a* | 0.6114(2) | 0.7474(5) | 0.2002(3) | 0.0252(14) | 1 |
| Si1 | 4*a* | 0.0566(6) | 0.8068(4) | 0.3485(8) | 0.0068(3) | 1 |
| Si2 | 4*a* | 0.7594(4) | 0.2086(10) | 0.3238(6) | 0.0068(3) | 1 |
| Si3 | 4*a* | 0.7511(4) | 0.4970(12) | 0.0632(7) | 0.0068(3) | 1 |
| Si4 | 4*a* | 0.3656(4) | 0.2090(10) | 0.3731(6) | 0.0068(3) | 1 |
| Si5 | 4*a* | 0.8532(4) | 0.0034(11) | 0.1276(7) | 0.0068(3) | 1 |
| N1 | 4*a* | 0.9848(10) | 0.635(2) | 0.432(2) | 0.0045(7) | 1 |
| N2 | 4*a* | 0.1324(9) | 0.021(2) | 0.9976(13) | 0.0045(7) | 1 |
| N3 | 4*a* | 0.7959(5) | 0.244(2) | 0.1678(7) | 0.0045(7) | 1 |
| N4 | 4*a* | 0.8023(7) | 0.755(2) | 0.1736(8) | 0.0045(7) | 1 |
| N5 | 4*a* | 0.9858(8) | 0.008(3) | 0.2221(13) | 0.0045(7) | 1 |
| N6 | 4*a* | 0.8343(6) | 0.006(1) | 0.9365(9) | 0.0045(7) | 1 |
| N7 | 4*a* | 0.6316(10) | 0.157(2) | 0.277(2) | 0.0045(7) | 1 |
| N8 | 4*a* | 0.7972(6) | 0.478(1) | 0.4124(9) | 0.0045(7) | 1 |

**Table A.4:** Fractional atomic coordinates, isotropic thermal displacement parameters, and site occupancies for starting material $Sr_2Si_5N_8$, standard deviations in parentheses.

| Atom | Wyckoff symbol | *x* | *y* | *z* | $U_{iso}$ | Occupancy |
|---|---|---|---|---|---|---|
| Sr1 | 2*a* | 0 | 0.86945 | 0.00000 | 0.0500(9) | 1 |
| Sr2 | 2*a* | 0 | 0.8822(3) | 0.3686(2) | 0.0129(10) | 1 |
| Si1 | 4*b* | 0.2516(5) | 0.6681(4) | 0.6819(13) | 0.0089 | 1 |
| Si2 | 2*a* | 0 | 0.0564(5) | 0.679(2) | 0.0089 | 1 |
| Si3 | 2*a* | 0 | 0.4137(14) | 0.4634(13) | 0.0089 | 1 |
| Si4 | 2*a* | 0 | 0.407(2) | 0.9025(13) | 0.0089 | 1 |
| N1 | 2*a* | 0 | 0.193(3) | 0.524(3) | 0.0089 | 1 |
| N2 | 4*b* | 0.2429(12) | 0.9128(10) | 0.674(2) | 0.0089 | 1 |
| N3 | 4*b* | 0.252(2) | 0.4462(12) | 0.0081(13) | 0.0089 | 1 |
| N4 | 2*a* | 0 | 0.585(2) | 0.7736(13) | 0.0089 | 1 |
| N5 | 2*a* | 0 | 0.168(3) | 0.840(3) | 0.0089 | 1 |
| N6 | 2*a* | 0 | 0.421(2) | 0.2725(14) | 0.0089 | 1 |

## A.4 Experimental Details on the Ion Exchange Reactions

Ion exchanges were carried out in fused silica ampoules under argon atmosphere. The nitridosilicate and the metal halide were thoroughly mixed in an agar mortar and filled into a dry (high vacuum, 400 °C) silica ampoule.

**Table A.5:** Weighted samples for the ion exchanges.

| **Synthesis of $Mg_2Si_5N_8$** | | **Synthesis of β-$Ca_2Si_5N_8$** | |
|---|---|---|---|
| α-$Ca_2Si_5N_8$ | $MgCl_2$ | $Sr_2Si_5N_8$ | $CaCl_2$ |
| 500 mg | 429.4 mg | 200 mg | 112.4 mg |
| 1.50 mmol | 4.51 mmol | 0.47 mmol | 1.40 mmol |
| | | | |
| | | $Sr_{2-x}Ca_xSi_5N_8$ | $CaCl_2$ |
| | | 180.0 mg | 140.1 mg |
| | | 0.42 mmol [a] | mmol |

[a] amount of substance was calculated using the sum formula $Sr_2Si_5N_8$

**Table A.6:** Temperature program of the tube furnace for the ion exchanges.

| **Step** | **Starting *T* / °C** | **Target *T* / °C** | ***t* / h** | **Δ*T* / °C · $h^{-1}$** |
|---|---|---|---|---|
| 1 | 25 | 850 | 3 | 275 |
| 2 | 850 | 850 | 3 | 0 |
| 3 | 850 | 500 | 10 | −35 |

After the reaction the silica ampoules were opened, the product chunks were pound and washed in water to remove the metal halides. $Mg_2Si_5N_8$ was obtained as a colorless solid. β-$Ca_2Si_5N_8$ was obtained as an off-white solid. The color of β-$Ca_2Si_5N_8$ may be explainable by intrinsic strain, crystallographic defects or impurities.

## A.5 Additional Crystallographic Data for $Mg_2Si_5N_8$

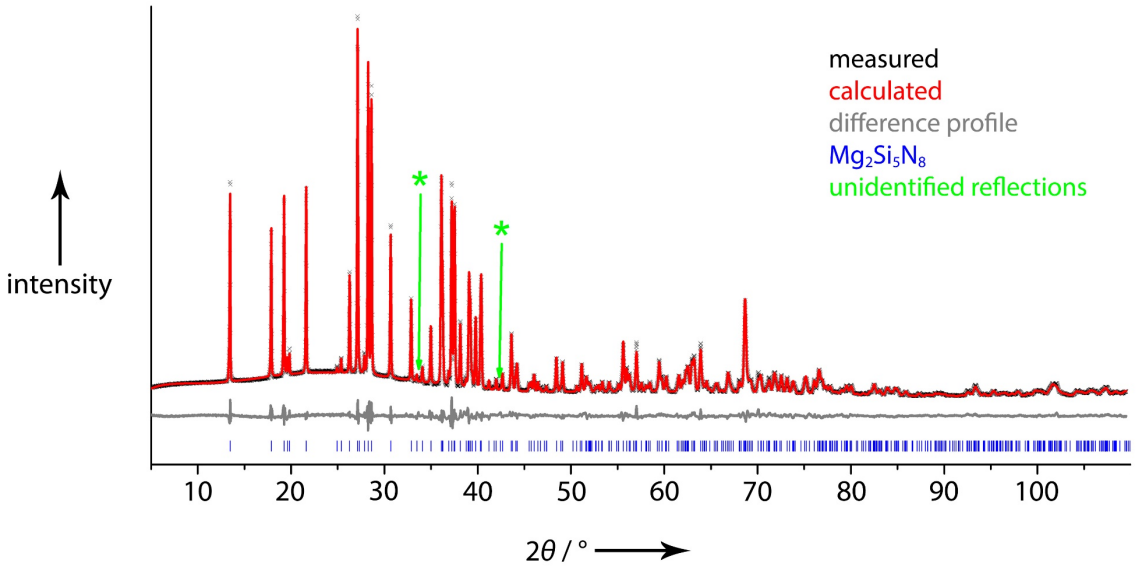


**Figure A.3:** RIETVELD refinement of $Mg_2Si_5N_8$.

RIETVELD refinement of $Mg_2Si_5N_8$ was performed with constrained isotropic thermal displacement parameters of nitrogen. The unidentified reflections may be related to a minor oxidic impurity.

**Table A.7:** Crystallographic information on $Mg_2Si_5N_8$, standard deviations in parentheses.

| **Formula** | **$Mg_2Si_5N_8$** |
|---|---|
| **Formula mass / g · mol$^{-1}$** | 301.09 |
| **Crystal system** | monoclinic |
| **Space group** | *Cc* (no. 9) |
| **Lattice parameters / Å, °** | $a$ = 14.0672(2)<br>$b$ = 5.35002(7)<br>$c$ = 9.57993(10)<br>$\beta$ = 111.0127(7) |
| **Cell volume / Å$^3$** | 673.038(15) |
| ***Z*** | 4 |
| **X-ray density / g · cm$^{-3}$** | 2.97144(6) |
| **Linear absorption coefficient / mm$^{-1}$** | 11.562 |
| **Radiation** | Cu-K$\alpha_1$ ($\lambda$ = 1.540598 Å) |
| **Monochromator** | Ge(111) |
| **Diffractometer** | Stoe StadiP |
| **Detector** | MYTHEN 1K |
| **2$\theta$-range / °** | 5.000–109.505 |
| **Temperature / °C** | 20 |
| **Data points** | 6968 |
| **Number of observed reflections** | 424 |
| **Number of parameters** | 83 |
| **Constraints** | 1 |
| **Program used** | TOPAS-Academic |
| **Structure refinement** | RIETVELD-Method |
| **Profile function** | fundamental parameters model |
| **Backround function** | shifted Chebyshev |
| ***R*$_{wp}$** | 4.756 |
| ***R*$_{exp}$** | 1.712 |
| ***R*$_{p}$** | 3.576 |
| ***R*$_{Bragg}$** | 1.675 |
| ***GOF*** | 2.779 |

**Table A.8:** List of interatomic distances / Å and bond angles / ° for $Mg_2Si_5N_8$, standard deviations in parentheses.

| Distances | | | | Angles | |
|---|---|---|---|---|---|
| Mg1–N1 | 1.957(10) | Si3–N2 | 1.612(12) | Si1–N1–Si4 | 112.9(7) |
| Mg1–N2 | 2.189(8) | Si3–N3 | 1.726(10) | | |
| Mg1–N6 | 2.566(10) | Si3–N4 | 1.743(10) | Si1–N2–Si3 | 123.4(8) |
| Mg1–N7 | 2.649(12) | Si3–N8 | 1.80(2) | | |
| Mg1–N5a | 2.708(11) | | | Si1–N5–Si5 | 118.6(6) |
| Mg1–N5b | 2.742(10) | Si4–N1 | 1.653(13) | | |
| | | Si4–N8 | 1.679(13) | Si1–N7–Si2 | 115.7(6) |
| Mg2–N5 | 1.962(12) | Si4–N6 | 1.786(10) | | |
| Mg2–N2 | 2.038(12) | Si4–N4 | 1.799(12) | Si2–N3–Si3 | 113.3(7) |
| Mg2–N7 | 2.146(11) | | | Si2–N3–Si5 | 116.8(6) |
| Mg2–N1 | 2.417(13) | Si5–N4 | 1.667(12) | Si3–N3–Si5 | 129.1(8) |
| | | Si5–N3 | 1.713(13) | | |
| Si1–N7 | 1.68(2) | Si5–N5 | 1.730(12) | Si2–N6–Si4 | 118.3(6) |
| Si1–N2 | 1.714(10) | Si5–N6 | 1.78(2) | Si2–N6–Si5 | 115.0(7) |
| Si1–N1 | 1.80(2) | | | Si4–N6–Si5 | 114.8(6) |
| Si1–N5 | 1.821(10) | | | | |
| | | | | Si3–N4–Si4 | 115.0(6) |
| Si2–N8 | 1.692(10) | | | Si3–N4–Si5 | 131.2(7) |
| Si2–N3 | 1.759(15) | | | Si4–N4–Si5 | 112.4(5) |
| Si2–N6 | 1.781(10) | | | | |
| Si2–N7 | 1.807(14) | | | Si2–N8–Si3 | 113.0(7) |
| | | | | Si2–N8–Si4 | 123.0(9) |
| | | | | Si3–N8–Si4 | 119.8(6) |

**Table A.9:** Fractional atomic coordinates, isotropic thermal displacement parameters, and site occupancies for $Mg_2Si_5N_8$, standard deviations in parentheses.

| Atom | Wyckoff symbol | *x* | *y* | *z* | $U_{iso}$ | Occupancy |
|---|---|---|---|---|---|---|
| Si1 | 4*a* | 0.0431(6) | 0.7728(5) | 0.3616(9) | 0.0154(9) | 1 |
| Si2 | 4*a* | 0.7399(5) | 0.1918(8) | 0.3235(9) | 0.0113(12) | 1 |
| Si3 | 4*a* | 0.7298(6) | 0.4971(11) | 0.0669(9) | 0.0105(12) | 1 |
| Si4 | 4*a* | 0.3454(5) | 0.1814(7) | 0.3759(9) | 0.0086(12) | 1 |
| Si5 | 4*a* | 0.8498(6) | 0.9972(9) | 0.1347(10) | 0.0080(11) | 1 |
| Mg1 | 4*a* | 0.00000 | 0.76370 | 0.00000 | 0.096(3) | 1 |
| Mg2 | 4*a* | 0.5642(4) | 0.7531(7) | 0.1680(7) | 0.0096(12) | 1 |
| N1 | 4*a* | 0.9636(8) | 0.577(2) | 0.4262(15) | 0.0094(7) | 1 |
| N2 | 4*a* | 0.1104(7) | 0.0623(13) | 1.0195(11) | 0.0094(7) | 1 |
| N3 | 4*a* | 0.7703(7) | 0.219(2) | 0.1612(10) | 0.0094(7) | 1 |
| N4 | 4*a* | 0.7985(6) | 0.742(2) | 0.1780(9) | 0.0094(7) | 1 |
| N5 | 4*a* | 0.9796(8) | 1.021(2) | 0.2311(11) | 0.0094(7) | 1 |
| N6 | 4*a* | 0.8344(8) | 0.012(2) | 0.9427(12) | 0.0094(7) | 1 |
| N7 | 4*a* | 0.6073(9) | 0.110(2) | 0.2743(14) | 0.0094(7) | 1 |
| N8 | 4*a* | 0.7619(8) | 0.480(2) | 0.4019(13) | 0.0094(7) | 1 |

## A.6 Comparison Between $Mg_2Si_5N_8$ and α-$Ca_2Si_5N_8$

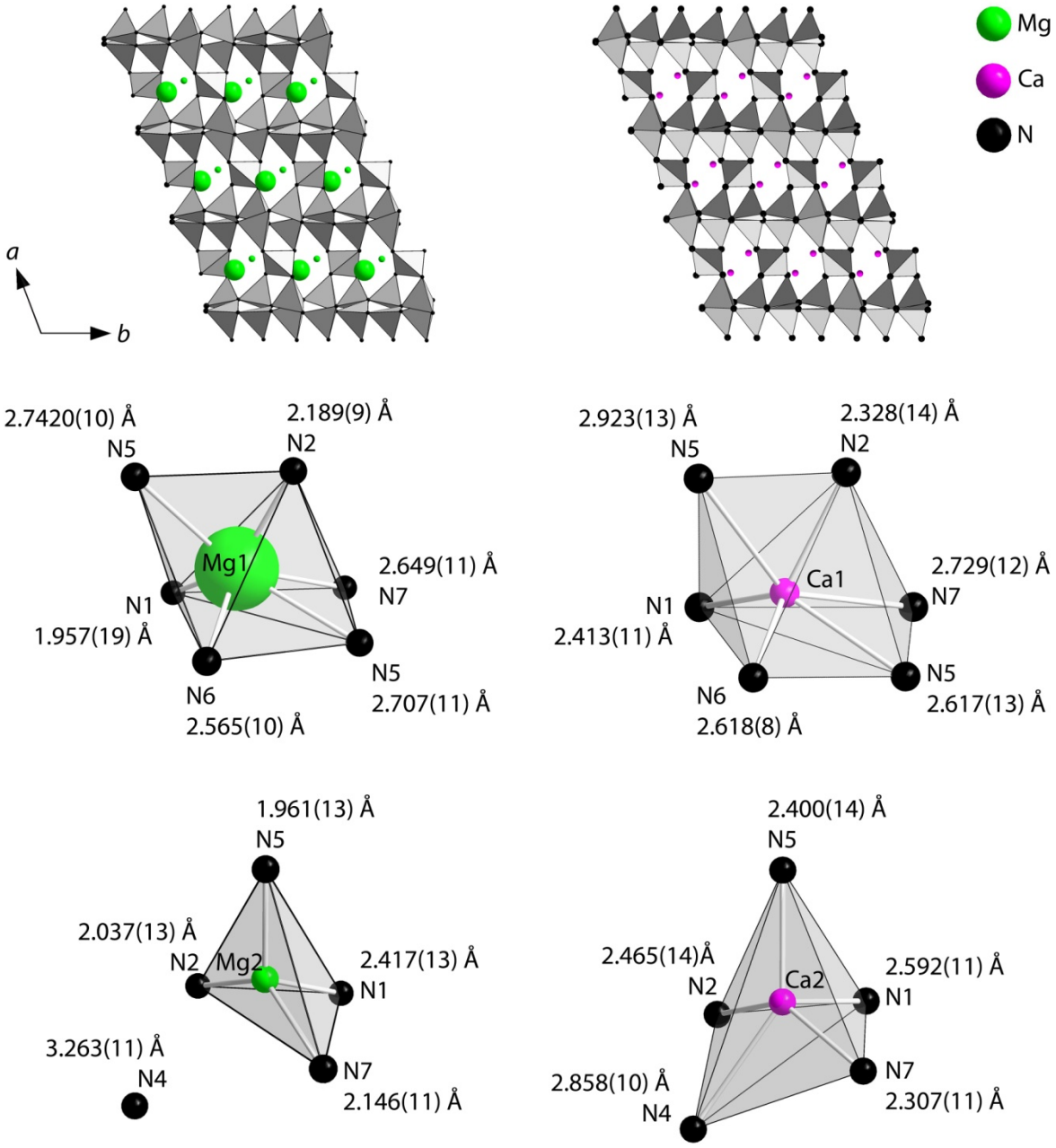


**Figure A.4:** Crystal structures along *b* (top), coordination spheres of the cations (middle and bottom) of $Mg_2Si_5N_8$ (left) and α-$Ca_2Si_5N_8$ (right; RIETVELD refinement of the starting material). The atoms are displayed with isotropic displacement parameters (90% probability).

The magnesium cations differ in its atomic displacement parameters (Table A.9) due to the space provided by the coordination spheres leading to larger values for Mg1 than for Mg2.

## A.7 Additional Crystallographic Data for β-$Ca_2Si_5N_8$

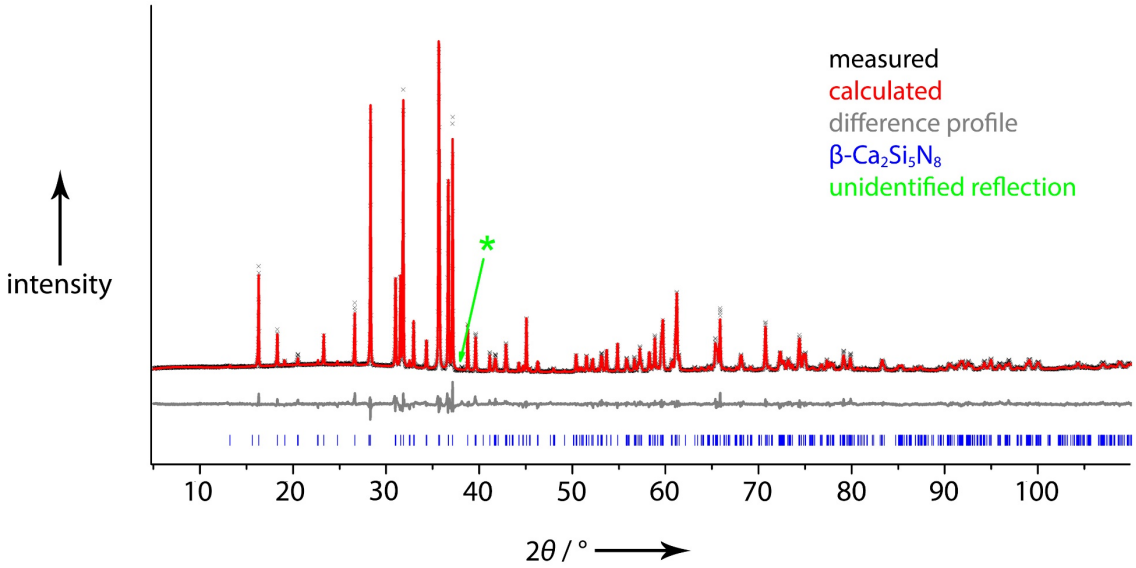


**Figure A.5:** RIETVELD refinement of β-$Ca_2Si_5N_8$.

RIETVELD refinement of β-$Ca_2Si_5N_8$ was performed with constrained isotropic thermal displacement parameters of nitrogen. One Reflection of the PXRD (Figure A.5) which could not be assigned to β-$Ca_2Si_5N_8$ may refer to a minor impurity. This impurity might explain the off-white color of the sample.

**Table A10:** Crystallographic information on β-$Ca_2Si_5N_8$, standard deviations in parantheses.

| **Formula** | **β-$Ca_2Si_5N_8$** |
|---|---|
| **Formula mass / g · mol$^{-1}$** | 332.64 |
| **Crystal system** | monoclinic |
| **Space group** | $P2_1$ (no. 4) |
| **Lattice parameters / Å, °** | $a$ = 5.66713(12)<br>$b$ = 9.2818(2)<br>$c$ = 6.6889(2)<br>$\beta$ = 90.1164(10) |
| **Cell volume / Å$^3$** | 351.843(13) |
| ***Z*** | 2 |
| **X-ray density / g · cm$^{-3}$** | 3.13978(12) |
| **Linear absorption coefficient / mm$^{-1}$** | 22.075 |
| **Radiation** | Cu-K$\alpha_1$ ($\lambda$ = 1.540598 Å) |
| **Monochromator** | Ge(111) |
| **Diffractometer** | Stoe StadiP |
| **Detector** | MYTHEN 1K |
| **2$\theta$-range / °** | 5.000–110.510 |
| **Temperature / °C** | 20 |
| **Data points** | 7035 |
| **Number of observed reflections** | 486 |
| **Number of parameters** | 80 |
| **Constraints** | 1 |
| **Program used** | TOPAS-Academic |
| **Structure refinement** | RIETVELD-Method |
| **Profile function** | fundamental parameters model |
| **Backround function** | shifted Chebyshev |
| ***$R_{wp}$*** | 6.221 |
| ***$R_{exp}$*** | 2.782 |
| ***$R_p$*** | 4.553 |
| ***$R_{Bragg}$*** | 2.499 |
| ***GOF*** | 2.237 |

**Table A.11:** List of interatomic distances / Å and bond angles / ° for β-$Ca_2Si_5N_8$, standard deviations in parentheses.

| Distances | | | | Angles | |
|---|---|---|---|---|---|
| Ca1–N5 | 2.495(12) | Si12–N22 | 1.652(14) | Si2–N1–Si3 | 135.4(10) |
| Ca1–N22 | 2.596(14) | Si12–N4 | 1.69(2) | | |
| Ca1–N1 | 2.614(14) | Si12–N32 | 1.70(2) | Si11–N21–Si2 | 121.7(9) |
| Ca1–N4 | 2.803(12) | Si12–N6 | 1.83(2) | Si12–N22–Si2 | 125.5(8) |
| Ca1–N21 | 2.828(14) | | | | |
| Ca1–N21 | 3.021(14) | Si2–N5 | 1.64(2) | Si2–N5–Si4 | 134.3(9) |
| Ca1–N1 | 3.121(14) | Si2–N22 | 1.708(14) | | |
| | | Si2–N21 | 1.73(2) | Si11–N31–Si3 | 121.6(11) |
| Ca2–N21 | 2.349(14) | Si2–N1 | 1.75(2) | Si11–N31–Si4 | 117.2(9) |
| Ca2–N1 | 2.369(15) | | | Si3–N31–Si4 | 120.2(11) |
| Ca2–N22 | 2.592(14) | Si3–N1 | 1.558(14) | | |
| Ca2–N5 | 2.75(2) | Si3–N6 | 1.738(12) | Si12–N32–Si3 | 117.8(10) |
| Ca2–N31 | 2.99(2) | Si3–N31 | 1.78(2) | Si12–N32–Si4 | 121.7(10) |
| Ca2–N5 | 3.02(2) | Si3–N32 | 1.84(2) | Si3–N32–Si4 | 120.5(12) |
| | | | | | |
| Si11–N31 | 1.67(2) | Si4–N4 | 1.570(14) | Si11–N6–Si12 | 106.4(7) |
| Si11–N6 | 1.70(2) | Si4–N32 | 1.73(2) | Si11–N6–Si3 | 122.2(11) |
| Si11–N21 | 1.70(2) | Si4–N31 | 1.81(2) | Si12–N6–Si3 | 114.6(11) |
| Si11–N4 | 1.94(2) | Si4–N5 | 1.818(13) | | |
| | | | | Si11–N4–Si12 | 102.9(7) |
| | | | | Si11–N4–Si4 | 120.6(12) |
| | | | | Si12–N4–Si4 | 134.5(13) |
| | | | | Si2–N1–Si3 | 135.4(10) |

**Table A.12:** Fractional atomic coordinates, isotropic thermal displacement parameters, and site occupancies for $Mg_2Si_5N_8$, standard deviations in parentheses.

| Atom | Wyckoff symbol | *x* | *y* | *z* | $U_{iso}$ | Occupancy |
|---|---|---|---|---|---|---|
| Ca1 | 2*a* | 0.25000 | 0.00000 | 0.86945 | 0.047(2) | 1 |
| Ca2 | 2*a* | 0.2463(10) | 0.3666(4) | 0.9061(5) | 0.0095(9) | 1 |
| Si11 | 2*a* | 0.5034(9) | 0.6798(11) | 0.6682(8) | 0.021(2) | 1 |
| Si12 | 2*a* | 0.0016(8) | 0.6827(11) | 0.6680(8) | 0.014(2) | 1 |
| Si2 | 2*a* | 0.2516(12) | 0.6740(8) | 0.0614(5) | 0.0137(10) | 1 |
| Si3 | 2*a* | 0.251(2) | 0.4611(8) | 0.4110(7) | 0.0077(14) | 1 |
| Si4 | 2*a* | 0.247(2) | 0.9044(7) | 0.4146(8) | 0.0143(14) | 1 |
| N1 | 2*a* | 0.205(3) | 0.514(2) | 0.193(2) | 0.0175(11) | 1 |
| N21 | 2*a* | 0.497(3) | 0.7135(14) | 0.918(2) | 0.0175(11) | 1 |
| N22 | 2*a* | 1.005(2) | 0.672(2) | 0.915(2) | 0.0175(11) | 1 |
| N31 | 2*a* | 0.510(3) | 0.015(2) | 0.432(2) | 0.0175(11) | 1 |
| N32 | 2*a* | 1.006(3) | 0.017(2) | 0.439(2) | 0.0175(11) | 1 |
| N4 | 2*a* | 0.226(4) | 0.7836(12) | 0.578(2) | 0.0175(11) | 1 |
| N5 | 2*a* | 0.278(3) | 0.834(2) | 0.162(2) | 0.0175(11) | 1 |
| N6 | 2*a* | 0.264(4) | 0.2742(10) | 0.422(2) | 0.0175(11) | 1 |

## A.8 Comparison Between β-$Ca_2Si_5N_8$ and $Sr_2Si_5N_8$

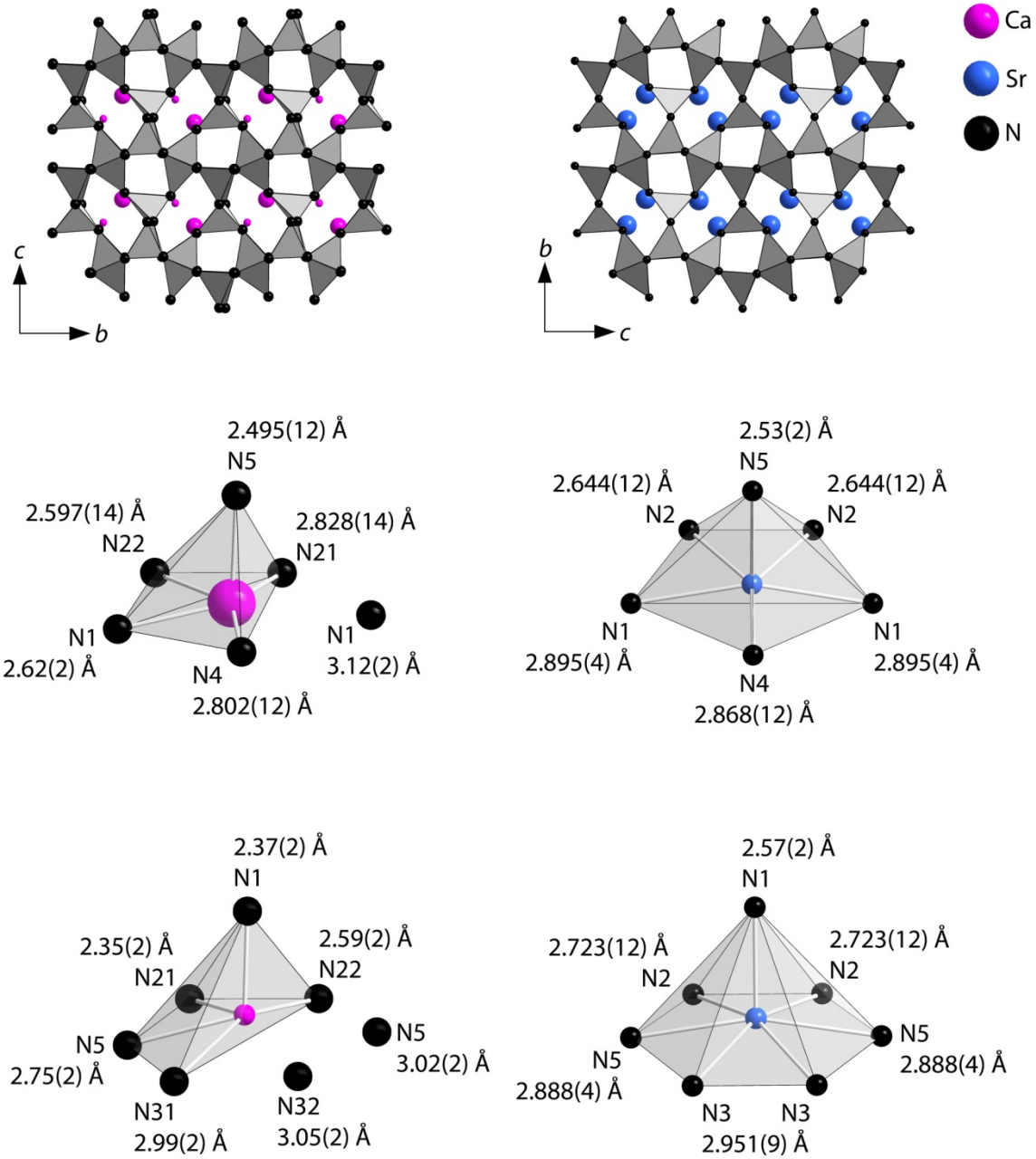


**Figure A.6:** Crystal structures along b (top), coordination spheres of the cations (middle and bottom) of $Mg_2Si_5N_8$ (left) and α-$Ca_2Si_5N_8$ (right; RIETVELD refinement of the starting material). The atoms are displayed with isotropic displacement parameters (90% probability).

The calcium cations differ in its atomic displacement parameters (Table A.12) due to the space provided by the coordination spheres leading to larger values for Ca1 than for Ca2.

## A.9 Optical Microscopy


**Figure A.7:** Optical micrograph of a $Mg_2Si_5N_8$ powder sample.

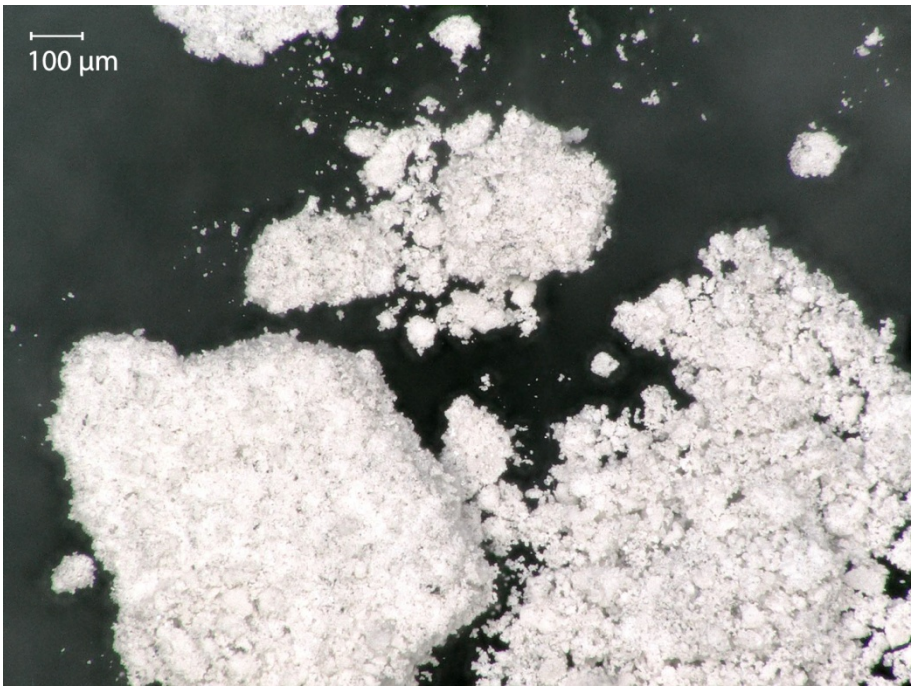


**Figure A.8:** Optical micrograph of a β-$Ca_2Si_5N_8$ powder sample.

## A.10 Details on SEM and EDX

### A.10.1. $Mg_2Si_5N_8$

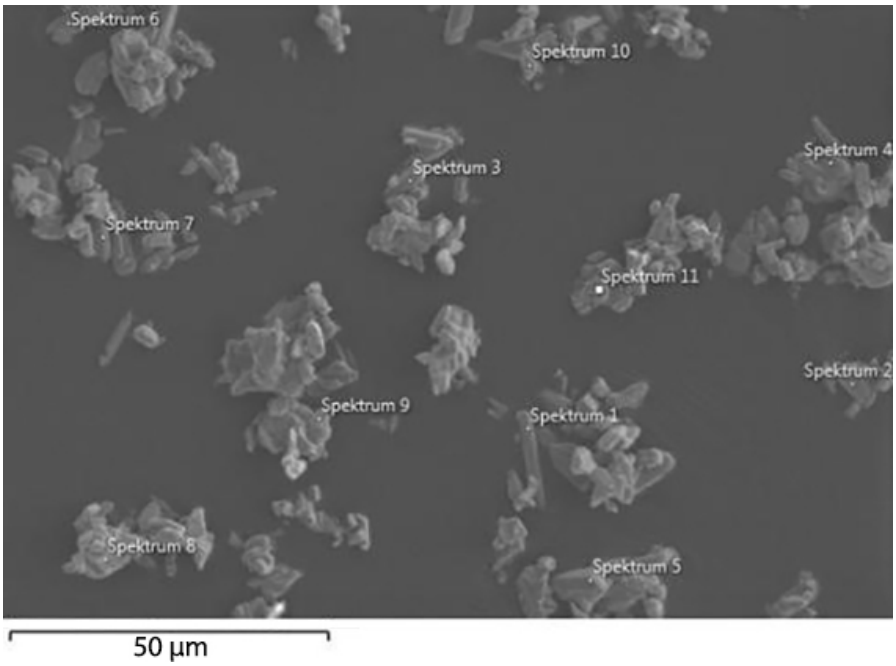


**Figure A.9:** Scanning electron micrograph of a $Mg_2Si_5N_8$ powder sample.

**Table A.13:** EDX analysis of $Mg_2Si_5N_8$ powder shown in Figure A.9.

| | Spektrum 1 | Spektrum 2 | Spektrum 3 | Spektrum 4 | Spektrum 5 | Spektrum 6 |
|---|---|---|---|---|---|---|
| **N** | 51.6 | 47.9 | 41.4 | 45.1 | 46.5 | 44.2 |
| **O** | 1.6 | 1.9 | 2.1 | 3.5 | 2.0 | 9.6 |
| **Mg** | 13.2 | 14.2 | 15.8 | 14.4 | 14.4 | 13.1 |
| **Si** | 33.6 | 36.1 | 40.7 | 36.3 | 37.1 | 33.1 |
| | | | | Al 0.7 | | |
| **Mg/Si** | 2/5.1 | 2/5.1 | 2/5.2 | 2/5.1 | 2/5.2 | 2/5.1 |
| | **Spektrum 7** | **Spektrum 8** | **Spektrum 9** | **Spektrum 10** | **Spektrum 11** | **Theoretical** |
| **N** | 46.5 | 47.0 | 27.2 | 46.6 | 1.3 | 53.33 |
| **O** | 2.2 | 6.6 | 19.6 | 1.7 | 38.4 | 0 |
| **Mg** | 14.4 | 13.0 | 14.7 | 14.3 | 39.3 | 13.33 |
| **Si** | 36.9 | 33.4 | 38.5 | 37.4 | 21.0 | 33.33 |
| **Mg/Si** | 2/5.1 | 2/5.1 | 2/5.2 | 2/5.2 | 2/1.1 | 2/5 |

The oxygen contents of Spektrum 1–10 are explainable by surface oxidation. Spektrum 11 may refer to the minor impurity visible in the PXRD (Figure A.3).

## A.10.2. β-$Ca_2Si_5N_8$

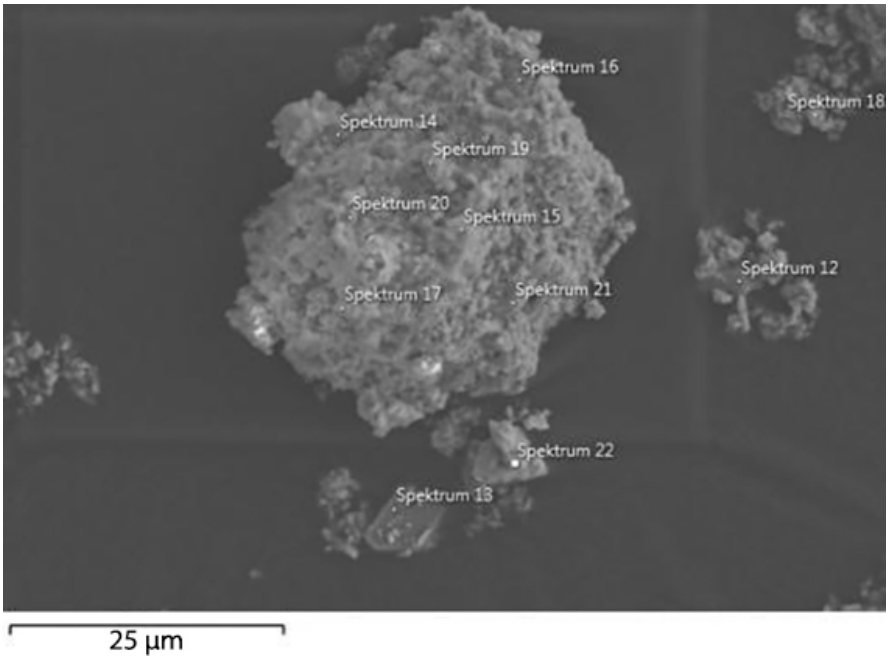


**Figure A.10:** Scanning electron micrograph of a $Mg_2Si_5N_8$ powder sample.

**Table A.14:** EDX analysis of β-$Ca_2Si_5N_8$ powder shown in Figure A.10.

| | **Spektrum 12** | **Spektrum 13** | **Spektrum 14** | **Spektrum 15** | **Spektrum 16** | **Spektrum 17** |
|---|---|---|---|---|---|---|
| **N** | 50.4 | 53.5 | 42.2 | 56.4 | 37.8 | 40.1 |
| **O** | 1.3 | 1.8 | 1.0 | 2.5 | 3.9 | 8.4 |
| **Si** | 34.6 | 32.3 | 40.7 | 29.6 | 40.8 | 36.1 |
| **Ca** | 13.7 | 12.4 | 16.1 | 11.5 | 17.4 | 15.3 |
| | | | | | | Na 0.2 |
| **Ca/Si** | 2/5.1 | 2/5.2 | 2/5.1 | 2/5.1 | 2/4.7 | 2/4.7 |
| | **Spektrum 18** | **Spektrum 19** | **Spektrum 20** | **Spektrum 21** | **Spektrum 22** | **Theoretical** |
| **N** | 58.7 | 53.1 | 55.7 | 41.8 | 63.8 | 53.33 |
| **O** | 5.0 | 2.3 | 1.7 | 5.5 | 3.1 | 0 |
| **Si** | 26.0 | 32.1 | 30.9 | 37.3 | 23.9 | 33.33 |
| **Ca** | 10.4 | 12.5 | 11.8 | 15.3 | 9.2 | 13.33 |
| | | | | Cl 0.2 | | |
| **Ca/Si** | 2/5 | 2/5.1 | 2/5.2 | 2/4.9 | 2/5.2 | 2/5 |

The oxygen contents of Spektrum 12–22 are explainable by surface oxidation. No impurities explaining the off-white color of β-$Ca_2Si_5N_8$ or the unidentified reflection in Figure A.5 were found in EDX.

## A.11 Details on ICP-OES

**Table A.15:** ICP-OES analysis of $Mg_2Si_5N_8$ and β-$Ca_2Si_5N_8$ powder samples.

| $Mg_2Si_5N_8$ | | β-$Ca_2Si_5N_8$ | |
|---|---|---|---|
| **Mg** | 173.88 mg · $g^{-1}$ | **Ca** | 213.88 mg · $g^{-1}$ |
| **Si** | 519.05 mg · $g^{-1}$ | **Si** | 431.28 mg · $g^{-1}$ |
| **Ca** | 4,16 mg · $g^{-1}$ | **Sr** | 0.34 mg · $g^{-1}$ |
| **Mg/Si** | 2/5.2 | **Ca/Si** | 2/5.7 |

The experimental values of ICP-OES for $Mg_2Si_5N_8$ and β-$Ca_2Si_5N_8$ are in agreement with the theoretical composition of the compounds. The divergences in the ratios Mg/Si for $Mg_2Si_5N_8$ and Ca/Si for β-$Ca_2Si_5N_8$ indicate minor side phases. These impurities could belong to the unidentified reflections in Figures A.3 and A.5. In case of β-$Ca_2Si_5N_8$ the side phase(s) could explain the off-white color.

## A.12 Details on TDPXRD

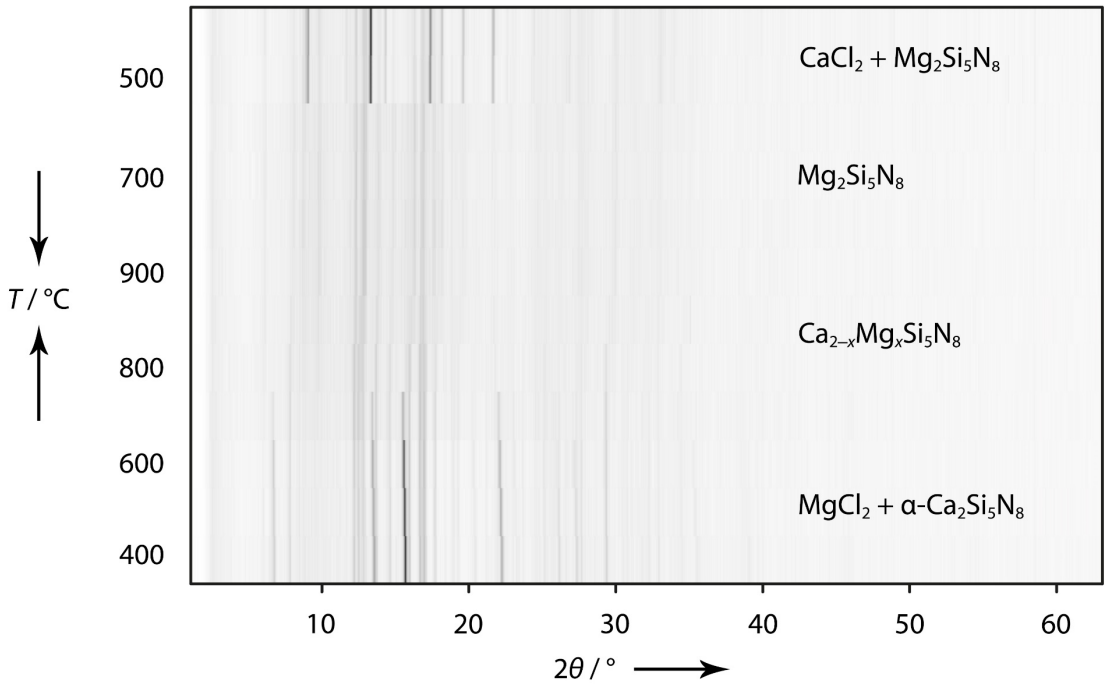


**Figure A.11:** *In situ* investigation on the ion exchange by TDPXRD.

**Table A.16:** Temperature program for the TDPXRD measurements.

| Step | Starting $T$ / °C | Target $T$ / °C | $t$ / min | $\Delta T$ / °C · min$^{-1}$ | XRD |
|---|---|---|---|---|---|
| 1 | 400 | 400 | 10 | 0 | ✓ |
| 2 | 400 | 500 | 20 | 5 | × |
| 3 | 500 | 500 | 10 | 0 | ✓ |
| 4 | 500 | 600 | 20 | 5 | × |
| 5 | 600 | 600 | 10 | 0 | ✓ |
| 6 | 600 | 700 | 20 | 5 | × |
| 7 | 700 | 700 | 10 | 0 | ✓ |
| 8 | 700 | 800 | 20 | 5 | × |
| 9 | 800 | 800 | 10 | 0 | ✓ |
| 10 | 800 | 900 | 20 | 5 | × |
| 11 | 900 | 900 | 10 | 0 | ✓ |
| 12 | 900 | 900 | 30 | 0 | × |
| 13 | 900 | 900 | 10 | 0 | ✓ |
| 14 | 900 | 800 | 20 | −5 | × |
| 15 | 800 | 800 | 10 | 0 | ✓ |
| 16 | 800 | 700 | 20 | −5 | × |
| 17 | 700 | 700 | 10 | 0 | ✓ |
| 18 | 700 | 600 | 20 | −5 | × |
| 19 | 600 | 600 | 10 | 0 | ✓ |
| 20 | 600 | 500 | 20 | −5 | × |
| 21 | 500 | 500 | 10 | 0 | ✓ |
| 22 | 500 | 400 | 20 | −5 | × |
| 23 | 400 | 400 | 10 | 0 | ✓ |

## A.13 Details on the HT Investigations on $Mg_2Si_5N_8$ and β-$Ca_2Si_5N_8$

Samples of $Mg_2Si_5N_8$ and β-$Ca_2Si_5N_8$ were filled into tungsten crucibles. The crucibles were put into a radio-frequency furnace under nitrogen atmosphere and the temperature program shown in Table A.17 was started. After the treatment colorless solids were obtained and analyzed by PXRD. The measurements of the decomposition product $Si_3N_4$ as well as the transformation product α-$Ca_2Si_5N_8$ are shown in Figures A.12 and A.13.

**Table A.17:** Temperature program of the radio-frequency furnace for the HT investigations of $Mg_2Si_5N_8$ and β-$Ca_2Si_5N_8$.

| Step | Starting $T$ / °C | Target $T$ / °C | $t$ / h | $\Delta T$ / °C · h$^{-1}$ |
|---|---|---|---|---|
| 1 | 25 | 1500 | 5 | 295 |
| 2 | 1500 | 1500 | 1 | 0 |
| 3 | 1500 | 500 | 5 | −200 |

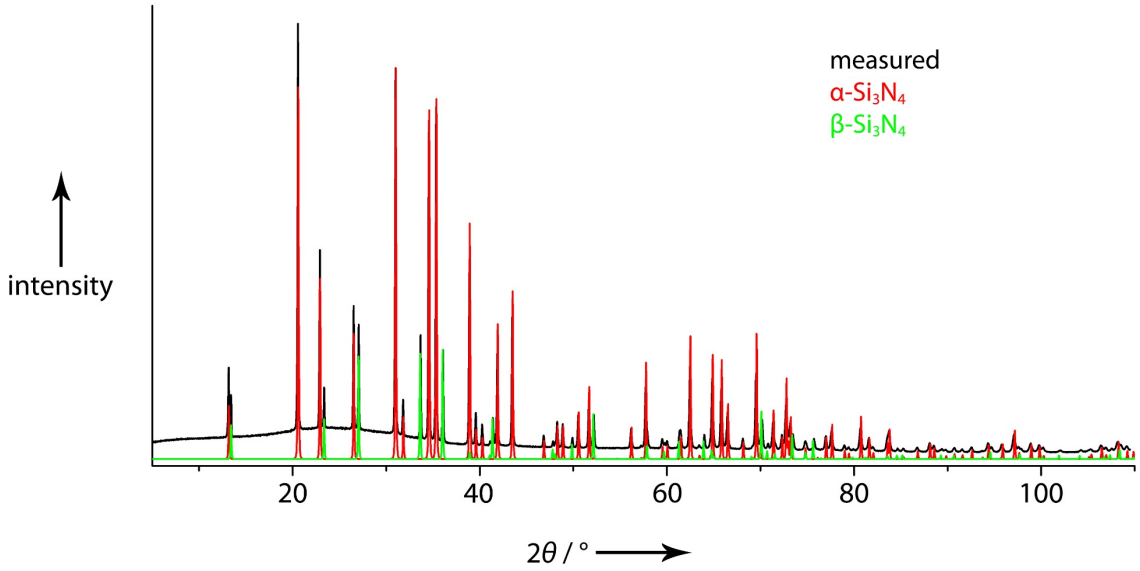


**Figure A.12:** PXRD of the $Mg_2Si_5N_8$ decomposition product (black) with references for α-$Si_3N_4$ (red) and β-$Si_3N_4$ (green).[9]

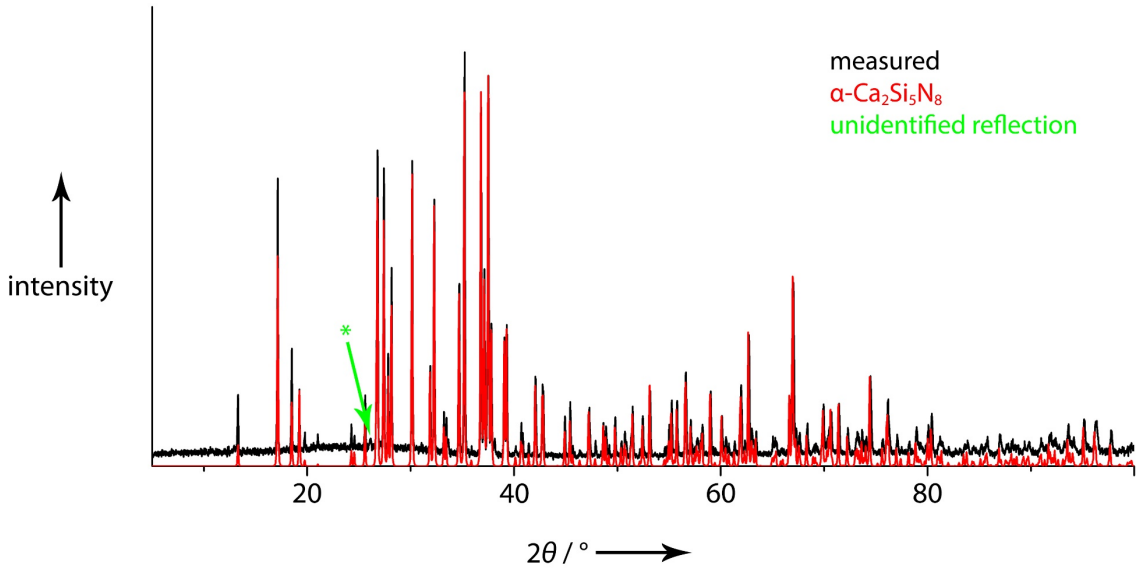


**Figure A.13:** PXRD of β-$Ca_2Si_5N_8$ transformation product (black) with reference for α-$Ca_2Si_5N_8$ (red).[7]

## A.14 References


[1] H. M. Rietveld, "A Profile Refinement Method for Nuclear and Magnetic Structures", *J. Appl. Crystallogr.* **1969**, *2*, 65–71.

[2] A. A. Coelho, *TOPAS-Academic*, Version 4.1, Coelho Software, Brisbane (Australia), **2007**.

[3] R. W. Cheary, A. Coelho, "A Fundamental Parameters Approach to X-Ray Line-Profile Fitting", *J. Appl. Crystallogr.* **1992**, *25*, 109–121.

[4] R. W. Cheary, A. A. Coelho, J. P. Cline, "Fundamental Parameters Line Profile Fitting in Laboratory Diffractometers", *J. Res. Natl. Inst. Stand. Technol.* **2004**, *109*, 1–25.

[5] *Origin 6.1*, OriginLab Corporation, **1991–2000**.

[6] K. Brandenburg, *Diamond Version 3.2k*, **2014**.

[7] T. Schlieper, W. Schnick, "Nitrido-Silicate. I Hochtemperatur-Synthese und Kristallstruktur von $Ca_2Si_5N_8$", *Z. Anorg. Allg. Chem.* **1995**, *621*, 1037–1041.

[8] T. Schlieper, W. Milius, W. Schnick, "Nitrido-silicate. II Hochtemperatur-Synthesen und Kristallstrukturen von $Sr_2Si_5N_8$ und $Ba_2Si_5N_8$", *Z. Anorg. Allg. Chem.* **1995**, *621*, 1380–1384.

[9] D. Hardie, K. H. Jack, "Crystal Structures of Silicon Nitride", *Nature* **1957**, *180*, 332–333.

# B Supporting Information – Chapter 3

## B.1 General

### Inert conditions

The weighted samples were prepared in a glove box (MBraun; $H_2O$, $O_2$ <1 ppm) filled with argon. The argon, that was used for the Schlenk line was purified over KOH, silica gel, molecular sieve (3 Å) and $P_4O_{10}$. Oxygen was removed by a BTS catalyst (170 °C). High vacuum pressures of the Schlenk line were measured to be $<7 \cdot 10^{-4}$ mbar at each work step provided by a rotary vane pump (RZ 8) by Vacuubrand.

### PXRD

The samples were measured on a Stoe Stadi P diffractometer ($\lambda$ = 0.7093 Å, Mo-K$\alpha_1$ with Ge(111)-monochromator) in a parafocussing Debye-Scherrer geometry using a MYTHEN 1K Si-strip detector (Dectris, Baden, Switzerland). RIETVELD refinements were carried out with TOPAS-Academic Version 4.1.[1,2] Peak shapes were fitted using a fundamental parameters approach and the background using a shifted Chebyshev function.[3,4]

### Visualization

RIETVELD refinements and PXRDs were visualized with Origin 6.1.[5] Crystal structures were visualized with Diamond 3k.[6]

### TDPXRD

The reaction mixture was measured on a Stoe Fixed Stage diffractometer ($\lambda$ = 0.7093 Å, Mo-K$\alpha_1$, Ge(111)-monochromator) with an IP detector (90°). The diffractometer was equipped with a graphite furnace for sample heating.

### HR-TDPXRD

α-$Ca_2Si_5N_8$ has been measured on a Stoe StadiP diffractometer equipped with a MYTHEN2 1K detector and a graphite furnace for sample heating.

### SEM and EDX

Scanning electron microscopy and EDX was performed on a Dualbeam Helios Nanolab G3 UC (FEI) microscope with X-Max 80 SDD detector.

### Optical microscopy

Optical microscopy was performed on a digital microscope "VHX-5000" (Keyence Microscope Europe) with the object lens VH-Z20T.

### Radio-frequency furnace

The radio-frequency furnace (TIG/100) by Trumpf Hüttinger is equipped with a pyrometer (METIS MI 3 by Sensortherm) and a water cooled reactor allowing work under inert atmosphere.

### TGA/DSC

Measurements have been performed on a NETZSCH STA ***F3 Jupiter***® device for thermal analysis in a platinum crucible under nitrogen atmosphere. The device is equipped with a rhodium furnace for sample heating.

### Mößbauer spectroscopy

A $^{57}$Co/Rh source was used for the Mößbauer spectroscopic experiments, which were conducted in transmission geometry. The measurements were conducted in a continuous flow cryostat system (Janis Research Co LLC) at 6 K, 78 K, and 20 °C. The temperature was controlled by a resistance thermometer (±0.5 °C accuracy). The samples were enclosed in small PVC containers at a thickness corresponding to about 20 mg Mößbauer active element per cm$^2$. The spectra were fitted with the Normos-90 software package.[7]

### Magnetic property measurements

The powdered samples of $Fe_{1.6}Ca_{0.4}Si_5N_8$ and $Fe_2Si_5N_8$ were packed into polyethylene (PE) capsules and attached to the sample holder rod of a Vibrating Sample Magnetometer unit (VSM) for measuring the magnetization $M(T,H)$ in a Quantum Design PPMS. The samples were investigated in the temperature range of 2.5 K until 27 °C with magnetic flux densities up to 80 kOe.

## B.2 Chemicals

**Table B.1:** List of chemicals for this work.

| Substance | Information | Producer |
|---|---|---|
| $Ar_{(g)}$ | 99.999% | Air Liquide |
| KOH | >85% | Bernd Kraft |
| Silica gel | humidity indicator (orange gel) | VWR |
| Molecular sieve | 3 Å | Fluka |
| $P_4O_{10}$ | ≥ 99% | Carl Roth |
| BTS catalyst | operating temperature = 170 °C | Merck Millipore |
| α-$Ca_2Si_5N_8$ | commercial sample | Lumileds Development Center Aachen |
| $FeCl_2$ | 99.99% | Alfa Aesar |
| $HCl_{(aq)}$ | 33% | Brenntag |

## B.4 Starting Material α-$Ca_2Si_5N_8$

### B.4.1. α-$Ca_2Si_5N_8$ at 19 °C

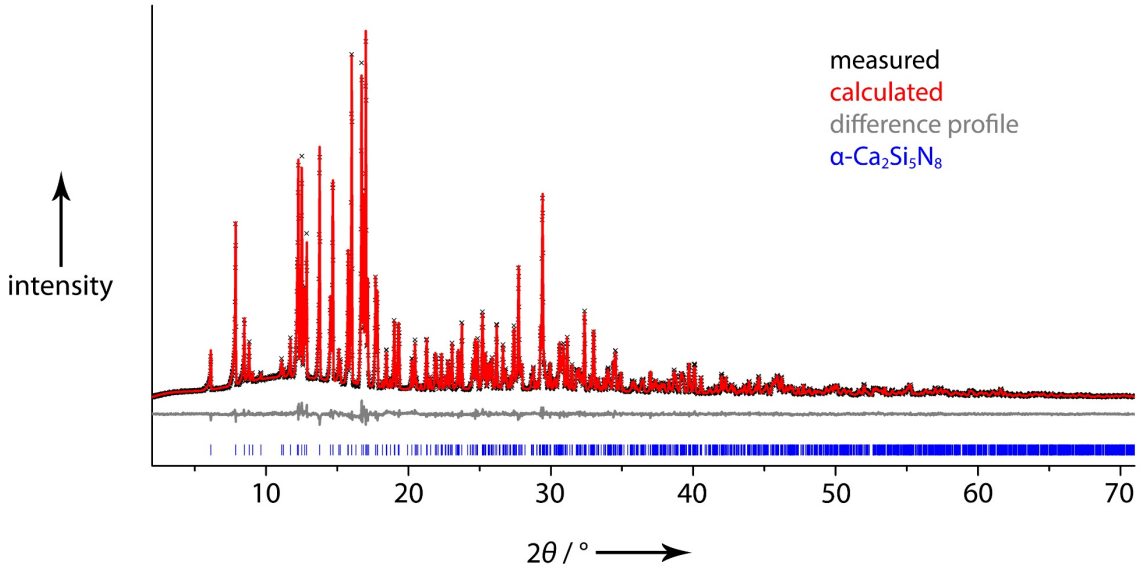


**Figure B.1:** RIETVELD refinement of α-$Ca_2Si_5N_8$ measured at 19 °C.[8]

RIETVELD refinement of α-$Ca_2Si_5N_8$ at 19 °C was performed using constraints for the isotropic displacement parameters of silicon and nitrogen.[8]

**Table B:2:** Crystallographic information on the starting material α-$Ca_2Si_5N_8$, standard deviations in parentheses.

| **Formula** | **α-$Ca_2Si_5N_8$** |
|---|---|
| **Formula mass / g · mol$^{-1}$** | 332.64 |
| **Crystal system** | monoclinic |
| **Space group** | *Cc* (no. 9) |
| **Lattice parameters / Å, °** | *a* = 14.32800(10)<br>*b* = 5.61165(4)<br>*c* = 9.69406(7)<br>*β* = 112.1484(5) |
| **Cell volume / Å$^3$** | 721.925(10) |
| ***Z*** | 4 |
| **X-ray density / g · cm$^{-3}$** | 3.06 |
| **Linear absorption coefficient / mm$^{-1}$** | 2.4 |
| **2*θ*-range / °** | 2.000–71.285 |
| **Temperature / °C** | 19(2) |
| **Data points** | 4620 |
| **Number of observed reflections** | 1709 |
| **Number of parameters** | 82 |
| **Constraints** | 2 |
| ***R*$_{wp}$** | 0.0380 |
| ***R*$_{exp}$** | 0.0298 |
| ***R*$_{p}$** | 0.0299 |
| ***R*$_{Bragg}$** | 0.0167 |
| ***GOF*** | 1.275 |

## B.4.2. α-$Ca_2Si_5N_8$ at 800 °C

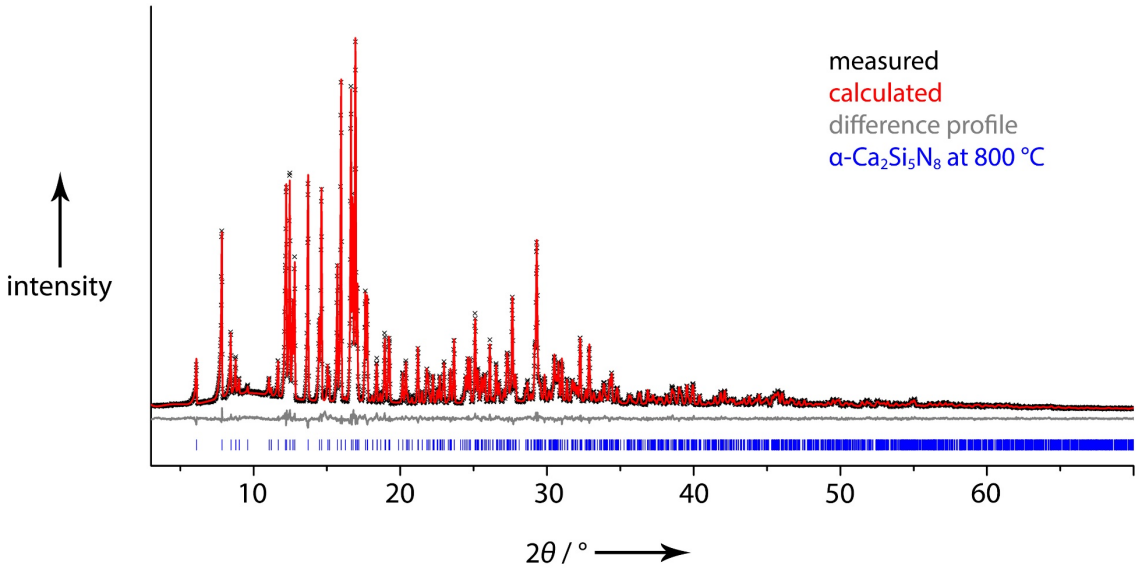


**Figure B.2:** RIETVELD refinement of α-$Ca_2Si_5N_8$ measured at 800 °C.[8]

**Table B.3:** Crystallographic information on the starting material α-$Ca_2Si_5N_8$ (commercial) at 800 °, standard deviations in parentheses.

| **Formula** | **α-$Ca_2Si_5N_8$** |
|---|---|
| **Formula mass / g · mol$^{-1}$** | 332.64 |
| **Crystal system** | monoclinic |
| **Space group** | *Cc* (no. 9) |
| **Lattice parameters / Å, °** | *a* = 14.3655(2)<br>*b* = 5.62932(6)<br>*c* = 9.73060(10)<br>*β* = 112.1366(8) |
| **Cell volume / Å$^3$** | 728.889(14) |
| ***Z*** | 4 |
| **X-ray density / g · cm$^{-3}$** | 3.03 |
| **Linear absorption coefficient / mm$^{-1}$** | 2.4 |
| **2*θ*-range / °** | 3.005–69.995 |
| **Temperature / °C** | 800 |
| **Data points** | 4467 |
| **Number of observed reflections** | 1647 |
| **Number of parameters** | 91 |
| **Constraints** | 2 |
| $R_{wp}$ | 0.0452 |
| $R_{exp}$ | 0.0345 |
| $R_p$ | 0.0342 |
| $R_{Bragg}$ | 0.0185 |
| ***GOF*** | 1.309 |

**Table B.4:** List of interatomic distances / Å and bond angles / ° in α-$Ca_2Si_5N_8$ at 800 °C, standard deviations in parentheses.

| **Distances** | | | | **Angles** | |
|---|---|---|---|---|---|
| Ca1–N1 | 2.361(12) | Si2–N6 | 1.706(10) | Si1–N1–Si4 | 114.3(8) |
| Ca1–N2 | 2.404(13) | Si2–N7 | 1.711(14) | Si1–N2–Si3 | 128.6(10) |
| Ca1–N6 | 2.623(8) | Si2–N8 | 1.774(10) | Si1–N5–Si5 | 125.3(8) |
| Ca1–N5 | 2.724(14) | Si2–N3 | 1.798(12) | Si1–N7–Si2 | 122.9(7) |
| Ca1–N7 | 2.790(12) | | | | |
| Ca1–N5 | 2.845(13) | Si3–N2 | 1.616(14) | Si2–N3–Si3 | 116.2(6) |
| Ca1–N8 | 3.010(9) | Si3–N3 | 1.732(11) | Si2–N3–Si5 | 116.1(6) |
| | | Si3–N4 | 1.758(11) | Si3–N3–Si5 | 126.7(6) |
| Ca2–N5 | 2.317(14) | Si3–N8 | 1.792(13) | | |
| Ca2–N7 | 2.324(12) | | | Si2–N6–Si4 | 125.4(6) |
| Ca2–N2 | 2.468(14) | Si4–N1 | 1.69(2) | Si2–N6–Si5 | 118.2(6) |
| Ca2–N1 | 2.628(12) | Si4–N8 | 1.739(11) | Si4–N6–Si5 | 114.2(5) |
| Ca2–N4 | 2.838(12) | Si4–N6 | 1.811(11) | | |
| Ca2–N8 | 3.099(8) | Si4–N4 | 1.835(10) | Si3–N4–Si4 | 118.1(5) |
| | | | | Si3–N4–Si5 | 128.1(7) |
| Si1–N2 | 1.725(12) | Si5–N3 | 1.718(12) | Si4–N4–Si5 | 105.7(5) |
| Si1–N5 | 1.744(12) | Si5–N4 | 1.754(12) | | |
| Si1–N1 | 1.75(2) | Si5–N5 | 1.755(13) | Si2–N8–Si3 | 108.0(6) |
| Si1–N7 | 1.78(2) | Si5–N6 | 1.758(13) | Si2–N8–Si4 | 129.1(7) |
| | | | | Si3–N8–Si4 | 122.8(6) |

**Table B.5:** Fractional atomic coordinates, isotropic displacement parameters, and site occupancies in α-$Ca_2Si_5N_8$ at 800 °C, standard deviations in parentheses.

| **Atom** | **Wyckoff symbol** | ***x*** | ***y*** | ***z*** | $U_{iso}$ | **Occupancy** |
|---|---|---|---|---|---|---|
| Ca1 | 4*a* | 0 | 0.7637 | 0 | 0.0233(12) | 1 |
| Ca2 | 4*a* | 0.6126(2) | 0.7489(5) | 0.2061(3) | 0.0339(14) | 1 |
| Si1 | 4*a* | 0.0572(6) | 0.8071(4) | 0.3536(9) | 0.0099(3) | 1 |
| Si2 | 4*a* | 0.7598(4) | 0.2069(10) | 0.3274(7) | 0.0099(3) | 1 |
| Si3 | 4*a* | 0.7538(5) | 0.4957(13) | 0.0653(8) | 0.0099(3) | 1 |
| Si4 | 4*a* | 0.3656(4) | 0.2117(10) | 0.3751(7) | 0.0099(3) | 1 |
| Si5 | 4*a* | 0.8548(4) | 0.0030(12) | 0.1287(8) | 0.0099(3) | 1 |
| N1 | 4*a* | 0.9893(10) | 0.643(2) | 0.436(2) | 0.0119(7) | 1 |
| N2 | 4*a* | 0.1330(9) | 0.024(2) | 0.0015(13) | 0.0119(7) | 1 |
| N3 | 4*a* | 0.7976(6) | 0.244(2) | 0.1722(8) | 0.0119(7) | 1 |
| N4 | 4*a* | 0.8010(8) | 0.750(2) | 0.1741(9) | 0.0119(7) | 1 |
| N5 | 4*a* | 0.9850(9) | 0.020(2) | 0.2283(14) | 0.0119(7) | 1 |
| N6 | 4*a* | 0.8339(6) | 0.009(2) | 0.9387(10) | 0.0119(7) | 1 |
| N7 | 4*a* | 0.6354(9) | 0.143(2) | 0.283(2) | 0.0119(7) | 1 |
| N8 | 4*a* | 0.8004(6) | 0.483(2) | 0.4189(10) | 0.0119(7) | 1 |

### B.4.3. α-$Ca_2Si_5N_8$ at 900 °C

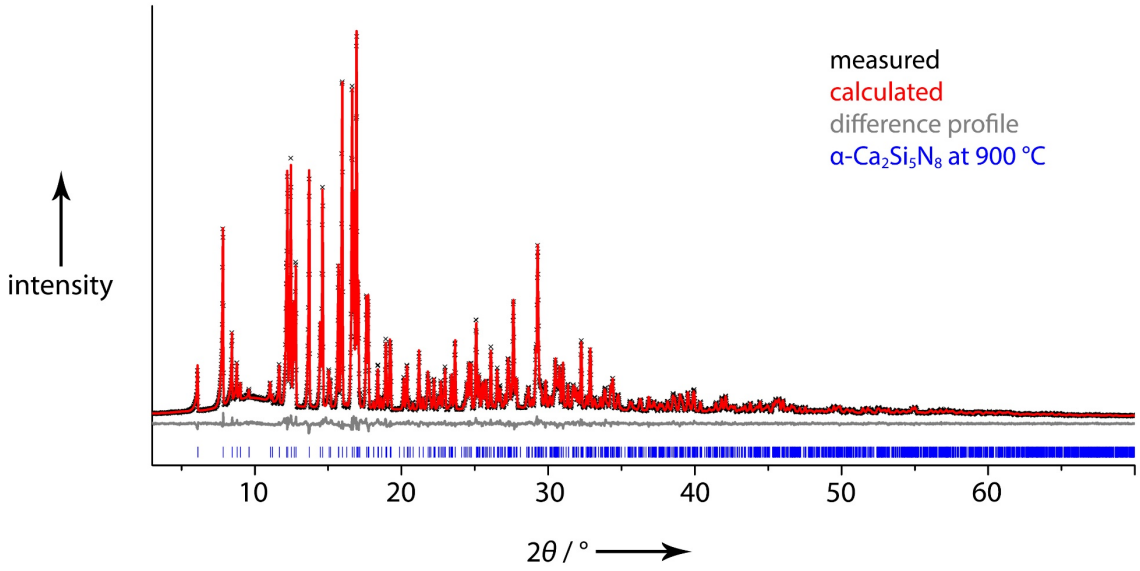


**Figure B.3:** RIETVELD refinement of commercial α-$Ca_2Si_5N_8$ measured at 900 °C.[8]

RIETVELD refinement of α-$Ca_2Si_5N_8$ at 900 °C was performed using constraints for the isotropic thermal displacement parameters of silicon and nitrogen.[8]

**Table B.6:** Crystallographic information on the starting material α-$Ca_2Si_5N_8$ at 900 °C, standard deviations in parentheses.

| **Formula** | **α-$Ca_2Si_5N_8$** |
|---|---|
| **Formula mass / g · mol$^{-1}$** | 332.64 |
| **Crystal system** | monoclinic |
| **Space group** | *Cc* (no. 9) |
| **Lattice parameters / Å, °** | *a* = 14.37019(14)<br>*b* = 5.63218(6)<br>*c* = 9.73567(9)<br>*β* = 112.1369(7) |
| **Cell volume / Å$^3$** | 729.877(13) |
| ***Z*** | 4 |
| **X-ray density / g · cm$^{-3}$** | 3.03 |
| **Linear absorption coefficient / mm$^{-1}$** | 2.3 |
| **2*θ*-range / °** | 3.005–69.995 |
| **Temperature / °C** | 900 |
| **Data points** | 4467 |
| **Number of observed reflections** | 1649 |
| **Number of parameters** | 97 |
| **Constraints** | 2 |
| ***R*$_{wp}$** | 0.0390 |
| ***R*$_{exp}$** | 0.0267 |
| ***R*$_p$** | 0.0296 |
| ***R*$_{Bragg}$** | 0.0187 |
| ***GOF*** | 1.461 |

**Table B.7:** List of interatomic distances / Å and bond angles / ° in α-$Ca_2Si_5N_8$ at 900 °C, standard deviations in parentheses.

| **Distances** | | | | **Angles** | |
|---|---|---|---|---|---|
| Ca1–N1 | 2.319(11) | Si2–N7 | 1.709(13) | Si1–N1–Si4 | 114.2(7) |
| Ca1–N2 | 2.387(11) | Si2–N6 | 1.716(9) | Si1–N2–Si3 | 127.0(8) |
| Ca1–N6 | 2.620(8) | Si2–N8 | 1.761(9) | Si1–N5–Si5 | 126.0(7) |
| Ca1–N7 | 2.767(11) | Si2–N3 | 1.810(10) | Si1–N7–Si2 | 122.9(7) |
| Ca1–N5 | 2.772(11) | | | | |
| Ca1–N5 | 2.794(11) | Si3–N2 | 1.618(11) | Si2–N3–Si3 | 116.1(5) |
| Ca1–N8 | 3.011(7) | Si3–N3 | 1.721(9) | Si2–N3–Si5 | 115.8(5) |
| | | Si3–N4 | 1.777(9) | Si3–N3–Si5 | 127.0(6) |
| Ca2–N5 | 2.331(11) | Si3–N8 | 1.798(12) | | |
| Ca2–N7 | 2.356(11) | | | Si2–N6–Si4 | 126.2(5) |
| Ca2–N2 | 2.430(11) | Si4–N1 | 1.693(13) | Si2–N6–Si5 | 118.3(6) |
| Ca2–N1 | 2.655(11) | Si4–N8 | 1.713(10) | Si4–N6–Si5 | 113.1(5) |
| Ca2–N4 | 2.858(10) | Si4–N6 | 1.841(10) | | |
| Ca2–N8 | 3.119(7) | Si4–N4 | 1.857(9) | Si3–N4–Si4 | 115.8(5) |
| | | | | Si3–N4–Si5 | 129.6(6) |
| Si1–N5 | 1.707(10) | Si5–N4 | 1.723(10) | Si4–N4–Si5 | 107.2(4) |
| Si1–N2 | 1.748(10) | Si5–N3 | 1.724(10) | | |
| Si1–N1 | 1.76(2) | Si5–N6 | 1.763(11) | Si2–N8–Si3 | 107.1(5) |
| Si1–N7 | 1.77(2) | Si5–N5 | 1.773(10) | Si2–N8–Si4 | 128.8(6) |
| | | | | Si3–N8–Si4 | 124.0(5) |

**Table B.8:** Fractional atomic coordinates, isotropic displacement parameters, and site occupancies in α-$Ca_2Si_5N_8$ at 900 °C, standard deviations in parentheses.

| **Atom** | **Wyckoff symbol** | ***x*** | ***y*** | ***z*** | $U_{iso}$ | **Occupancy** |
|---|---|---|---|---|---|---|
| Ca1 | 4*a* | 0 | 0.7637 | 0 | 0.0232(10) | 1 |
| Ca2 | 4*a* | 0.6122(2) | 0.7501(5) | 0.2061(3) | 0.0421(14) | 1 |
| Si1 | 4*a* | 0.0571(5) | 0.8074(4) | 0.3533(7) | 0.0105(3) | 1 |
| Si2 | 4*a* | 0.7598(3) | 0.2113(10) | 0.3310(6) | 0.0105(3) | 1 |
| Si3 | 4*a* | 0.7531(4) | 0.4969(11) | 0.0678(7) | 0.0105(3) | 1 |
| Si4 | 4*a* | 0.3660(3) | 0.2073(9) | 0.3783(6) | 0.0105(3) | 1 |
| Si5 | 4*a* | 0.8548(4) | 0.0051(10) | 0.1319(7) | 0.0105(3) | 1 |
| N1 | 4*a* | 0.9889(9) | 0.634(2) | 0.4339(13) | 0.0121(6) | 1 |
| N2 | 4*a* | 0.1322(8) | 0.025(2) | 0.0060(10) | 0.0121(6) | 1 |
| N3 | 4*a* | 0.7978(5) | 0.2479(14) | 0.1749(7) | 0.0121(6) | 1 |
| N4 | 4*a* | 0.8023(7) | 0.7553(14) | 0.1755(8) | 0.0121(6) | 1 |
| N5 | 4*a* | 0.9860(7) | 0.020(2) | 0.2348(11) | 0.0121(6) | 1 |
| N6 | 4*a* | 0.8341(5) | 0.0071(13) | 0.9416(9) | 0.0121(6) | 1 |
| N7 | 4*a* | 0.6349(8) | 0.151(2) | 0.2812(14) | 0.0121(6) | 1 |
| N8 | 4*a* | 0.8010(5) | 0.4840(13) | 0.4221(9) | 0.0121(6) | 1 |

## B.5 Migration Pathways of $Ca^{2+}$ in α-$Ca_2Si_5N_8$ at 800 and 900 °C

Voids in the structure of α-$Ca_2Si_5N_8$ at 800 °C and 900 °C were calculated with TOPOS employing Voronoi-Dirichlet polyhedra.[9] Migration pathways for $Ca^{2+}$ were calculated based on ionic radii in nitrides ($r(Ca^{2+})$ = 0.96 Å; $r(N^{3-})$ = 1.42 Å).[10] It was assumed that channels are accessible for $Ca^{2+}$ if the sum of ionic radii of $Ca^{2+}$ and $N^{3-}$ does not exceed the channel radius more than 15%.

### B.5.1. 800 °C

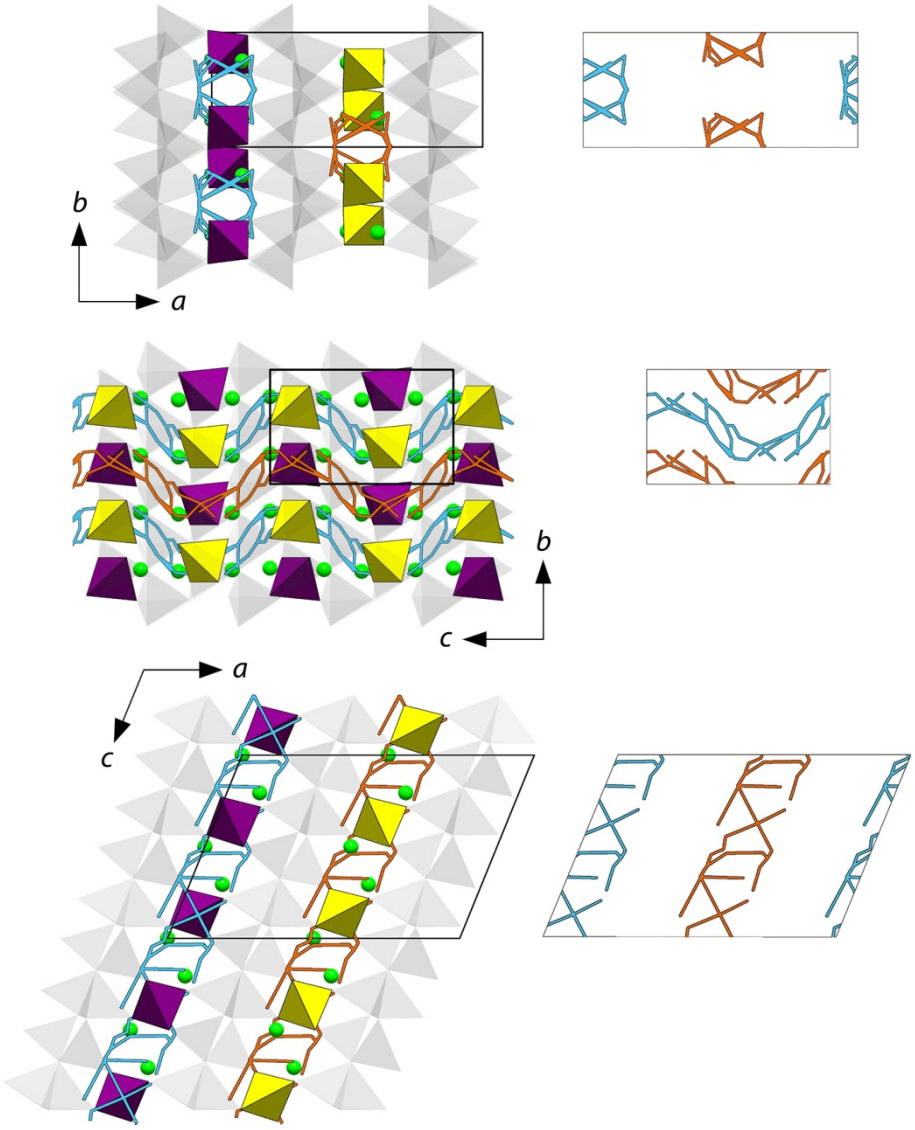


**Figure B.4:** Structure with channels of α-$Ca_2Si_5N_8$ at 800 °C (left) and channels (right) along *c* (top), along *a* (middle) and along *b* (bottom) with planar $SiN_4$ tetrahedral layers (gray), connecting $SiN_4$ tetrahedra (violet, yellow) and calculated migration pathways (blue, orange) for $Ca^{2+}$ (green).

### B.5.2. 900 °C

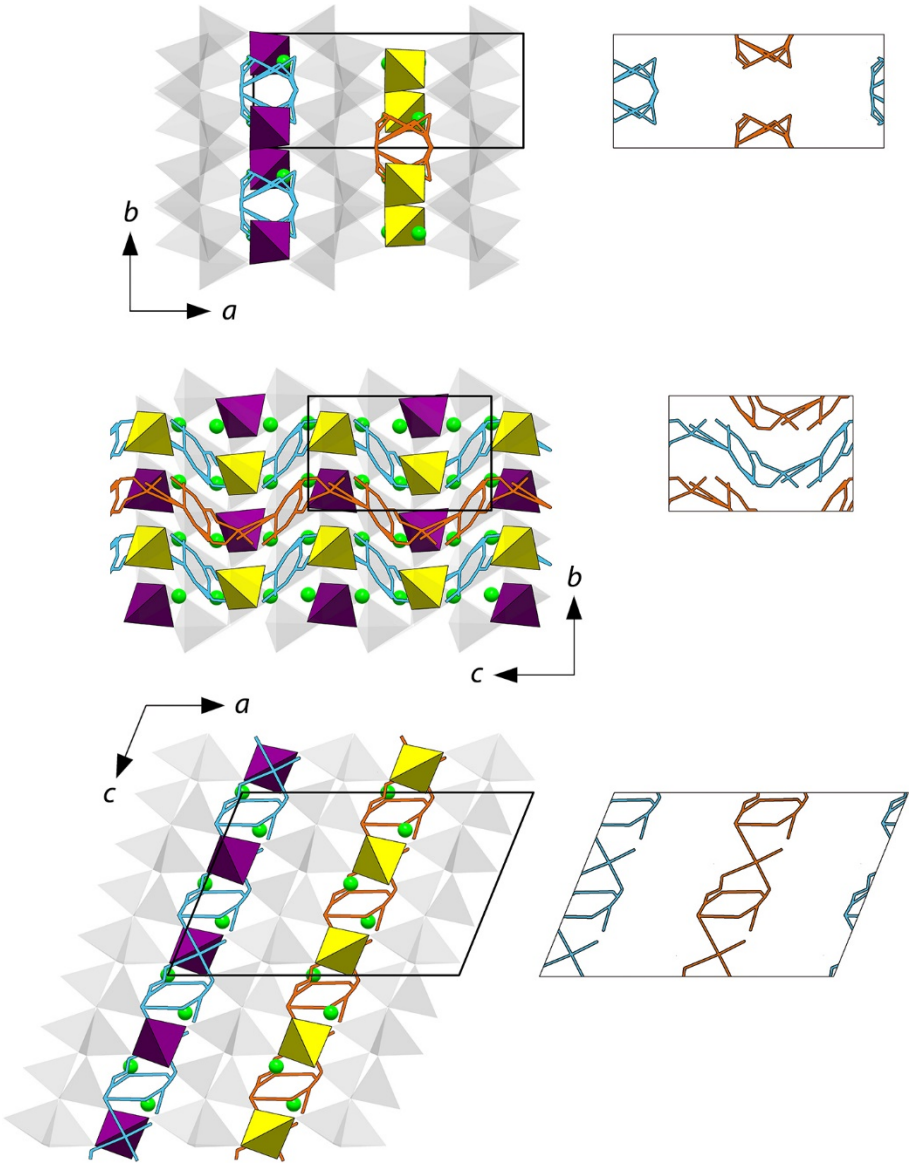


**Figure B.5:** Structure with channels of α-$Ca_2Si_5N_8$ at 900 °C (left) and channels (right) along *c* (top), along *a* (middle) and along *b* (bottom) with planar $SiN_4$ tetrahedral layers (gray), connecting $SiN_4$ tetrahedra (violet, yellow) and calculated migration pathways (blue, orange) for $Ca^{2+}$ (green).

## B.6 $Fe_2Si_5N_8$

### B.6.1. Experimental Details on the Ion Exchange Reaction

Ion exchange was carried out in a fused silica ampoule under argon atmosphere. α-$Ca_2Si_5N_8$ and $FeCl_2$ were thoroughly mixed in an agate mortar and filled into a dry (high vacuum, 400 °C) silica ampoule.

**Table B.9:** Weighted sample for the ion exchange to $Fe_2Si_5N_8$.

| α-$Ca_2Si_5N_8$ | $FeCl_2$ |
|---|---|
| 500.0 mg | 571.6 mg |
| 1.5 mmol | 4.5 mmol |

**Table B.10:** Temperature program of the tube furnace for the ion exchange leading to $Fe_2Si_5N_8$.

| Step | Starting *T* / °C | Target *T* / °C | *t* / h | Δ*T* / °C · $h^{-1}$ |
|---|---|---|---|---|
| 1 | 25 | 980 | 3 | 318 |
| 2 | 980 | 980 | 3 | 0 |
| 3 | 980 | 500 | 10 | –48 |

After the reaction, the silica ampoule was opened, the product chunk was ground and washed in water to remove the metal halides and subsequently in concentrated hydrochloric acid (33%) to remove elemental Fe formed throughout the reaction. $Fe_2Si_5N_8$ was obtained as a brown solid powder.

### B.6.2. Rietveld Refinement

RIETVELD Refinement of $Fe_2Si_5N_8$ was initially performed using the structural model of α-$Ca_2Si_5N_8$. Afterwards $F_{obs}$–$F_{calc}$ showed significant residual electron density near to the Fe1 and Fe2 positions (Figure B.4). Therefore, a second refinement with split positions for Fe1 (Fe12 and Fe22) and Fe2 (Fe21 and Fe22) was performed.

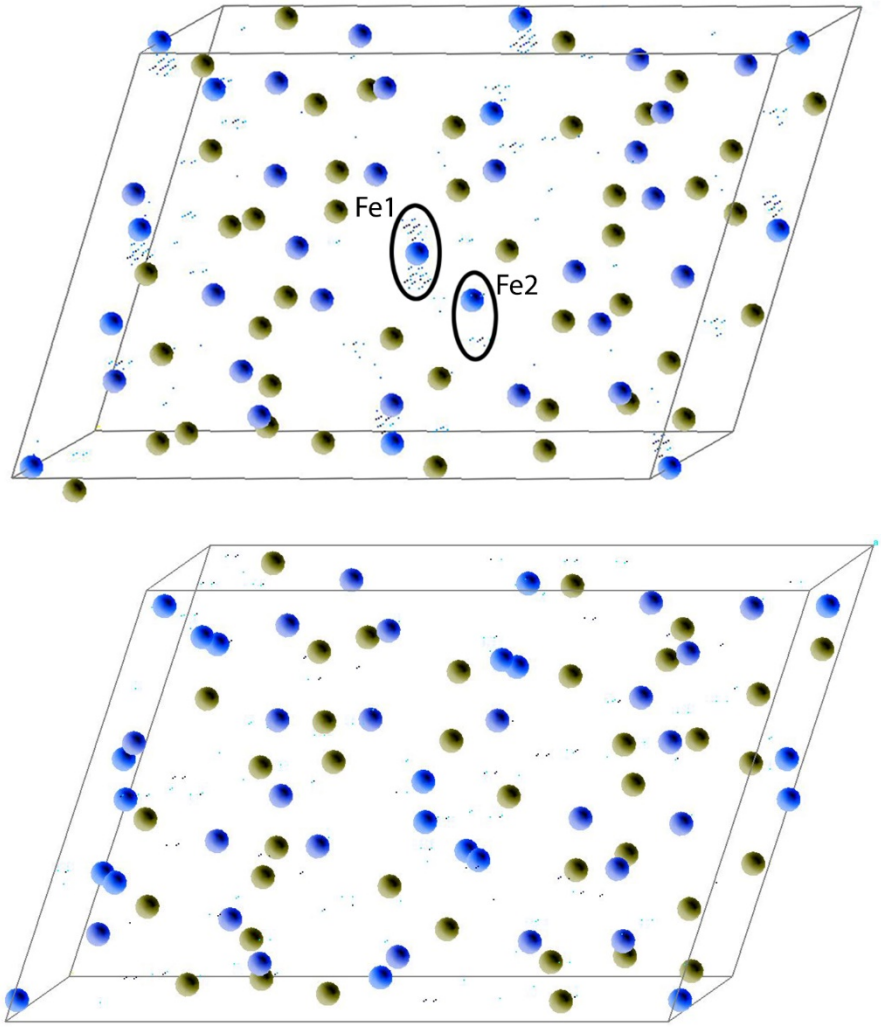


**Figure B.6:** $F_{obs}$–$F_{calc}$ of the RIETVELD refinements (top: $Ca_2Si_5N_8$ model; bottom: split positions).

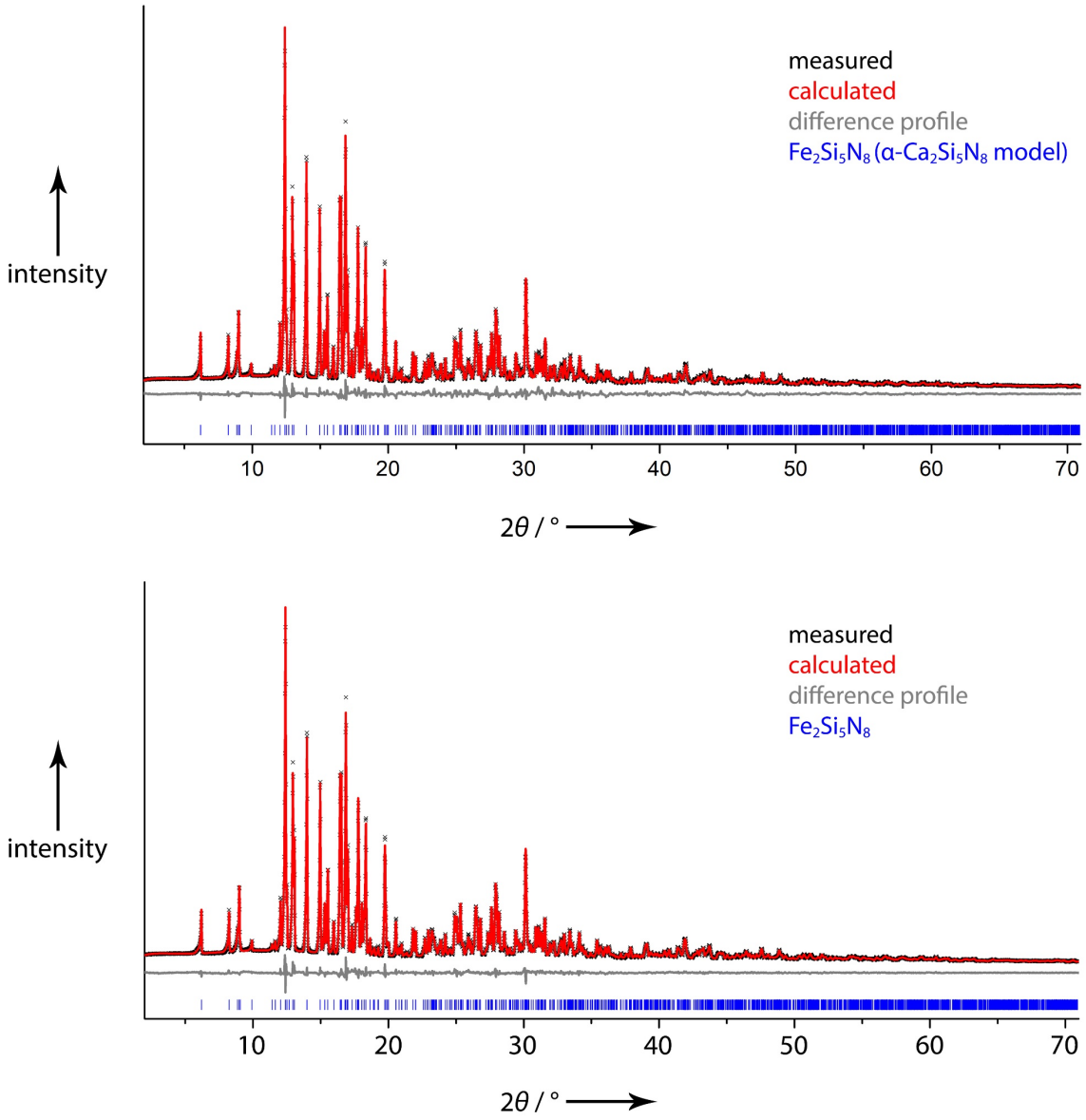


**Figure B.7:** RIETVELD plots of the refinements for $Fe_2Si_5N_8$ (top: $Ca_2Si_5N_8$ model; bottom: split positions)

As it can already be seen in the difference profiles shown in Figure B.7, refinement applying split positions works even better than using the α-$Ca_2Si_5N_8$ model. Additionally, *R* values of the refinements support the model with split positions (Table B.11).

**Table B.11:** Crystallographic information on $Fe_2Si_5N_8$ ($Ca_2Si_5N_8$ model and with split positions), standard deviations in parentheses.

| Formula | $Fe_2Si_5N_8$ ($Ca_2Si_5N_8$ model) | $Fe_2Si_5N_8$ (split positions) |
|---|---|---|
| **Formula mass / g · mol$^{-1}$** | 364.23 | |
| **Crystal system** | Monoclinic | |
| **Space group** | *Cc* (no. 9) | |
| **Lattice parameters / Å, °** | *a* = 14.0408(2) | *a* = 14.04056(14) |
| | *b* = 5.32635(8) | *b* = 5.32626(5) |
| | *c* = 9.5913(2) | *c* = 9.59064(9) |
| | *β* = 110.7281(10) | *β* = 110.7304(6) |
| **Cell volume / Å$^3$** | 670.86(2) | 670.788(12) |
| ***Z*** | 4 | |
| **X-ray density / g · cm$^{-3}$** | 3.61 | 3.61 |
| **Linear absorption coefficient / mm$^{-1}$** | 5.2 | 5.2 |
| **2*θ*-range / °** | 2.000–71.330 | |
| **Temperature / °C** | 19 | |
| **Data points** | 4623 | |
| **Number of observed reflections** | 1589 | |
| **Number of parameters** | 78 | 86 |
| **Constraints** | 2 | 6 |
| $R_{wp}$ | 0.0545 | 0.0352 |
| $R_{exp}$ | 0.0150 | 0.0150 |
| $R_p$ | 0.0412 | 0.0277 |
| $R_{Bragg}$ | 0.0253 | 0.0128 |
| ***GOF*** | 3.642 | 2.351 |

## Constraints

RIETVELD refinement of $Fe_2Si_5N_8$ ($Ca_2Si_5N_8$ model) was performed with constrained isotropic displacement parameters of Si and N.

RIETVELD refinement of $Fe_2Si_5N_8$ (split positions) was performed with constrained isotropic displacement parameters of silicon and nitrogen. Additionally the isotropic displacement parameters of Fe11 & Fe12 as well as Fe21 & Fe22 were constrained. The occupations of Fe11, Fe12, Fe21 and Fe22 were refined using the constraints *occ*(Fe12) = 1 − *occ*(Fe11) and *occ*(Fe22) = 1 − *occ*(Fe21).

**Table B.12:** List of interatomic distances / Å and bond angles / ° in $Fe_2Si_5N_8$ (α-$Ca_2Si_5N_8$ model), standard deviations in parentheses.

| Distances | | | | Angles | |
|---|---|---|---|---|---|
| Fe1–N1 | 1.959(12) | Si3–N2 | 1.59(2) | Si1–N1–Si4 | 110.9(7) |
| Fe1–N2 | 2.101(12) | Si3–N4 | 1.615(12) | Si1–N2–Si3 | 122.8(8) |
| Fe1–N5 | 2.688(14) | Si3–N3 | 1.779(12) | Si1–N5–Si5 | 119.6(8) |
| Fe1–N7 | 2.704(13) | Si3–N8 | 1.86(2) | Si1–N7–Si2 | 117.1(9) |
| Fe1–N6 | 2.710(10) | | | | |
| Fe1–N5 | 2.776(13) | Si4–N6 | 1.643(12) | Si2–N3–Si3 | 109.6(6) |
| | | Si4–N8 | 1.651(12) | Si2–N3–Si5 | 115.9(7) |
| Fe2–N5 | 1.990(14) | Si4–N1 | 1.739(14) | Si3–N3–Si5 | 131.7(7) |
| Fe2–N7 | 2.027(14) | Si4–N4 | 1.843(12) | | |
| Fe2–N2 | 2.151(14) | | | Si2–N6–Si4 | 123.5(8) |
| Fe2–N1 | 2.368(13) | Si5–N3 | 1.587(13) | Si2–N6–Si5 | 113.9(7) |
| | | Si5–N5 | 1.681(14) | Si4–N6–Si5 | 113.3(6) |
| Si1–N1 | 1.68(2) | Si5–N4 | 1.740(14) | | |
| Si1–N5 | 1.781(12) | Si5–N6 | 1.89(2) | Si3–N4–Si4 | 117.1(6) |
| Si1–N7 | 1.85(2) | | | Si3–N4–Si5 | 134.3(7) |
| Si1–N2 | 1.869(12) | | | Si4–N4–Si5 | 107.8(6) |
| | | | | | |
| Si2–N7 | 1.69(2) | | | Si2–N8–Si3 | 108.8(6) |
| Si2–N6 | 1.719(11) | | | Si2–N8–Si4 | 126.8(8) |
| Si2–N8 | 1.721(11) | | | Si3–N8–Si4 | 116.3(7) |
| Si2–N3 | 1.852(14) | | | | |

**Table B.13:** Fractional atomic coordinates, isotropic displacement parameters, and site occupancies in $Fe_2Si_5N_8$ (α-$Ca_2Si_5N_8$ model), standard deviations in parentheses.

| Atom | Wyckoff symbol | *x* | *y* | *z* | $U_{iso}$ | Occupancy |
|---|---|---|---|---|---|---|
| Fe1 | 4*a* | 0 | 0.76370 | 0 | 0.0654(13) | 1 |
| Fe2 | 4*a* | 0.5540(2) | 0.7686(3) | 0.1665(4) | 0.0065(6) | 1 |
| Si1 | 4*a* | 0.0318(4) | 0.7684(6) | 0.3572(7) | 0.0030(4) | 1 |
| Si2 | 4*a* | 0.7354(4) | 0.1811(8) | 0.3238(7) | 0.0030(4) | 1 |
| Si3 | 4*a* | 0.7289(4) | 0.5061(9) | 0.0694(7) | 0.0030(4) | 1 |
| Si4 | 4*a* | 0.3386(4) | 0.1868(8) | 0.3755(6) | 0.0030(4) | 1 |
| Si5 | 4*a* | 0.8469(5) | 0.0082(8) | 0.1366(8) | 0.0030(4) | 1 |
| N1 | 4*a* | 0.9628(10) | 0.578(2) | 0.424(2) | 0.0080(10) | 1 |
| N2 | 4*a* | 0.1093(10) | 0.046(2) | 0.0241(14) | 0.0080(10) | 1 |
| N3 | 4*a* | 0.7673(7) | 0.207(2) | 0.1528(11) | 0.0080(10) | 1 |
| N4 | 4*a* | 0.7927(7) | 0.733(2) | 0.1720(11) | 0.0080(10) | 1 |
| N5 | 4*a* | 0.9736(10) | 0.012(2) | 0.2277(14) | 0.0080(10) | 1 |
| N6 | 4*a* | 0.8245(8) | 0.028(2) | 0.9309(14) | 0.0080(10) | 1 |
| N7 | 4*a* | 0.6124(11) | 0.092(3) | 0.274(2) | 0.0080(10) | 1 |
| N8 | 4*a* | 0.7546(8) | 0.483(2) | 0.3920(13) | 0.0080(10) | 1 |

**Table B.14:** List of interatomic distances / Å and bond angles / ° in $Fe_2Si_5N_8$ (split positions), standard deviations in parentheses.

| **Distances** | | | | **Angles** | |
|---|---|---|---|---|---|
| Fe11–Fe12 | 0.831(4) | Si1–N1 | 1.700(12) | Si1–N1–Si4 | 112.5(5) |
| Fe11–N1 | 2.098(9) | Si1–N2 | 1.739(8) | Si1–N2–Si3 | 121.2(6) |
| Fe11–N2 | 2.149(8) | Si1–N5 | 1.814(12) | Si1–N5–Si5 | 121.0(5) |
| Fe11–N7 | 2.322(8) | Si1–N7 | 1.836(8) | Si1–N7–Si2 | 115.9(6) |
| Fe11–N5 | 2.429(9) | | | | |
| Fe11–Fe21 | 2.749(4) | Si2–N6 | 1.721(8) | Si2–N3–Si3 | 113.6(5) |
| | | Si2–N7 | 1.726(12) | Si2–N3–Si5 | 115.5(5) |
| Fe12–Fe11 | 0.8310(4) | Si2–N8 | 1.733(8) | Si3–N3–Si5 | 130.1(5) |
| Fe12–N1 | 1.998(9) | Si2–N3 | 1.775(10) | | |
| Fe12–N2 | 2.110(9) | | | Si2–N6–Si4 | 117.4(5) |
| Fe12–N5 | 2.427(9) | Si3–N2 | 1.650(11) | Si2–N6–Si5 | 117.4(5) |
| Fe12–N6 | 2.528(9) | Si3–N4 | 1.689(8) | Si4–N6–Si5 | 114.5(4) |
| | | Si3–N3 | 1.722(8) | | |
| Fe21–Fe22 | 0.35(2) | Si3–N8 | 1.800(11) | Si3–N4–Si4 | 116.2(5) |
| Fe21–N5 | 1.964(11) | | | Si3–N4–Si5 | 131.5(5) |
| Fe21–N7 | 1.995(10) | Si4–N8 | 1.684(9) | Si4–N4–Si5 | 112.0(5) |
| Fe21–N2 | 2.169(12) | Si4–N1 | 1.724(11) | | |
| Fe21–N1 | 2.314(10) | Si4–N6 | 1.768(8) | Si2–N8–Si3 | 112.6(4) |
| Fe21–Fe11 | 2.749(4) | Si4–N4 | 1.775(8) | Si2–N8–Si4 | 122.3(5) |
| | | | | Si3–N8–Si4 | 119.4(5) |
| Fe22–Fe21 | 0.35(2) | Si5–N4 | 1.681(10) | | |
| Fe22–N7 | 1.98(2) | Si5–N3 | 1.681(9) | | |
| Fe22–N5 | 2.04(3) | Si5–N5 | 1.695(9) | | |
| Fe22–N2 | 2.07(2) | Si5–N6 | 1.788(11) | | |
| Fe22–N1 | 2.57(2) | | | | |
| Fe22–Fe11 | 2.96(2) | | | | |

**Table B.15:** Fractional atomic coordinates, isotropic displacement parameters, and site occupancies in $Fe_2Si_5N_8$ (split positions), standard deviations in parentheses.

| Atom | Wyckoff symbol | *x* | *y* | *z* | $U_{iso}$ | Occupancy |
|---|---|---|---|---|---|---|
| Fe11 | 4*a* | 0.01623 | 0.74735 | 0.06311 | 0.0125(6) | 0.527(4) |
| Fe12 | 4*a* | 0.9910(3) | 0.7817(6) | 0.9729(4) | 0.0125(6) | 0.473(4) |
| Fe21 | 4*a* | 0.5535(6) | 0.7741(8) | 0.1847(6) | 0.0065(5) | 0.78(3) |
| Fe22 | 4*a* | 0.078(2) | 0.250(3) | 0.204(2) | 0.0065(5) | 0.22(3) |
| Si1 | 4*a* | 0.0396(4) | 0.7720(4) | 0.3782(6) | 0.0043(2) | 1 |
| Si2 | 4*a* | 0.7382(4) | 0.1835(6) | 0.3343(5) | 0.0043(2) | 1 |
| Si3 | 4*a* | 0.7300(4) | 0.5010(7) | 0.0813(6) | 0.0043(2) | 1 |
| Si4 | 4*a* | 0.3412(4) | 0.1849(6) | 0.3848(5) | 0.0043(2) | 1 |
| Si5 | 4*a* | 0.8476(4) | 0.9996(8) | 0.1459(6) | 0.0043(2) | 1 |
| N1 | 4*a* | 0.9664(7) | 0.588(2) | 0.4445(10) | 0.0058(6) | 1 |
| N2 | 4*a* | 0.1071(7) | 0.0553(12) | 0.0363(9) | 0.0058(6) | 1 |
| N3 | 4*a* | 0.7697(5) | 0.2197(14) | 0.1717(7) | 0.0058(6) | 1 |
| N4 | 4*a* | 0.7998(5) | 0.734(2) | 0.1893(7) | 0.0058(6) | 1 |
| N5 | 4*a* | 0.9749(6) | 0.012(2) | 0.2399(8) | 0.0058(6) | 1 |
| N6 | 4*a* | 0.8290(5) | 0.0119(12) | 0.9517(9) | 0.0058(6) | 1 |
| N7 | 4*a* | 0.6140(8) | 0.087(2) | 0.2948(10) | 0.0058(6) | 1 |
| N8 | 4*a* | 0.7577(5) | 0.4814(12) | 0.4122(9) | 0.0058(6) | 1 |

### B.6.3. Statistical vs. Ordered Distribution of the Iron Split Positions

Refinement of the split positions Fe11/Fe12 and Fe21/Fe22 was performed based on a statistical distribution between the split positions. Assumed that this distribution would not be statistical, symmetry reduction or enlargement of the unit cell should be observed.

#### Symmetry reduction

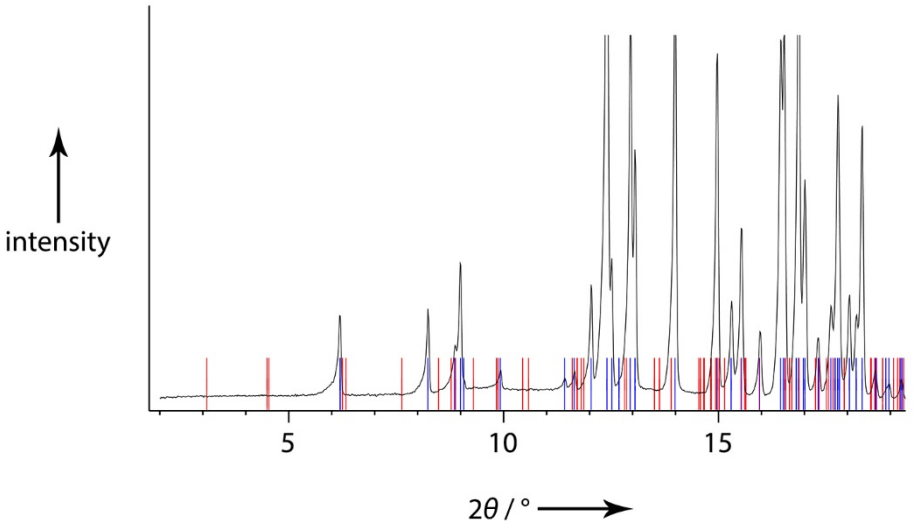


**Figure B.8:** Measured PXRD (black) of $Fe_2Si_5N_8$ with calculated reflection positions ($a = 14.04$ Å, $b = 5.33$ Å, $c = 9.59$ Å, $\beta = 110.73°$, $\lambda = 0.7093$ Å) for space group *Cc* (blue) and for hypothetical elimination of *C*-centering and glide reflection along *c* (red).

Figure B.8 shows calculated (CMPR)[11] reflection positions (red) where intensity would be expected in case of a symmetry reduction due to ordering of the split positions. Based on our measured data no reflection could be observed corroborating such a theory.

#### Cell enlargement

A bigger unit cell would generate reflections at smaller angles than the original cell. Focusing on Figure B.8 no reflection position besides to the positions marked in blue (original cell) can be observed.

In conclusion the measured PXRD data indicate that the distribution between the split positions is statistical.

## B.6.4. Structure

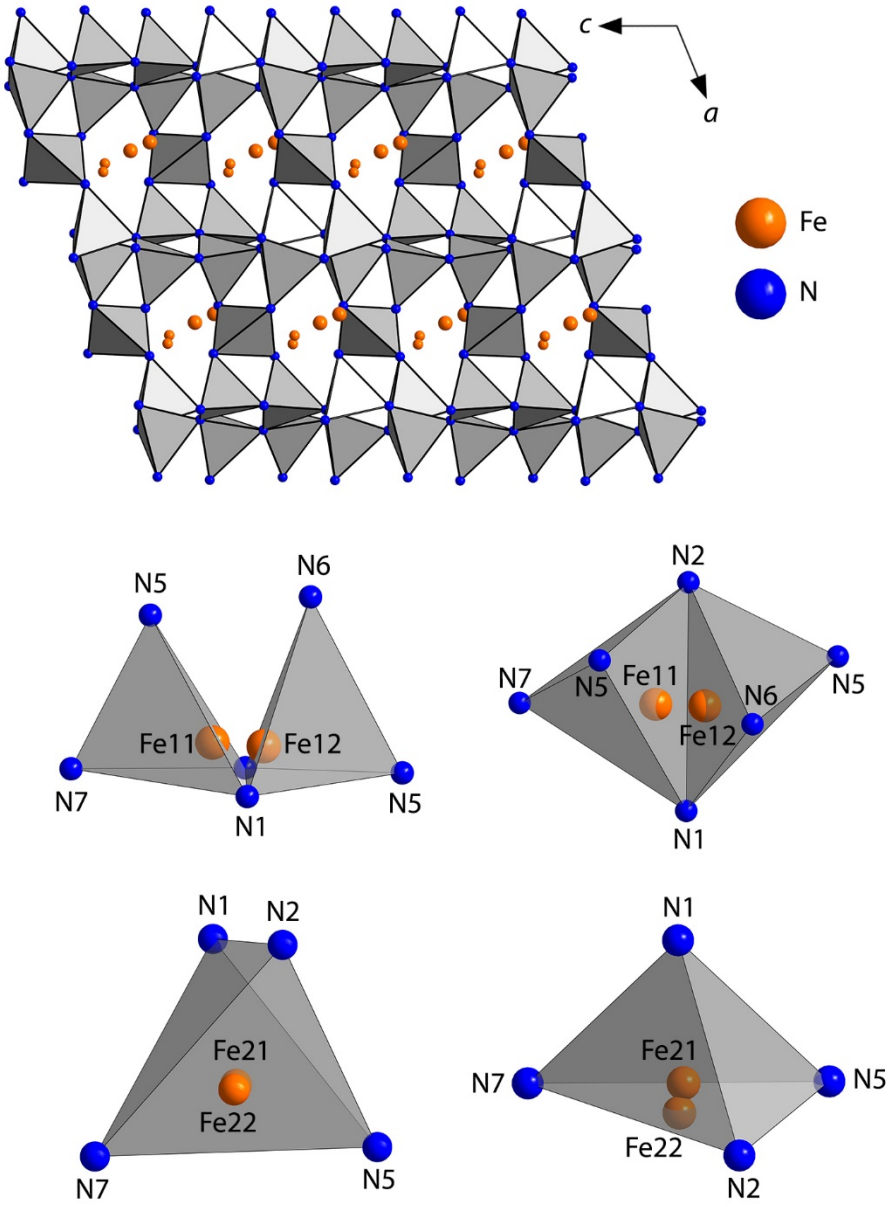


**Figure B.9:** Crystal structure of $Fe_2Si_5N_8$ (along *b* (top), coordination environments of the cations (middle and bottom)). The atoms are displayed with isotropic displacement parameters (90% probability).

## B.6.5. Details on SEM and EDX

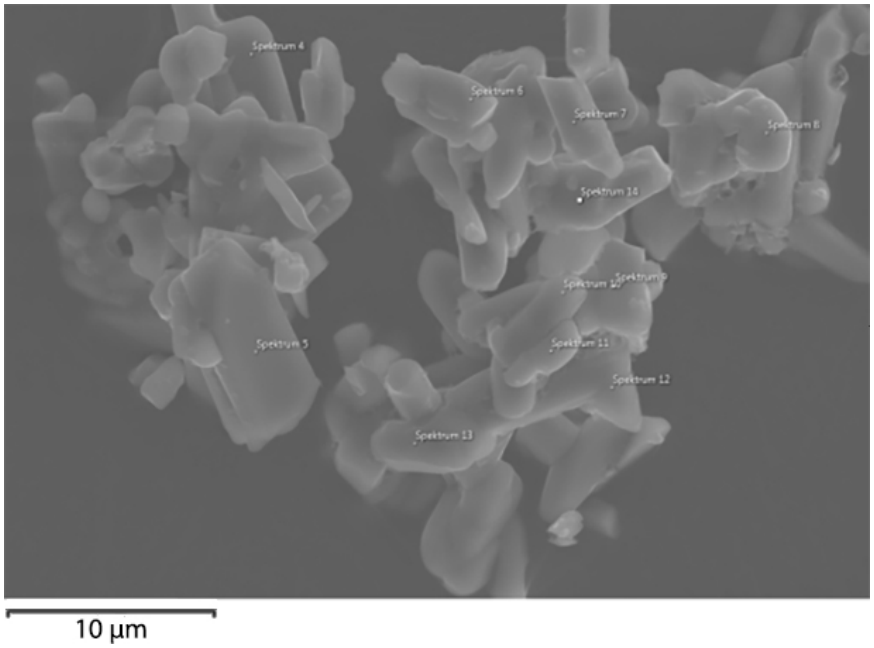


**Figure B.10:** Scanning electron micrograph of a $Fe_2Si_5N_8$ powder sample.

**Table B.16:** EDX analysis (atomic percent) of $Fe_2Si_5N_8$ powder shown in Figure B.10.

| | Spektrum 4 | Spektrum 5 | Spektrum 6 | Spektrum 7 | Spektrum 8 | Spektrum 9 | Spektrum 10 |
|---|---|---|---|---|---|---|---|
| **N** | 54 | 57 | 59 | 57 | 54 | 57 | 49 |
| **O** | 3 | 3 | 8 | 5 | 13 | 3 | 5 |
| **Si** | 32 | 29 | 24 | 28 | 24 | 29 | 33 |
| **Ca** | -- | -- | -- | -- | -- | -- | -- |
| **Fe** | 12 | 11 | 9 | 10 | 9 | 11 | 13 |
| **Cl** | -- | <1 | <1 | <1 | <1 | -- | <1 |
| **Fe/Si** | 2/5.3 | 2/5.3 | 2/5.3 | 2/5.6 | 2/5.3 | 2/5.3 | 2/5.1 |

| | Spektrum 11 | Spektrum 12 | Spektrum 13 | Spektrum 14 | Theoretical | Average |
|---|---|---|---|---|---|---|
| **N** | 53 | 42 | 51 | 45 | 53.3 | 53 |
| **O** | 4 | 9 | 5 | 8 | 0 | 6 |
| **Si** | 31 | 35 | 32 | 33 | 33.3 | 30 |
| **Ca** | -- | <1 | -- | -- | 0 | 0 |
| **Fe** | 12 | 14 | 12 | 14 | 13.3 | 12 |
| **Cl** | <1 | <1 | <1 | <1 | 0 | <1 |
| **Fe/Si** | 2/5.2 | 2/5 | 2/5.3 | 2/4.7 | 2/5 | 2/5 |

The values detected for oxygen may refer to one or more side phases originated from surface oxidation of the nitridosilicate $Fe_2Si_5N_8$.

## B.6.6. Details on ICP-OES

**Table B.17:** ICP-OES analysis of $Fe_2Si_5N_8$.

| Element | Amount / mg · g$^{-1}$ | Atomic% | $Fe_2Si_5N_8$ theoretical atomic% |
|---|---|---|---|
| **Fe** | 323.0 | 14.5 | 13.33 |
| **Ca** | not detectable | 0 | 0 |
| **Si** | 395.2 | 35.2 | 33.33 |
| **Na** | 281.8 | 50.3 | 53.33 |
| | | | |
| **Fe/Si** | 2/4.9 | | |

[a] values for nitrogen were calculated from the difference to 1 g

The experimental values of ICP-OES for $Fe_2Si_5N_8$ are in good agreement with the theoretical composition of the compound.

## B.6.7. Details on CHNS Analysis

Nitrogen content of a $Fe_2Si_5N_8$ sample was determined to 29.7 mass%. The theoretical value for $Fe_2Si_5N_8$ is 30.7 mass%. The difference may also be explained by oxygen at the surface of the nitridosilicate.

### B.6.8. TGA/DSC Measurement

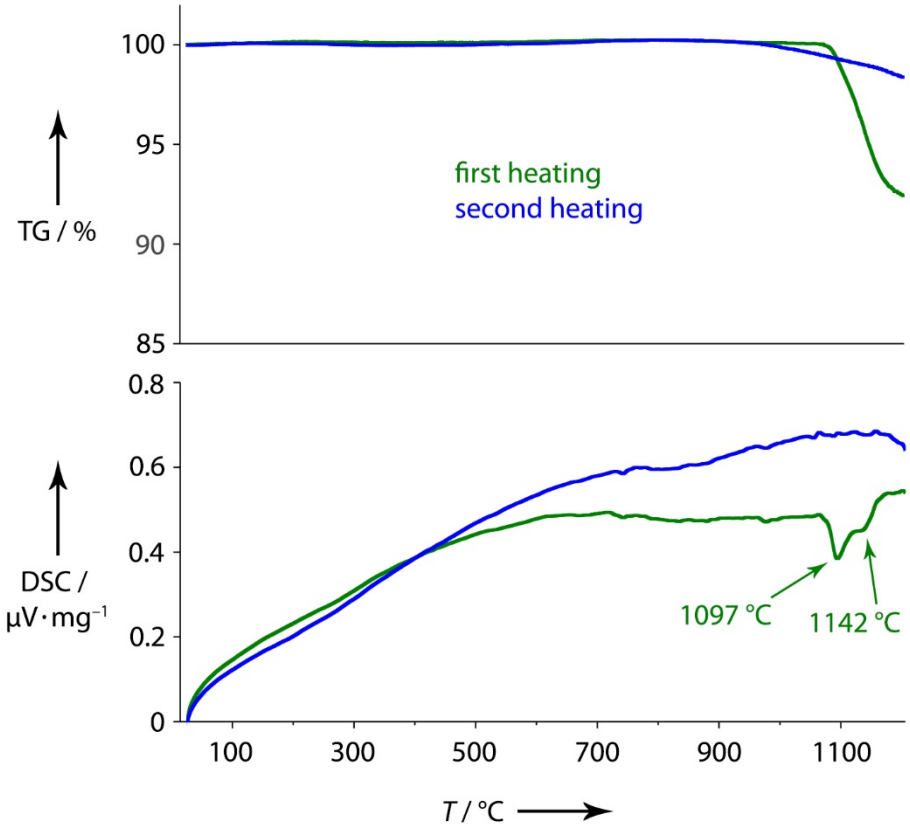


**Figure B.11:** TGA/DSC investigation of $Fe_2Si_5N_8$. Heating with 10 °C · min$^{-1}$.

According to Figure B.11, $Fe_2Si_5N_8$ decomposes at 1097 °C (exothermic) combined with a mass loss.

### B.6.9. Decomposition Products

A sample of $Fe_2Si_5N_8$ was filled into a tungsten crucible. The crucible was put into a radio-frequency furnace under nitrogen atmosphere and the temperature program shown in Table B.18 was started. After the treatment a gray, ferromagnetic powder was obtained and analyzed by PXRD. A measurement illustrating the decomposition products $Si_3N_4$ and Fe is shown in Figure B.12.

**Table B.18:** Temperature program of the radio-frequency furnace for the HT investigation on $Fe_2Si_5N_8$.

| Step | Starting *T* / °C | Target *T* / °C | *t* / h | Δ*T* / °C · h$^{-1}$ |
|---|---|---|---|---|
| 1 | 25 | 1200 | 2 | 588 |
| 2 | 1200 | 1200 | 1 | 0 |
| 3 | 1200 | 500 | 10 | −70 |

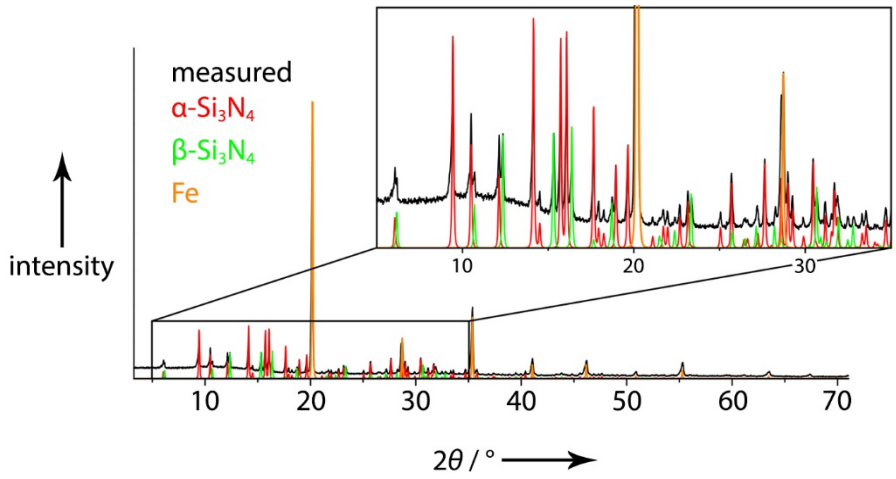


**Figure B.12:** PXRD of the $Fe_2Si_5N_8$ decomposition products (black) with references for α-$Si_3N_4$ (red), β-$Si_3N_4$ (green) and Fe (orange).[12,13]

In conclusion TGA/DSC and decomposition products indicate that $Fe_2Si_5N_8$ decomposes into Fe, $Si_3N_4$ and $N_2$ according to Equation B.1.

$$3\ Fe_2Si_5N_8 \rightarrow 6\ Fe + 5\ Si_3N_4 + 2\ N_2\uparrow \qquad \text{B.1}$$

### B.6.10. Optical Microscopy

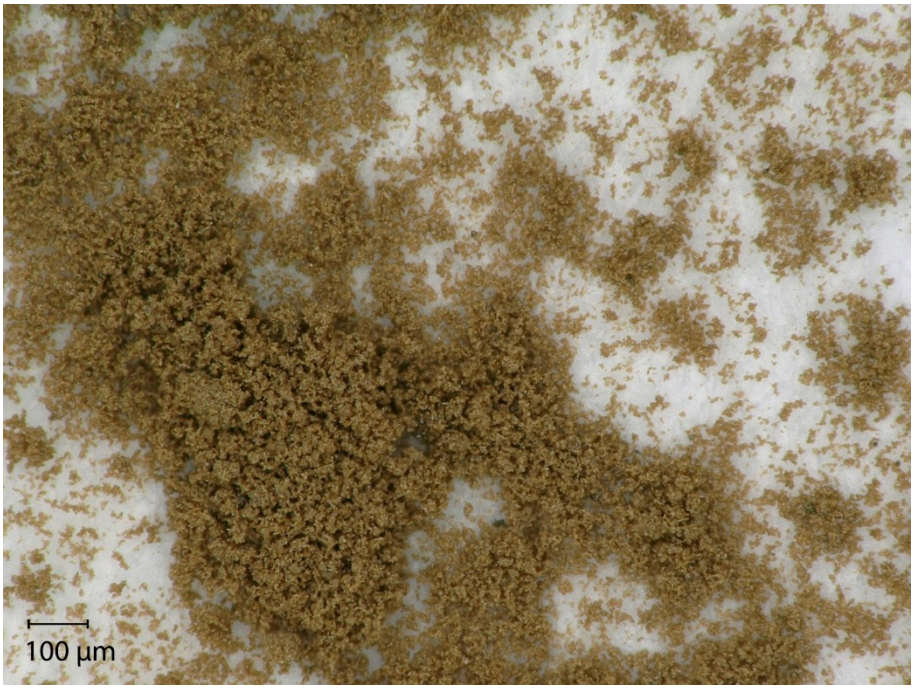


**Figure B.13:** Picture of a $Fe_2Si_5N_8$ sample.

## B.6.11. Mößbauer Spectroscopy

**Table B.19:** Fitting parameters of $^{151}$Eu Mößbauer spectroscopic measurements of the $Fe_2Si_5N_8$ sample at 78 K; $\delta$ = isomer shift, $\Delta EQ$ = electric quadrupole splitting, $\Gamma$ = experimental line width. Parameters marked with an asterisk were kept fixed during the fitting procedure, standard deviations in parentheses.

| Signal | $\delta$ / mm · s$^{-1}$ | $\Delta EQ$ / mm · s$^{-1}$ | $\Gamma$ / mm · s$^{-1}$ | Ratio |
|---|---|---|---|---|
| 1 | 0.837(2) | 1.587(6) | 0.454(6) | 45.9%* |
| 2 | 0.816(2) | 1.952(5) | 0.455(7) | 45.9%* |
| 3 | 1.31* | 3.17* | 0.4* | 5.2% |
| 4 | −0.18(1) | 1.78(3) | 0.31(5) | 2.9% |

The Mößbauer spectra at 78 and 6 K are shown in Figure B.14 along with the transition integral fits of the 78 K spectrum.

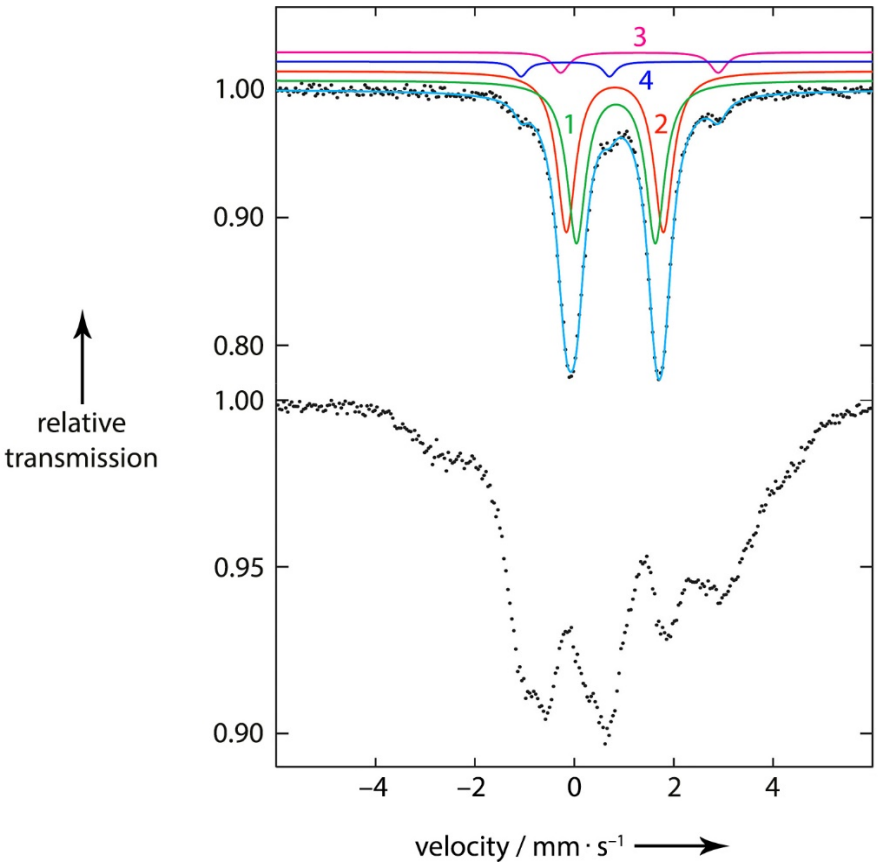


**Figure B.14:** Experimental (data points) and simulated (continuous lines) $^{57}$Fe Mößbauer spectra of $Fe_2Si_5N_8$ at 78 K (top) and 6 K (bottom). The obtained fitting parameters are listed in Table B.19.

The minor signals exhibit area ratio of 5.2(3) and 2.9(4)%. The first one (signal 3) could be well reproduced with an isomer shift of $\delta = 1.31\ \mathrm{mm \cdot s^{-1}}$ and quadrupole splitting of $\Delta E_Q = 3.17\ \mathrm{mm \cdot s^{-1}}$, in line with the reported values of $Fe_2Si_2O_6$ ($\delta = 1.30\ \mathrm{mm \cdot s^{-1}}$, $\Delta E_Q = 3.02\ \mathrm{mm \cdot s^{-1}}$) and $CaFeSi_2O_6$ ($\delta = 1.31\ \mathrm{mm \cdot s^{-1}}$, $\Delta E_Q = 3.17\ \mathrm{mm \cdot s^{-1}}$).[14] The last signal (4) shows an isomer shift of $-0.18(1)\ \mathrm{mm \cdot s^{-1}}$, which is in the typical range for Fe(III) species or Fe(II) low spin compounds, for example $Na_2Fe(CN)_5NO$.[15,16] Therefore, this signal has to be ascribed to an additional impurity phase.

The $^{57}$Fe Mößbauer spectrum recorded at 6 K is shown in Figure B.14 (bottom). The spectrum shows an extremely broad signal, which could not be fitted and reproduced by the individual contributions of the sample and the observed impurities. Signal broadening can be caused by magnetic ordering (hyperfine field splitting), field distributions originating from magnetic inhomogeneities (domains with slightly different degrees of magnetic order) or atomic disorder in the crystal structure. Since magnetic ordering was only observed for the impurity phases (see magnetism) it is not possible to add hyperfine field splitting for signals 3 and 4.

### B.6.12. Magnetic Measurements

According to magnetic susceptibility measurements at an external field of 10 kOe, $Fe_2Si_5N_8$ shows paramagnetism and a presumably antiferromagnetic magnetic anomaly at low temperatures. Subsequently, ZFC/FC measurements at different external fields (0.2–10 kOe) were conducted (Figure 3.4, top). They confirm the anomaly, with antiferromagnetic character in the ZFC and a ferromagnetic character in the FC measurements, pointing towards an instable antiferromagnetic ground state. As expected, the susceptibility diminishes with increasing field and therefore confirms that the observed phase-transition belongs to an impurity phase. The Néel temperature was determined to $T_N$ = 36.1(5) K from the 200 Oe measurement. The Néel temperature is close to what has been observed for $Fe_2Si_2O_6$ ($T_N$ = 43 K)[17] and $CaFeSi_2O_6$ ($T_N$ = 38 K).[18] Disorder in the observed impurity according to $Fe_{2-x}Ca_xSi_2O_6$ can shift the ordering temperature to even lower values (chapter B.6.11). A magnetization isotherm, recorded at 10 K (Figure 3.4, middle) and therefore below the ordering temperature, confirmed the instable antiferromagnetic ground state along with a hysteresis, typically observed for weak permanent magnetic materials. The saturation magnetization of $\mu_{sat}$ = 0.15(1) $\mu_B$ at 80 kOe, however, is significantly lower compared to the expected 2.83 $\mu_B$ for a tetrahedrally coordinated high-spin $Fe^{2+}$ ion ($d^6$, two unpaired electrons). This indicates, that the observed magnetic ordering phenomenon has to be attributed to an impurity.

Similar results were obtained for solid solution $Fe_{1.9}Ca_{0.1}Si_5N_8$ (incomplete ion exchange at 850 °C; chapter B.7). The Néel temperature of the impurity phase was shifted to $T_N$ = 35.7(5) K, therefore one can conclude that the impurity is the same in both samples ($Fe_2Si_5N_8$ and $Fe_{1.9}Ca_{0.1}Si_5N_8$) but with different values of $x$ in solid solutions $Fe_{2-x}Ca_xSi_2O_6$.

## B.6.13. Details on TDPXRD

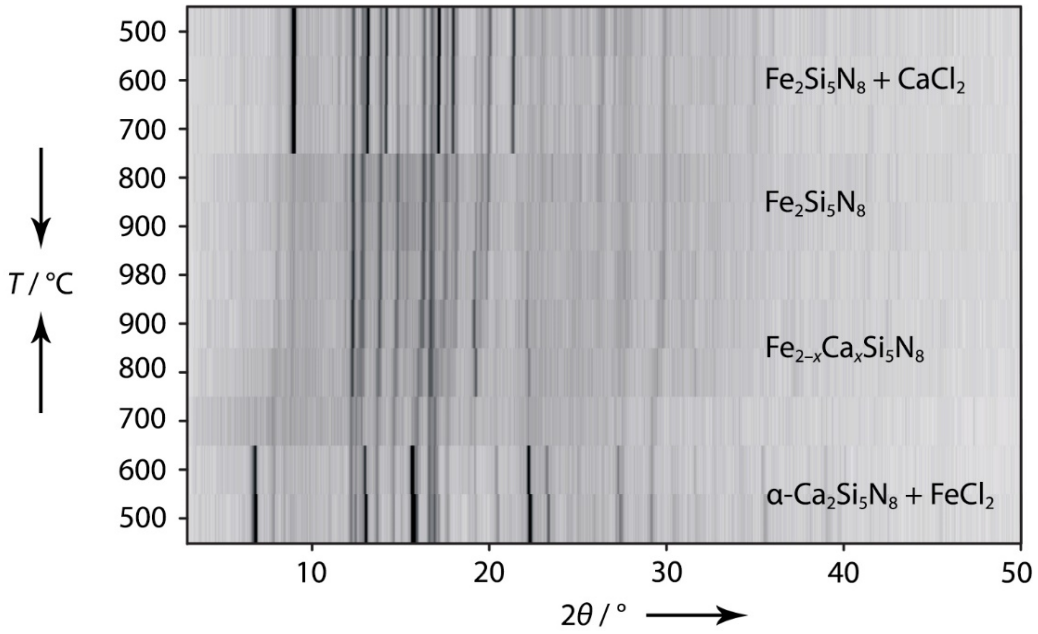


**Figure B.15:** *In situ* investigation on the ion exchange (2 $FeCl_2$ + α-$Ca_2Si_5N_8$) by TDPXRD.

**Table B.20:** Temperature program for the TDPXRD measurement shown in Figure B.15.

| Step | Starting *T* / °C | Target *T* / °C | *t* / min | Δ*T* / °C · min$^{-1}$ | XRD |
|---|---|---|---|---|---|
| 1 | 500 | 500 | 10 | 0 | ✓ |
| 2 | 500 | 600 | 20 | 5 | × |
| 3 | 600 | 600 | 10 | 0 | ✓ |
| 4 | 600 | 700 | 20 | 5 | × |
| 5 | 700 | 700 | 10 | 0 | ✓ |
| 6 | 700 | 800 | 20 | 5 | × |
| 7 | 800 | 800 | 10 | 0 | ✓ |
| 8 | 800 | 900 | 20 | 5 | × |
| 9 | 900 | 900 | 10 | 0 | ✓ |
| 10 | 900 | 980 | 16 | 5 | × |
| 11 | 980 | 980 | 10 | 0 | ✓ |
| 12 | 980 | 900 | 16 | −5 | × |
| 13 | 900 | 900 | 10 | 0 | ✓ |
| 14 | 900 | 800 | 20 | −5 | × |
| 15 | 800 | 800 | 10 | 0 | ✓ |
| 16 | 800 | 700 | 20 | −5 | × |
| 17 | 700 | 700 | 10 | 0 | ✓ |
| 18 | 700 | 600 | 20 | −5 | × |
| 19 | 600 | 600 | 10 | 0 | ✓ |
| 20 | 600 | 500 | 20 | −5 | × |
| 21 | 500 | 500 | 10 | 0 | ✓ |

## B.7 $Fe_{1.9}Ca_{0.1}Si_5N_8$

### B.7.1. Experimental Details on the Ion Exchange Reaction

Ion exchange was carried out in a fused silica ampoule under argon atmosphere. α-$Ca_2Si_5N_8$ and $FeCl_2$ were thoroughly mixed in an agate mortar and filled into a dry (high vacuum, 400 °C) silica ampoule.

**Table B.21:** Weighted sample for the ion exchange to $Fe_2Si_5N_8$.

| α-$Ca_2Si_5N_8$ | $FeCl_2$ |
|---|---|
| 300.0 mg | 457.3 mg |
| 0.9 mmol | 3.6 mmol |

**Table B.22:** Temperature program of the tube furnace for the ion exchange leading to $Fe_2Si_5N_8$.

| Step | Starting *T* / °C | Target *T* / °C | *t* / h | Δ*T* / °C · $h^{-1}$ |
|---|---|---|---|---|
| 1 | 25 | 850 | 3 | 275 |
| 2 | 850 | 850 | 3 | 0 |
| 3 | 850 | 500 | 10 | −35 |

After the reaction, the silica ampoule was opened, the product chunk was pound and washed in water to remove the metal halides and subsequently in concentrated nitric acid (65%) to remove elemental Fe formed throughout the reaction. $Fe_{1.9}Ca_{0.1}Si_5N_8$ was obtained as a brown solid.

### B.7.2. Details on ICP-OES

**Table B.23:** ICP-OES analysis of $Fe_{1.9}Ca_{0.1}Si_5N_8$.

| Element | Amount / mg · $g^{-1}$ | Atomic % | $Fe_{1.9}Ca_{0.1}Si_5N_8$ theoretical atomic % |
|---|---|---|---|
| **Fe** | 284.4 | 12.4 | 12.67 |
| **Ca** | 15.0 | 0.9 | 0.67 |
| **Si** | 401.1 | 34.7 | 33.33 |
| **Na** | 299.5 | 52.0 | 53.33 |
| | | | |
| **Fe+Ca/Si** | 2/5.2 | | |

[a] values for nitrogen were calculated from the difference to 1 g

## B.7.3. Details on SEM and EDX

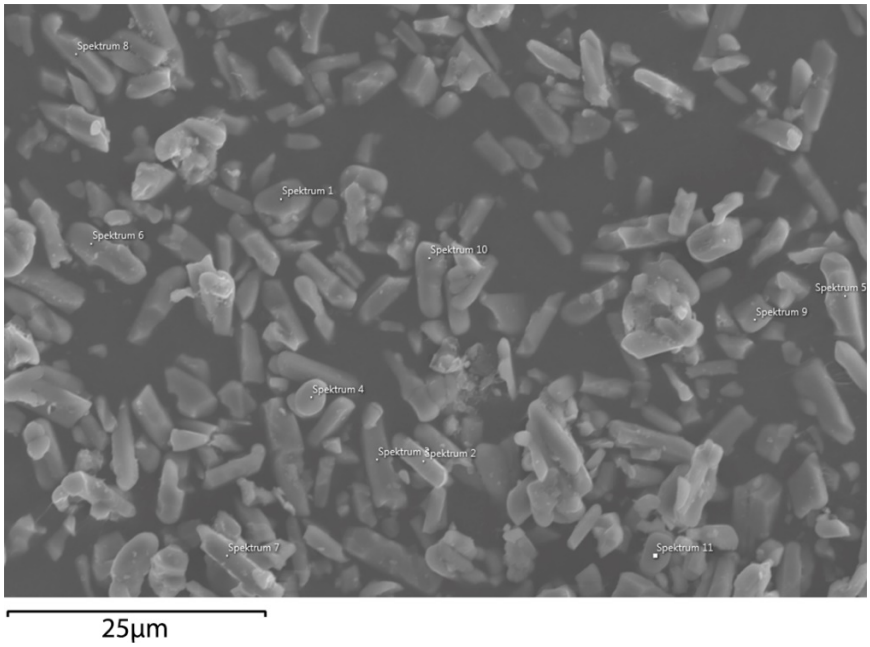


**Figure B.16:** Scanning electron micrograph of a $Fe_{1.9}Ca_{0.1}Si_5N_8$ powder sample.

**Table B.24:** EDX analysis (atomic percent) of $Fe_{1.9}Ca_{0.1}Si_5N_8$ powder shown in Figure B.16.

| | Spektrum 1 | Spektrum 2 | Spektrum 3 | Spektrum 4 | Spektrum 5 | Spektrum 6 |
|---|---|---|---|---|---|---|
| **N** | 44 | 50 | 53 | 55 | 58 | 51 |
| **O** | 3 | 4 | 3 | 3 | 6 | 4 |
| **Si** | 38 | 33 | 32 | 30 | 25 | 32 |
| **Ca** | 1 | 1 | 1 | <1 | 1 | 1 |
| **Fe** | 14 | 13 | 12 | 11 | 9 | 11 |
| **Cl** | -- | -- | -- | <1 | -- | -- |
| **(Fe+Ca)/Si** | 2/5.1 | 2/4.7 | 2/4.9 | 2/5.3 | 2/5 | 2/5.3 |

| | Spektrum 7 | Spektrum 8 | Spektrum 9 | Spektrum 10 | Spektrum 11 | Average |
|---|---|---|---|---|---|---|
| **N** | 53 | 52 | 55 | 57 | 28 | 52.8 |
| **O** | 2 | 3 | 3 | 4 | 2 | 3.5 |
| **Si** | 32 | 33 | 30 | 28 | 47 | 31.3 |
| **Ca** | 1 | 1 | 1 | 1 | 1 | 1 |
| **Fe** | 12 | 12 | 11 | 10 | 22 | 11.5 |
| **Cl** | -- | -- | -- | -- | -- | <1 |
| **(Fe+Ca)/Si** | 2/4.9 | 2/5.1 | 2/5 | 2/5.1 | 2/4.1 | 2/5 |

The values detected for Spektrum 11 may refer to one or more side phases.

## B.7.4. Comparison Between PXRDs of $Fe_2Si_5N_8$ and $Fe_{1.9}Ca_{0.1}Si_5N_8$

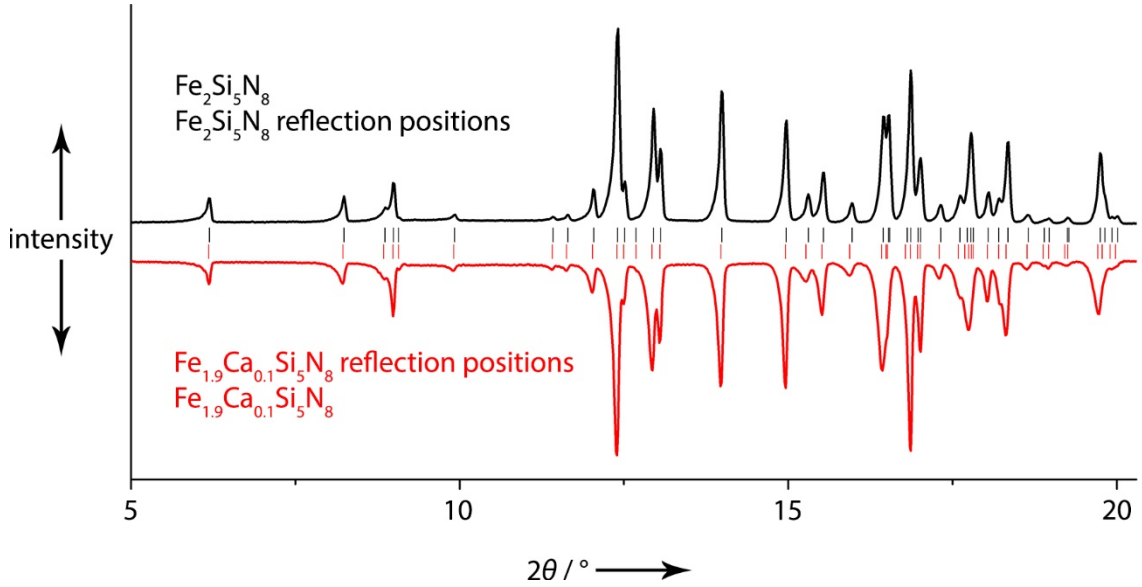


**Figure B.17:** Comparison of PXRDs of $Fe_2Si_5N_8$ (black) and $Fe_{1.9}Ca_{0.1}Si_5N_8$ (red) with reflection positions. As expected a full exchange of $Ca^{2+}$ by $Fe^{2+}$ leads to smaller lattice parameters and therefore a shift of reflection positions to larger angles, compared to partial exchange.

## B.7.5. Optical Microscopy


**Figure B.18:** Picture of a $Fe_{1.9}Ca_{0.1}Si_5N_8$ sample.

## B.8 References


[1] H. M. Rietveld, "A Profile Refinement Method for Nuclear and Magnetic Structures", *J. Appl. Crystallogr.* **1969**, *2*, 65–71.

[2] A. A. Coelho, *TOPAS-Academic*, Version 4.1, Coelho Software, Brisbane (Australia), **2007**.

[3] R. W. Cheary, A. Coelho, "A Fundamental Parameters Approach to X-Ray Line-Profile Fitting", *J. Appl. Crystallogr.* **1992**, *25*, 109–121.

[4] R. W. Cheary, A. A. Coelho, J. P. Cline, "Fundamental Parameters Line Profile Fitting in Laboratory Diffractometers", *J. Res. Natl. Inst. Stand. Technol.* **2004**, *109*, 1–25.

[5] *Origin 6.1*, OriginLab Corporation, **1991–2000**.

[6] K. Brandenburg, *Diamond Version 3.2k*, **2014**.

[7] R. A. Brand, *Normos Mössbauer Fitting Program*, University of Duisburg, Duisburg (Germany), **2002**.

[8] T. Schlieper, W. Schnick, "Nitrido-Silicate. I Hochtemperatur-Synthese und Kristallstruktur von $Ca_2Si_5N_8$", *Z. Anorg. Allg. Chem.* **1995**, *621*, 1037–1041.

[9] a) V. A. Blatov, A. P. Shevchenko, *TOPOS Version 4.0*, Samara State University, **1989 – 2010**; b) V. A. Blatov, A. P. Shevchenko, V. N. Serezhkin, "*TOPOS*3.1 – program package for multipurpose geometrical and topological analysis of crystal structures", *J. Appl. Crystallogr.* **1999**, *32*, 377; c) V. A. Blatov, "VORONOI–DIRICHLET POLYHEDRA IN CRYSTAL CHEMISTRY: THEORY AND APPLICATIONS", *Crystallogr. Rev.* **2004**, *10*, 249–318; d) V. A. Blatov, G. D. Ilyushin, O. A. Blatov, N. A. Anurova, A. K. Ivanov-Schits, L. N. Dem'yanets, "Analysis of migration paths in fast-ion conductors with Voronoi-Dirichlet partition", *Acta Crystallogr., Sect. B: Struc. Sci.* **2006**, *62*, 1010–1018; e) N. A. Anurova, V. A. Blatov, G. D. Ilyushin, O. A. Blatova, A. K. Ivanov-Schitz, L. N. Dem'yanets, "Migration maps of $Li^+$ cations in oxygen-containing compounds", *Solid State Ionics* **2008**, *179*, 2248–2254.

[10] W. H. Baur, "Effective Ionic Radii in Nitrides", *Crystallogr. Rev.* **1987**, *1*, 59–83.

[11] B. H. Toby, "*CMPR* – a powder diffraction toolkit", *J. Appl. Crystallogr.* **2005**, *38*, 1040–1041.

[12] D. Hardie, K. H. Jack, "Crystal Structures of Silicon Nitride", *Nature* **1957**, *180*, 332–333.

[13] D. R. Wilburn, W. A. Bassett, "Hydrostatic compression of iron and related compounds: an overview", *Am. Mineral.* **1978**, *63*, 591–596.

[14] E. Dowty, D. H. Lindsley, "Mössbauer Spectra of Synthetic Ca–Fe Pyroxenoids and Lunar Pyroxferroite", *Contrib. Mineral. Petrol.* **1974**, *48*, 229–232.

[15] N. L. Costa, J. Danon, R. M. Xavier, "MEASUREMENT OF NUCLEAR QUADRUPOLE INTERACTION IN IRON COMPLEXES USING THE MOSSBAUER EFFECT", *J. Phys. Chem. Solids* **1962**, *23*, 1783–1785.

[16] G. K. Shenoy, F. E. Wagner, *Mössbauer Isomer Shifts*, North-Holland Publishing Company, Amsterdam, **1978**.

[17] A. Sawaoka, S. Miyahara, S.-i. Akimoto, "Magnetic Properties of Several Metasilicates and Metagermanates with Pyroxene Structure", *J. Phys. Soc. Jpn.* **1968**, *25*, 1253–1257.

[18] J. M. D. Coey, S. Ghose, "MAGNETIC ORDER IN HEDENBERGITE: $CaFeSi_2O_6$", *Solid State Commun.* **1985**, *53*, 143–145.

# C Supporting Information – Chapter 4

## C.1 General

### Inert conditions

All work, except for the washing steps, was carried out excluding humidity and air in an atmosphere of dried and purified argon (99.999% Westfalen AG or, Air Liquide) using high-vacuum glass lines ($<1\cdot10^{-3}$ mbar) or a glovebox (MBraun). Glass vessels used for reactions up to 450 °C were made of borosilicate glass. For reactions at temperatures higher than 450 °C. silica glass ampoules were used. All vessel materials were flame-dried under vacuum before use.

### PXRD

Data were measured on Stoe Stadi P diffractometers ($\lambda$ = 0.7093 Å, Mo-K$\alpha_1$ or $\lambda$ = 1.5406 Å, Cu-K$\alpha_1$, both with Ge(111)-monochromator) in parafocussing modified Debye-Scherrer geometry using MYTHEN 1K Si-strip detectors (Dectris, Baden, Switzerland). RIETVELD refinements were carried out with TOPAS-Academic Version 4.1.[1,2] Peak shapes were fitted using a fundamental parameters approach and the background using a shifted Chebyshev function.[3,4]

### Visualization

RIETVELD refinements and powder patterns were visualized with Origin 6.1.[5] Crystal structures were visualized with VESTA 3.[6]

### SEM and EDX

Scanning electron microscopy and EDX was performed on a Dualbeam Helios Nanolab G3 UC (FEI) microscope with X-Max 80 SDD detector. At each measuring spot, an area measurement was performed in order to receive information about the average compositions of $M_{0.2}AE_{1.7}Si_5N_8$ samples.

## TEM

For sample preparation, part of a bulk sample with the nominal composition $U_{0.2}Sr_{1.7}Si_5N_8$ were ground in absolute ethanol and drop-cast on copper grids covered with continuous carbon film (Plano GmbH, Germany). The grids were mounted on a double-tilt holder and transferred into a FEI Tecnai G20 with thermal emitter ($LaB_6$) operating at 200 keV. Selected area diffraction (SAED) patterns and bright-field images were recorded using a TVIPS camera (TemCam F216, Tietz) with a resolution of 2048 × 2048 pixels. EDX spectra were recorded using an Apollo XLT (EDAX) detector. Suitable crystals for single crystal structure determination were found by means of SAED patterns and EDX. For later positioning of these crystals in the synchrotron beam, maps of the grids were recorded.

For STEM-HAADF, crystals of $U_{0.5x}Sr_{2-0.75x}Si_5N_8$ ($x \approx 1.05$) were ground in absolute ethanol and drop-cast on copper grids covered with holey carbon film (Plano GmbH, Germany). The grids were mounted on a double-tilt holder and transferred into a Cs DCOR probe-corrected Titan Themis 300 (FEI, USA) TEM equipped with X-FEG, post-column filter (Enfinium ER-799), US1000XP/FT camera system (Gatan, Germany) and a windowless, 4-quadrant Super-X EDX detector. TEM images were recorded using a 4k × 4k FEI Ceta CMOS camera. The microscope was operated at 300 kV accelerating voltage for SAED and STEM-HAADF (convergence angle of 16.6 mrad, 50 µm aperture, detector inner half angle 63 mrad for 100 mm camera length). For evaluation of the TEM data, the following software was used: Digital Micrograph (Fourier filtering of STEM images), ProcessDiffraction7 (geometric calculations for SAED), JEMS (SAED simulations), ES Vision (EDX spectra) and quantitative STEM-HAADF simulations.

## Single-crystal XRD

A single crystal of $U_{0.5x}Sr_{2-0.75x}Si_5N_8$ ($x \approx 1.05$) was centered optically and by fluorescence scans in the synchrotron beam of the beamline ID11, ESRF, Grenoble, on a Symétrie Hexapods Nanopos device ($\lambda$ = 0.309 Å). Data were collected with a Frelon CCD detector. Intensities were integrated with CrysAlisPro (Agilent Technologies)[7] and semi-empirical absorption correction was performed with SADABS.[8] A correction for incomplete absorption of high-energy radiation in the phosphor of the CCD detector was applied.[9] The structure was solved and refined with SHELX-97.[10]

### Optical microscopy

Optical microscopy was performed on a digital microscope "VHX-5000" (Keyence Microscope Europe) with the object lens VH-Z20T.

## C.2 Chemicals

**Table C.1:** List of chemicals for this work.

| Substance | Information | Producer |
|---|---|---|
| $Ar_{(g)}$ | 99.999% | Air Liquide |
| KOH | >85% | Bernd Kraft |
| Silica gel | humidity indicator (orange gel) | VWR |
| Molecular sieve | 3 Å | Fluka |
| $P_4O_{10}$ | ≥ 99% | Carl Roth |
| BTS catalyst | operating temperature = 170 °C | Merck Millipore |
| α-$Ca_2Si_5N_8$ | commercial sample | Lumileds Development Center Aachen |
| $HNO_{3(aq)}$ | 69% | Brenntag |
| **Substance** | **Information** | |
| $Sr_2Si_5N_8$ | prepared from $SrH_2$ and $Si_3N_4$ in $N_2$ according to P. J. SCHMIDT *et al.*[11] | |
| $ScCl_3$ | prepared from Sc and HCl(g) according to L. F. DRUDING *et al.*[12] | |
| $UCl_3$ | prepared from $UCl_4$ and Si according to S. S. RUDEL *et al.*[13] | |

## C.3 $Sc_{0.2}Ca_{1.7}Si_5N_8$

### C.3.1. Experimental Details on the Ion Exchange Reaction

$Sc_{0.2}Ca_{1.7}Si_5N_8$ was prepared by ion exchange between α-$Ca_2Si_5N_8$ and $ScCl_3$ in a sealed tantalum ampoule.[12, 14]

**Table C.2:** Weighted sample for the ion exchange toward $Sc_{0.2}Ca_{1.7}Si_5N_8$.

| α-$Ca_2Si_5N_8$ | $ScCl_3$ |
|---|---|
| 219.8 mg | 20 mg |
| 0.7 mmol | 0.1 mmol |

**Table C.3:** Temperature program of the tube furnace for the ion exchange leading to $Sc_{0.2}Ca_{1.7}Si_5N_8$.

| Step | Starting *T* / °C | Target *T* / °C | *t* / h | Δ*T* / °C · $h^{-1}$ |
|---|---|---|---|---|
| 1 | 25 | 980 | 3 | 318 |
| 2 | 980 | 980 | 3 | 0 |
| 3 | 980 | 500 | 10 | –48 |

The product mixture was subsequently washed in water to remove $CaCl_2$ formed during the reaction.

### C.3.2. Rietveld Refinement

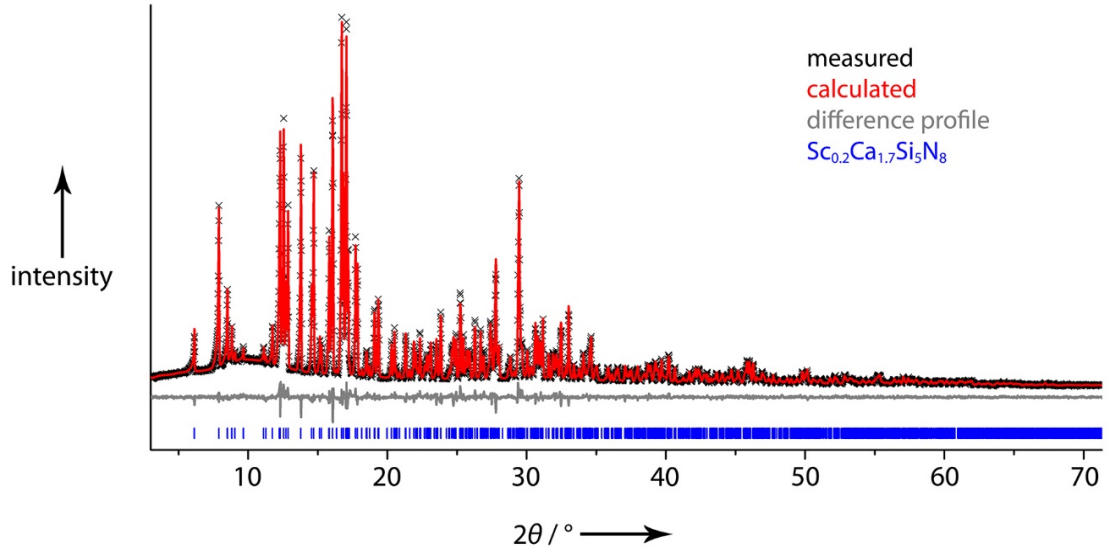


**Figure C.1:** RIETVELD refinement of $Sc_{0.2}Ca_{1.7}Si_5N_8$ (Mo-$K\alpha_1$).

In order to approximately take into account a certain range of homogeneity in terms of $Sc_xCa_{2-1.5x}Si_5N_8$ with different $x$, anisotropic peak broadening was modelled by the LeBail-Jouanneaux algorithm.[15]

## Constraints

RIETVELD refinement of $Sc_{0.2}Ca_{1.7}Si_5N_8$ was performed with common isotropic displacement parameters of Si and N, respectively.

Due to the mixed sites Ca1/Sc1 and Ca2/Sc2, isotropic displacement parameters and the coordinates ($x$, $y$, $z$) were set equal.

Since Sc and Ca cannot be differentiated by conventional X-ray data due to their similar electron count, both cation sites were refined as uniformly occupied by Ca, Sc and vacancies using the equations:

$$occ(\mathrm{Ca1}) + occ(\mathrm{Sc1}) + 0.5\ occ(\mathrm{Sc1}) = 1$$

$$occ(\mathrm{Ca2}) + occ(\mathrm{Sc2}) + 0.5\ occ(\mathrm{Sc2}) = 1$$

**Table C.4:** Crystallographic information on $Sc_{0.2}Ca_{1.7}Si_5N_8$, standard deviations in parentheses.

| **Formula** | **$Sc_{0.2}Ca_{1.7}Si_5N_8$** |
|---|---|
| **Formula mass / g · mol$^{-1}$** | 329.60 |
| **Crystal system** | monoclinic |
| **Space group** | *Cc* (no. 9) |
| **Lattice parameters / Å, °** | *a* = 14.2891(2)<br>*b* = 5.59340(8)<br>*c* = 9.69356(12)<br>*β* = 112.0205(8) |
| **Cell volume / Å$^3$** | 718.24(2) |
| ***Z*** | 4 |
| **X-ray density / g · cm$^{-3}$** | 3.05 |
| **Linear absorption coefficient / mm$^{-1}$** | 2.346 |
| **Radiation** | Synchrotron, $\lambda$ = 0.309 Å |
| **2*θ*-range / °** | 2.000–71.330 |
| **Temperature / °C** | 25(2) |
| **Data points** | 4623 |
| **Number of observed reflections** | 1703 |
| **Number of parameters** | 117, thereof 35 background |
| **Le Bail Jouanneaux parameters** | 12 of total 117 parameters |
| **Constraints** | 12 |
| $R_{wp}$ | 0.0465 |
| $R_p$ | 0.0355 |
| $R_{Bragg}$ | 0.0192 |
| $R_{exp}$ | 0.0327 |
| ***GOF*** | 1.421 |

**Table C.5:** List of interatomic distances / Å and bond angles / ° in $Sc_{0.2}Ca_{1.7}Si_5N_8$, standard deviations in parentheses.

| **Distances** | | | | **Angles** | |
|---|---|---|---|---|---|
| Ca1/Sc1–N1 | 2.235(12) | Si2–N6 | 1.73(10) | Si1–N1–Si4 | 111.5(9) |
| Ca1/Sc1–N2 | 2.385(13) | Si2–N8 | 1.747(11) | Si1–N2–Si3 | 129.7(8) |
| Ca1/Sc1–N7 | 2.636(12) | Si2–N7 | 1.76(2) | Si1–N5–Si5 | 124.2(8) |
| Ca1/Sc1–N5 | 2.648(13) | Si2–N3 | 1.778(12) | Si1–N7–Si2 | 125.1(10) |
| Ca1/Sc1–N6 | 2.672(9) | | | | |
| Ca1/Sc1–N5 | 2.920(12) | Si3–N2 | 1.589(14) | Si2–N3–Si3 | 116.4(5) |
| Ca1/Sc1–N8 | 3.059(10) | Si3–N3 | 1.726(11) | Si2–N3–Si5 | 117.1(6) |
| | | Si3–N4 | 1.782(11) | Si3–N3–Si5 | 125.7(6) |
| Ca2/Sc2–N5 | 2.285(14) | Si3–N8 | 1.791(14) | | |
| Ca2/Sc2–N7 | 2.404(12) | | | Si3–N4–Si4 | 115.6(5) |
| Ca2/Sc2–N2 | 2.420(14) | Si4–N8 | 1.680(12) | Si3–N4–Si5 | 128.7(6) |
| Ca2/Sc2–N1 | 2.657(12) | Si4–N1 | 1.69(2) | Si4–N4–Si5 | 108.7(5) |
| Ca2/Sc2–N4 | 2.853(11) | Si4–N6 | 1.815(11) | | |
| Ca2/Sc2–N8 | 3.071(9) | Si4–N4 | 1.855(10) | Si2–N6–Si4 | 126.8(5) |
| | | | | Si2–N6–Si5 | 117.5(6) |
| Si1–N7 | 1.70(2) | Si5–N3 | 1.719(12) | Si4–N6–Si5 | 113.9(6) |
| Si1–N2 | 1.742(12) | Si5–N4 | 1.721(12) | | |
| Si1–N5 | 1.748(12) | Si5–N5 | 1.739(13) | Si2–N8–Si3 | 107.8(6) |
| Si1–N1 | 1.78(2) | Si5–N6 | 1.742(12) | Si2–N8–Si4 | 128.7(6) |
| | | | | Si3–N8–Si4 | 123.5(7) |

**Table C.6:** Fractional atomic coordinates, isotropic displacement parameters and site occupancies in $Sc_{0.2}Ca_{1.7}Si_5N_8$, standard deviations in parentheses.

| **Atom** | **Wyckoff symbol** | ***x*** | ***y*** | ***z*** | $U_{iso}$ | **Occupancy** |
|---|---|---|---|---|---|---|
| Sc1 | 4*a* | 0.00000 | 0.7618(10) | 0.00000 | 0.0144(14) | 0.08(6) |
| Sc2 | 4*a* | 0.6076(2) | 0.7464(12) | 0.1953(3) | 0.018(2) | 0.12(6) |
| Ca1 | 4*a* | 0.00000 | 0.7618(10) | 0.00000 | 0.0144(14) | 0.887(7) |
| Ca2 | 4*a* | 0.6076(2) | 0.7464(12) | 0.1953(3) | 0.018(2) | 0.813(7) |
| Si1 | 4*a* | 0.0513(6) | 0.8032(5) | 0.3445(9) | 0.0045(3) | 1 |
| Si2 | 4*a* | 0.7561(5) | 0.2102(11) | 0.3207(7) | 0.0045(3) | 1 |
| Si3 | 4*a* | 0.7484(5) | 0.4954(13) | 0.0573(7) | 0.0045(3) | 1 |
| Si4 | 4*a* | 0.3617(4) | 0.2025(10) | 0.3700(7) | 0.0045(3) | 1 |
| Si5 | 4*a* | 0.8512(5) | 0.0047(12) | 0.1208(7) | 0.0045(3) | 1 |
| N1 | 4*a* | 0.9839(10) | 0.619(2) | 0.4255(14) | 0.0020(7) | 1 |
| N2 | 4*a* | 0.1292(9) | 0.027(2) | 0.9941(13) | 0.0020(7) | 1 |
| N3 | 4*a* | 0.7925(6) | 0.244(2) | 0.1654(8) | 0.0020(7) | 1 |
| N4 | 4*a* | 0.7992(7) | 0.754(2) | 0.1669(9) | 0.0020(7) | 1 |
| N5 | 4*a* | 0.9811(9) | 1.019(2) | 0.2174(12) | 0.0020(7) | 1 |
| N6 | 4*a* | 0.8296(6) | 0.0136(14) | 0.9317(10) | 0.0020(7) | 1 |
| N7 | 4*a* | 0.6263(10) | 0.158(2) | 0.271(2) | 0.0020(7) | 1 |
| N8 | 4*a* | 0.7946(7) | 0.485(2) | 0.4096(10) | 0.0020(7) | 1 |

## C.3.3. Details on SEM and EDX

**Table C.7:** EDX analysis (atomic percent) of a $Sc_{0.2}Ca_{1.7}Si_5N_8$ sample, standard deviations in parentheses.

| | Spot 1 | Spot 2 | Spot 3 | Spot 4 | Spot 5 | Spot 6 | Spot 7 | Spot 8 |
|---|---|---|---|---|---|---|---|---|
| **N** | 58 | 53 | 54 | 57 | 57 | 59 | 58 | 57 |
| **Si** | 30 | 33 | 34 | 30 | 31 | 30 | 30 | 31 |
| **Ca** | 10 | 12 | 12 | 11 | 10 | 10 | 10 | 11 |
| **Sc** | 1 | 1 | 1 | 1 | 1 | 1 | 1 | 1 |
| **(Ca+Sc)/Si** | 1.8/5 | 2/5 | 1.9/5 | 2/5 | 1.8/5 | 1.8/5 | 1.8/5 | 1.9/5 |
| | **Spot 9** | **Spot 10** | | **Calculated for $Sc_{0.2}Ca_{1.7}Si_5N_8$** | | | **Average** | |
| **N** | 53 | 51 | | 53.7 | | | 56(3) | |
| **Si** | 34 | 36 | | 33.6 | | | 32(2) | |
| **Ca** | 13 | 12 | | 11.5 | | | 11(1) | |
| **Sc** | 1 | 2 | | 1.3 | | | 1(0) | |
| **(Ca+Sc)/Si** | 2.1/5 | 1.9/5.3 | | 1.9/5 | | | 1.9/5 | |

Experimental determined EDX values fit well to the composition $Sc_{0.2}Ca_{1.7}Si_5N_8$.

## C.3.4. Details on ICP-OES

**Table C.8:** ICP-OES analysis of $Sc_{0.2}Ca_{1.7}Si_5N_8$.

| Element | Amount / mg · g$^{-1}$ | Atomic % | Atomic % calculated for $Sc_{0.2}Ca_{1.7}Si_5N_8$ |
|---|---|---|---|
| **Sc** | 22.4 | 1.1 | 1.3 |
| **Ca** | 222.7 | 12.6 | 11.5 |
| **Si** | 440.9 | 35.5 | 33.6 |
| **Na** | 314 | 50.8 | 53.7 |
| | | | |
| **(Ca+Sc)/Si** | 1.9/5 | | |

[a] values for nitrogen were calculated from the difference to 1 g

The experimental values of ICP-OES are in good agreement with the composition of $Sc_{0.2}Ca_{1.7}Si_5N_8$.

## C.3.5. Optical Microscopy

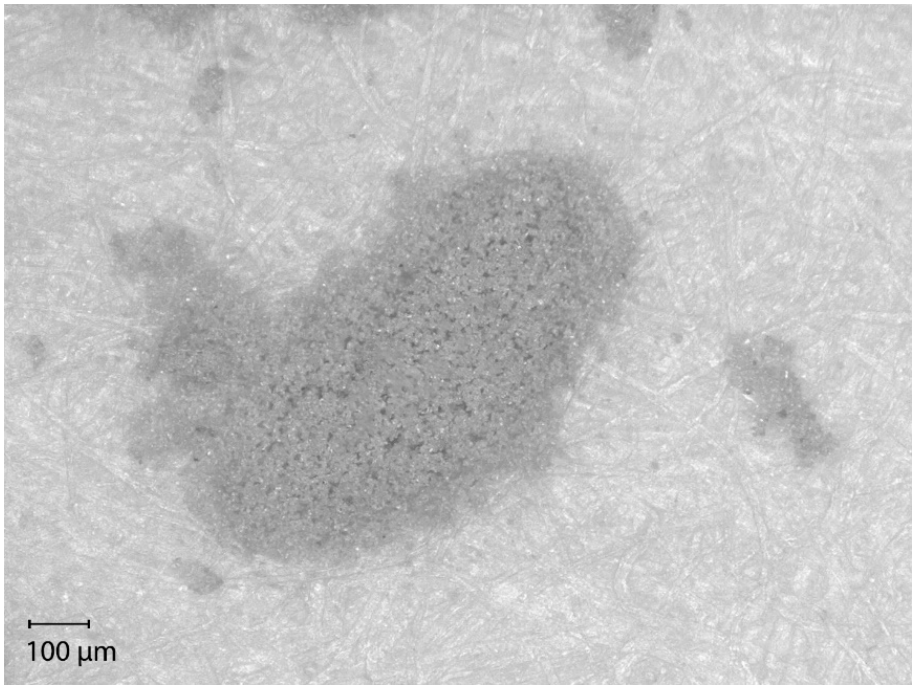


**Figure C.2:** Image of a $Sc_{0.2}Ca_{1.7}Si_5N_8$ (gray) sample on a filter paper (white).

## C.4 $U_{0.5x}Sr_{2-0.75x}Si_5N_8$ ($x \approx 1.05$)

### C.4.1. TEM

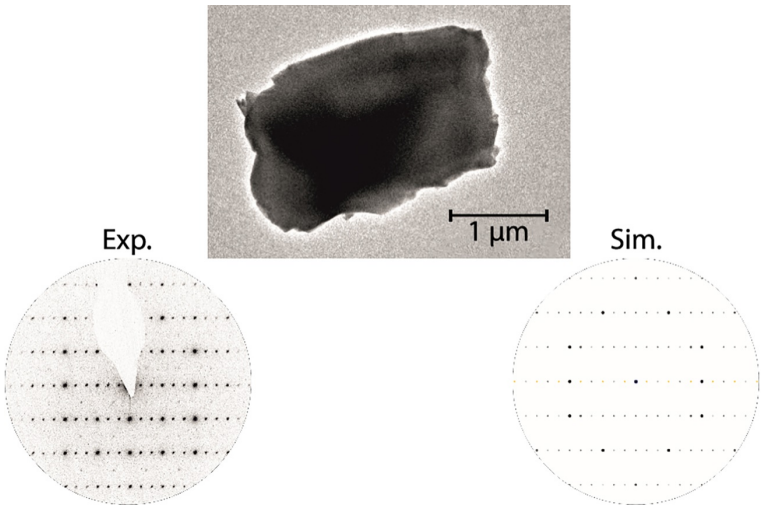


**Figure C.3:** Top: Crystal of $U_{0.5x}Sr_{2-0.75x}Si_5N_8$ ($x \approx 1.05$) used for collection of synchrotron data; bottom: SAED pattern along [101] and simulation based on the refined structure model.

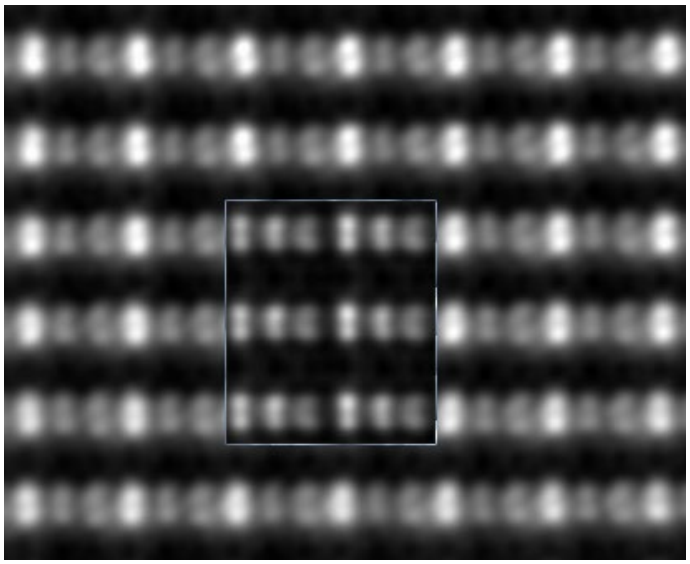

**Figure C.4:** STEM-HAADF image of an $U_{0.5x}Sr_{2-0.75x}Si_5N_8$ ($x \approx 1.05$) particle and simulation (inset) along [101] showing the triplication of the a lattice parameter due to partial ordering of U atoms.

## C.4.2. Single crystal XRD

**Table C.9:** Crystallographic information on $U_{0.5x}Sr_{2-0.75x}Si_5N_8$ ($x \approx 1.05$), standard deviations in parentheses.

| **Formula** | **$U_{0.5x}Sr_{2-0.75x}Si_5N_8$ ($x \approx 1.05$)** |
|---|---|
| **Formula mass / g · mol$^{-1}$** | 483.64 |
| **Crystal system** | orthorhombic |
| **Space group** | *Pmn*2$_1$ (no. 31) |
| **Cell parameters / Å** | *a* = 17.1295(3)<br>*b* = 6.7890(2)<br>*c* = 9.3079(2) |
| **Cell volume / Å$^3$** | 1082.44(4) |
| ***Z*** | 6 |
| ***F*(000)** | 1322.1 |
| **Calculated density $\rho$ / g · cm$^{-3}$** | 4.452 |
| **Absorption coefficient $\mu$ /mm$^{-1}$** | 3.295 |
| **Radiation** | Synchrotron, $\lambda$ = 0.309 Å |
| **Temperature / °C** | 25(2) |
| **$\theta$-range / deg.** | $1.819 \leq \theta \leq 14.193$ |
| **Total no. of reflections** | 5984 |
| **Independent reflections** | 3475 |
| **Absorption correction** | semi-empirical |
| **$R_{int}$, $R_\sigma$** | 0.082, 0.134 |
| **Refined parameters** | 108 |
| **Constraints** | 8 |
| **Restraints** | 7 |
| **Goodness of fit** | 1.013 |
| **$R_1$ (all data), $R_1$ [$F^2 > 2\sigma(F^2)$]** | 0.099, 0.087 |
| **$wR_2$ (all data), $wR_2$ [$F^2 > 2\sigma(F^2)$]** | 0.241, 0.224 |
| **$\Delta\rho_{max}$, $\Delta\rho_{min}$ / e · Å$^{-3}$** | 7.202, −6.008 |

## Constraints and Restraints

Refinement of $U_{0.5x}Sr_{2-0.75x}Si_5N_8$ ($x \approx 1.05$) was performed with common isotropic displacement parameters for…

… the mixed site Sr3/U3,

… the mixed site Sr2A/U2A,

… the two sites U1A and U1B due the short interatomic distance,

… N atoms linked to two Si atoms,

… N atoms linked to three Si atoms,

… all Si atoms.

Refinement of $U_{0.5x}Sr_{2-0.75x}Si_5N_8$ ($x \approx 1.05$) was performed with shared *x*,*y*,*z* coordinates for…

… the mixed site Sr3/U3,

… the mixed site Sr2A/U2A.

Charge neutrality constraint: ∑(cation charges) = ∑(anion charges)

Sums of site occupation for sites…

…U1A and U1B,

…Sr2A, U2A and Sr2B,

…Sr3 and U3 were each constrained to 1 after refinement pointed towards values close to 1.

In case of distances shorter as commonly found between cation positions the sum of their occupations were also fixed to 1. This was done for U1A and Sr4 as well as for Sr2A/U2A and Sr4.

**Table C.10:** Fractional atomic coordinates, isotropic displacement parameters and site occupancies in $U_{0.5x}Sr_{2-0.75x}Si_5N_8$ ($x \approx 1.05$), standard deviations in parentheses.

| Atom | Wyckoff symbol | *x* | *y* | *z* | $U_{iso}$ / $U_{eq}$ | Occupancy |
|---|---|---|---|---|---|---|
| U1A | 2*a* | 1/2 | 0.0927(9) | 0.3295(4) | 0.0115(5) | 0.7882(3) |
| U1B | 2*a* | 1/2 | 0.110(4) | 0.308(3) | 0.0115(5) | 0.2118(3) |
| Sr2A | 4*b* | 0.63932(12) | 0.9236(3) | 0.7676(3) | 0.0142(4) | 0.6195(3) |
| U2A | 4*b* | 0.63932(12) | 0.9236(3) | 0.7676(3) | 0.0142(4) | 0.1687(3) |
| Sr2B | 4*b* | 0.6687(11) | 0.908(3) | 0.803(3) | 0.041(5) | 0.2118(3) |
| Sr3 | 4*b* | 0.67045(9) | 0.8812(3) | 0.1484(3) | 0.0155(4) | 0.8805(3) |
| U3 | 4*b* | 0.67045(9) | 0.8812(3) | 0.1484(3) | 0.0155(4) | 0.1195(3) |
| Sr4 | 2*a* | 1/2 | 0.116(4) | 0.660(4) | 0.041(5) | 0.2118(3) |
| Si11 | 4*b* | 0.5832(3) | 0.3442(9) | 0.9649(7) | 0.0040(4) | 1 |
| Si12 | 4*b* | 0.7513(3) | 0.6826(9) | 0.4596(7) | 0.0040(4) | 1 |
| Si13 | 4*b* | 0.4167(3) | 0.6683(9) | 0.4675(7) | 0.0040(4) | 1 |
| Si21 | 2*a* | 1/2 | 0.9621(13) | 0.9851(9) | 0.0040(4) | 1 |
| Si22 | 4*b* | 0.8333(3) | 0.9286(9) | 0.9640(7) | 0.0040(4) | 1 |
| Si31 | 2*a* | 1/2 | 0.5965(12) | 0.1887(10) | 0.0040(4) | 1 |
| Si32 | 4*b* | 0.6691(3) | 0.4339(9) | 0.6833(7) | 0.0040(4) | 1 |
| Si41 | 2*a* | 1/2 | 0.6014(12) | 0.7504(10) | 0.0040(4) | 1 |
| Si42 | 4*b* | 0.6629(3) | 0.4074(9) | 0.2426(7) | 0.0040(4) | 1 |
| N11 | 2*a* | 1/2 | 0.838(4) | 0.155(3) | 0.0111(12) | 1 |
| N12 | 4*b* | 0.1807(10) | 0.788(3) | 0.112(2) | 0.0111(12) | 1 |
| N21 | 4*b* | 0.5839(10) | 0.098(3) | 0.992(2) | 0.0111(12) | 1 |
| N22 | 4*b* | 0.7491(10) | 0.930(3) | 0.438(2) | 0.0111(12) | 1 |
| N23 | 4*b* | 0.4154(10) | 0.915(3) | 0.482(2) | 0.0111(12) | 1 |
| N31 | 4*b* | 0.5839(9) | 0.573(3) | 0.640(2) | 0.0070(12) | 1 |
| N32 | 4*b* | 0.7499(9) | 0.405(3) | 0.140(2) | 0.0070(12) | 1 |
| N33 | 4*b* | 0.5851(8) | 0.474(3) | 0.131(2) | 0.0070(12) | 1 |
| N41 | 4*b* | 0.3329(9) | 0.584(3) | 0.377(2) | 0.0070(12) | 1 |
| N42 | 2*a* | 1/2 | 0.416(4) | 0.872(3) | 0.0070(12) | 1 |
| N51 | 4*b* | 0.6374(8) | 0.185(3) | 0.309(2) | 0.0111(12) | 1 |
| N52 | 2*a* | 1/2 | 0.815(4) | 0.840(3) | 0.0111(12) | 1 |
| N61 | 4*b* | 0.8330(9) | 0.578(3) | 0.378(2) | 0.0070(12) | 1 |
| N62 | 2*a* | 1/2 | 0.576(4) | 0.382(3) | 0.0070(12) | 1 |

**Table C.11:** Anisotropic displacement parameters for $U_{0.5x}Sr_{2-0.75x}Si_5N_8$ ($x \approx 1.05$), least-squares standard deviations in parentheses.

| Atom | $U_{11}$/ Å$^2$ | $U_{22}$ / Å$^2$ | $U_{33}$ / Å$^2$ | $U_{23}$ / Å$^2$ | $U_{13}$ / Å$^2$ | $U_{12}$ / Å$^2$ |
|---|---|---|---|---|---|---|
| U1A | 0.0125(4) | 0.0070(13) | 0.015(2) | 0.0041(8) | 0 | 0 |
| U1B | 0.0125(4) | 0.0070(13) | 0.015(2) | 0.0041(8) | 0 | 0 |
| Sr2A | 0.0167(8) | 0.0099(9) | 0.0159(10) | −0.0008(6) | 0.0031(7) | −0.0050(5) |
| U2A | 0.0167(8) | 0.0099(9) | 0.0159(10) | −0.0008(6) | 0.0031(7) | −0.0050(5) |
| Sr3 | 0.0169(6) | 0.0114(8) | 0.0183(9) | 0.0044(6) | 0.0004(6) | 0.0015(5) |
| U3 | 0.0169(6) | 0.0114(8) | 0.0183(9) | 0.0044(6) | 0.0004(6) | 0.0015(5) |

### C.4.3. CHARDI Calculations

Vesta 3 was used to calculate CHARDI values according to the theory of HOPPE *et al.*[6, 16] The results are shown in Table C.12 for the cation positions in $U_{0.5x}Sr_{2-0.75x}Si_5N_8$ ($x \approx 1.05$).

**Table C.12:** CHARDI values calculated for the cation sites in $U_{0.5x}Sr_{2-0.75x}Si_5N_8$ ($x \approx 1.05$), where $Q$ is the charge received by the cation and $q$ is the formal charge depending on the occupancy.

| Cation site | $Q$ | $q$ |
|---|---|---|
| U1A | 2.332 | 2.365 |
| U1B | 0.622 | 0.635 |
| Sr2A/U2A | 1.682 | 1.745 |
| Sr2B | 0.397 | 0.424 |
| Sr3/U3 | 2.025 | 2.120 |
| Sr4 | 0.418 | 0.424 |

## C.5 Bulk Sample with the Average Composition $U_{0.2}Sr_{1.7}Si_5N_8$

### C.5.1. Experimental Details on the Ion Exchange Reaction

$U_{0.2}Sr_{1.7}Si_5N_8$ was prepared by ion exchange between $Sr_2Si_5N_8$ (186.3 mg) and $UCl_3$ (30 mg) in a sealed tantalum ampoule.[14,17]

**Table C.13:** Weighted sample for the ion exchange toward $U_{0.2}Sr_{1.7}Si_5N_8$.

| $Sr_2Si_5N_8$ | $UCl_3$ |
|---|---|
| 186.3 mg | 30 mg |
| 0.4 mmol | 0.1 mmol |

**Table C.14:** Temperature program of the tube furnace for the ion exchange leading to $U_{0.2}Sr_{1.7}Si_5N_8$.

| Step | Starting $T$ / °C | Target $T$ / °C | $t$ / h | $\Delta T$ / °C · h$^{-1}$ |
|---|---|---|---|---|
| 1 | 25 | 980 | 3 | 275 |
| 2 | 980 | 980 | 3 | 0 |
| 3 | 980 | 500 | 10 | −35 |

After the reaction, the tantalum ampoule was opened, the product mixture was washed in water at 25 °C and afterwards treated with $H_2O$, $HNO_3$ and KOH in several step given in Table C.15.

### C.5.2. Treatment of $U_{0.2}Sr_{1.7}Si_5N_8$ in Different Agents and ICP-MS

**Table C.15:** Treatment of $U_{0.2}Sr_{1.7}Si_5N_8$ with dissolved U-content according to ICP-MS.

| Step | Reagent | Volume / mL | Duration / h | Temperature / °C | $c$(U) | Percentage of total U |
|---|---|---|---|---|---|---|
| 1 | $H_2O$ | 15 | 24 | 25 | 70.8 µg/L | 0.005% |
| 2 | $H_2O$ | 15 | 24 | 90 | 684 µg/L | 0.049% |
| 3 | $HNO_3$ | 15 | 24 | 90 | 156.8 mg/L | 11.343% |
| 4 | $H_2O$ | 15 | 24 | 90 | 718 µg/L | 0.051% |
| 5 | KOH | 15 | 24 | 90 | 93.8 mg/L | 6.786% |
| 6 | $H_2O$ | 15 | 24 | 90 | 1.2 mg/L | 0.0868% |

## C.5.3. Details on SEM and EDX

**Table C.16:** EDX analysis (atomic percent) of an $U_{0.2}Sr_{1.7}Si_5N_8$ powder sample, standard deviations in parentheses.

| | Spot 1 | Spot 2 | Spot 3 | Spot 4 | Spot 5 | Spot 6 | Spot 7 | Spot 8 |
|---|---|---|---|---|---|---|---|---|
| **N** | 54 | 55 | 60 | 53 | 61 | 58 | 51 | 57 |
| **Si** | 34 | 33 | 30 | 37 | 30 | 31 | 36 | 32 |
| **Sr** | 12 | 11 | 10 | 3 | 8 | 11 | 12 | 11 |
| **U** | 0 | 1 | 0 | 7 | 2 | 0 | 1 | 0 |
| **(Sr+U)/Si** | 1.8/5 | 1.8/5 | 1.7/5 | 1.4/5 | 1.7/5 | 1.8/5 | 1.8/5 | 1.7/5 |
| | **Spot 9** | **Spot 10** | | **Calculated for $U_{0.2}Sr_{1.7}Si_5N_8$** | | | **Average** | |
| **N** | 53 | 65 | | 53.7 | | | 57(4) | |
| **Si** | 35 | 26 | | 33.6 | | | 32(3) | |
| **Sr** | 12 | 9 | | 11.5 | | | 10(3) | |
| **U** | 0 | 0 | | 1.3 | | | 1(2) | |
| **(Sr+U)/Si** | 1.7/5 | 1.7/5 | | 1.9/5 | | | 1.7/5 | |

The values fit well to the overall composition of the sample. Furthermore EDX analyses confirm that $U_{0.2}Sr_{1.7}Si_5N_8$ is composed of a phase similar to $Sr_2Si_5N_8$ containing small amounts of U and a second phase that contains high amounts of U.

## C.5.4. PXRD

**Table C.17:** Crystallographic information on the RIETVELD refinement of $U_{0.2}Sr_{1.7}Si_5N_8$ as mixture of $Sr_2Si_5N_8$ and $U_{0.5x}Sr_{2-0.75x}Si_5N_8$ ($x \approx 1.05$), standard deviations in parentheses.

| **Formula** | **$Sr_2Si_5N_8$** | **$U_{0.5x}Sr_{2-0.75x}Si_5N_8$ ($x \approx 1.05$)** |
|---|---|---|
| **Formula mass / g · mol$^{-1}$** | 427.72 | 483.64 |
| **Crystal system** | orthorhombic | |
| **Space group** | *Pmn*2$_1$ (no. 31) | |
| **Lattice parameters / Å, °** | *a* = 5.70962(4)<br>*b* = 6.81736(5)<br>*c* = 9.33401(7) | *a* = 17.1251(10)<br>*b* = 6.7838(2)<br>*c* = 9.3063(4) |
| **Cell volume / Å$^3$** | 363.322(5) | 1081.15(8) |
| ***Z*** | 2 | 6 |
| **X-ray density / g · cm$^{-3}$** | 3.90974(5) | 4.4578(4) |
| **Linear absorption coefficient / mm$^{-1}$** | 27.194 | 55.638 |
| **2*θ*-range / °** | 5.000–119.500 | |
| **Radiation** | Cu-K$\alpha_1$ ($\lambda$ = 1.5406 Å) | |
| **Temperature / °C** | 25(2) | |
| **Data points** | 7638 | |
| **Number of observed reflections** | 322 | 899 |
| **Number of parameters** | 42 | |
| ***R*$_{wp}$** | 0.0663 | |
| ***R*$_p$** | 0.0488 | |
| ***R*$_{Bragg}$** | 0.0276 | |
| ***R*$_{exp}$** | 0.0392 | |
| ***GOF*** | 1.691 | |

### C.5.5. Optical Microscopy

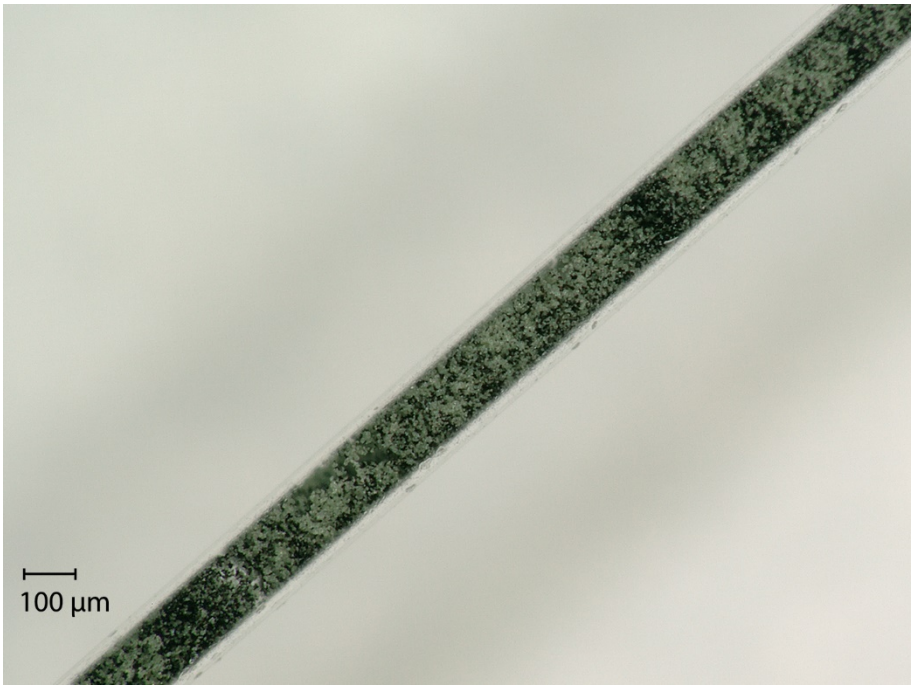


**Figure C.5:** Image of an $U_{0.2}Sr_{1.7}Si_5N_8$ sample composed of two phases (U-poor and U-rich).

## C.6 References

[1] H. M. Rietveld, "A Profile Refinement Method for Nuclear and Magnetic Structures", *J. Appl. Crystallogr.* **1969**, *2*, 65–71.

[2] A. A. Coelho, *TOPAS-Academic*, Version 4.1, Coelho Software, Brisbane (Australia), **2007**.

[3] R. W. Cheary, A. Coelho, "A Fundamental Parameters Approach to X-Ray Line-Profile Fitting", *J. Appl. Crystallogr.* **1992**, *25*, 109–121.

[4] R. W. Cheary, A. A. Coelho, J. P. Cline, "Fundamental Parameters Line Profile Fitting in Laboratory Diffractometers", *J. Res. Natl. Inst. Stand. Technol.* **2004**, *109*, 1–25.

[5] *Origin 6.1*, OriginLab Corporation, **1991–2000**.

[6] K. Momma, F. Izumi, "VESTA 3 for three-dimensional visualization of crystal, volumetric and morphology data", *J. Appl. Crystallogr.* **2011**, *44*, 1272–1276.

[7] Agilent Technologies, *CrysAlis Pro*, Yarnton, Oxfordshire, England, **2011**.

[8] Bruker AXS, Inc., *SADABS*, Madison, Wisconsin, USA, **2001**.

[9] G. Wu, B. L. Rodrigues, P. Coppens, "The correction of reflection intensities for incomplete absorption of high-energy X-rays in the CCD phosphor", *J. Appl. Crystallogr.* **2002**, *35*, 356–359.

[10] G. M. Sheldrick, "Crystal structure refinement with *SHELXL*", *Acta Crystallogr., Sect. C: Struct. Chem.* **2015**, *71*, 3–8.

[11] P. J. Schmidt, W. Mayr, B. S. Schreinemacher, J. Meyer, H. H. Bechtel, "Red Emitting Luminescent Materials", PCT/IB2011/055329, **2011**.

[12] L. F. Druding, J. D. Corbett, "Lower Oxidation States of the Lanthanides. Neodymium(II) Chloride and Iodide", *J. Am. Chem. Soc.* **1961**, *83*, 2462–2467.

[13] S. S. Rudel, H. L. Deubner, B. Scheibe, M. Conrad, F. Kraus, "Facile Syntheses of pure Uranium(III) Halides: $UF_3$, $UCl_3$, $UBr_3$, and $UI_3$", *Z. Anorg. Allg. Chem.* **2018**, *644*, 323–329.

[14] T. Schlieper, W. Schnick, "Nitrido-Silicate. I Hochtemperatur-Synthese und Kristallstruktur von $Ca_2Si_5N_8$", *Z. Anorg. Allg. Chem.* **1995**, *621*, 1037–1041.

[15] A. Le Bail, A. Jouanneaux, "A Qualitative Account for Anisotropic Broadening in Whole-Powder-Diffraction-Pattern Fitting by Second-Rank Tensors", *J. Appl. Crystallogr.* **1997**, *30*, 265–271.

[16] R. Hoppe, S. Voigt, H. Glaum, J. Kissel, H. P. Müller, K. Bernet, "A new route to charge distributions in ionic solids", *J. Less-Common Met.* **1989**, *156*, 105–122.

[17] T. Schlieper, W. Milius, W. Schnick, "Nitrido-silicate. II Hochtemperatur-Synthesen und Kristallstrukturen von $Sr_2Si_5N_8$ und $Ba_2Si_5N_8$", *Z. Anorg. Allg. Chem.* **1995**, *621*, 1380–1384.

# D Supporting Information – Chapter 5

## D.1 General

### Combustion analysis (CHNS)

The N content of $Pb_2Si_5N_8$ was determined by burning a sample in oxygen atmosphere using a Vario Micro Cube device from Elementar.

### ICP-OES

Elemental composition (Si and Pb) of $Pb_2Si_5N_8$ was determined by ICP-OES on a Varian CCD Simultaneous ICP AES Vista-RL device equipped with an autosampler SPS5.

### SEM

$Pb_2Si_5N_8$ crystal sizes and shapes were investigated with a Dualbeam Helios Nanolab G3 UC scanning electron microscope (FEI) equipped with a X-Max 80 SDD EDX detector (Oxford Instruments) for EDX. The sample was coated (BAL-TEC MED 020, BalTec AG) with carbon to reduce electrical charging due to the non-conducting character of the sample.

### Raman spectroscopy

of $Pb_2Si_5N_8$ was performed on a confocal Raman microscope (LabRSM HG UV/Vis, Horiba Jobin Ivon GmbH, combined with an Olympus BX 41 microscope) with a He-Ne laser with a 1 mm focus and a CCD detector.

### XPS

XPS was performed using non-monochromated Mg-Kα radiation (Al-filter) of a VSW TA10 X-ray source and a VSW HA100 hemispherical analyzer. Peak shifts due to charging of the sample were corrected by setting the C 1*s* peak to 284.8 eV, corresponding to adventitious carbon.[1] Spectra were acquired after cleaning of a $Pb_2Si_5N_8$ sample by $Ar^+$ sputtering (1 kV; ~7 µA). Prolonged $Ar^+$

sputtering did not lead to a significant change in Pb/$PbO_x$ ratio of the sample composition. The recorded peaks were fitted with a Doniach-Sunjic line shape convoluted with a Gaussian and linear background subtraction.[2]

## UV-Vis spectroscopy

Spectra were recorded on a Jasco V-650 UV-Vis spectrophotometer, equipped with a deuterium and a halogen lamp (Czerny-Turner monochromator with 1200 lines/mm concave grating, photomultiplier tub detector). Diffuse reflectance spectra were measured in the range of 200–800 nm (step size 1 nm).

## TEM

For sample preparation, crystals of $Pb_2Si_5N_8$ were ground in absolute ethanol and drop cast on copper finder grids covered with a continuous carbon film (Plano GmbH, Germany). The latter were mounted on a double-tilt holder and transferred into a FEI Tecnai G20 with thermal emitter ($LaB_6$) operating at 200 keV. SAED patterns and bright-field images were recorded using a TVIPS camera (TemCam F216, Germany) with a resolution of 2048 × 2048 pixels. EDX spectra were recorded using an Apollo XLT (EDAX) detector. The suitable crystal for single crystal structure determination was found by means of SAED patterns and EDX.

## Single-crystal XRD

XRD data of a $Pb_2Si_5N_8$ crystal, which was recovered by optical centering and fluorescence scans, were collected on the beamline ID11, ESRF, Grenoble, on a Symétrie Hexapods Nanopos device ($\lambda$ = 0.309 Å). Integration was done with CrysAlisPro (Agilent Technologies)[3] and multi-scan absorption correction with SADABS[4] as well as a correction for incomplete absorption of high-energy radiation in the phosphor of the CCD detector was applied.[5] The structure was solved and refined with SHELX-97.[6]

## PXRD

PXRD measurements were performed in cylindrical glass capillaries with a diameter of 0.3 ($Sr_2Si_5N_8$) or 0.5 mm ($Pb_2Si_5N_8$, diluted with 150 equivalents LiH) on a Stoe Stadi P diffractometer ($\lambda$ = 1.5406 Å, Cu-K$\alpha_1$, Ge(111) monochromator) in parafocussing Debye-Scherrer geometry using a MYTHEN 1K Si strip detector (Dectris, Baden, Switzerland). Data points were collected with 0.015° steps in the range of 5.000° ≤ 2$\theta$ ≤ 119.555°. RIETVELD refinements were performed using TOPAS-Academic Version 4.1.[7] Peak shapes were fitted by a fundamental parameters approach and the background by a shifted Chebyshev function.[8] Preferred crystal orientation was refined with spherical harmonics of fourth order. Absorption effects were corrected by a cylindrical absorption correction considering the capillary diameter and linear absorption coefficients of the phases.

## DFT-calculations

To model both phononic and electronic properties most effectively, DFT calculations followed two different strategies. We first utilized VASP[9] based on the projector augmented wave method[10] and plane-wave basis sets with a kinetic energy up to 500 eV. Exchange and correlation were described by the GGA parametrized by PBE but adding the D3 correction by Grimme to better approximate van-der-Waals-like interactions affecting vibrations. [11–12] The Brillouin zone was sampled on a Monkhorst-Pack mesh of 8 × 7 × 5 points in reciprocal space.[13] The electronic (atomic) structure was optimized until the difference between two iterative steps was below $10^{-9}$ eV ($10^{-7}$ eV) per simulation cell. Phonon properties were computed using Phonopy based on a 2 × 2 × 1 supercell and forces calculated with VASP on a 4 × 3 × 5 Monkhorst-Pack mesh.[14] For DPS the vibrational Brillouin zone was sampled on a 35 × 29 × 21 Monkhorst-Pack mesh, and the vibrational states were accounted within 1 $cm^{-1}$ steps. The DPS can be directly compared to infrared or Raman spectra in terms of the wavenumbers.[15] To analyse the vibrational modes, we also calculated their eigenvectors and visualized them with wxDragon.[16] Second, the electronic-structure calculations targeted at bonding properties also employed GGA-PBE[11] and the PAW method[10] but were carried out using ABINIT.[17] To anticipate effects of relativity and spin-orbit coupling due to the heavy element Pb, both SOC and non-SOC calculations were performed. Since all PAW potentials for ABINIT have been generated using the scalar-relativistic approximation,[18] all the relativistic effects within this approximation were also naturally included in the calculations. To achieve convergence, the *k*-point mesh of size 7 × 5 × 3 was set up based on the Monkhorst-Pack scheme,[13] whereas the cutoff energy

of 680 eV was used to control the number of plane waves. All crystallographic data were taken from the experimental results because DFT structure optimizations resulted in virtually unchanged lattice parameters and symmetry (Table D.14). Therefore, we only present results as obtained using experimental crystallographic data. To understand chemical bonding as well as to calculate Mulliken charges in $Pb_2Si_5N_8$ we further processed the electronic-structure data using the LOBSTER package,[19] a tool to reconstruct electronic structures through projection of PAW-based wavefunctions onto atomic-like basis sets. In order to show the difference between non-SOC and SOC calculations, a new LOBSTER routine capable of processing SOC data was developed. For the projection, we employed the local basis functions as given by pbeVaspFit2015[19b] including 6*s* and 6*p* for Pb, 3*s* and 3*p* for Si, and 2*s* and 2*p* for N.

## DTA/TGA investigation

A sample of $Pb_2Si_5N_8$ located in a corundum crucible was heated to 1300 °C in $N_2$ with a rate of 15 °C/min in a STA 449 F5 Jupiter device (Netzsch) equipped with a type W thermal element.

## Visualization

RIETVELD refinements were visualized with Origin 6.1.[20] Crystal structures were visualized with Diamond 3k.[21]

## D.2 Chemicals

**Table D.1:** List of chemicals for this work.

| Substance | Information | Producer |
|---|---|---|
| Ar(g) | 99.999% | Air Liquide |
| KOH | >85% | Bernd Kraft |
| Silica gel | humidity indicator (orange gel) | VWR |
| Molecular sieve | 3 Å | Fluka |
| $P_4O_{10}$ | ≥ 99% | Carl Roth |
| Ti (sponge) | operating temperature = 730 °C | Alfa Aesar |
| $Si_3N_4$ | amorphous | Ube Industries, Ltd. |
| $SrH_2$ | 99.5% | Materion |
| $PbCl_2$ | 98% | Sigma Aldrich |
| $HNO_3$ | 65% | Brenntag |
| LiH | phase pure by PXRD | |

## D.3 Starting Material $Sr_2Si_5N_8$

The starting material $Sr_2Si_5N_8$ was prepared by the hydride route.[22] $SrH_2$ and $Si_3N_4$ (Table D.2) were mixed in an agate mortar, filled into a tungsten crucible and transferred into the reactor of a radio-frequency furnace (Trumpf Hüttinger, Germany) purged by $N_2$. The reaction was performed in $N_2$ atmosphere applying the temperature program shown in Table D.3. $Sr_2Si_5N_8$ was obtained as a phase pure colorless solid.

**Table D.2:** Weighted sample for the preparation of $Sr_2Si_5N_8$.

| $SrH_2$ | $Si_3N_4$ |
|---|---|
| 300 mg | 391.2 mg |
| 3.3 mmol | 2.8 mmol |

**Table D.3:** Temperature program of the radio-frequency furnace for the preparation of $Sr_2Si_5N_8$.

| Step | Starting T / °C | Target T / °C | t / h | ΔT / °C · $h^{-1}$ |
|---|---|---|---|---|
| 1 | 25 | 1600 | 3 | 525 |
| 2 | 1600 | 1600 | 3 | 0 |
| 3 | 1600 | 500 | 5 | −211 |

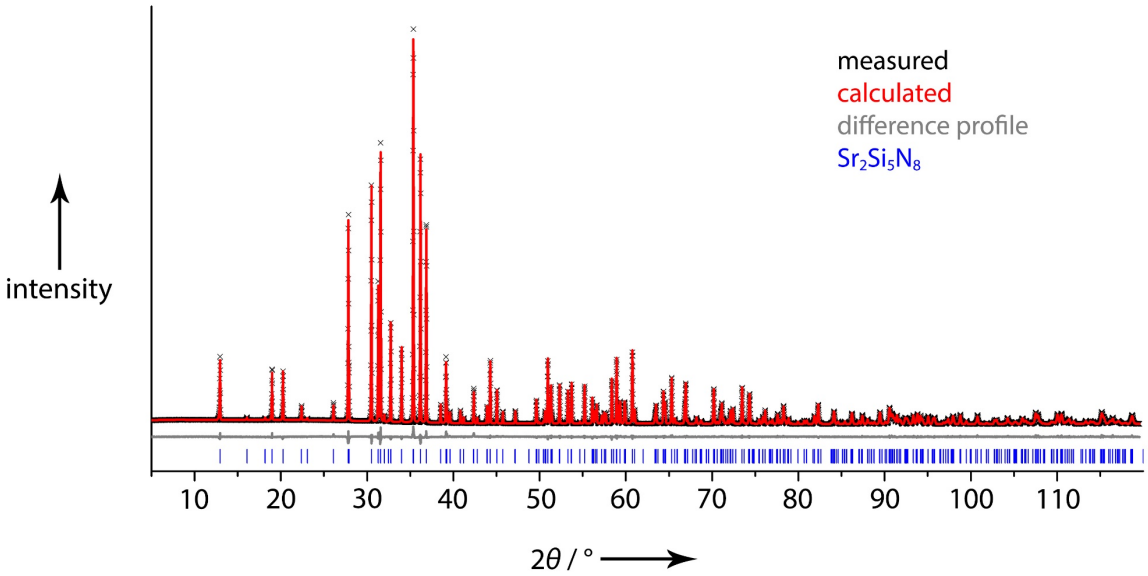


**Figure D.1:** RIETVELD refinement of $Sr_2Si_5N_8$ measured with Cu-K$\alpha_1$ radiation ($\lambda$ = 1.5406 Å).[23]

**Table D.4:** Crystallographic information on the starting material $Sr_2Si_5N_8$, least squares standard deviations in parentheses.

| **Formula** | **$Sr_2Si_5N_8$** |
|---|---|
| **Formula mass / g · mol$^{-1}$** | 427.72 |
| **Crystal system** | Orthorhombic |
| **Space group** | *Pmn*2$_1$ (no. 31) |
| **Lattice parameters / Å, °** | *a* = 5.71006(4)<br>*b* = 6.81914(5)<br>*c* = 9.33599(6) |
| **Cell volume / Å$^3$** | 363.522(4) |
| ***Z*** | 2 |
| **X-ray density / g · cm$^{-3}$** | 3.908 |
| **Linear absorption coefficient / mm$^{-1}$** | 27.1798(3) |
| **2*θ*-range / °** | 5.000–119.550 |
| **Temperature / °C** | 25(2) |
| **Data points** | 7638 |
| **Number of observed reflections** | 322 |
| **Number of parameters** | 33, thereof 12 for background |
| ***R*$_{wp}$** | 0.0399 |
| ***R*$_{exp}$** | 0.0202 |
| ***R*$_p$** | 0.0301 |
| ***R*$_{Bragg}$** | 0.0158 |
| ***GOF*** | 1.976 |

## D.4 Experimental Details on the Ion Exchange Reaction

Ion exchange was carried out in a fused silica ampoule under argon atmosphere. $Sr_2Si_5N_8$ and $PbCl_2$ were thoroughly mixed in an agate mortar and filled into a dry (high vacuum, 400 °C) silica ampoule.

**Table D.5:** Weighted sample for the ion exchange toward $Pb_2Si_5N_8$.

| $Sr_2Si_5N_8$ | $PbCl_2$ |
|---|---|
| 256.3 mg | 500 mg |
| 0.6 mmol | 1.8 mmol |

**Table D.6:** Temperature program of the tube furnace for the ion exchange leading to $Pb_2Si_5N_8$.

| Step | Starting T / °C | Target T / °C | t / h | ΔT / °C · h$^{-1}$ |
|---|---|---|---|---|
| 1 | 25 | 920 | 3 | 298 |
| 2 | 920 | 920 | 3 | 0 |
| 3 | 920 | 500 | 10 | −42 |

## D.5 Additional Crystallographic Data on $Pb_2Si_5N_8$

**Table D.7:** Crystallographic data for $Pb_2Si_5N_8$, least-squares standard deviations in parentheses.

| Formula | $Pb_2Si_5N_8$ |
|---|---|
| Formula mass / g · mol$^{-1}$ | 666.90 |
| Crystal system | orthorhombic |
| Space group | *Pmn*2$_1$ (no. 31) |
| *Z* | 2 |
| *F*(000) | 580 |
| Cell parameters / Å | *a* = 5.774(1)<br>*b* = 6.837(1)<br>*c* = 9.350(1) |
| Cell volume / Å$^3$ | 369.11(9) |
| Calculated density *ρ* / g · cm$^{-3}$ | 6.001 |
| Abs. coefficient $\mu$ /mm$^{-1}$ | 5.362 |
| Radiation | Synchrotron, $\lambda$ = 0.309 Å |
| Temperature / °C | 25(2) |
| $\theta$ range / deg. | $1.604 \leq \theta \leq 13.120$ |
| Total no. of reflections | 6540 |
| Independent reflections | 1268 |
| $R_{int}$, $R_\sigma$ | 0.051, 0.049 |
| Refined parameters | 60 |
| Goodness of fit | 1.058 |
| $R_1$ (all data), $R_1$ [$F^2 > 2\sigma(F^2)$] | 0.023, 0.023 |
| $wR_2$ (all data), $wR_2$ [$F^2 > 2\sigma(F^2)$] | 0.055, 0.055 |
| $\Delta\rho_{max}$, $\Delta\rho_{min}$ / e · Å$^{-3}$ | 1.433, −2.439 |

**Table D.8:** List of interatomic distances (Å) in $Pb_2Si_5N_8$, least-squares standard deviations in parentheses.

| **Distances** | | | | | |
|---|---|---|---|---|---|
| Pb1–N5 | 2.362(10) | Pb2–Pb1 | 3.1902(5) | Si2–N5 | 1.726(10) |
| Pb1–N2 | 2.453(7) | Pb2–N3 | 3.311(6) | Si2–N2 | 1.732(6) |
| Pb1–N1 | 2.977(2) | Pb2–N2 | 3.328(9) | Si2–N1 | 1.736(10) |
| Pb1–Pb2 | 3.1902(5) | Pb2–Pb1 | 3.4175(5) | | |
| Pb1–N4 | 3.293(9) | | | Si3–N1 | 1.704(10) |
| Pb1–Pb2 | 3.4175(5) | Si1–N2 | 1.714(5) | Si3–N3 | 1.765(8) |
| | | Si1–N4 | 1.738(5) | Si3–N6 | 1.770(12) |
| Pb2–N1 | 2.397(9) | Si1–N6 | 1.741(6) | | |
| Pb2–N2 | 2.496(7) | Si1–N3 | 1.750(6) | Si4–N5 | 1.705(10) |
| Pb2–N5 | 2.970(2) | | | Si4–N4 | 1.736(10) |
| | | | | Si4–N3 | 1.755(8) |

**Table D.9:** List of bond angles (°) in $Pb_2Si_5N_8$, least squares standard deviations in parentheses.

| **Angles** | | | | | |
|---|---|---|---|---|---|
| Si3–N1–Si2 | 142.9(6) | Si2–N2–Pb2 | 101.6(3) | Si1–N4–Si1 | 113.0(5) |
| Si3–N1–Pb2 | 118.1(4) | Pb1–N2–Pb2 | 80.3(2) | | |
| Si2–N1–Pb2 | 99.0(4) | | | Si4–N5–Si2 | 138.2(6) |
| | | Si1–N3–Si4 | 117.2(4) | Si4–N5–Pb1 | 118.0(5) |
| Si1–N2–Si2 | 126.7(4) | Si1–N3–Si3 | 115.4(4) | Si2–N5–Pb1 | 103.9(4) |
| Si1–N2–Pb1 | 120.8(4) | Si4–N3–Si3 | 127.4(4) | | |
| Si1–N2–Pb2 | 114.3(4) | | | Si1–N6–Si1 | 111.3(5) |
| Si2–N2–Pb1 | 102.5(3) | Si4–N4–Si1 | 123.4(3) | Si1–N6–Si3 | 119.5(3) |

**Table D.10:** Fractional atomic coordinates, isotropic displacement parameters, and site occupancies in $Pb_2Si_5N_8$, least-squares standard deviations in parentheses.

| **Atom** | **Wyckoff site** | ***x*** | ***y*** | ***z*** | $U_{iso}$, $U_{eq}$ / Å$^2$ | **Occupancy** |
|---|---|---|---|---|---|---|
| Pb1 | 2*a* | 0 | 0.08528(5) | 0.99944(3) | 0.01059(14) | 1 |
| Pb2 | 2*a* | 0 | 0.07056(5) | 0.65841(3) | 0.01135(14) | 1 |
| Si1 | 4*a* | 0.7490(3) | 0.3451(3) | 0.3291(3) | 0.0048(3) | 1 |
| Si2 | 2*a* | 0 | 0.9476(4) | 0.3313(6) | 0.0051(4) | 1 |
| Si3 | 2*a* | 0 | 0.5755(4) | 0.5495(6) | 0.0057(7) | 1 |
| Si4 | 2*a* | 0 | 0.5942(4) | 0.1061(5) | 0.0042(7) | 1 |
| N1 | 2*a* | 0 | 0.8096(12) | 0.4872(10) | 0.009(2) | 1 |
| N2 | 4*a* | 0.7559(11) | 0.0947(7) | 0.3365(10) | 0.0072(9) | 1 |
| N3 | 4*a* | 0.7535(14) | 0.5525(8) | 0.0006(6) | 0.0072(12) | 1 |
| N4 | 2*a* | 0 | 0.4283(11) | 0.2466(11) | 0.007(2) | 1 |
| N5 | 2*a* | 0 | 0.8286(13) | 0.1686(10) | 0.011(2) | 1 |
| N6 | 2*a* | 0 | 0.5816(12) | 0.7388(11) | 0.004(2) | 1 |

**Table D.11:** Anisotropic displacement parameters for $Pb_2Si_5N_8$, least-squares standard deviations in parentheses.

| Atom | $U_{11}$/ Å² | $U_{22}$ / Å² | $U_{33}$ / Å² | $U_{23}$ / Å² | $U_{13}$ / Å² | $U_{12}$ / Å² |
|---|---|---|---|---|---|---|
| Pb1 | 0.0102(3) | 0.0098(2) | 0.0117(2) | −0.00027(12) | 0 | 0 |
| Pb2 | 0.0110(3) | 0.0113() | 0.0118(2) | −0.00031(13) | 0 | 0 |
| Si1 | 0.0028(7) | 0.0050(7) | 0.0066(5) | 0.0002(7) | −0.0003(8) | 0.0004(5) |
| Si2 | 0.0023(11) | 0.0053(9) | 0.0076(9) | 0.0010(12) | 0 | 0 |
| Si3 | 0.003(2) | 0.0056(13) | 0.0088(14) | 0.0009(7) | 0 | 0 |
| Si4 | 0.003(2) | 0.0052(11) | 0.0042(13) | 0.0013(9) | 0 | 0 |

## D.6 Rietveld Refinement of $Pb_2Si_5N_8$

A sample of $Pb_2Si_5N_8$ was rarefied with 150 equivalents of LiH to circumvent strong absorption effects using Cu-K$\alpha_1$ radiation. The RIETVELD refinement has been performed using the single crystal structure of $Pb_2Si_5N_8$ only refining the lattice parameters.

**Table D.12:** Crystallographic information (PXRD) on $Pb_2Si_5N_8$, least squares standard deviations in parentheses.

| Formula | $Pb_2Si_5N_8$ |
|---|---|
| **Formula mass / g · mol$^{-1}$** | 666.88 |
| **Crystal system** | orthorhombic |
| **Space group** | *Pmn*2$_1$ (no. 31) |
| **Lattice parameters / Å, °** | *a* = 5.77174(5)<br>*b* = 6.83689(6)<br>*c* = 9.35102(8) |
| **Cell volume / Å$^3$** | 368.998(6) |
| ***Z*** | 2 |
| **Radiation** | 1.5406 Å |
| **Radiation source** | Cu-K$\alpha_1$ |
| **X-ray density / g · cm$^{-3}$** | 6.00212(9) |
| **Linear absorption coefficient / mm$^{-1}$** | 93.2598(13) |
| **2$\theta$-range / °** | 5.000–119.555 |
| **Temperature / °C** | 25(2) |
| **Data points** | 7638 |
| **Number of observed reflections** | 328 |
| **Number of parameters,** | 44, thereof 16 background |
| $R_{wp}$ | 0.0918 |
| $R_{exp}$ | 0.0940 |
| $R_p$ | 0.0693 |
| $R_{Bragg}$ | 0.0213 |
| ***GOF*** | 0.976 |

## D.7 Details on SEM and EDX

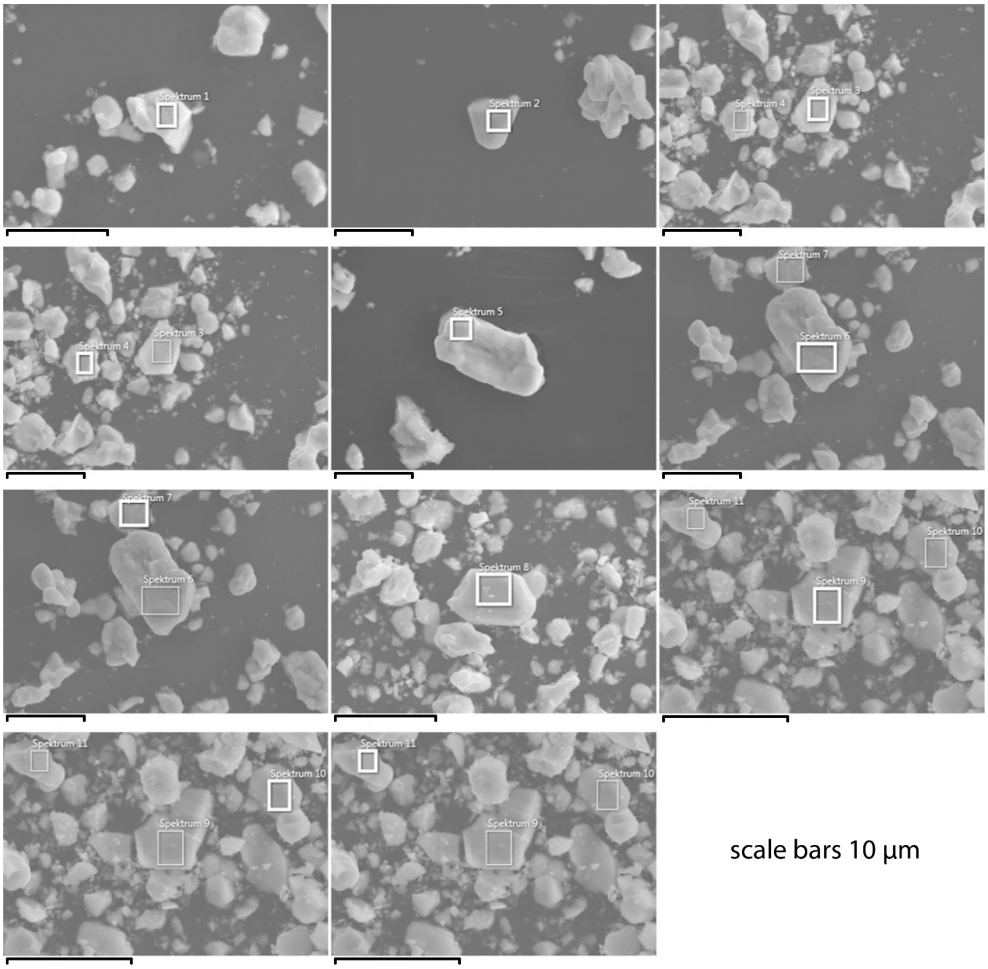


**Figure D.2:** Scanning electron micrographs of a $Pb_2Si_5N_8$ powder sample.

**Table D.13:** EDX analysis (atomic percent of Pb and Si) of $Pb_2Si_5N_8$ powder shown in Figure D.2.

| | Spectrum 1 | Spectrum 2 | Spectrum 3 | Spectrum 4 | Spectrum 5 | Spectrum 6 | Spectrum 7 |
|---|---|---|---|---|---|---|---|
| **Si** | 29 | 30 | 28 | 34 | 27 | 32 | 29 |
| **Pb** | 12 | 13 | 10 | 13 | 11 | 11 | 12 |
| **Pb/Si** | 2/4.8 | 2/4.6 | 2/5.6 | 2/5.2 | 2/4.9 | 2/5.8 | 2/4.8 |

| | Spectrum 8 | Spectrum 9 | Spectrum | Spectrum | Theoretical | Average |
|---|---|---|---|---|---|---|
| **Si** | 32 | 32 | 32 | 25 | 33 | 30 |
| **Pb** | 14 | 12 | 13 | 10 | 13 | 12 |
| **Pb/Si** | 2/4.6 | 2/5.3 | 2/4.9 | 2/5 | 2/5 | 2/5 |

The analysis of Pb and Si by EDX fits well to the theoretical composition "$Pb_2Si_5N_8$".

## D.8 Details on ICP-OES

**Table D.14:** ICP-OES analysis of $Pb_2Si_5N_8$.

| Element | Amount / mg · g$^{-1}$ | Atomic % | Atomic % calculated for $Pb_2Si_5N_8$ |
|---|---|---|---|
| Pb | 621.5 | 13.4 | 13.3 |
| Sr | not detectable | 0.0 | 0.0 |
| Si | 211.7 | 33.6 | 33.3 |
| Na | 166.8 | 53.0 | 53.3 |

[a] values for nitrogen were calculated from the difference to 1 g

The experimental values of ICP-OES for $Pb_2Si_5N_8$ are in good agreement with the assumed composition of the compound.

## D.9 Details on CHNS Analysis

Nitrogen content was determined to 17.2(3) mass%. The result matches the theoretical value for $Pb_2Si_5N_8$ of 16.8 mass%.

## D.10 Details on UV-Vis

The measured reflectance ($R$) spectrum was converted to a pseudoabsorption spectrum applying the Kubelka-Munk function $F(R) = (1-R)^2/2R$.[24] Concerning uncertainties, the choice of the Kubelka-Munk exponent $1/n$ ($n$ = ½ for direct or $n$ = 2 for indirect band gap) has no significant influence due to similar values for the resulting band gap (Figure D.3).

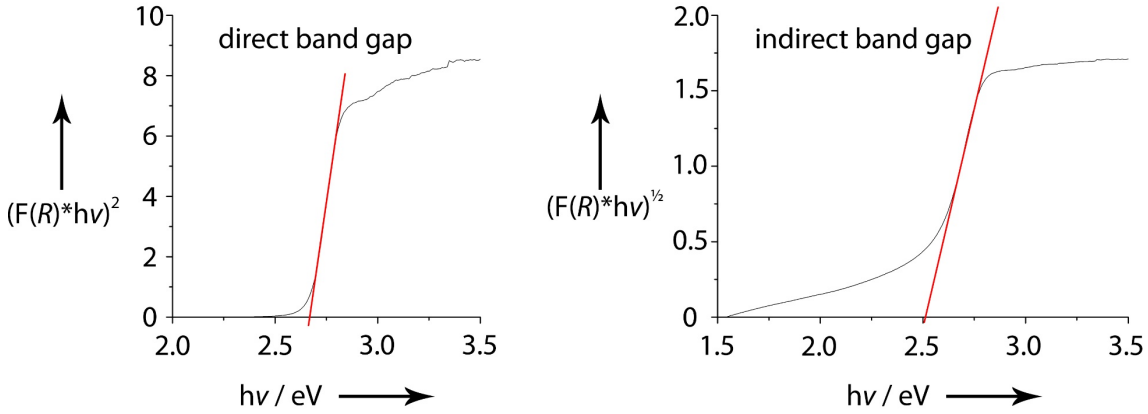


**Figure D.3:** Tauc plots ($n$ = ½, left; $n$ = 2, right) for $Pb_2Si_5N_8$.

## D.11 XPS

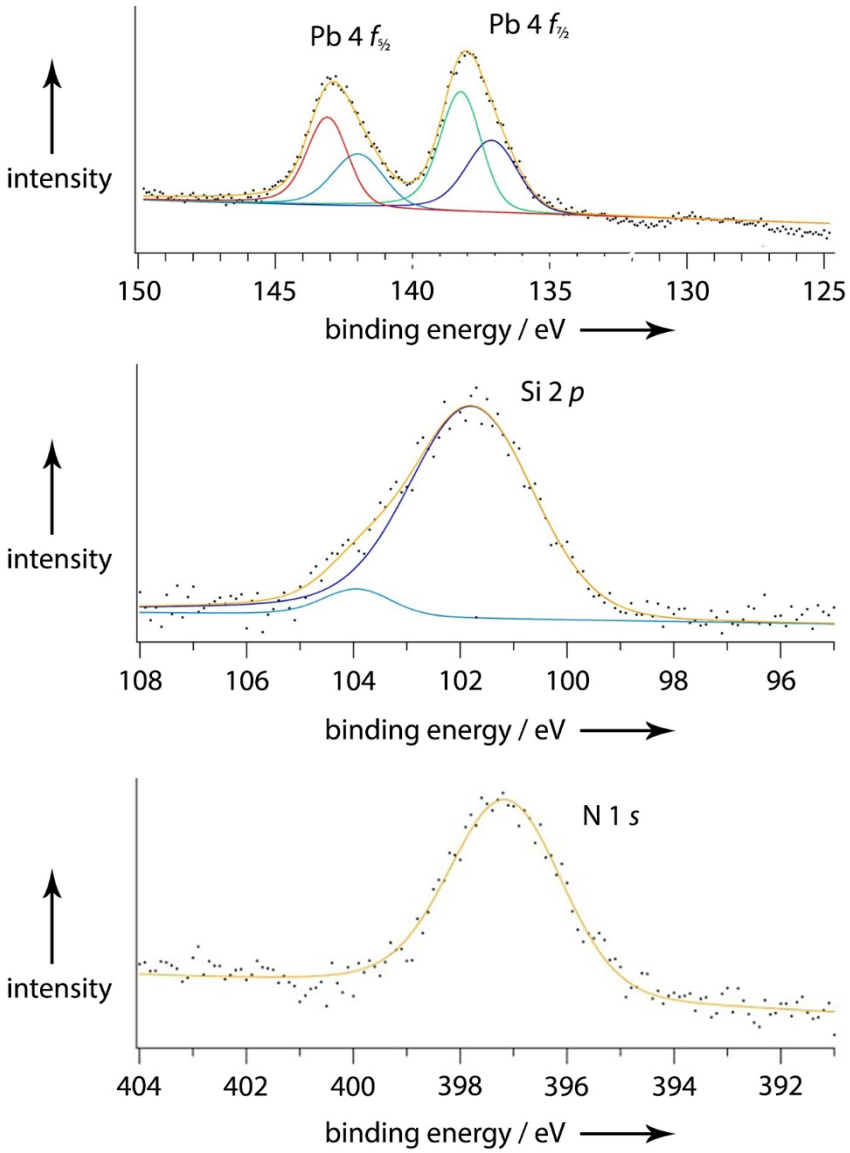


**Figure D.4:** X-ray photoelectron spectra of a $Pb_2Si_5N_8$ sample.

On the one hand, lead species are observed at binding energies that are attributed to lead oxides in the literature.[25] This observation can be attributed to possible amorphous Pb/Si/N phases on the sputtered surface. On the other hand, the analysis of the Pb $4f_{7/2}$ signal clearly shows the presence of a second Pb component at lower binding energies. The signal at around 137.0 eV, which is attributed to elemental Pb in literature, thus hints at the presence of a more covalently bound Pb species as indicated by the reduced charge for Pb(II).[26] The data were validated by the Si 2*p* and N 1*s* signals showing excellent agreement with literature values for silicon nitride at 101.7 and 397.1 eV, respectively.[27]

## D.12 Raman vs. DPS

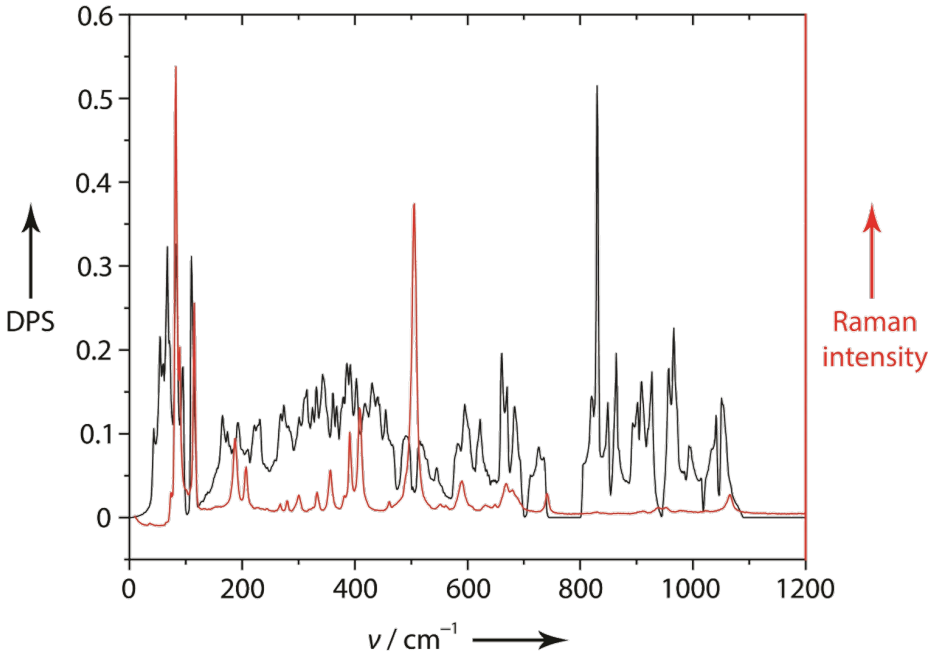


**Figure D.5:** Raman spectrum of a $Pb_2Si_5N_8$ sample (red) compared to calculated DPS states (black).

Figure D.5 depicts the calculated DPS compared to the experimentally determined Raman spectrum. The DPS does not show any imaginary phonon modes which would indicate dynamical instability. Therefore, the crystal structure is at least a local minimum on the potential energy surface. The signals of the Raman spectrum can all be found in the DPS. The Raman modes therefore can be assigned by the analysis of the eigenvectors of the theoretical DPS. The intensities cannot be compared directly, since the DPS is a picture of the number of states accessible in a given frequency range over the whole Brillouin zone. The experimental Raman intensity depends on other factors.

At wavenumbers of ca. 117 $cm^{-1}$, a stretching vibration of the Pb atoms is clearly visible. The crystal structure together with the respective eigenvectors is shown in Figure D.6.

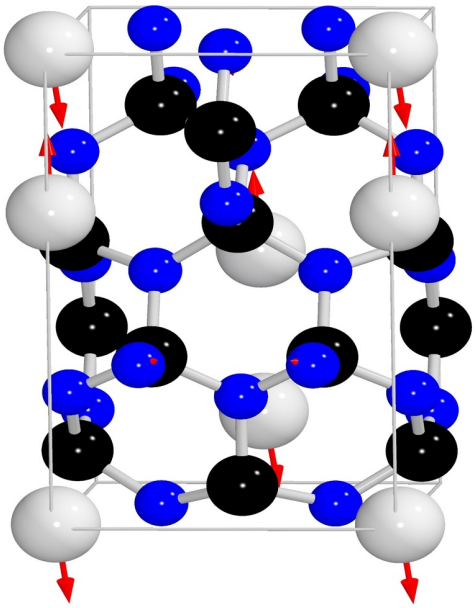

**Figure D.6:** Crystal structure of $Pb_2Si_5N_8$ together with the eigenvectors (red arrows) of the 14$^{th}$ vibrational mode ($\nu$ = 117 $cm^{-1}$) at the gamma point; gray: Pb, black: Si, blue: N.

## D.13 DFT

**Table D.15:** Crystallographic data from the experiment and optimization calculations without and with spin-orbit coupling (SOC), standard deviations in parentheses.

| Parameter / Å | Experimental | Opt. non-SOC | Opt. SOC |
|---|---|---|---|
| ***a*** | 5.774(1) | 5.808 | 5.810 |
| ***b*** | 6.837(1) | 6.900 | 6.905 |
| ***c*** | 9.350(1) | 9.431 | 9.430 |
| **first-nearest Pb–Pb** | 3.190(1) | 3.241 | 3.232 |
| **second-nearest Pb–Pb** | 3.4175(5) | 3.457 | 3.451 |
| **first-nearest Pb–Si** | 3.172(6) | 3.197 | 3.197 |
| **second-nearest Pb–Si** | 3.243(5) | 3.276 | 3.276 |
| **first-nearest Pb–N** | 2.362(9) | 2.434 | 2.434 |
| **second-nearest Pb–N** | 2.397(9) | 2.459 | 2.459 |

**Table D.16:** Total energy (measured relative to the non-SOC total energy), band gap, and integrated COHP (ICOHP) of the 1.71 Å Si–N bond, the 2.36 Å Pb–N bond, and the 3.19 Å Pb–Pb bond for the non-SOC and SOC calculations.

| Quantity | Non-SOC | SOC |
|---|---|---|
| **Δ*E* / eV** | 0 | −0.903 |
| **band gap / eV** | 1.7 | 1.5 |
| **ICOHP(Si–N) / eV** | −7.68 | −7.61 |
| **ICOHP(Pb–N) / eV** | −2.62 | −2.63 |
| **ICOHP(Pb–Pb) / eV** | −1.26 | −1.25 |

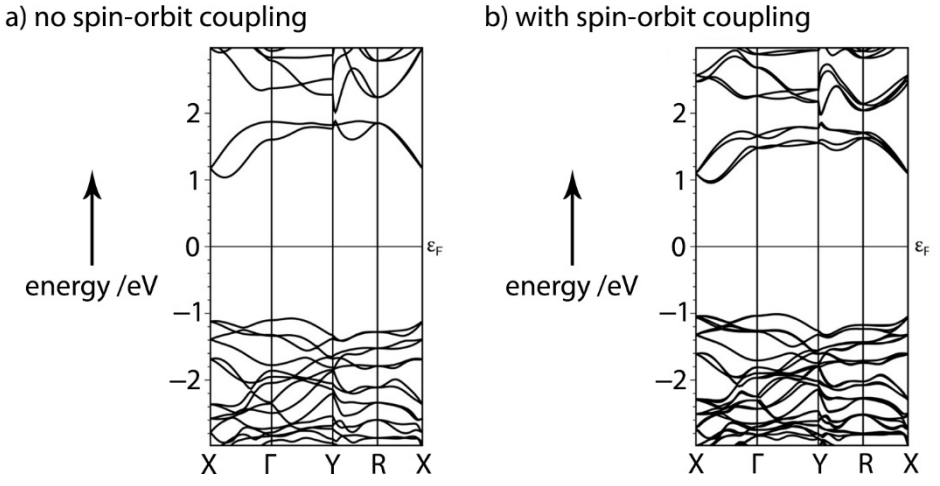


**Figure D.7:** Electronic band structure without a) and b) with spin-orbit coupling for $Pb_2Si_5N_8$, both calculated using the experimental crystallographic data. The energy axis is shown relative to the Fermi level ($\varepsilon_F$). The effects of spin-orbit splitting (right) are hardly visible within the valence region but become slightly more prominent in the conduction bands.

## D.14 DTA/TGA Investigation of $Pb_2Si_5N_8$

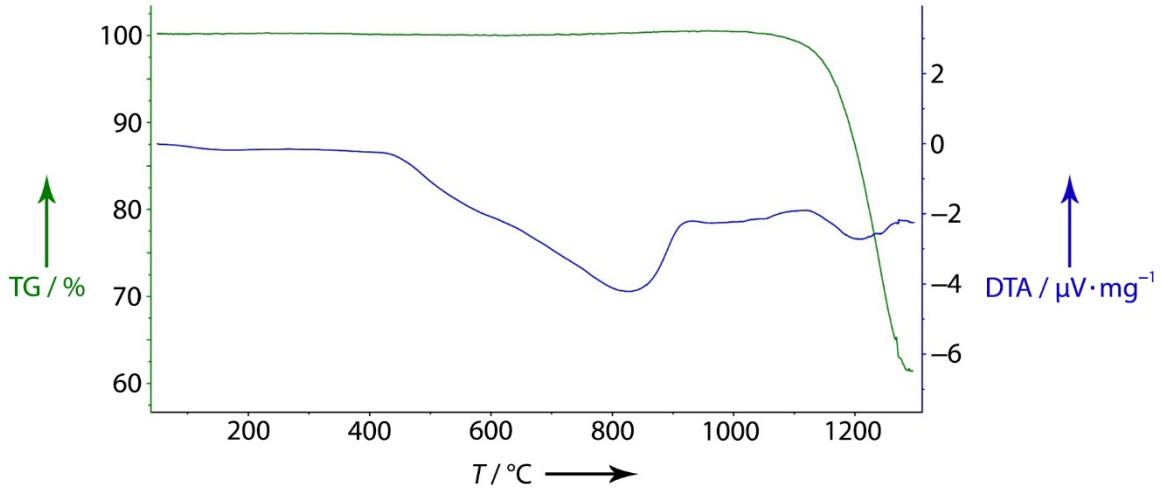


**Figure D.8:** DTA/TGA investigation (15 °C · $min^{-1}$) of a $Pb_2Si_5N_8$ sample ($N_2$ atmosphere) showing a mass loss of about 40% at temperatures greater than 1000 °C.

## D.15 References

[1] T. L. Barr, S. Seal, "Nature of the use of adventitious carbon as a binding energy standard", *J. Vac. Sci. Technol., A* **1995**, *13*, 1239–1246.

[2] S. Doniach, M. Šunjić, "Many-electron singularity in X-ray photoemission and X-ray line spectra from metals", *J. Phys. C: Solid State Phys.* **1970**, *3*, 285–291.

[3] Agilent Technologies, *CrysAlis Pro*, Yarnton, Oxfordshire, England, **2011**.

[4] Bruker AXS, Inc., *SADABS*, Madison, Wisconsin, USA, **2001**.

[5] G. Wu, B. L. Rodrigues, P. Coppens, "The correction of reflection intensities for incomplete absorption of high-energy X-rays in the CCD phosphor", *J. Appl. Crystallogr.* **2002**, *35*, 356–359.

[6] a) G. M. Sheldrick, *Acta Crystallogr., Sect. A: Found. Crystallogr.* **2008**, *64*, 112–122; b) G. M. Sheldrick, *SHELXS* – A Program for Crystal Structure Solution, University of Göttingen, Germany, **1997**.

[7] a) H. M. Rietveld, "A Profile Refinement Method for Nuclear and Magnetic Structures", *J. Appl. Crystallogr.* **1969**, *2*, 65–71; b) A. A. Coelho, *TOPAS-Academic*, Version 4.1, Coelho Software, Brisbane (Australia), **2007**.

[8] a) R. W. Cheary, A. Coelho, "A Fundamental Parameters Approach to X-Ray Line-Profile Fitting", *J. Appl. Crystallogr.* **1992**, *25*, 109–121; b) R. W. Cheary, A. A. Coelho, J. P. Cline,

"Fundamental Parameters Line Profile Fitting in Laboratory Diffractometers", *J. Res. Natl. Inst. Stand. Technol.* **2004**, *109*, 1–25.

[9] a) G. Kresse, J. Furthmüller, "Efficiency of ab-initio total energy calculations for metals and semiconductors using a plane-wave basis set", *Comput. Mater. Sci.* **1996**, *6*, 15–50; b) G. Kresse, D. Joubert, "From ultrasoft pseudopotentials to the projector augmented-wave method", *Phys. Rev. B* **1999**, *59*, 1758–1775.

[10] P. E. Blöchl, "Projector augmented-wave method", *Phys. Rev. B* **1994**, *50*, 17953–17979.

[11] J. P. Perdew, K. Burke, M. Ernzerhof, "Generalized Gradient Approximation Made Simple", *Phys. Rev. Lett.* **1996**, *77*, 3865–3868.

[12] a) S. Grimme, J. Antony, S. Ehrlich, H. Krieg, "A consistent and accurate ab initio parametrization of density functional dispersion correction (DFT-D) for the 94 elements H–Pu", *J. Chem. Phys.* **2010**, *132*, 154104; b) S. Grimme, S. Ehrlich, L. Goerigk, "Effect of the Damping Function in Dispersion Corrected Density Functional Theory", *J. Comput. Chem.* **2011**, *32*, 1456–1465.

[13] H. J. Monkhorst, J. D. Pack, "Special points for Brillouin-zone integrations", *Phys. Rev. B* **1976**, *13*, 5188–5192.

[14] A. Togo, I. Tanaka, "First principles phonon calculations in materials science", *Scr. Mater.* **2015**, *108*, 1–5.

[15] a) R. P. Stoffel, C. Wessel, M.-W. Lumey, R. Dronskowski, "Ab Initio Thermochemistry of Solid-State Materials", *Angew. Chem., Int. Ed.* **2010**, *49*, 5242–5266; "Ab-initio-Thermochemie fester Stoffe", *Angew. Chem.* **2010**, *122*, 5370–5395; b) R. P. Stoffel, K. Philipps, R. Conradt, R. Dronskowski, "A First-Principles Study on the Electronic, Vibrational, and Thermodynamic Properties of Jadeite and its Tentative Low-Density Polymorph", *Z. Anorg. Allg. Chem.* **2016**, *642*, 590–596; c) R. P. Stoffel, R. Dronskowski, "Barium Peroxide: a Simple Test Case for First-Principles Investigations on the Temperature Dependence of Solid-State Vibrational Frequencies", *Z. Anorg. Allg. Chem.* **2012**, *638*, 1403–1406.

[16] B. Eck, *wxDragon 2.1.6*, RWTH Aachen University **1994–2018**.

[17] a) X. Gonze, B. Amadon, P.-M. Anglade, J.-M. Beuken, F. Bottin, P. Boulanger, F. Bruneval, D. Caliste, R. Caracas, M. Côté, T. Deutsch, L. Genovese, Ph. Ghosez, M. Giantomassi, S.

Goedecker, D. R. Hamann, P. Hermet, F. Jollet, G. Jomard, S. Leroux, M. Mancini, S. Mazevet, M. J. T. Oliveira, G. Onida, Y. Pouillon, T. Rangel, G.-M. Rignanese, D. Sangalli, R. Shaltaf, M. Torrent, M. J. Verstraete, G. Zerah, J. W. Zwanziger, "ABINIT: First-principles approach to material and nanosystem properties", *Comput. Phys. Commun.* **2009**, *180*, 2582–2615; b) M. Torrent, F. Jollet, F. Bottin, G. Zérah, X. Gonze, "Implementation of the projector augmented-wave method in the ABINIT code: Application to the study of iron under pressure", *Comput. Mater. Sci.* **2008**, *42*, 337–351.

[18] F. Jollet, M. Torrent, N. Holzwarth, "Generation of Projector Augmented-Wave atomic data: A 71 element validated table in the XML format", *Comput. Phys. Commun.* **2014**, *185*, 1246–1254.

[19] a) S. Maintz, V. L. Deringer, A. L. Tchougréeff, R. Dronskowski, "Analytic Projection From Plane-Wave and PAW Wavefunctions and Application to Chemical-Bonding Analysis in Solids", *J. Comput. Chem.* **2013**, *34*, 2557–2567; b) S. Maintz, V. L. Deringer, A. L. Tchougréeff, R. Dronskowski, "LOBSTER: A Tool to Extract Chemical Bonding from Plane-Wave Based DFT", *J. Comput. Chem.* **2016**, *37*, 1030–1035.

[20] *Origin 6.1*, OriginLab Corporation, **1991–2000**.

[21] K. Brandenburg, *Diamond Version 3.2k* **2014**.

[22] P. J. Schmidt, W. Mayr, B. S. Schreinemacher, J. Meyer, H. H. Bechtel, "Red Emitting Luminescent Materials", PCT/IB2011/055329, **2011**.

[23] T. Schlieper, W. Milius, W. Schnick, "Nitrido-silicate. II Hochtemperatur-Synthesen und Kristallstrukturen von $Sr_2Si_5N_8$ und $Ba_2Si_5N_8$", *Z. Anorg. Allg. Chem.* **1995**, *621*, 1380–1384.

[24] R. López, R. Gómez, "Band-gap energy estimation from diffuse reflectance measurements on sol–gel and commercial $TiO_2$: a comparative study", *J. Sol-Gel Sci. Technol.* **2012**, *61*, 1–7.

[25] K. S. Kim, T. J. O'Leary, N. Winograd, "X-Ray Photoelectron Spectra of Lead Oxides", *Anal. Chem.* **1973**, *45*, 2214–2218.

[26] M. J. Bozack, K. W. Bryant, "Elemental Lead by XPS", *Surf. Sci. Spectra* **1992**, *1*, 324–327.

[27] a) T. N. Wittberg, J. R. Hoenigman, W. E. Moddeman, C. R. Cothern, M. R. Gulett, "AES and XPS of silicon nitride films of varying refractive indices", *J. Vac. Sci. Technol.* **1978**, *15*, 348–352; b) Z. H. Lu, S. P. Tay, R. Cao, P. Pianetta, "The effect of rapid thermal $N_2O$ nitridation on the oxide/Si(100) interface structure", *Appl. Phys. Lett.* **1995**, *67*, 2836–2838.

# E Miscellaneous

## E.1 List of Publications

### 1. Increased Synthetic Control –Gaining Access to Predicted $Mg_2Si_5N_8$ and β-$Ca_2Si_5N_8$

P. Bielec, W. Schnick,

published in: *Angew. Chem., Int. Ed.* **2017**, *56*, 4810–4813.

published in: *Angew. Chem.* **2017**, *129*, 4888–4891.

Reprinted (adapted) in this thesis with permission from *Angewandte Chemie, International Edition* (4543630978968) and *Angewandte Chemie* (4543631322947).

Conceptualization, syntheses, analyses, and composition of the article were done by Philipp Bielec. Wolfgang Schnick supervised the work. Both authors revised the manuscript.

### 2. $Fe_2Si_5N_8$: Access to Open-Shell Transition-Metal Nitridosilicates

P. Bielec, O. Janka, T. Block, R. Pöttgen, W. Schnick

published in: *Angew. Chem., Int. Ed.* **2018**, 57, 2409–2412.

published in: *Angew. Chem.* **2018**, *130*, 2433–2436.

Reprinted (adapted) in this thesis with permission from *Angewandte Chemie, International Edition* (4543640314417) and *Angewandte Chemie* (4543640092908).

Conceptualization, syntheses, analyses and organization of the project was done by Philipp Bielec. Oliver Janka performed magnetic characterization, Theresa Block performed Mößbauer spectroscopy. Rainer Pöttgen supervised the magnetic and Mößbauer characterization. The manuscript was written by Philipp Bielec in a leading role with support of all co-authors. Wolfgang Schnick supervised the project. All authors revised the manuscript.

## 3. Targeting Vacancies in Nitridosilicates: Aliovalent Substitution of $M^{2+}$ ($M$ = Ca, Sr) by $Sc^{3+}$ and $U^{3+}$

P. Bielec, L. Eisenburger, H. L. Deubner, D. Günther, F. Kraus, O. Oeckler, W. Schnick

published in: *Angew. Chem., Int. Ed.* **2019**, *58*, 840–843.

published in: *Angew. Chem.* **2019**, *131*, 850–853.

Reprinted (adapted) in this thesis with permission from *Angewandte Chemie, International Edition* (4543640576393) and *Angewandte Chemie* (4543640505064).

Conceptualization, most of the syntheses, part of the analyses and organization of the project was done by Philipp Bielec. Preparation and postprocessing of the microfocused X-ray analysis were done by Lucien Eisenburger, supported by Daniel Günther. STEM investigations were performed by Lucien Eisenburger. Preparation of the precursor $UCl_3$ was done by H. Lars Deubner. Florian Kraus supervised the handling of uranium compounds. Oliver Oeckler supervised the microfocused X-ray analysis. Wolfgang Schnick supervised the project. The manuscript was written by Philipp Bielec in a leading role with support of all co-authors. All authors revised the manuscript.

## 4. Cationic $Pb_2$ Dumbbells Stabilized in the Highly Covalent Lead Nitridosilicate $Pb_2Si_5N_8$

P. Bielec, R. Nelson, R. Stoffel, L. Eisenburger, D. Günther, A.-K. Henß, J. P. Wright, O. Oeckler, R. Dronskowski, W. Schnick

published in: *Angew. Chem., Int. Ed.* **2019**, *58*, 1432–1436.

published in: *Angew. Chem.* **2019**, *131*, 1446–1450.

Reprinted (adapted) in this thesis with permission from *Angewandte Chemie, International Edition* (4543640664015) and *Angewandte Chemie* (4543640730482).

Conceptualization, syntheses, part of the analyses and organization of the project was done by Philipp Bielec. Ryky Nelson analyzed the bonding situation by DFT methodes. Ralf Stoffel performed DFT based phonon calculations. Preparation and postprocessing of the microfocused X-ray analysis were done by Lucien Eisenburger, supported by Daniel Günther. Ann-Kathrin Henß performed XPS analysis. Jonathan P. Wright and Oliver Oeckler supervised the microfocused X-ray analysis. Richard

Dronskowski supervised the theoretical investigations on $Pb_2Si_5N_8$. Wolfgang Schnick supervised the project. The manuscript was written by Philipp Bielec in a leading role with support of all co-authors. All authors revised the manuscript.

## E.2 Conference Talks

### 1. Scandium – Die Suche nach neuen Verbindungen

2nd Obergurgl-Seminar Festkörperchemie, **2016**

### 2. Partnertausch

52nd Hemdsärmelkolloquium, Augsburg, **2017**

### 3. Den Silicaten auf den Fersen

3rd Obergurgl-Seminar Festkörperchemie, **2018**

### 4. Im Grenzbereich

53rd Hemdsärmelkolloquium, Leipzig, **2018**

### 5. $U_{0.5x}Sr_{2-0.75x}Si_5N_8$ – Immobilisierung von Uran

4th Obergurgl-Seminar Festkörperchemie, **2019**